High-Pressure Experiments with Application to Naturally Fractured Chalk Reservoirs

1. Constant Volume Diffusion

2. Gas-Oil Capillary Pressure

by

Kjell R. Christoffersen

A Dissertation for the Partial Fulfillment
of Requirements for the
Degree of Doktor Ingeniør

Division of Petroleum Engineering
and Applied Geophysics
The Norwegian Institute of Technology
University of Trondheim

December 1992

Preface

This work has been a part of the Joint Chalk Research Program, Phase III from June 1990 to June 1992, and divided into two subprojects; *Constant Volume Diffusion Experiment* (4-1a) and *High-Pressure Capillary Pressure Experiment* (4-1b).

Two papers were presented that contained most of the results in Chapter 2 and 3:

Christoffersen, K.R., Whitson, C.H., da Silva, F.V., and Haldoupis, A.J.: "Measuring Capillary Pressure of Chalk Samples at Elevated Pressures and Varying Interfacial Tension," Fourth North Sea Chalk Symposium, Sept. 21-23, Deauville, France (1992).

Christoffersen, K.R., Whitson, C.H., da Silva, F.V., and Haldoupis, A.J.: "A Simple Method for Measuring Liquid Diffusion Coefficients at High Pressure," Fourth North Sea Chalk Symposium, Sept. 21-23, Deauville, France (1992).

Trondheim, December 1992
Kjell Christoffersen

Acknowledgement

I wish to express my deepest and sincerest thanks to my supervisor Professor Curtis H. Whitson for his excellent guidance and encouragement through many fruitful discussions. I also wish to thank Andreas J. Haldoupis for doing most of the initial experiments and core characterization, and helping me with the time-consuming laboratory work. During the four years of this study I have also had several useful discussions with other colleagues at the Division of Petroleum Engineering and Applied Geophysics.

The constant volume diffusion simulations would not have been possible without the help from Michael L. Michelsen at DTH, Denmark. He developed and wrote the core of the numerical simulation model, using an exceptionally efficient solution method.

I would like to thank François Kalaydjian from IFP (Institut Français du Pétrole) and Flavio da Silva from Petrofina S.A. for serving in my Graduate Committee. I would also like to thank Alf Svindland in Fina Exploration Norway for his cooperation.

Financial support for this work was provided by:

- The North Sea Chalk Research Program - Phase III
- The Norwegian Institute of Technology Scholarship Fund
- Society of Petroleum Engineers - Stavanger Section
- Lise and Arnfinn Hejes Fund
- The Norwegian Institute of Technology Fund

Finally, I will thank my wife, Sigrid Eri, for her patience with my work and support when I most needed it.

Summary

Constant Volume Diffusion

Accurately estimated diffusion coefficients are important for evaluating enhanced oil recovery by gas injection into naturally fractured chalk reservoirs. If the fracture spacing is small, the recovery mechanism may be affected significantly by molecular diffusion, particularly when injecting a non-equilibrium gas such as nitrogen.

A fast and simple procedure for obtaining experimental liquid diffusion coefficients at high pressures has been developed. A constant volume cell is charged initially with a liquid such as decane and a vapor such as nitrogen. The transient change in pressure and liquid level as the system approaches equilibrium is mainly determined by the liquid diffusion coefficient, and to a lesser extent by the vapor diffusion coefficient.

This experiment is simulated with a numerical model, and the measured pressure and liquid level changes are matched by modifying the liquid diffusion coefficient. An initial estimate of the diffusion coefficient is given by the extended Sigmund correlation, which is simple and requires only component critical properties and other parameters used in an equation of state compositional simulator. The extended Sigmund correlation is also tested with 356 published experimental high-pressure vapor and liquid diffusion coefficients. Both binary and self diffusion data were used and are included in Appendix A.

Data are presented for 27 binary systems using nitrogen and methane as the gas phase, and n-pentane, n-octane, n-decane, and n-hexadecane as the liquid phase. Initial pressures of 100 and 180 bar were used, except for the C_1-nC_5 system where the maximum pressure was 150 bar to maintain two-phase conditions. The temperature was held constant at about 22°C. The measured diffusion coefficients follow the extended Sigmund correlation quite well for both the nitrogen and the methane experiments, with a few exceptions. For the 180 bar experiments, when the methane concentration in the liquid is high, the extended Sigmund correlation underpredicts the diffusion coefficients for C_1-nC_8 and C_1-nC_{10} by almost 50%. For C_1-nC_{16} the diffusion correction factor at 180 bar was higher than at 100 bar but the deviation from the extended Sigmund correlation was less than 15%. For N_2-nC_{16} at both 100 and 180 bar the extended Sigmund correlation overpredicted the diffusion by 75%. The absolute average deviation using the extended Sigmund correlation was 22% for the methane experiments and 27% for the nitrogen experiments.

This method can be used on most binary gas-oil and gas-water systems that have a measurable solubility or swelling effect. The maximum pressure for the apparatus used is 700 bar. Although the method is tested only with binary systems, it can also be used for multicomponent systems, like reservoir oil and gas. The accuracy of the measured diffusion coefficients depends mainly on the amount of pressure drop in the system. One experiment lasts for 10 to 20 days. Further experiments using ternary and multicomponent systems should be performed using the developed procedure to study the effect of multicomponent diffusion.

Gas-Oil Capillary Pressure

Accurate capillary pressure curves are essential for studying the recovery mechanism by gas injection into naturally fractured chalk reservoirs. Questions have been raised about the validity of the Young-Laplace equation for scaling low pressure laboratory capillary pressure curves to reservoir conditions in simulation studies of the Ekofisk reservoir.

A simple and fast method to determine high-pressure drainage capillary pressure curves has been established, and the effect of gas-oil interfacial tension on the capillary pressure curves of chalk cores has been determined for a methane n-pentane system.

Measuring capillary pressure curves on low permeability chalk using a standard procedure with a 6 mm thick porous ceramic plate, requires several months. Use of a 6 μm thick track-etched membrane instead of the traditional porous plate reduced the time required to achieve a capillary pressure curve to 14 days for the 5 md chalk cores used. This is about the same time as needed for centrifuge capillary pressure experiments. To keep the differential and absolute pressures constant, two computer controlled positive displacement pumps were used, which also measured the produced oil volume. The apparatus is fully automated. The developed experimental procedure can be used for all types of drainage capillary pressure measurements at both high and low pressures and temperatures.

The cores used were drilled from the Danish outcrop Stevens from Upper Danian in the Faxe area. The Stevens chalk is quite homogenous, it has no macro fractures, porosity of 48%, and permeability of 5 md. Five drainage gas-oil capillary pressure curves were determined for three different gas-oil interfacial tensions (IFT) using a high-pressure methane n-pentane system. The interfacial tensions were 1.5, 3.2 and 6.3 mN/m. The results are compared with centrifuge runs at low pressure using air-oil with IFT = 24 mN/m, and mercury injection with IFT = 480 mN/m. All of the high-pressure chalk experiments used the same core sample, without remounting the core for each new experiment.

The measured capillary pressure of the chalk was significantly lower than estimated by the Young-Laplace equation for low values of interfacial tension. It appears that the deviation starts at an IFT of about 5 mN/m, and increases at increasing pressures, and as interfacial tension decreases. The nonlinearity may be explained as an increasing apparent contact angle as IFT decreases, and/or as a redistribution of phases caused by the Cahn transition, starting in the larger pores and then, as IFT decreases, also in the finer pores. For values of IFT below about 2 mN/m, it appears that another effect changes the shape of the capillary pressure curve for high wetting phase saturations. This effect could be the Cahn transition. The capillary pressure is further reduced, and becomes very low compared to scaling low pressure measurements by IFT only. The core samples contained no irreducible water in these experiments. The presence of irreducible water may effect the results, and should be examined further.

The recovery of oil by gravity-capillary drainage will be underestimated if low-pressure capillary pressure curves are scaled by interfacial tension only. This underestimation of the oil recovery starts at about 5 mN/m and becomes very important as the interfacial tension is reduced below 2 mN/m. This indicates a much more effective gas-oil gravity-capillary drainage process for shorter effective core (matrix block) heights in chalk, than would be predicted by applying linear scaling by interfacial tension to low-pressure capillary pressure data.

Contents

Chapter 1

Introduction

Two important properties in oil recovery calculations in naturally fractured chalk reservoirs are capillary pressure and molecular diffusion. Capillary pressure may strongly influence the saturation distribution in matrix blocks. Molecular diffusion is important to the mass exchange between fluid in the fractures and the liquid in the matrix blocks. Fig. 1.1 shows a drawing of an actual fractured chalk and an idealized model used in most numerical simulators. By adjusting the properties used in the idealized model, simulators can give results similar to the real reservoir. Accurate capillary pressure curves and diffusion coefficients are important to obtain an accurate representation of the mechanisms that produce oil in naturally-fractured reservoirs.

Several simulation studies have shown the importance of accurate diffusion data to match laboratory experiments with chalk (Coats, 1989; da Silva and Belery, 1989). The fracture spacing in the Ekofisk reservoir is usually 10 to 100 cm. This makes diffusion a relatively fast process.

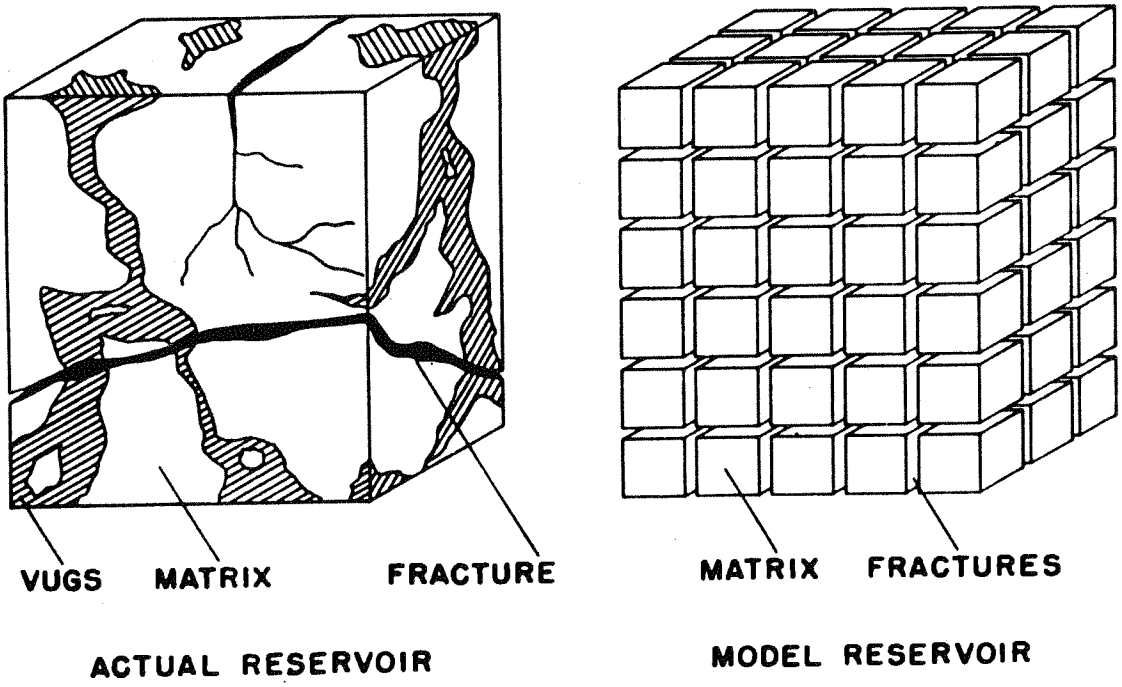

Fig. 1.1 Idealization of the heterogeneous porous medium (Warren and Root, 1963)

For miscible gas flooding, diffusion rates may be important for determining the extent of the mixing zone and the amount of solvent to be injected to achieve high recoveries (Stalkup, 1984).

Another important transport process in a chalk reservoir is gravity-capillary drainage. This process is controlled by the capillary pressure. Numerical simulations with inaccurate capillary pressure data will not reproduce the behavior of chalk reservoirs undergoing a gravity-capillary drainage process.

Diffusion has an important effect on the capillary pressure in the matrix block. When injected gas or liquid diffuses into the oil in the matrix, the capillary pressure is changed. The capillary pressure should be scaled continuously using the local interfacial tension calculated from composition. Other important effects on the recovery are fracture spacing, fracture orientation, oil reimbibition, and the degree of capillary continuity across fractures.

Very few high-pressure data are available for capillary pressure and molecular diffusion. Scaling of low-pressure measurements are based on equations that may not be accurate enough for use in reservoir simulations. The objective of this work has been to:

1. Build an apparatus for simple measurement of liquid diffusion coefficients at high pressure for binary and multicomponent systems using a constant volume cell.

2. Check the Sigmund correlation for estimating liquid diffusion coefficients, particularly for high reduced molar densities.

3. Establish a method to determine high-pressure, gas-oil drainage capillary pressure curves on chalk samples.

4. Determine the effect of low gas-oil interfacial tension on the drainage gas-oil capillary pressure curve of chalk.

The following two chapters give a description of the theory, the experimental apparatus and procedures, together with results of the conducted high-pressure experiments. Conclusions and recommendations for further experiments are given at the end of each chapter, together with nomenclature and reference lists. Details about data acquisition, computer control, and the operating procedure for the capillary pressure apparatus are given in an appendix.

References

Coats, K.H.: "Implicit Compositional Simulation of Single-Porosity and Dual-Porosity Reservoirs," paper SPE 18427 presented at the SPE Symposium on Reservoir Simulation, Houston, TX, Feb. 6-8 (1989).

da Silva, F.V. and Belery, P.: "Molecular Diffusion in Naturally Fractured Reservoirs: A Decisive Recovery Mechanism," paper SPE 19672 presented at the 1989 SPE Annual Technical Conference and Exhibition, San Antonio, TX, Oct. 8-11.

Stalkup, F.I., Jr.: *Miscible Displacement*, Monograph, SPE, Richardson, TX (1984) **8**.

Warren, J.E. and Root, P.J.: "The Behavior of Naturally Fractured Reservoirs," *SPEJ* (Sept. 1963) 245-255; *Trans.*, AIME, **228**.

Chapter 2

Constant Volume Diffusion

2.1 Introduction

Injection of a non-equilibrium gas into oil and condensate reservoirs may be used to increase oil recovery. For gas injection into naturally fractured chalk reservoirs, there is a need for information on the rate and amount of mass transfer by diffusion.

In rich-gas flooding, injection gases containing intermediate hydrocarbons may develop miscibility with in-place oil. Molecular diffusion is responsible for mixing at the pore level, and has been shown to be an important rate-controlling mechanism in gas flooding (Grogan and Pinczewski, 1987). Also diffusion rates are important for determining the extent of the mixing zone and the amount of solvent to be injected to achieve high recoveries.

The need for an accurate method to estimate liquid diffusion coefficients has been shown by da Silva and Belery (1989), by Coats (1989), and by Hu, Whitson, and Yuanchang (1991). In recent years, the problem of diffusion in naturally fractured reservoirs has received increasing attention. The need to include liquid-liquid diffusion as well as vapor-liquid diffusion has been pointed out by Coats (1992). However, there is still a lack of appropriate models for the diffusion process, as well as experimental diffusion coefficients at high pressures in multicomponent reservoir fluids. Reported high-pressure diffusion coefficients sometimes differ by more than 100% from one source to another.

Most conventional methods for measuring diffusion coefficients require compositional analysis which are both expensive and time consuming. In addition, significant errors may be associated with reported values of diffusion coefficients for multicomponent mixtures at high pressures. This is due to various approximations made for the models used in calculation of diffusion coefficients from experimental data, and it is the main reason for significant differences reported for diffusion coefficients measured for the same system. Extrapolation of available data to high pressure through existing correlations may not be accurate. Most correlations are developed based on data available on binary diffusion coefficients of relatively light compounds at high pressure.

The purpose of this work was to develop a simple method to measure liquid diffusion coefficients at high pressures for binary systems and for real oils. The method involves bringing a gas into contact with a liquid in a constant volume cell with known initial pressure and temperature. Initially, the system is not in thermodynamic equilibrium. By measuring the pressure drop and liquid level increase as a function of time, diffusion coefficients can be determined with a numerical simulator by matching the experimental results. The measured diffusion coefficients were used to check the extended Sigmund correlation, particularly for high reduced molar densities. The advantage of the proposed method is that it requires simple equipment, it gives the possibility to use reservoir fluids at reservoir conditions, and the process is similar to gas injection into an oil reservoir. The equations used in the numerical model are the same as used in compositional reservoir simulators which include molecular diffusion.

2.2 Theory and Definitions

Diffusion is the process by which matter is transported from one part of a system to another as a result of random molecular motions. Diffusion is driven by a gradient in chemical potential. This gradient can be caused by a difference in concentration, temperature, pressure, electrical potential, etc. An example of gravitational and thermal diffusion is the process that causes an initial compositional gradient in most petroleum reservoirs. Diffusion caused by concentration gradients is considered in the proposed method; i.e., an isothermal, isobaric (i.e., no diffusion caused by pressure gradients) system with no external force field gradients.

2.2.1 Fick Diffusion

Transfer of heat by conduction is also due to random molecular motions, and there is an obvious analogy between the two processes. In 1855 Fick adopted the mathematical equation of heat conduction derived by Fourier in 1822, and presented the basic equation for molecular diffusion. Fick stated that the rate of transfer of diffusing substance through a unit area of a cross section is proportional to the concentration gradient measured perpendicular to the cross section. This gives Fick's first law for steady-state one-dimensional binary diffusion:

$$u_A = -D_{AB} \frac{dC_A}{dx} \tag{2.1}$$

where

C_A = molar concentration of A, gmol/cm^3
D_{AB} = diffusion coefficient (diffusivity) of A in B, cm^2/s
u_A = flux of species A per unit area, gmol/(cm^{2}s)
x = position, cm

Fick's second law of diffusion eliminates the dependent variable u_A from Eq. (2.1):

$$\frac{\partial C_A}{\partial t} = D_{AB} \frac{\partial^2 C_A}{\partial x^2} \tag{2.2}$$

where t is time in seconds. This is the equation for unsteady state diffusion in one dimension when D_{AB} is constant. General solutions of the diffusion equation can be obtained for a variety of initial and boundary conditions, but only for a constant diffusion coefficient. These solutions are usually of the form of a series of error functions or a trigonometrical series. For more details about analytical solutions of Eq. (2.2) and variable diffusion coefficients, see Crank (1975).

For gases at low pressure and for diffusion in dilute solutions, the diffusion coefficient can usually be treated as independent of concentration. For liquids and for dense gases (at high pressure) the diffusion coefficients are often dependent on the concentration of the diffusing components. Therefore, for the presented experiments, the diffusion coefficients can not be treated as a constant, and will depend on concentration and pressure. For a variable diffusion coefficient, Eq. (2.2) can be written as

$$\frac{\partial C_A}{\partial t} = \frac{\partial}{\partial x}\left(D_{AB}\frac{\partial C_A}{\partial x}\right) \tag{2.3}$$

For diffusion in gases there are several equations based on kinetic theory of gases. The equations for predicting diffusion coefficients in liquids are mostly semiempirical, because the theory for diffusion in liquids is not well established. The molecules in a liquid are very close together compared with a gas. Hence, the molecules of a liquid collide more frequently and the diffusion coefficient is lower than for a gas. Diffusion coefficients in gases may be as much as 10,000 times higher than in liquids at low pressure, while for high pressures the diffusion coefficients may be almost equal. The higher concentration in liquids compensates some for the lower diffusion coefficient, making the flux in a liquid not that much smaller than the flux in a gas.

For gases it is usually assumed that the diffusion coefficients D_{AB} and D_{BA} are equal. This is not generally true for diffusion in liquids (Geankoplis, 1983). If the pressure is uniform, then fluxes are different for different size molecules, and the net flux is not zero. If the net flux is zero, a small pressure gradient must exist to counter the tendency for the component fluxes to be different (Marrero, 1970). For most engineering purposes the diffusion coefficients D_{AB} and D_{BA} are assumed equal.

2.2.2 Other Types of Diffusion

Diffusion in oil reservoirs is a *mutual diffusion* or Fickian diffusion of different components driven by concentration gradients. Mutual diffusion is also called inter diffusion. Molecules will also move in a liquid without any gradients. This is *self diffusion* and can for most normal paraffins be converted to mutual diffusion by empirical and molecular correlations. However, the accuracy is not good. In fact, Reid, Prausnitz, and Poling (1987) state that there is no general relationship between self diffusion and mutual diffusion. *Tracer diffusion coefficients* or intra diffusion coefficients give the diffusion of a labeled component within a homogenous mixture. An example of this would be labeled A molecules diffusing through a mixture of A and B. Like mutual diffusion coefficients, tracer diffusion coefficients can be a function of composition. Except for very dilute systems, tracer diffusion coefficients differ from binary diffusion coefficients, and there is no way to relate the two coefficients (Reid, Prausnitz, and Poling, 1987).

2.2.3 Estimating Low-Pressure Diffusion Coefficients

Binary diffusion coefficients for low pressure gases can be calculated using the Chapman-Enskog dilute gas theory resulting in the Hirschfelder *et al.* equation (Bird, Stewart, and Lightfoot, 1960; Reid, Prausnitz, and Poling, 1987)

$$D_{ij} = \frac{188.29}{p\,\sigma_{ij}^2\,\Omega_{ij}}\sqrt{T^3\left(\frac{1}{M_i}+\frac{1}{M_j}\right)} \tag{2.4}$$

The low-pressure density-diffusivity product can be calculated using the ideal gas law $p = \rho_m RT$ inserted into Eq. (2.4) (Bird, Stewart, and Lightfoot, 1960; Sigmund, 1976a; Whitson and Brulé, 1993)

$$\rho_m^o D_{ij}^o = \frac{2.2648\times10^{-5}}{\sigma_{ij}^2\,\Omega_{ij}}\sqrt{T\left(\frac{1}{M_i}+\frac{1}{M_j}\right)} \tag{2.5}$$

where

D_{ij}^o = low-pressure diffusion coefficient of i in j, cm^2/s
M = molecular weight, g/gmol
p = pressure, Pa
R = universal gas constant, 8.31438×10^6 Pa cm^3/(K gmol)
T = temperature, K
ρ_m = molar density, gmol/cm^3
σ_{ij} = Lennard-Jones 12-6 collision diameter, Å
Ω_{ij} = binary diffusion collision integral, dimensionless

The collision integral Ω_D can be estimated using an accurate correlation given by Reid, Prausnitz, and Poling (1987):

$$\Omega_{ij} = \frac{1.06036}{T_{ij}^{0.1561}} + \frac{0.193}{\exp(0.47635T_{ij})} + \frac{1.03587}{\exp(1.52996T_{ij})} + \frac{1.76474}{\exp(3.89411T_{ij})}$$
$$T_{ij} = \frac{T}{(\varepsilon/\kappa)_{ij}} \tag{2.6}$$

where

ε = Lennard-Jones 12-6 force constant, J
κ = Boltzmann constant, J/K

This correlation was developed using the Lennard-Jones 12-6 force potential as the expression for the intermolecular forces between the molecules. Estimation of the

Lennard-Jones collision diameter and the temperature force constants are taken from correlations by Stiel and Thodos (1962) which are based on viscosity data for 16 hydrocarbon and 11 nonhydrocarbon gases. The correlations are given as

$$\sigma_i = 0.1866 \frac{v_{ci}^{1/3}}{z_{ci}^{6/5}} \quad \text{and} \quad \sigma_{ij} = \frac{\sigma_i + \sigma_j}{2} \tag{2.7}$$

$$\left(\frac{\varepsilon}{\kappa}\right)_i = 65.3 T_{ci} z_{ci}^{18/5} \quad \text{and} \quad \left(\frac{\varepsilon}{\kappa}\right)_{ij} = \sqrt{\left(\frac{\varepsilon}{\kappa}\right)_i \left(\frac{\varepsilon}{\kappa}\right)_j} \tag{2.8}$$

where

T_{ci} = critical temperature, K
v_{ci} = critical molar volume, $cm^3/gmol$
z_{ci} = critical compressibility factor, $cm^3/gmol$

Stiel and Thodos reported an average deviation of 6.6% for the temperature force constant ε/κ, and 1.9% for the collision diameter σ. According to Reid, Prausnitz, and Poling (1987), the calculated value of D_{ij} is relatively insensitive to the value of ε/κ and even to the form of the assumed potential function. Therefore, the average deviation of 6.6% in Eq. (2.8) can be neglected. Eqs. (2.4) through (2.8) were developed for nonpolar gases but have been used for liquids with acceptable results in the lack of better estimation methods. When combined with the Sigmund correction factor given in the next section, these equations give more accurate estimates for binary liquid diffusion coefficients than the traditional equations for estimating infinite dilution binary liquid diffusion coefficients.

2.2.4 The Extended Sigmund Correlation

Diffusion coefficients are approximately inversely proportional to pressure. Both Dawson, Khoury, and Kobayashi (1970) and Khoury and Kobayashi (1970) have shown how a temperature independent expression for the ratio of the high-pressure and the low-pressure density-diffusivity product $\rho_m D/(\rho_m D)^0$ may be developed. They start with a hard sphere model for self-diffusion and the simplified kinetic theory of dilute gases in Eq. (2.4) given as

$$\rho_m D = \frac{1}{4}\sigma\rho_m \sqrt{\frac{\pi RT}{M}} \left[\frac{(pv)}{(RT)} - 1\right]^{-1} \quad \text{and} \quad (\rho_m D)^o \propto \sqrt{T} \tag{2.9}$$

It is then possible to write the reduced value of the density-diffusivity product as

$$\frac{\rho_m D}{(\rho_m D)^o} = \beta\rho_m\left[\frac{(pv)}{(RT)} - 1\right]^{-1} \tag{2.10}$$

Use of the virial equation of state for $pv/(RT)$ gives

$$\frac{\rho_m D}{(\rho_m D)^o} = \beta\rho_m\left(1 + \frac{B}{v} + \frac{C}{v^2} + \cdots - 1\right)^{-1} \tag{2.11}$$

$$= \beta\rho_m (B\rho_m + C\rho_m^2 + D\rho_m^3 \cdots)^{-1}$$

The virial coefficients B, C, ... are temperature independent for hard spheres. Modifying the polynomial, and assuring that the value of $\rho_m D/(\rho_m D)^0$ approaches unity as the density approaches zero, results in the following equation:

$$\frac{\rho_m D}{(\rho_m D)^o} = 1 + b\rho_m + c\rho_m^2 + d\rho_m^3 + \cdots \tag{2.12}$$

The Sigmund correlation for estimating high-pressure binary diffusion coefficients is based on Eq. (2.12) and has been used in reservoir simulators for both vapor and liquid. This correlation is simple and requires only the component critical properties and other parameters available in a compositional simulator. Binary diffusion coefficients are given as a function of the mixture molar density, the low pressure diffusion coefficient, and a correction factor (Sigmund, 1976a):

$$D_{ij} = \frac{\rho_m^o D_{ij}^o}{\rho_m}\alpha_D \tag{2.13}$$

where

D_{ij} = high-pressure diffusion coefficient of i in j, cm^2/s
α_D = diffusivity product correction factor, dimensionless

The correction factor α_D is given by Sigmund as

$$\alpha_D = 0.99589 + 0.096016\,\rho_{mr} - 0.22035\,\rho_{mr}^2 + 0.032874\,\rho_{mr}^3 \tag{2.14}$$

For a mixture reduced molar density $\rho_{mr} > 3.0$, an empirical correlation was recommended by da Silva and Belery (1989)

$$\alpha_D = 0.18839\, e^{(3-\rho_{mr})} \tag{2.15}$$

to avoid negative values calculated from Eq. (2.14). Eq. (2.15) has not been verified experimentally. Fig. 2.1 gives a plot of the extended Sigmund correlation indicating the range of reduced molar densities for hydrocarbon vapor and liquid. Note that the extended Sigmund correlation is very sensitive to reduced density for liquids and dense gases ($\rho_{mr} > 1.5$). Eq. (2.14) was based on 344 vapor diffusion coefficients for pressures up to 690 bar, and 52 liquid diffusion coefficients of light hydrocarbons for pressures up to 275 bar. The average absolute deviation was 10% for gases and 40% for liquids. Both binary and self-diffusion data were used.

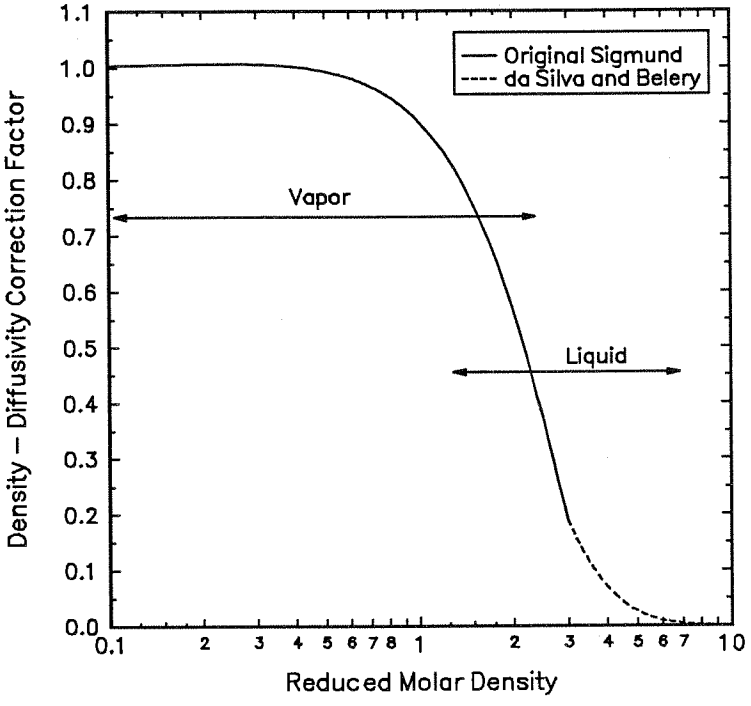

Fig. 2.1 The modified Sigmund diffusion coefficient correlation

The key parameter in the extended Sigmund correlation is the mixture reduced molar density, defined as

$$\rho_{mr} = \frac{\rho_m}{\rho_{mc}} \tag{2.16}$$

where the mixture pseudo-critical molar density is obtained from (Reid, Prausnitz, and Poling, 1987)

$$\rho_{mc} = \frac{\sum_{i=1}^{n} z_i v_{ci}^{2/3}}{\sum_{i=1}^{n} z_i v_{ci}^{5/3}} \tag{2.17}$$

where v_{ci} is the critical molar volume. For the liquid phase $z_i = x_i$ and $\rho_m = \rho_{mL}$ in Eqs. (2.16) and (2.17), and for the vapor phase $z_i = y_i$ and $\rho_m = \rho_{mV}$.

2.2.5 Comparing the Sigmund Correlation with Published Data

Several published binary and self-diffusion data for gases, dense gases, and liquids were used to check the extended Sigmund correlation. Binary vapor data from Sigmund (1976a) for C_1-C_3, C_1-C_4, and C_1-N_2, and from Berry and Koeller (1960) for C_1-C_2, C_1-N_2, and C_2-N_2 were used, together with self-diffusion data of C_1 from Dawson, Koury, and Kobayashi (1970). For liquid systems C_1-nC_5 data were taken from Reamer, Duffy, and Sage (1956), C_1-nC_{10} data from Reamer, Opfell, and Sage (1956), and self-diffusion data in C_3 and CO_2 from Robinson and Stewart (1968). The procedure outlined above was used to calculate the low-pressure $(\rho_m D)^0$ value and combined with the reported density and diffusion data to give the value of $\rho_m D/(\rho_m D)^0$. The results are plotted in Fig. 2.2 together with the extended Sigmund correlation and are also summarized in tables in Appendix A. All these results were also used by Sigmund in deriving his correlation.

Note that the diffusion coefficients for methane are underpredicted by the extended Sigmund correlation. Also for the C_1-nC_{10} data by Reamer *et al.* the extended Sigmund correlation underpredicts the diffusion coefficient. However, for the C_1-nC_5 data by Reamer *et al.* and the C_1-C_3 and C_1-nC_4 data by Sigmund, the experimental data fall on both sides of the extended Sigmund correlation. The deviation from the extended Sigmund correlation for the data by Reamer was examined further to check the effect of pressure, temperature, molar density and methane fraction. However, no distinct correlation was found. Some of the authors used density predicted by an equation of state, thereby introducing a possible error.

Erkey and Akgerman (1989) reported accurate infinite dilution liquid diffusion coefficients for C_1, C_2, nC_3, nC_5, nC_7, nC_{10}, nC_{12}, and nC_{14} in nC_8 at 17.2 bar for temperatures between 31 and 162°C. The Taylor dispersion technique was used and the reported diffusion coefficients were stated to be within ± 1%. Densities were not given so procedure 6A2.22 of the API technical data book (1976) was used to estimate the density of pure C_8 with an accuracy better than 1%. Table 2.1 gives the calculated densities and the reduced molar densities for each temperature.

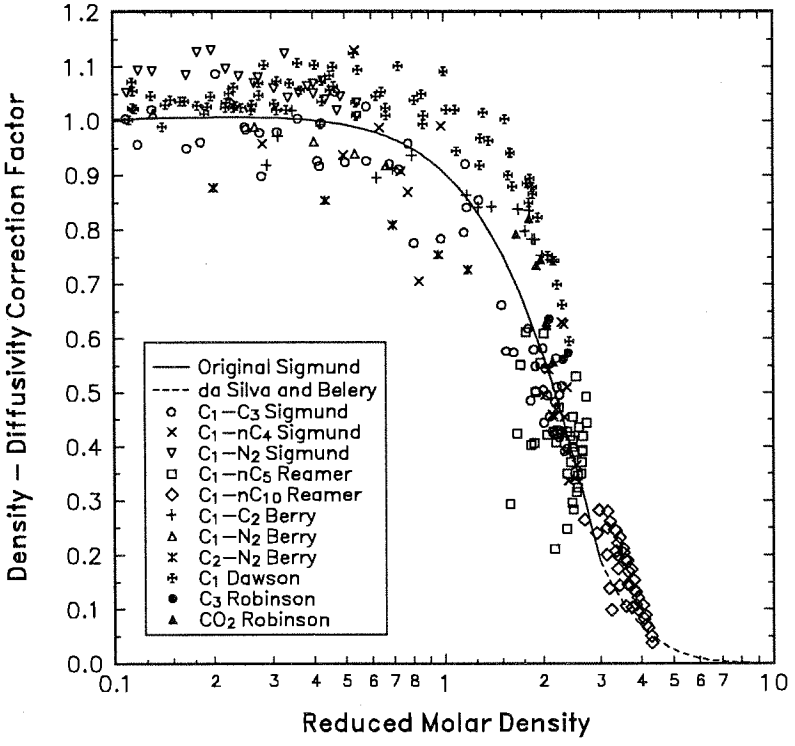

Fig. 2.2 Literature diffusion data together with the Sigmund correlation

Table 2.1 Calculated densities of pure nC_8 for various temperatures at 17.2 bara

Temperature (°C)	Density (g/cm^3)	Reduced Molar Density
31	0.6957	2.997
62	0.6715	2.893
88	0.6503	2.801
114	0.6278	2.705
138	0.6054	2.608
162	0.5810	2.503

The low-pressure $(\rho_m D)^0$ values were calculated and combined with the reported diffusion data and calculated densities to give the value of $\rho_m D/(\rho_m D)^0$. The density-diffusivity correction factor α_D was then calculated from Eq. (2.13) and the results are plotted together with the extended Sigmund correlation in Fig. 2.3. The tables in Appendix A include all the data. Note that the extended Sigmund correlation gives good predictions for C_1 to C_3 but underpredicts the diffusion for heavier components in C_8, especially for high temperatures. Remember that these data are infinite dilution diffusion coefficients and not equivalent to binary diffusion coefficients where the concentration of the diffusing component is important.

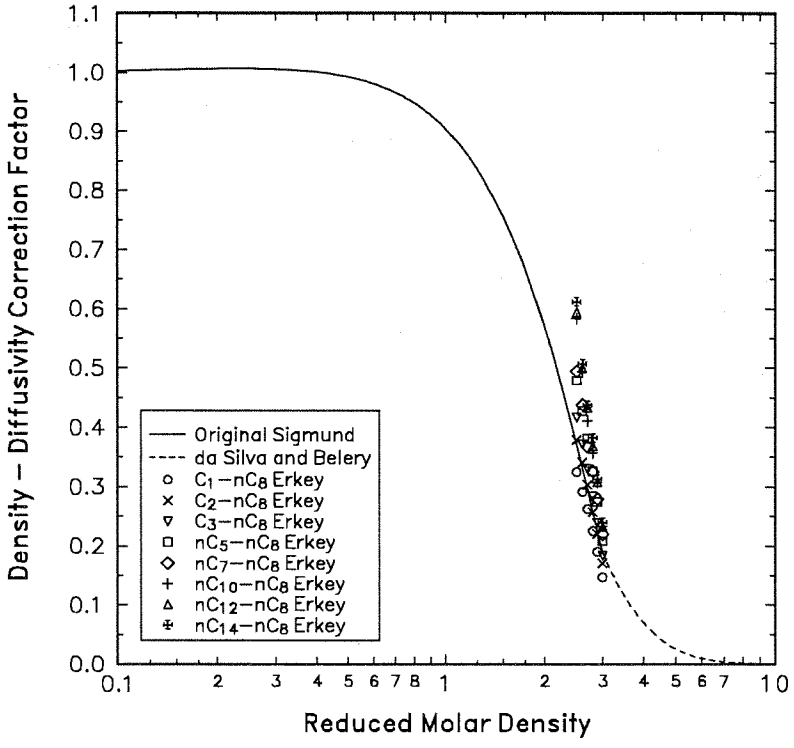

Fig. 2.3 Infinite dilution coefficients from Erkey and Akgerman (1989)

2.2.6 Viscosity Based Correlations

There also exist correlations for high-pressure gas and liquid diffusion coefficients based on viscosity. However, these correlations do not give more accurate predictions than the extended Sigmund correlation unless experimental viscosity data are available. Both viscosity and density are often estimated using the same type of equations, and result therefore in about the same accuracy in the estimates.

An example of a viscosity based equation is the Wilke-Chang equation (Reid, Prausnitz, and Poling, 1987) that was modified slightly by Fayers and Lee (1992):

$$D_{ij} = \frac{7.4\times10^{-8}\sqrt{M'_m}\,T}{\mu_m\, v_i^{0.6}} \quad \text{and} \quad M'_m = \sum_{j\neq1} y'_j M_j \tag{2.18}$$

where y'_j is the normalized mole fraction of j when component i is excluded. This equation was used by Fayers and Lee in modeling of the N_2-C_1-C_5 diffusion experiment conducted at IFP (Morel, *et al.*, 1990) with about the same results as obtained by Hu, Whitson, and Yuanchang (1991) using the extended Sigmund

correlation. Eq. (2.18) does not give better liquid diffusion coefficients than the extended Sigmund correlation. When used on dense gas systems, the average absolute deviation (AAD) from experimental data is several times higher than for the Sigmund correlation. The method proposed by Fayers and Lee is useful as a simple equation for estimating liquid diffusion coefficients but should not be used for gases.

Riazi and Whitson (1989) used some of the experimental data included in Fig. 2.2 together with experimental data for C_1 and C_3 in oil to develop a high-pressure correction factor similar to the Sigmund correction factor. The main parameter in this correlation is the mixture viscosity instead of the mixture reduced density. The correction factor is given as

$$\frac{\rho D_{ij}}{(\rho D_{ij})^o} = 1.07\left(\frac{\mu}{\mu^o}\right)^{a+bp_r} \qquad (2.19)$$

$$a = -0.27 - 0.38\,\omega$$

$$b = -0.05 + 0.1\,\omega$$

where

μ = high-pressure viscosity, cp
μ^o = low-pressure viscosity, cp
p_r = reduced pressure p/p_c, dimensionless
ω = Pitzer's acentric factor, dimensionless

Linear mixing rules for critical pressure and acentric factor are given by

$$p_c = z_i p_c + z_j p_{cj}$$
$$\omega = z_i \omega_i + z_j \omega_j \qquad (2.20)$$

This correlation gave better estimates than the Sigmund correlation when using experimental mixture viscosities. The Riazi and Whitson correlation was used on the diffusion data in Figs. 2.2 and 2.3 to compare it with the extended Sigmund correlation when using estimated instead of experimental viscosities. The correlation by Stiel and Thodos was used for μ^o, and the correlation by Jossi, Stiel, and Thodos for μ-μ^o. This is the same procedure as recommended by Lohrenz, Bray, and Clark (1964) and has become a standard in compositional reservoir simulation. The average absolute deviation (AAD) of the estimated diffusion coefficients are compared with the AAD data given by Riazi and Whitson in Table 2.2. When using estimated viscosity data the extended Sigmund correlation is more accurate than Eq. (2.19) for the binary and self diffusion data in Figs. 2.2 and 2.3. The results from the calculations are included in Appendix A. Slightly better viscosity estimates could have been obtained by using the more complicated method by Chung *et al.* (1988). However, their method is not recommended for ρ_r above 2.5.

Table 2.2 Comparing the accuracy of the Sigmund correlation with Eq. (2.19) giving the average absolute deviation (AAD)

Fluid Type and Viscosity Data	Number of Data Points	Sigmund Correlation Eq. (2.13) AAD	Riazi Correlation Eq. (2.19) AAD
Vapor* w/experimental μ	140	10.2	8.1
Liquid* w/experimental μ	143	48.9	15.4
Vapor** w/estimated μ	217	9.4	11.8
Liquid† w/estimated μ	91	27.8	34.9
Liquid‡ w/estimated μ	48	19.8	27.3

* =Data used by Riazi and Whitson (1989)
** =Data from Sigmund (1976), Berry and Koeller (1960), Dawson *et al.* (1970)
† =Data from Reamer *et al.* (1956), Robinson and Stewart (1968)
‡ =Data from Erkey and Akgerman (1989)

2.2.7 Diffusion in Multicomponent Systems

For multicomponent systems, the effective diffusion coefficient D_{im} for each component can be estimated by Wilke's equation (Wilke, 1950)

$$D_{im} = (1-z_i)\left(\sum_{\substack{j=1 \\ j\neq i}}^{n} \frac{z_j}{D_{ij}}\right)^{-1} \tag{2.21}$$

where

D_{ij} = binary diffusion coefficients, cm^2/s
z_i = vapor or liquid mole fractions y_i or x_i

This equation is based on the Stefan-Maxwell diffusion equations, and is simply a weighted harmonic mean. Sigmund (1976b) stated that Eq. (2.21), which was developed for gas mixtures, may also be fairly accurate for liquid mixtures.

Some other more complicated methods exist for calculating multicomponent diffusion coefficients. These may be considered if Wilke's equation is found insufficiently accurate for engineering calculations on the basis of experimental data for multicomponent hydrocarbon systems. Measurements of diffusion in multicomponent systems are not included in this work, so the accuracy of Wilke's equation will not be discussed further.

2.2.8 Diffusion in Porous Media

The diffusion coefficients used above represent free-space diffusion. For use in a porous media, diffusion coefficients must be corrected for the tortuosity and porosity. The following formula is often used

$$D_e = \frac{D}{F\phi} \tag{2.22}$$

where

D_e = effective diffusion coefficient, cm^2/s
F = formation electrical resistivity factor, dimensionless
ϕ = porosity, fraction

This equation can be combined with the following approximation (Amyx, Bass, and Whiting, 1960)

$$F = \frac{1}{\phi^m} \tag{2.23}$$

where m is the cementation exponent ranging from 1 to 2. Substitution of Eq. (2.23) into Eq. (2.22) yields the relationship

$$D_e = D\phi^{m-1} \tag{2.24}$$

2.2.9 Methods for Measuring Liquid Diffusion Coefficients

Several methods exist for measuring binary liquid diffusion coefficients at elevated pressures. Often these methods require measurement of composition as a function of time. This usually means withdrawal of samples during the experiment. Sample withdrawal complicates the experiment and usually involves some disturbance of the system. For sampling hydrocarbon vapor or liquid at high pressures, it is usually necessary to flash the sample to atmospheric pressure, and analyze the composition of the resulting vapor and liquid phase. These measured compositions have to be recombined to obtain the composition of the original sample.

A relatively common method for measuring diffusion coefficients is the porous diaphragm method where two containers with different concentrations of a mixture are connected through a porous membrane of sintered glass. The equipment has to be calibrated with a solute having a known diffusivity, and the method requires samples to be taken. This method is most useful at low pressures, and is a pseudosteady state method.

Another common method is the chromatographic peak broadening technique or the Taylor dispersion method. This method is primarily used at low pressures, but has also been used up to 35 bar by Matthews, Rodden, and Akgerman (1987). A narrow pulse of solute diluted in the solvent is injected into a capillary tube in which the solvent is moving in slow laminar flow. At the end of the diffusion tube the concentration vs. time is recorded as the peak is broadened.

Killie (1991) described an interferometric method for determination of diffusion coefficients at elevated pressure and temperature. The method requires the diffusing solution to be transparent and the refractive index of the system to be a linear function of concentration. Diffusion coefficients are determined from the change in concentration profiles based on analysis of a sequence of refractive interference patterns using a phase shift technique. The equipment is rather complicated and one measurement lasts for a few hours. The accuracy is stated to be about ± 10%. Ongoing research will try to improve the accuracy and measure the diffusion coefficients within ± 5%.

Helbæk (1992) described a method that measures self diffusion based on nuclear magnetic resonance (NMR) equipment with an accuracy of ± 5%. The self-diffusion coefficient is based on measurements of the spin-echo resulting from changing the energy level of molecules in a magnetic field by a radio-frequency pulse. Mutual diffusion coefficients are estimated based on a relationship between self diffusion and mutual diffusion. The equipment is rather expensive and the relationship between self-diffusion and binary diffusion coefficients is not particularly accurate. However, the main purpose of this ongoing work is to examine the relationship between self diffusion and binary diffusion coefficients.

A method used by Grogan *et al.* (1988) measures the decrease in size of a 10 mm long vapor bubble in contact with a liquid in a 0.61 mm ID glass capillary over a period of several days. The diffusion coefficient is determined by fitting a mathematical model to the observed motion of the interfaces. Grogan *et al.* measured the diffusion of CO_2 in pentane, decane, and hexadecane at 25°C and pressures up to 60 bara. The resulting liquid diffusion coefficients show a scatter of up to ± 50%.

Reamer *et al.* (1956) described a method based on injection of methane into the gas phase of a constant volume cell with a liquid initially in equilibrium with a vapor. The quantity of methane necessary to maintain the resulting nonequilibrium system at constant pressure is determined as a function of time. The diffusion coefficient is based on the slope in a plot of the mass of gas injected vs. the square root of time. Methods similar to this one have been used by several other authors.

Renner (1988) described a similar method for measuring liquid diffusion coefficients in a porous media. A core sample is mounted in a sleeve inside a cell and saturated with a liquid. Gas is injected on top of the core while increasing the cell volume and

keeping the pressure constant. As time passes, gas is injected to keep the pressure constant to compensate for the volume of gas that diffuses into the core sample. The apparatus was calibrated with the methane-decane diffusion coefficients given by Reamer *et al.* so the results are dependent of the accuracy of these measurements. Renner reported data for CO_2 in decane and brine up to 58 bara, and ethane in decane at pressures up to 41 bara.

The method proposed in this work is quite similar to the methods used by Reamer *et al.* (1956) and Renner (1988). The only difference is that instead of maintaining the pressure by injecting gas, the pressure transient and swelling of the liquid is used to determine the diffusion coefficient. This makes the equipment much simpler but the numerical modelling more complicated.

2.2.10 The Effect of Interface Resistance

When mass transfer occurs across a vapor-liquid interface, there is a small interface resistance. This resistance will increase with the vapor-liquid interfacial tension, and the effect will be most important when the flux across the interface is high. To predict which binary systems may be affected by interfacial resistance, the interfacial tensions of each system in this study were estimated at 24°C. Fig. 2.4 shows the interfacial tension for each of the binary systems used in the experiments as a function of pressure. The interfacial tension for nC_5 is significantly lower than for nC_8, nC_{10}, and nC_{16} for both the methane and nitrogen systems. The interfacial tensions for the nC_8, nC_{10}, and nC_{16} systems are almost the same. Note also that the interfacial tension of the nitrogen systems are higher than for the methane systems, especially for high pressures. As expected, the interfacial tension decreases with pressure for all the binary systems.

The conclusion must be that if the interfacial resistance is important it should decrease with increasing pressure, be higher for the nitrogen experiments, and lower for nC_5 than for nC_8, nC_{10}, and nC_{16}. The interface resistance should also decrease with time as the flux across the vapor-liquid interface decreases. Reamer, Opfell, and Sage (Reamer, Opfell, and Sage, 1956) have considered the effect of the interface resistance and state that it is only important at low pressure. The interface resistance will therefore be neglected in the numerical simulator described in Section 2.4.

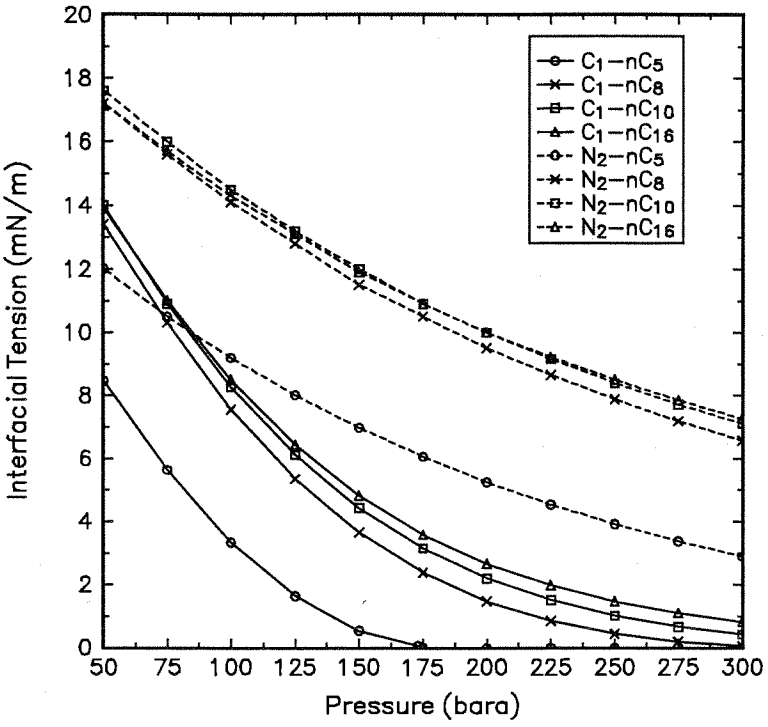

Fig. 2.4 Estimated interfacial tensions for methane and nitrogen in equilibrium with nC_5, nC_8, nC_{10}, and nC_{16} as a function of pressure at 24°C

2.3 Apparatus and Methods

One of the main advantages with the constant volume diffusion method is the simple equipment required, and the need to only read the pressure and liquid level once or twice a day. The time needed to start an experiment is less than one hour. Another advantage is that experiments can be run at reservoir conditions; up to 700 bar and 150°C with the cell used in this work. A description of the apparatus and the experimental procedure follows.

2.3.1 The Constant Volume Cell

A Ruska high-pressure visual cell was used for the experiments. The inner diameter of the cell is 3.568 cm (A=10 cm^2) with a height of 48.3 cm giving a total volume of 483 cm^3. The temperature in the gas phase is measured with a temperature transducer that has a short response time, mounted inside the cell. A pressure transducer is connected to the top of the cell measuring the absolute pressure. Both pressure and temperature are recorded by a personal computer (PC), while the liquid level is read manually using a cathetometer. Continuous reading of the pressure and temperature was not required but made it easier to check the temperature effect on pressure. The temperature in the room was controlled by an accurate electronic proportional thermostat. Table 2.3 gives the accuracy and resolution for the measurements.

Table 2.3 Transducer accuracy and resolution

Transducer	Unit	Range	Accuracy	Resolution
Pressure	(bar)	0 - 300	0.5	0.06
Temperature	(°C)	0 - 50	0.2	0.01
Liquid Level	(cm)	0 - 49.5	-	0.001

A diverting plate is mounted at the gas inlet to avoid disturbance of the liquid when charging the cell with gas. A detailed drawing of the cell is given in Fig. 2.5 (parts list is not included). Fig. 2.6 shows a schematic drawing of the apparatus including the cathetometer and the PC. The height of the cell reduces the disturbance of the liquid during initialization, and results in a high accuracy of the estimated liquid diffusion coefficients. The volume in the lines between the top of the cell and the pressure transducer was about 10 cm^3. This is less than 2 % of the total cell volume and should not cause problems as long as the liquid level is not too high. Two experiments were repeated after reducing this volume to about 2 cm^3 to check the effect of the additional gas volume.

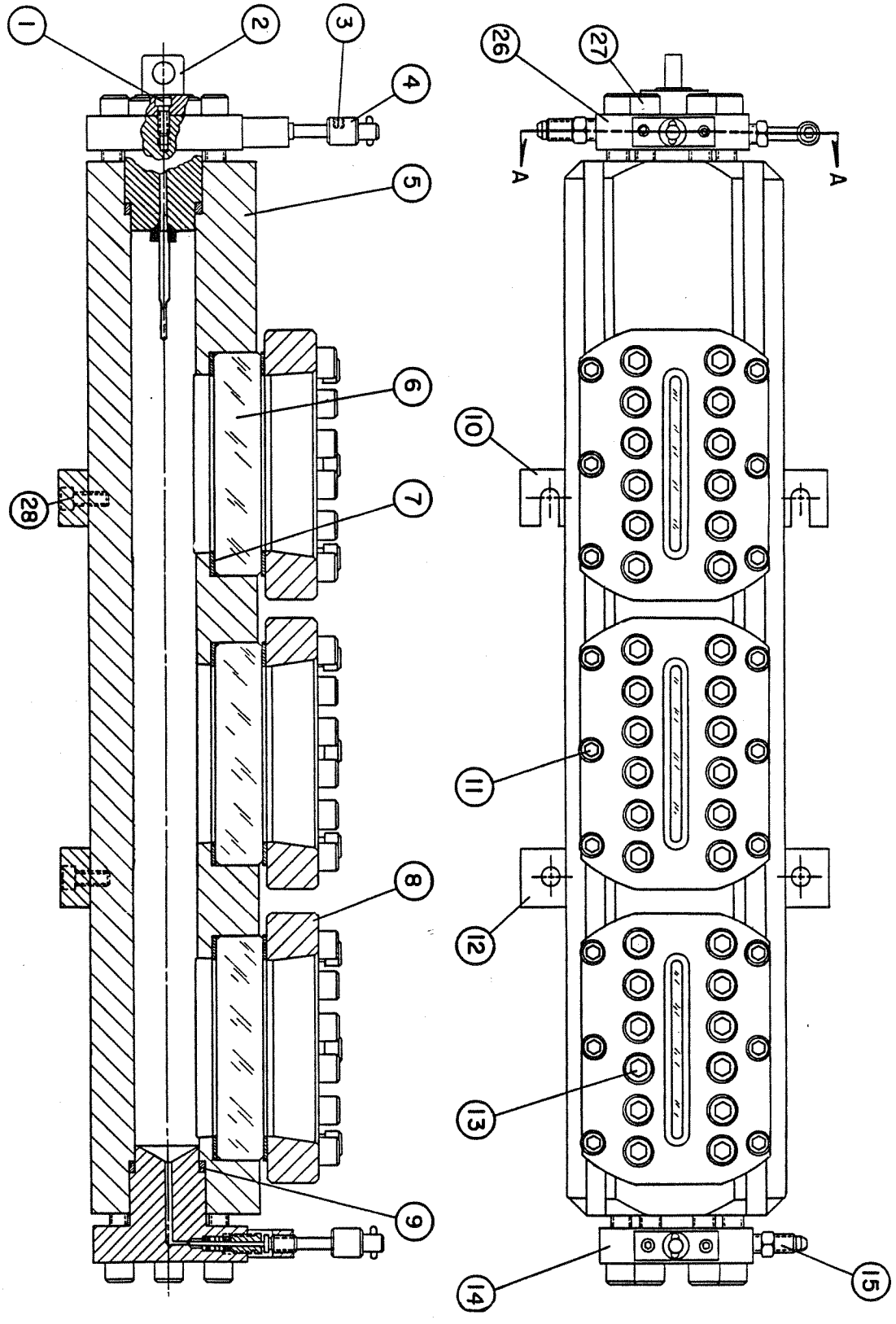

Fig. 2.5 Detailed drawing of the constant volume diffusion cell

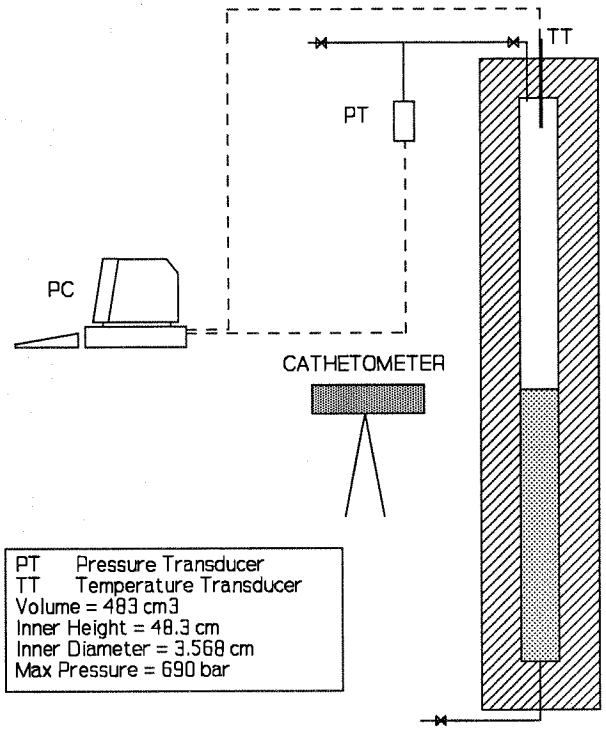

Fig. 2.6 Constant volume diffusion apparatus

2.3.2 Experimental Procedure

The cell is evacuated and filled with a given amount of liquid and then evacuated again for 10 to 20 minutes to remove all air from the system. Gas is then injected into the top of the cell until the desired pressure is reached. The charging takes about 10 sec. The pressure and the liquid level change is monitored for a sufficient amount of time, usually 10 to 20 days. The measured pressure and liquid level changes are matched with a numerical simulator by modifying the liquid diffusion coefficients.

The chemicals used were 99.5% methane and nitrogen from Hydrogas and >99% nC_5 from KeboLab, nC_8 from Rathburn, and nC_{10} and nC_{16} from Merck. Isopropanol was used for cleaning the cell. For the 30,000 ppm brine-CO_2 experiments, 2 g/l (0.012 mol%) potassium di-chromate ($K_2Cr_2O_7$) were used to inhibit corrosion. A vacuum pump with a cold trap was used, obtaining a vacuum of about 0.001 mbar.

The change in composition will be largest for the liquid phase, and liquid diffusion coefficients are smaller than gas diffusion coefficients. This makes the liquid diffusion coefficients dominate the change in pressure and liquid level with time.

2.4 Constant Volume Diffusion Simulator

Using the constant volume diffusion method simplifies the experiments but requires accurate numerical modelling to give reliable diffusion coefficients. The system consists of a vapor and a liquid phase, and this has to be modelled as two separate systems with the concentration at the boundary given by equilibrium ratios (equal chemical potential). The swelling of the liquid makes the vapor-liquid interface move, so there are in fact two separate moving-boundary systems. The simulator is based on a cubic equation of state (EOS) including volume translation (VLT) (Peneloux, Rauzy, and Freze, 1982) which is important to obtain correct estimated liquid densities. Liquid density is the main parameter in the extended Sigmund correlation.

The experiment is similar to gas injection into an oil reservoir, and the laboratory simulator is based on the same equations used in compositional reservoir simulators. Any limitations in these models are then accounted for in the resulting diffusion coefficients.

The mathematical models and computer algorithms for simulating the constant volume diffusion experiment were developed by Michelsen. The discussion that follows in Section 2.4.1 to 2.4.3 is taken from his report on this work (Michelsen, 1992).

2.4.1 Setting Up the Equations

Consider a cell of height h, with the bottom part of the cell filled with liquid to a height ℓ, and the top part filled with gas (Fig. 2.7). Liquid phase concentration is denoted C_i^L and vapor phase concentrations by C_i^V. The concentration profile depends on the cell position x, and time t. It is assumed that thermodynamic equilibrium exists between the two phases at the gas-oil boundary at all times.

The numerical simulator is based on Fick's second law, Eq. (2.2), but including a concentration dependent diffusion coefficient which gives

$$\frac{\partial C}{\partial t} = \frac{\partial}{\partial x}\left(D\frac{\partial C}{\partial x}\right) = D\frac{\partial^2 C}{\partial x^2} + \frac{\partial D}{\partial x}\frac{\partial C}{\partial x} \tag{2.25}$$

Values of D and $\partial D/\partial x$ are calculated at the previous time step. The boundary conditions used are

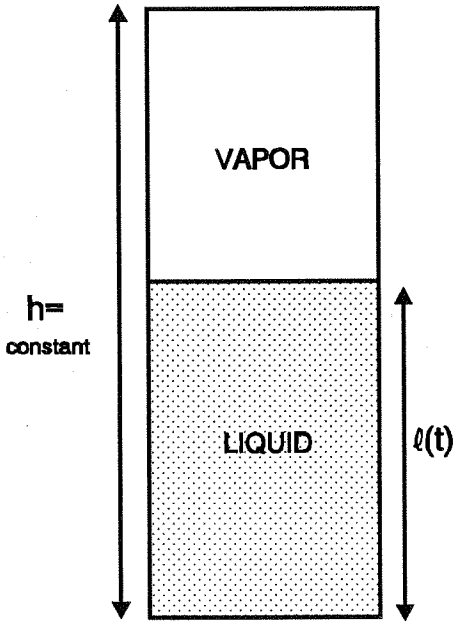

Fig. 2.7 Explanation of variables in the simulator

$$
\begin{aligned}
t = 0: &\qquad C_i^L = C_{i0}^L \,,\; C_i^V = C_{i0}^V \,,\; \ell = \ell_0 \\
x = 0: &\qquad \frac{\partial C_i^L}{\partial x} = 0 \\
x = \ell: &\qquad f_i^L = f_i^V \\
x = h: &\qquad \frac{\partial C_i^V}{\partial x} = 0
\end{aligned}
\tag{2.26}
$$

One important decision in developing the simulator was the use of an overall material balance instead of boundary flux balances. The interface position varies with time and is given by an overall material balance for the components

$$
N_i = \int_0^{\ell} C_i^L(x,t)\,dx + \int_{\ell}^{h} C_i^V(x,t)\,dx = \ell_0 C_{i0}^L + (h-\ell_0) C_{i0}^V \tag{2.27}
$$

The overall material balances are completely equivalent to the conventional boundary flux balances. Differentiation of the material balance gives

$$\frac{d}{dt}\int_0^{\ell} C_i^{\,L}(x,t)\,dx + \frac{d}{dt}\int_{\ell}^{h} C_i^{\,V}(x,t)\,dx = 0 \tag{2.28}$$

Derivation of the liquid term, taking into account that ℓ is a function of time, and substituting Eq. (2.25) into the integral, yields

$$\frac{d}{dt}\int_0^{\ell} C_i^{\,L}(x,t)\,dx = \int_0^{\ell}\frac{\partial C_i^{\,L}}{\partial t}dx + \frac{d\ell}{dt}C_i^{\,L}(\ell) = \left(D_i^{\,L}\frac{\partial C_i^{\,L}}{\partial x}\right)_{x=\ell} + \frac{d\ell}{dt}C_i^{\,L}(\ell) \tag{2.29}$$

which combined with the equivalent vapor term gives the boundary balance. The reason for selecting the overall material balance is because Eq. (2.27) guarantees satisfaction of the material balance at all steps, and thus results in the correct solution (a constant-volume equilibrium flash) at infinite time. Use of the boundary balance in Eq. (2.29), combined with integration errors, could result in a small drift of the material balance, and thereby give an incorrect estimate for the final pressure and liquid level.

To keep the pressure in both phases equal, the following procedure is used

1. Define $p^{\,L} = p(\bar{C}^{\,L},T)$ and $p^{\,V} = p(\bar{C}^{\,V},T)$ using average concentrations.
2. Let the condition of interface equilibrium relate to the interface mole fractions and the phase pressures defined above.
3. Introduce the condition $p^{\,L} = p^{\,V}$

2.4.2 Solving the Equations

One problem with solving Eq. (2.25) is that boundary ℓ is a function of time. To avoid continuous regridding because of the moving interface, a set of independent variables are introduced:

$$\tau = t \qquad \chi = \frac{x}{\ell(t)} \text{ (liquid)} \qquad \chi = \frac{h-x}{h-\ell(t)} \text{ (vapor)} \tag{2.30}$$

The spatial variable χ for both phases ranges from 0 to 1, with 1 corresponding to the interface and 0 to the top and bottom of the cell. Note that χ has opposite direction in the vapor and liquid phases. The transport equations, Eq. (2.25) in the new variables become

$$\frac{\partial C}{\partial \tau} = \frac{D}{\ell^2}\frac{\partial^2 C}{\partial \chi^2} + \frac{1}{\ell^2}\frac{\partial D}{\partial \chi}\frac{\partial C}{\partial \chi} + \frac{1}{\ell}\frac{d\ell}{dt}\chi\frac{\partial C}{\partial \chi} \tag{2.31}$$

and the new boundary conditions become

$$\begin{aligned} \tau = 0: &\quad C_i^L = C_{i0}^L \,,\; C_i^V = C_{i0}^V \,,\; \ell = \ell_0 \\ \chi = 1: &\quad f_i^L = f_i^V \\ \chi = 0: &\quad \frac{\partial C_i^L}{\partial \chi} = 0 \,,\quad \frac{\partial C_i^V}{\partial \chi} = 0 \end{aligned} \tag{2.32}$$

To simplify the implementation of the boundary conditions, a new variable $\eta = \chi^2$ is introduced, which gives

$$\frac{\partial C}{\partial \chi} = 2\chi \frac{\partial C}{\partial \eta} \quad \text{and} \quad \frac{\partial^2 C}{\partial \chi^2} = 4\eta \frac{\partial^2 C}{\partial \eta^2} + 2\frac{\partial C}{\partial \eta} \tag{2.33}$$

In the new variables the boundary conditions for $\chi = 0$ are automatically satisfied, and Eq. (2.31) becomes simpler to solve.

The equations are solved using an implicit Euler scheme for time, and *orthogonal collocation* (Villadsen and Michelsen, 1978) for the spatial variable. Orthogonal collocation is a discretization method characterized by high order interpolation, and "smart" placement of grid points. The advantage is that fairly few grid points are required. A drawback is that the equations are dense, rather than sparse. The closing relations are solved by Newton's method.

2.4.3 More Rigorous Formulation

To check the effect of including a fluid velocity term, a second formulation was used where Eq. (2.25) is written as

$$\frac{\partial C}{\partial t} = \frac{\partial}{\partial x}\left(D\frac{\partial C}{\partial x}\right) - \frac{\partial (vC)}{\partial x} \tag{2.34}$$

with the spatial variation in velocity v included as shown. To force the pressure gradient to zero, the following equation was used

$$v = -\beta \frac{\partial p}{\partial x} \tag{2.35}$$

where the constant β is chosen very large. This gives a far more complex set of equations to solve, and also slows down the simulator. Two preliminary versions of

both models, both using constant diffusion coefficients, were tested with the C_1-nC_5 system. Results from the simulations are given in Figs. 2.8 and 2.9. The equilibrium conditions with a liquid reduced molar density of 2.7 were used to estimate the diffusion coefficients using the extended Sigmund correlation.

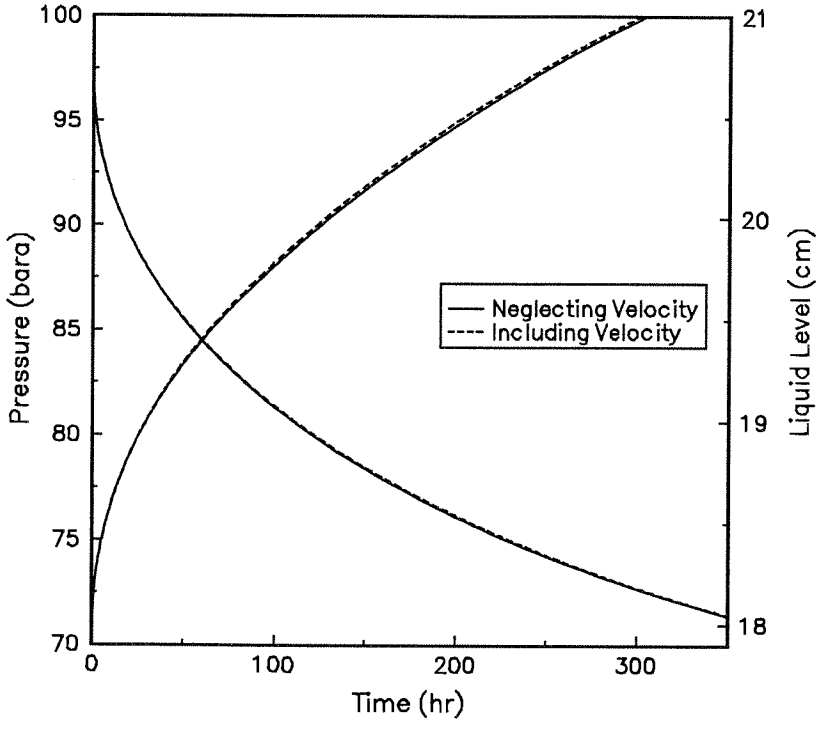

Fig. 2.8 Comparing CVD simulators for C_1-C_5 (no volume translation)

The difference between the two model formulations is only apparent during the first hour. It was therefore decided to use the simpler formulation of the simulator based on Eq. (2.25) for further development, including volume translation to get correct liquid levels. The final model uses concentration dependent diffusion coefficients, and can be used for multicomponent systems, such as crude oil. Appendix C gives a call tree for the simulator together with an example of an input and output file.

Efficient formulation and numerical procedures make the simulator fast (about 10 sec for a single run on a 486/33 MHz PC running at about 1 MFLOP). Only 16 collocation points (grid points) were used in the simulations, compared with more than 100 for ordinary finite-difference simulations. This shows one of the main advantages of orthogonal collocation. Increasing the number of collocation points had no effect on the simulation results. The speed is important when regression is used to determine the liquid diffusion coefficient by matching the experimental data.

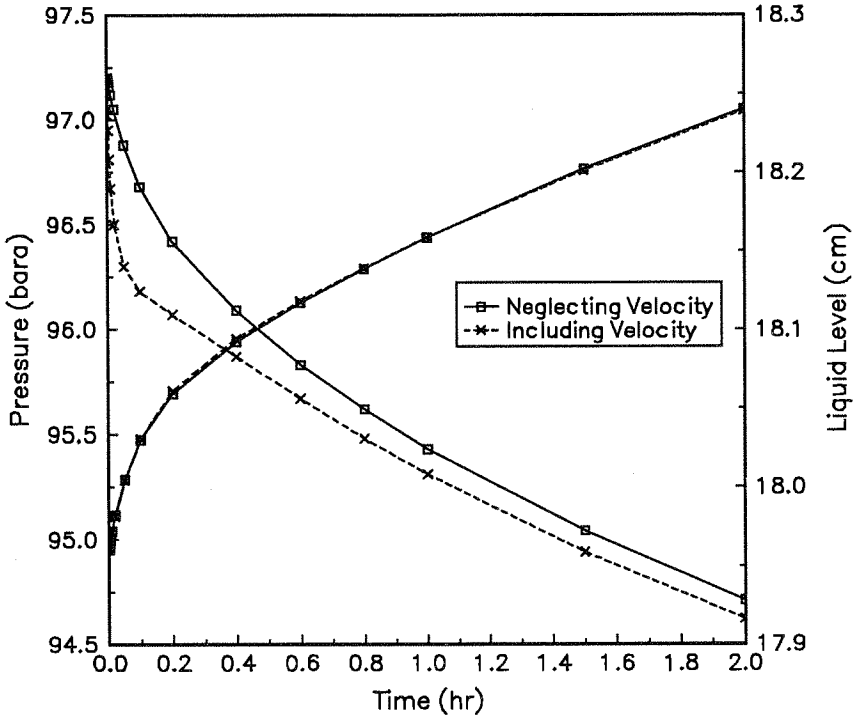

Fig. 2.9 Comparing CVD simulators at first two hours for C_1-C_5 (no VLT)

2.4.4 Matching Procedure

The simulations are done in two steps to match the experimental data:

1. Final equilibrium volumetric condition, p_f and ℓ_f, by slight adjustments of the initial liquid level ℓ_o and the binary interaction parameter k_{12} in the cubic EOS.

2. Pressure and liquid level change with time, $p(t)$ and $\ell(t)$, by adjusting the liquid diffusion coefficient correction factor $c_{\alpha L}$.

The implementation of the liquid diffusion correction factor $c_{\alpha L}$ in Eq. (2.13) gives

$$D_{ij} = \frac{\rho_m^o D_{ij}^o}{\rho_m} \alpha_D \, c_{\alpha L} \tag{2.36}$$

To scale the matching of experimental data, normalized pressure and liquid level were used

$$p_n = \frac{p - p_f}{p_0 - p_f} \qquad \ell_n = \frac{\ell - \ell_0}{\ell_f - \ell_0} \tag{2.37}$$

where p_n drops from 1 to 0, and the liquid level ℓ_n rises from 0 to 1 at infinite time. The liquid diffusion correction factor $c_{\alpha L}$ is determined by minimizing the following sum of squares (SSQ)

$$\text{SSQ} = \sum (p_n - p_{n,sim})^2 + \sum (\ell_n - \ell_{n,sim})^2 \tag{2.38}$$

A sample of the sum of squares as a function of the liquid diffusion correction factor for one of the experiments is given in Fig. 2.10. This figure shows that the SSQ is very sensitive to a small change in the diffusion correction factor, which is important to obtain accurate diffusion coefficients. To minimize the number of iterations needed to find the minimum SSQ, a parabolic interpolation method called Brent's method (Press, *et al.*, 1986) was used. This method proved to be faster than an ordinary Newton-Raphson method based on a numerical second derivative of the SSQ function. One complete simulation of the experiment is needed to get one value for the SSQ function.

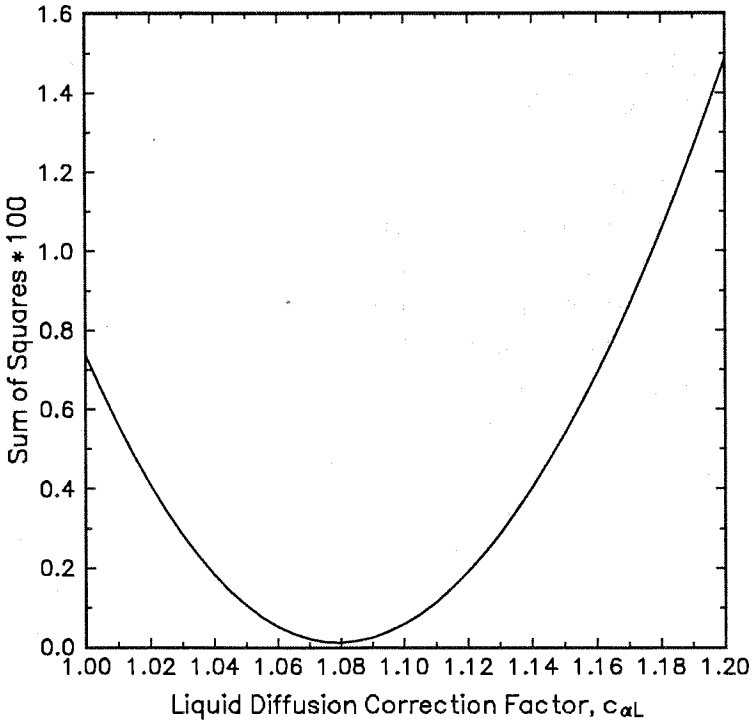

Fig. 2.10 Sample of SSQ as a function of the liquid diffusion correction factor

Data for the first hour of the experiment may be influenced by the initialization of the cell, and is not included in the regression. The final liquid level measured after shaking the cell was slightly increased for some of the experiments to obtain a match of the measured liquid level transient. Shaking the cell changes the reference point slightly and some liquid drops may be hanging on the walls of the cell. However, the

adjustments were less than 1.0 mm (0.5 % of the total liquid height in the cell).

Liquid levels were not measured for some of the earliest experiments. The final liquid level was then adjusted until the simulator returned the same binary interaction parameter k_{12} as obtained for the same binary system including liquid level measurements.

2.4.5 Properties Used in the Simulations

The Soave-Redlich-Kwong (SRK) cubic equation of state is used in the numerical simulator. The final equilibrium conditions calculated by the simulator have been verified by a phase behavior program (PVTx (Whitson, 1992)). Both the pressure, the liquid volume fraction, and the phase densities matched almost exactly.

To get accurate simulations, it is important to use reliable properties for the components in the SRK equation of state. Molecular weight and acentric factor ω were taken from Edmister and Lee (1983). The critical properties p_c, T_c, and z_c were taken from the API data book (1976).

Both high-pressure pure component data and binary volumetric vapor-liquid equilibria data (Kohn and Bradish, 1964; Beaudoin and Kohn, 1967; Berry and Sage, 1970; Glaser, *et al.*, 1985) were used to tune the SRK equation of state to assure accurate estimated densities, compositions, and concentration profiles. First the binary interaction coefficients k_{12} were adjusted to match the vapor and liquid compositions for the range of pressures used in the experiments. Then the volume translation parameters s_i were adjusted to match the phase densities. This procedure gave almost the same results as estimating s_i from pure component data available for nC_{10} and nC_{16} (Beaudoin and Kohn, 1967; Glaser, *et al.*, 1985). All the matching were done using the multiparameter regression option of the phase behavior program PVTx (Whitson, 1992). The volume translation data for C_1 and N_2 were taken from a correlation by Søreide (1989). Table 2.4 gives the results from the match together with the properties used.

Table 2.4 Volume translation- and binary interaction parameters determined from pure component- and vapor-liquid equilibrium data, together with pure component properties used in the simulations.

Component	M (g/gmol)	T_c (K)	p_c (bara)	z_c	ω_{SRK}	s_i	C_1 k_{12}
N_2	28.01	126.3	33.99	0.2916	0.0358	0.085	
C_1	16.04	190.6	46.04	0.2884	0.0074	0.100	
nC_5	72.15	469.6	33.69	0.2623	0.2522	0.104	0.024
nC_8	114.23	568.8	24.86	0.2587	0.3998	0.160	0.044
nC_{10}	142.29	617.6	20.96	0.2462	0.4916	0.200	0.052
nC_{16}	226.43	720.5	14.20	0.2260	0.7667	0.268	0.045

2.4.6 Temperature Correction

A temperature of about 22 ± 1°C was used in the experiments. The temperature is lower at night and higher during the day. Both the total cell volume and the liquid volume are influenced by the temperature, making the pressure in the cell vary slightly with temperature. The pressure in the cell can be corrected before matching the pressure with the simulator by the following equation

$$p^* = p\,(1+(T_{ref}-T)k_{TP}) \tag{2.39}$$

This equation is derived from the real gas law. A correction factor k_{TP} of about 0.008 bar/°C was used for the methane experiments, and about 0.004 bar/°C for the nitrogen experiments. T_{ref} is chosen close to the average temperature for the experiment, thereby minimizing the effect on the estimated diffusion coefficient. The liquid level can also be corrected using an equation similar to Eq. (2.39):

$$\ell^* = \ell\,(1+(T_{ref}-T)k_{TL}) \tag{2.40}$$

This correction was used for the experiments that had large temperature fluctuations and a small total change in liquid level. A correction factor k_{TL} of 0.001 cm/°C was then used. Both the pressure and liquid level corrections resulted in less "noise" in experimental values, but had little effect on the estimated diffusion coefficients.

2.5 Data and Results

Table 2.5 gives an overview of the binary systems measured and the pressures used in the constant volume diffusion experiment. Some of the experiments were repeated for the same initial conditions, giving good repeatability. High initial liquid level was tried on some of the experiments to increase the total pressure drop and thereby get more accurate results. However, the high liquid level experiments were significantly affected by the 10 cm^3 dead volume in the lines between the top of the cell and the pressure transducer.

Table 2.5 Overview of binary systems and pressures used in the experiments at 22°C

Liquid	Vapor			
	N_2 (bar)	C_1 (bar)	CO_2 (bar)	N_2+CO_2 (bar)
C_5	100(2) 180(2)	100(3) 150(1) 180(2)^s		
C_8	100(1)	100(3)	50^c	
C_{10}	100(1) 185(1)	100(1) 180(1) 100(1)^h	50^c	50^h 100^h 150^h
C_{16}	100(2) 180(1) 100(1)^h 180(2)^f 180(1)^h	100(2) 180(2) 180(2)^f 100(1)^h 180(1)^h	50^c	
H_2O	185(2)^n		50(2)^c	50(1) 100(1)^h 150(1)^h
Brine	185(1)^n		50(2)^c	

c = Convection dominated
f = Part of the liquid froze when pressure was increased
h = High initial liquid level: No good match
n = No pressure drop
s = Initially single phase at interface

All experiments with CO_2 gave diffusion coefficients that were 100 to 150 times higher than reported by Grogan *et al.* (1988) and by Renner (1988). Simulations showed that the liquid density at top of the liquid column (containing CO_2) was higher than at the bottom of the cell (no CO_2). This caused convective mixing that dominated the experiments.

There were also problems with the nC_{16} experiments at 21°C and 180 bar where the pure nC_{16} "froze" when the pressure was increased. The freezing point of nC_{16} is 18.2°C at 1 bar, increasing slightly with pressure. Two experiments with C_1-nC_{16} and one with N_2-nC_{16} were run at 180 bar using a temperature of 25.7°C without problems. One of the C_1-nC_{16} and the N_2-nC_{16} experiments were run after reducing the volume in the lines between the cell and the pressure transducer to about 2 cm^3.

Initial and final values for pressure and liquid level together with the resulting parameters from the simulations are given in Table 2.6 for the methane systems, and in Table 2.7 for the nitrogen systems. A liquid diffusion correction factor $c_{\alpha L} = 1.13$ indicates a diffusion coefficient 13% higher than predicted by the extended Sigmund correlation. The correction factor was constant during each run, and determined for the range of reduced molar densities covered by each experiment, and not a single value. Tables 2.6 and 2.7 also give the total time of the experiment before shaking the cell, the range of reduced molar densities and diffusion coefficients together with the equilibrium composition of both the liquid and vapor phase. Note that the vapor diffusion coefficients are 2 to 15 times higher than the liquid diffusion coefficients. The goodness-of-fit is given by the standard deviation of the normalized pressure and liquid level data. Shaded liquid level data indicates simulated and not measured values.

Table 2.6 Measured and calculated properties from experiments with methane

T=22°C Binary system	Run	Time (hr)	p_0 p_{end} p_f (bara)	ℓ_0 ℓ_{end} ℓ_f (cm)	SRK BIP k_{12}	Diff. corr. factor $c_{\alpha L}$	Reduced molar density ρ_{mrL} ρ_{mrV}	Diffusion coefficients D_L D_V (10^{-4} cm^2/s)	Equil. comp. x_1 y_1 (frac)	Standard Deviation p_n ℓ_n
C_1-nC_5	90n	162	94.9	22.37	0.032	1.13	2.70 - 2.76	1.01 - 1.36	0.2546	0.0007
			73.5	24.52			0.37 - 0.45	7.84 -11.07	0.9729	–
			54.1	26.80						
C_1-nC_5	90o	266	94.3	21.52	0.033	1.12	2.69 - 2.76	0.99 - 1.34	0.2595	0.0017
			69.1	24.17			0.36 - 0.45	7.90 -11.25	0.9729	–
			55.4	25.85						
C_1-nC_5	91h	328	96.7	17.96	0.034	1.09	2.69 - 2.76	0.98 - 1.34	0.2924	0.0026
			72.3	21.09			0.37 - 0.48	7.73 -10.86	0.9706	0.0181
			64.1	22.30						
C_1-nC_5	91i	312	149.5	17.43	0.029	1.21	2.68 - 2.78	0.95 - 1.40	0.4362	0.0075
			112.4	22.41			0.62 - 0.78	4.64 - 7.08	0.9645	0.0197
			98.8	25.15						
C_1-nC_8	91c	264	93.9	19.66	0.050	1.27	3.05 - 3.46	0.50 - 0.99	0.2770	0.0030
			81.5	21.01			0.38 - 0.44	6.02 - 7.29	0.9984	0.0043
			68.9	22.42						
C_1-nC_8	90b	225	95.8	20.20	0.049	1.32	3.06 - 3.48	0.51 - 1.02	0.2815	0.0026
			83.8	21.51			0.39 - 0.46	5.81 - 7.02	0.9985	–
			69.4	23.10						
C_1-nC_8	90c	284	95.0	20.09	0.049	1.29	3.06 - 3.48	0.49 - 0.99	0.2803	0.0017
			82.0	21.52			0.38 - 0.45	5.86 - 7.14	0.9985	–
			69.0	22.95						
C_1-nC_8	91d	308	177.2	19.21	0.050	1.85	3.09 - 3.73	0.45 - 1.37	0.4601	0.0025
			153.9	22.02			0.78 - 0.87	2.89 - 3.52	0.9955	0.0042
			133.3	25.05						
C_1-nC_8	90e	350	178.8	19.00	0.048	1.91	3.09 - 3.75	0.45 - 1.39	0.4699	0.0035
			154.1	22.04			0.79 - 0.89	2.78 - 3.40	0.9956	–
			134.9	24.95						
C_1-nC_8	90d	400	183.7	19.16	0.049	1.90	3.09 - 3.76	0.44 - 1.39	0.4753	0.0022
			156.9	22.44			0.81 - 0.91	2.71 - 3.32	0.9953	–
			138.2	25.30						
C_1-nC_{10}	90t	310	97.2	20.91	0.069	1.10	3.13 - 3.67	0.34 - 0.81	0.2764	0.0019
			87.0	21.96			0.40 - 0.46	4.85 - 5.65	0.9997	–
			73.5	23.31						
C_1-nC_{10}	90u	259	180.5	20.10	0.059	1.78	3.16 - 4.06	0.31 - 1.25	0.4602	0.0024
			165.3	21.98			0.81 - 0.89	2.35 - 2.74	0.9987	0.0025*
			142.5	25.08						
C_1-nC_{16}	90f	250	95.6	22.76	0.069	0.86	3.27 - 4.11	0.18 - 0.58	0.2940	0.0012
			90.6	23.27			0.42 - 0.46	3.45 - 3.76	1.0000	–
			77.1	24.60						
C_1-nC_{16}	90g	404	95.8	22.76	0.070	0.86	3.27 - 4.11	0.18 - 0.58	0.2943	0.0015
			89.5	23.40			0.42 - 0.46	3.44 - 3.79	1.0000	–
			77.3	24.60						
C_1-nC_{16}	92b	271	179.6	17.75	0.070	1.12	3.28 - 4.66	0.11 - 0.75	0.4666	0.0070
			173.5	18.60			0.81 - 0.87	1.74 - 1.88	1.0000	0.0030
			158.8	20.67						
C_1-nC_{16}	92c	309	184.6	17.66	0.069	1.22	3.28 - 4.69	0.12 - 0.81	0.4738	0.0057
			177.6	18.62			0.83 - 0.89	1.68 - 1.83	0.9999	0.0030
			163.0	20.65						

= Liquid level not measured: ℓ_{end} adjusted so k_{12} matches runs with liquid level data.

* = Liquid level corrected for temperature fluctuations.

Table 2.7 Measured and calculated properties from experiments with nitrogen

T=22°C Binary system	Run	Time (hr)	p_0 p_{end} p_f (bara)	ℓ_0 ℓ_{end} ℓ_f (cm)	SRK BIP k_{12}	Diff. corr. factor $c_{\alpha L}$	Reduced molar density ρ_{mrL} ρ_{mrV}	Diffusion coefficients D_L D_V (10^{-4} cm^2/s)	Equil. comp. x_1 y_1 (frac)	Standard Deviation p_n ℓ_n
N_2-nC_5	90s	235	98.5 91.0 86.7	17.10 17.72 18.19	0.140	1.07	2.70 - 2.74 0.36 - 0.36	1.02 - 1.14 8.02 - 8.74	0.1161 0.9830	0.0028 –
N_2-nC_5	91k	207	100.1 92.2 86.0	19.14 19.76 20.41	0.143	1.11	2.69 - 2.73 0.36 - 0.37	1.09 - 1.21 8.04 - 8.79	0.1153 0.9816	0.0049 0.0195
N_2-nC_5	91j	234	178.8 165.7 156.7	17.69 18.75 19.70	0.137	1.15	2.74 - 2.82 0.63 - 0.63	0.93 - 1.16 4.54 - 4.96	0.1974 0.9809	0.0049 0.0262
N_2-nC_5	90r	240	181.8 168.3 159.1	17.91 19.00 19.97	0.135	1.18	2.75 - 2.83 0.64 - 0.65	0.92 - 1.16 4.40 - 4.80	0.1992 0.9818	0.0030 –
N_2-nC_8	91b	332	98.7 94.0 89.6	19.81 20.20 20.58	0.205	1.11	3.06 - 3.18 0.34 - 0.36	0.61 - 0.75 5.91 - 6.26	0.0979 0.9994	0.0054 0.0071*
N_2-nC_8	91a	236	179.4 173.7 165.0	19.70 20.18 20.95	0.211	1.07	3.09 - 3.31 0.62 - 0.64	0.49 - 0.69 3.25 - 3.41	0.1584 0.9992	0.0038 0.0082*
N_2-nC_{10}	90w	313	97.2 94.1 89.8	20.09 20.34 20.70	0.235	0.84	3.13 - 3.28 0.34 - 0.36	0.42 - 0.53 4.98 - 5.18	0.0939 0.9999	0.0070 0.0077*
N_2-nC_{10}	90v	234	184.6 180.3 172.3	20.07 20.43 21.07	0.238	0.97	3.16 - 3.43 0.63 - 0.65	0.39 - 0.59 2.65 - 2.76	0.1575 0.9999	0.0032 0.0045*
N_2-nC_{16}	90m	90	93.6 92.7 88.0	21.79 21.85 22.20	0.282	0.56	3.26 - 3.47 0.34 - 0.34	0.24 - 0.32 3.58 - 3.65	0.0911 1.0000	0.0020 –
N_2-nC_{16}	90l	67	95.4 94.7 89.8	21.78 21.84 22.20	0.279	0.58	3.27 - 3.48 0.34 - 0.35	0.25 - 0.33 3.51 - 3.59	0.0931 1.0000	0.0020 –
N_2-nC_{16}	92d	530	177.8 175.0 171.0	17.64 17.88 18.22	0.282	0.55	3.28 - 3.65 0.61 - 0.62	0.19 - 0.31 1.96 - 2.00	0.1549 1.0000	0.0114 0.0133*

= Liquid level not measured: ℓ_{end} adjusted so k_{12} matches runs with liquid level data.
* = Liquid level corrected for temperature fluctuations.

The result from matching the C_1-nC_8 experiment 91d at 180 bar is given in Fig. 2.11. The dotted lines show the results of changing the liquid diffusion coefficient with ± 5%. Fig. 2.12 shows the effect of using the extended Sigmund correlation without any correction factor for this system. As can be seen in Table 2.6, the C_1-nC_8 system at 180 bar is the system that deviated most from the extended Sigmund correlation.

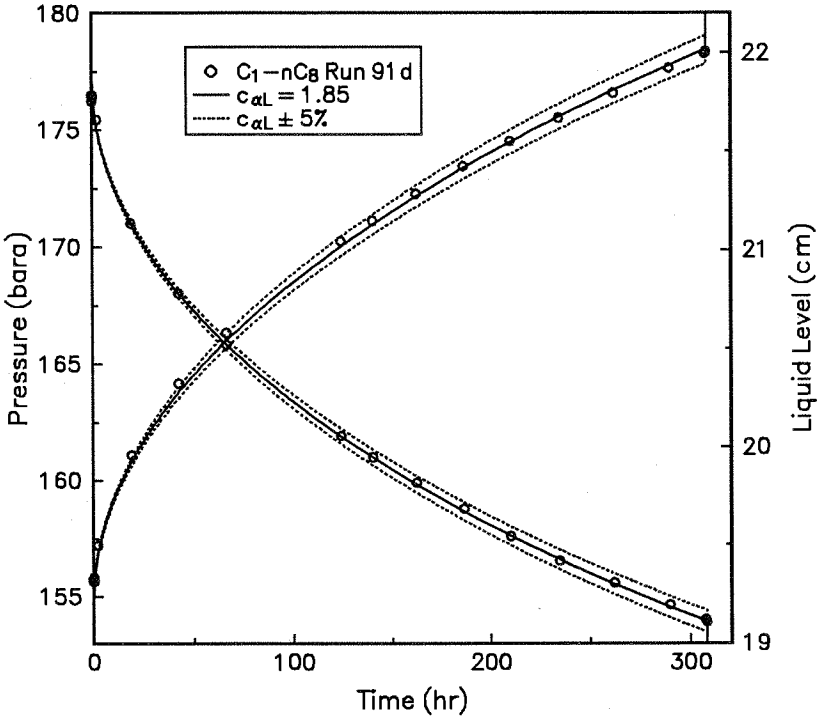

Fig. 2.11 Results from matching a C_1-nC_8 experiment at 180 bar

To check the effect of the vapor diffusion coefficient on the experiment, the simulation was repeated twice without regression, using a vapor diffusion coefficient of – 20% and + 20%. The results are given in Fig. 2.13, and show practically no effect on the simulated pressure and liquid level (less than 2% change). Two simulations with temperatures of + 1°C and – 1°C were also made, but influenced the resulting liquid diffusion correction factor by less than 1%.

Fig. 2.14 shows the concentration profile in the cell as a function of time for the C_1-nC_5 experiment at 150 bar. Note the slower change in concentration and the larger change in composition in the liquid phase than in the gas phase. The time before the concentration front reached the top and bottom of the cell was determined by plotting the concentration for each cell position as a function of time. The results were 7 hours for the 31 cm high gas column, and 18 hours for the 17 cm high liquid column. For the C_1-nC_{10} experiment at 180 bar the time was 35 hours both for the 28 cm high gas column and the 20 cm high liquid column. This shows that at high pressures, liquid diffusion is almost as fast as vapor diffusion even though the diffusion coefficient is more than three times lower.

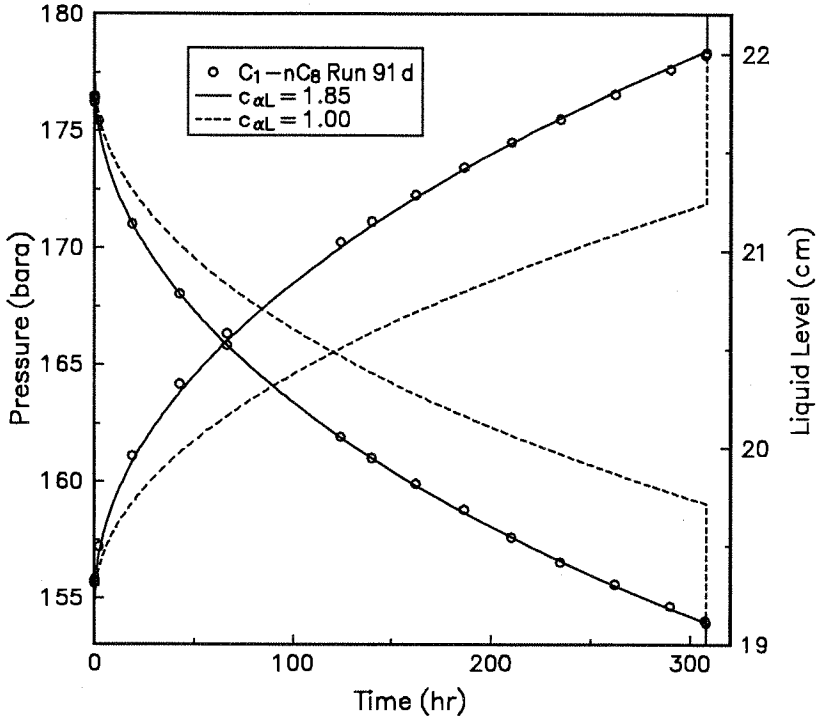

Fig. 2.12 Comparing Sigmund diffusion correlation with C_1-nC_8 experimental data at 180 bar

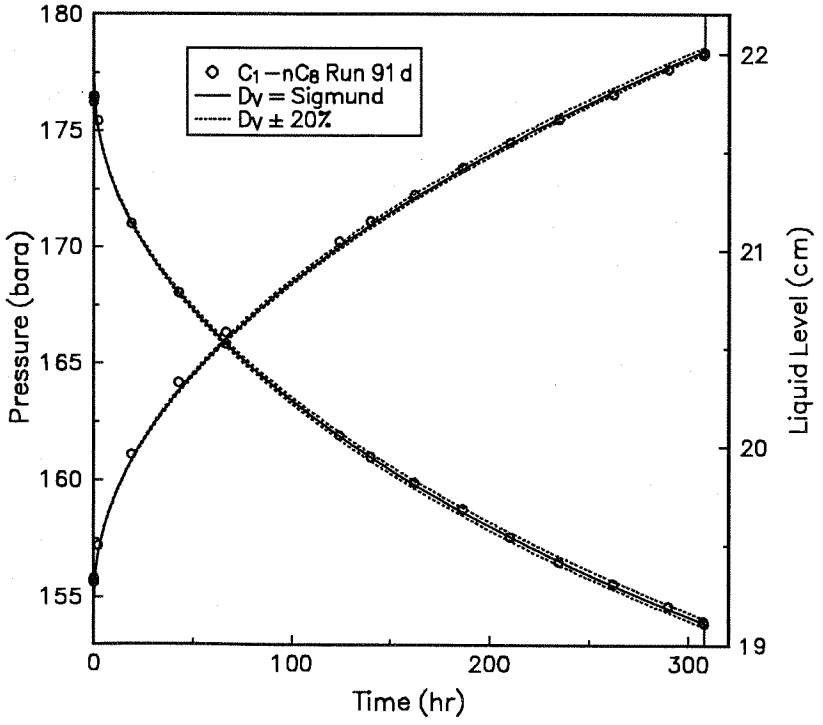

Fig. 2.13 Vapor diffusion sensitivity for the C_1-nC_8 experiment at 180 bar

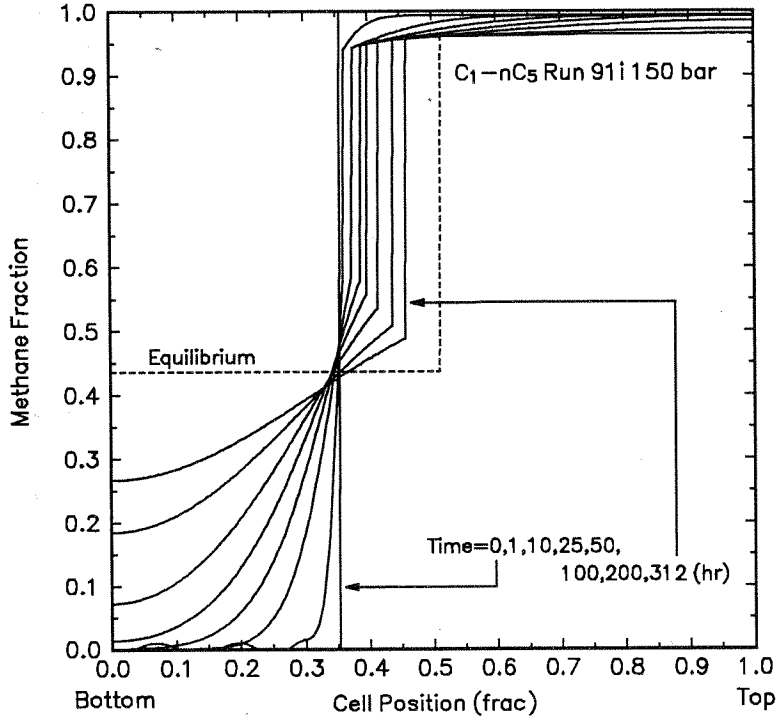

Fig. 2.14 Concentration profiles in the cell vs. time for the C_1-nC_5 experiment at 150 bar

The C_1-nC_5 system at 150 bar was very close to single phase at the interface in the first minutes of the experiment. Some simulation problems were encountered if the initial time steps were small. The meniscus was almost flat, which indicates a low interfacial tension as expected close to critical conditions. Near critical conditions are difficult to estimate correctly and this probably explains the high values on the standard deviation of the pressure and liquid level match in Table 2.6 for this system. This may have influenced the estimated diffusion correction factor.

For some of the methane experiments with heavier liquids, the difference in reduced molar density between the bottom and the top of the liquid phase is large, especially for the 180 bar experiments. This is because the smaller methane molecules that diffuse into the heavier liquid phase increases the number of moles per cm^3, thereby increasing the reduced molar density. In the vapor phase, the reduced molar density is more constant. An example of this is given in Fig. 2.15 where the reduced molar density is plotted as a function of time for several positions in both the vapor and liquid phase for the C_1-nC_{10} run 90u at 180 bar.

For some of the early experiments in 1990 the temperature varied as much as ± 1°C. This caused some fluctuations in the pressure and liquid level, especially for the nC_{10} and nC_{16} experiments. Eq. (2.39) was used to correct the pressure and liquid level for temperature fluctuations before matching, and an example is given in Figs. 2.16 and

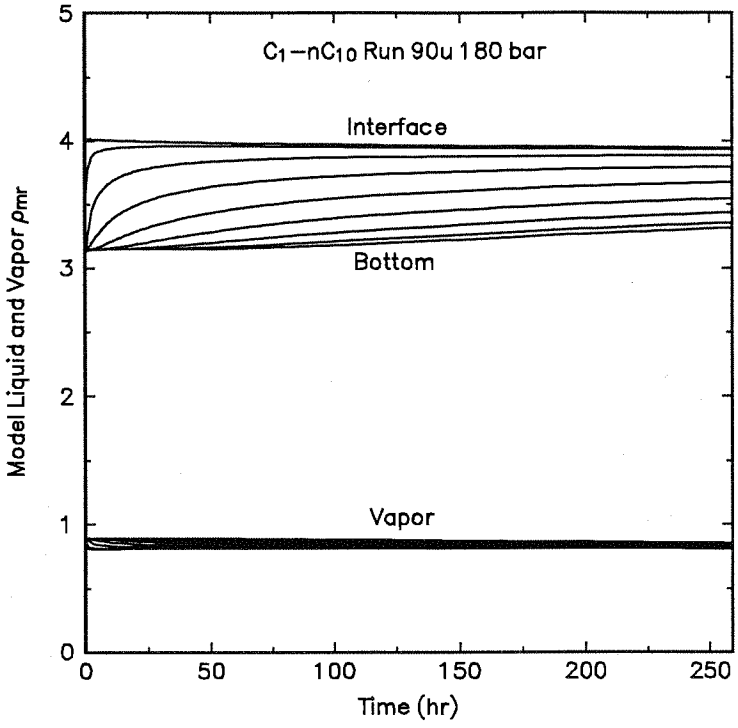

Fig. 2.15 Reduced molar density in vapor and liquid as a function of time

2.17. This shows that both the pressure and liquid level fluctuations are smoothed. The resulting match is given in Fig. 2.18 and shows that the corrected measurements are matched within the ± 5% lines. Note that the total liquid level change is only 3 mm during this experiment.

The upper limit for the reduced molar density in the methane experiments was 4.7 for the C_1-nC_{16} system. To check how high reduced molar densities can be obtained using C_1-nC_{16}, two simulated constant volume diffusion experiments were run using initial pressures of 300 and 450 bar. The resulting range of reduced molar densities were 3.3 to 5.2 for the 300 bar experiment and 3.3 to 5.6 for the 450 bar experiment. The pressure in the gas cylinders used were 200 bar, so no experiments above this pressure were possible without additional equipment. However, the pressure limit of the cell is 700 bar so experiments at higher pressures can be run.

Plots of the results from matching each experiment are given in Appendix B.

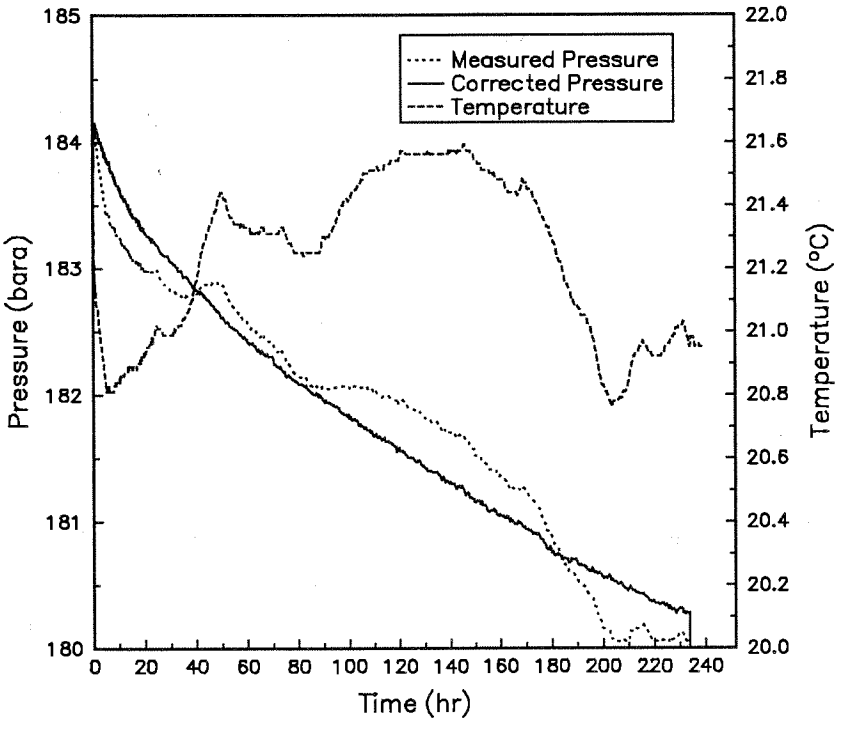

Fig. 2.16 Measured and temperature corrected pressure for N_2-nC_{10} run 90V

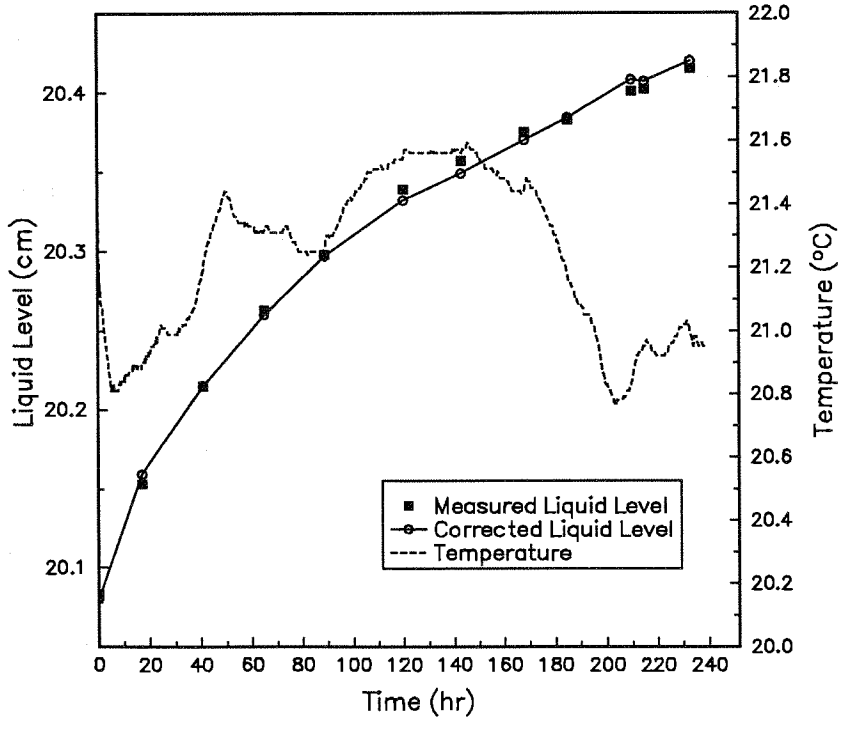

Fig. 2.17 Measured and temperature corrected liquid level for N_2-nC_{10} run 90V

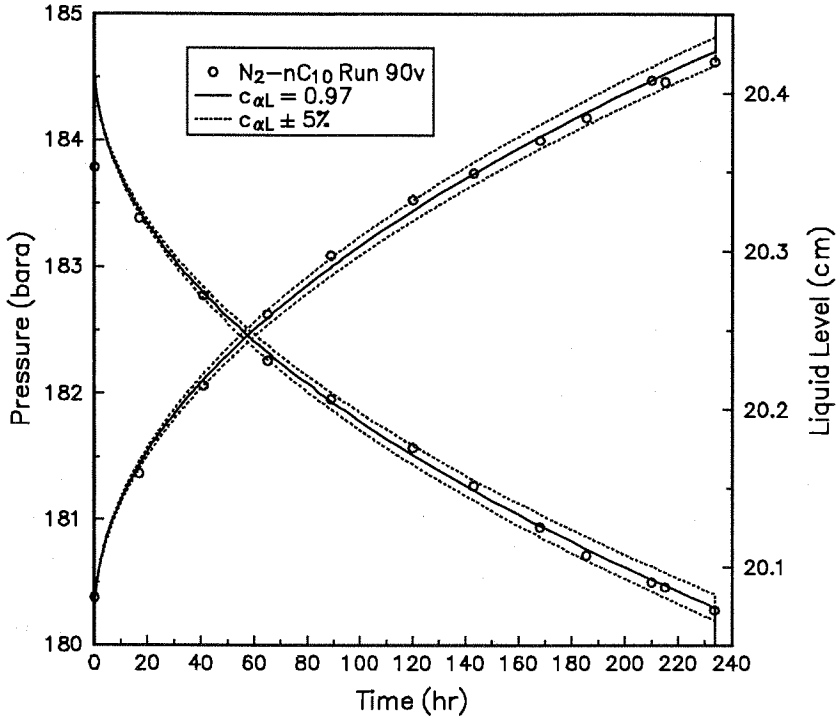

Fig. 2.18 Results from matching the N_2-nC_{10} experiment at 185 bar

2.6 Interpretation and Discussion

The results from the analyzed experiments show that the pressure and liquid level transients are sensitive to the liquid diffusion coefficient, but not particularly sensitive to the vapor diffusion coefficient. This confirms the assumptions made when designing the experiment. All the analyzed experiments give a good match between the measured and simulated pressure and liquid level changes with time. The calculated diffusion coefficients appear to be within ± 5%.

The results from the methane experiments together with the extended Sigmund correlation is given in Fig. 2.19 for reduced molar density between 1 and 10. The numbers in parenthesis give the number of experiments at each pressure. In Fig. 2.20 the methane results are plotted on a semilog scale with a linear scale for reduced density from 1 to 6. This makes the extended Sigmund correlation plot as a straight line. Figs. 2.19 and 2.20 show that the diffusion coefficient correction factor increases with pressure and thereby liquid methane mole fraction. Sigmund (1976a) also shows that measured diffusion coefficients for methane are underpredicted by his correlation for reduced molar densities higher than 0.5. The published methane self diffusion data and the C_1-nC_{10} data in Fig. 2.2 in Section 2.2.4 also show that methane diffusion coefficients are underpredicted by the Sigmund correlation both for high and low pressures. Fig. 2.21 plots the determined diffusion correction factor for each system as a function of the methane fraction, and indicates that increased methane fraction increases the diffusion coefficient relative to the Sigmund correlation. Except for the high-pressure nC_8 and nC_{10} experiments, the extended Sigmund correlation is accurate to within ± 20%. For nC_{16}, which consists of long straight chains, the measured diffusion correction factor at 180 bar is closer to the extended Sigmund correlation than for nC_8 and nC_{10}. The nC_{16} experiment at 100 bar is overpredicted by about 16% by the extended Sigmund correlation.

Figs. 2.22 and 2.23 give the results for the nitrogen experiments, indicating diffusion coefficients close to the extended Sigmund correlation, except for the N_2-nC_{16} experiments. For the nitrogen experiments the diffusion correction factor is almost insensitive to pressure. Also the nitrogen experiments show that for nC_{16} the diffusion correction factor is lower than for the lighter hydrocarbons at the same reduced molar density. The extended Sigmund correlation overpredicts the diffusion coefficients for N_2-nC_{16} by 75%. Note that running the 100 bar N_2-nC_{16} experiments for only 67 and 90 hours give the same results as the 180 bar experiment run for 530 hours. This indicates that even for a system with very low diffusion coefficients, the experiments can be completed within one week (168 hours).

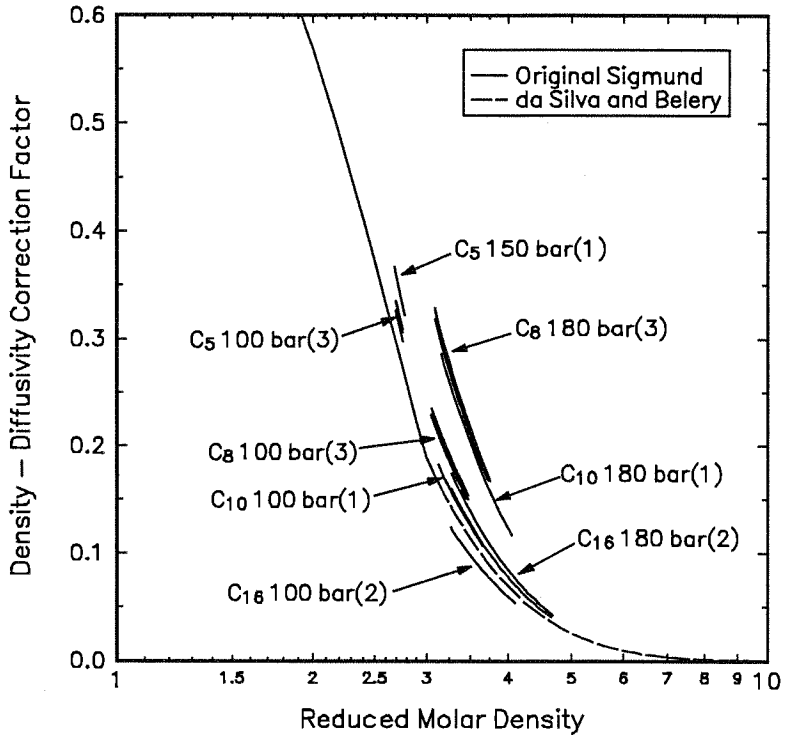

Fig. 2.19 The extended Sigmund correlation with results from methane experiments, ( ) = number of experiments

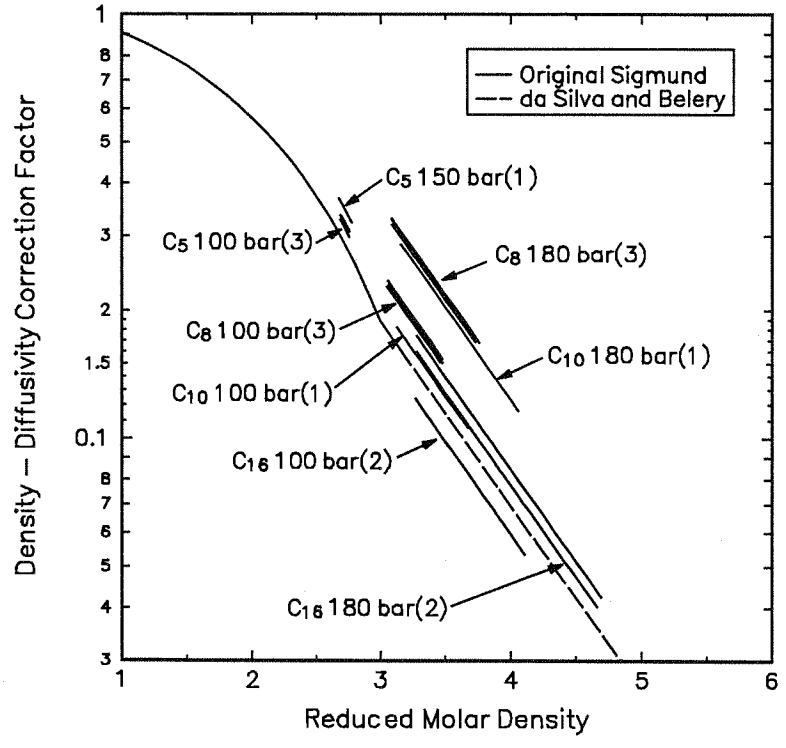

Fig. 2.20 The extended Sigmund correlation with results from methane experiments, ( ) = number of experiments

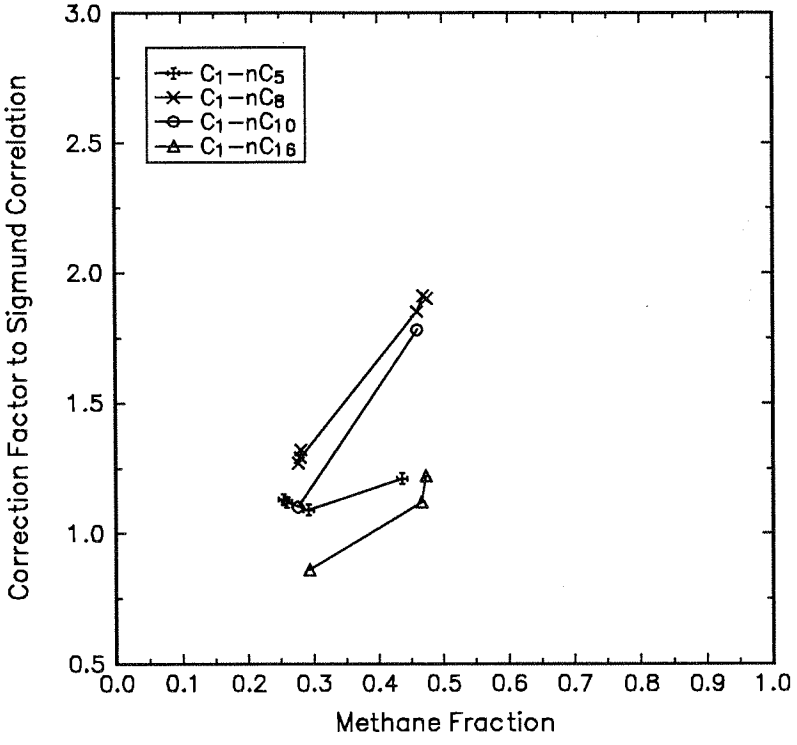

Fig. 2.21 The diffusion correction factor to the extended Sigmund correlation as a function of liquid methane fraction

The binary interaction parameters k_{12} resulting from the regression to match the final equilibrium volumetric conditions for the methane experiments are slightly higher than the values obtained from matching the binary systems in Table 2.4. This may be caused by some less-significant conditions not included in the model. The liquid diffusion correction factor was only changed a few percent when increasing the binary interaction parameter by 20%. Therefore, the higher binary interaction parameters should not influence the accuracy of the estimated binary diffusion coefficients for the methane experiments.

For the nitrogen experiments no binary VLE data were available, so it is more difficult to evaluate the resulting binary interaction coefficients. However, the binary interaction parameters are too high and should be closer to 0.1. The reason for these high binary interaction coefficients is not known. The too-high binary interaction coefficients may give an incorrect concentration profile in the cell and therefore reduce the accuracy of the measured nitrogen diffusion coefficients. Reducing the binary interaction parameter for the N_2-nC_{10} experiment 90v from 0.238 to 0.1 increased the initial (t = 0.2 hr) interface liquid mole fraction of N_2 from 0.17 to 0.22. This gives an increased concentration gradient and will cause an increased diffusion flux and therefore, affect the resulting diffusion coefficient. For nC_{10} and nC_{16}, almost no heavy components vaporized, so the vapor was basically pure C_1 or N_2.

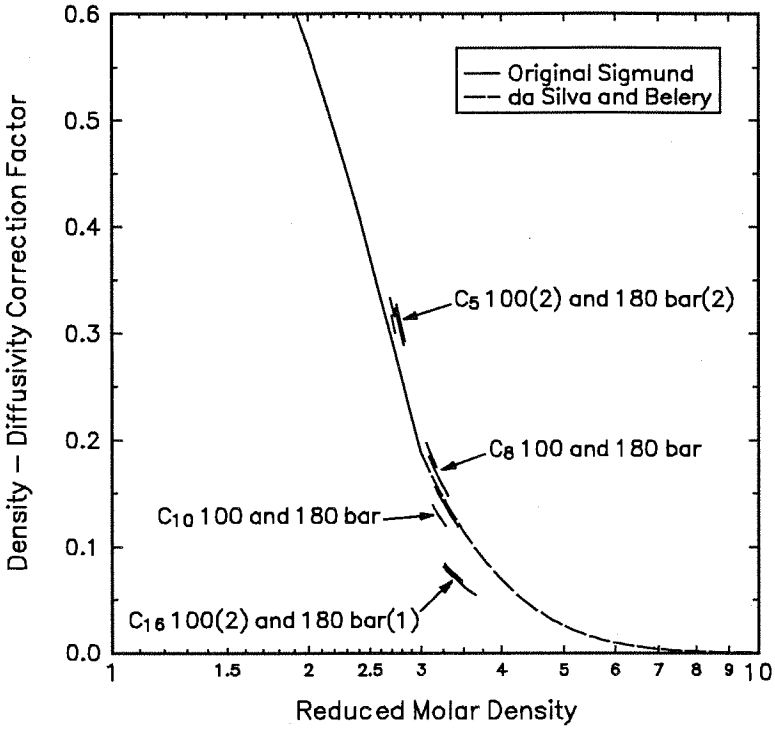

Fig. 2.22 The extended Sigmund correlation with results from nitrogen experiments, ( ) = number of experiments

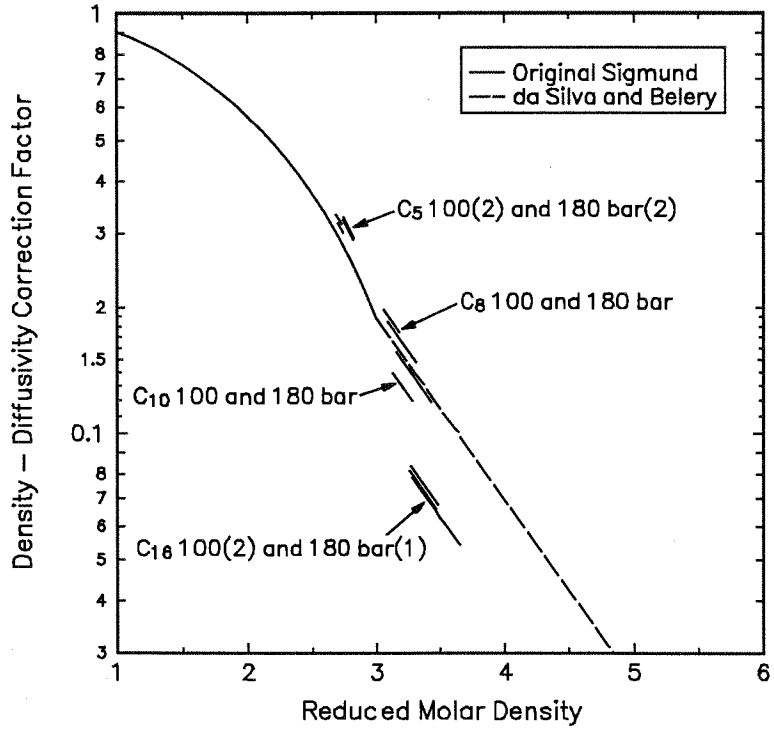

Fig. 2.23 The extended Sigmund correlation with results from nitrogen experiments, ( ) = number of experiments

Assuming the experimental diffusion coefficients are correct, the deviation, the average deviation (AD), and the average absolute deviation (AAD) were calculated for each system. The number of experiments at each pressure were not included. Table 2.8 gives the results for both the methane and nitrogen experiments.

Table 2.8 Deviations from the experimental diffusion coefficients by using the extended Sigmund correlation

	Methane		Nitrogen	
System	100 bar	180 bar	100 bar	180 bar
nC_5	-11%	-17%	-9%	-14%
nC_8	-22%	-47%	-10%	-7%
nC_{10}	-9%	-44%	19%	3%
nC_{16}	16%	-11%	75%	82%
AD	-7%	-30%	19%	16%
AAD	15%	30%	28%	27%

The da Silva and Belery extension to the Sigmund correlations appears to give a good prediction of the measured diffusion coefficients up to the maximum reduced molar density ρ_{mr} of 4.7. The results follow the extended Sigmund correlation quite well for both the nitrogen and the methane experiments with a few exceptions. At 180 bar, when the methane concentration in the liquid is high, the extended Sigmund correlation underpredicts the diffusion coefficients for nC_8 and nC_{10} by almost 50%. The extended Sigmund correlation overpredicts the diffusion coefficients for N_2-nC_{16} at both 100 and 180 bar with 75%. The absolute average deviation by using the extended Sigmund correlation was 22% for the methane experiments and 27% for the nitrogen experiments. No improvements of the extended Sigmund correlation were possible based on the measured diffusion coefficients. It appears that the deviation between the extended Sigmund correlation and the experimental data is caused by the length or size of the molecules, and not by the reduced molar density alone.

To check the effect of any systematic errors, the effect of incorrect measurements were examined. Simulations for three systems were made with pressures that were 1 bar higher than measured. This changed the resulting diffusion correction factor 0.5 to 1.3%. The calibration of the pressure transducer was checked after all experiments were performed and was found within the limit given in Table 2.3 (± 0.5 bar). As a result, the effect of incorrect absolute pressure should be less than 0.5%. The effect of the temperature and the vapor diffusion coefficient was examined in Section 2.5 and found to have little effect. The reference point for the liquid level was also changed with 0.5 cm but had only a small effect on the resulting binary interaction parameter and negligible effect on the diffusion correction factor. All these effects combined should give a systematic error less than 5%.

If the interfacial resistance mentioned in Section 2.2.10 was important, the simulated results should diffuse too fast for early times when the diffusion flux across the vapor-liquid interface is high. This effect would also give a lower diffusion coefficient at low pressures than at high pressures. The diffusion coefficient for nC_5 should also be lower than for nC_8, nC_{10}, and nC_{16}. By examining the data, it was not possible to find anything that indicated that interfacial resistance had influenced the results. The match of the experimental data were good for both early and late times for all the experiments. Both the 100 bar and 150 bar C_1-nC_5 experiment give similar results. The interfacial tension is about 10 times higher for the low-pressure C_1-nC_5 experiment, so if the interfacial resistance was important, the low-pressure experiment should have resulted in a lower diffusion correction factor. The lower diffusion correction factor for the nC_{16} experiments can not be related to the interface resistance because the interfacial tension is almost the same for both nC_8, nC_{10}, and nC_{16}.

The use of the simplified model in the numerical simulations makes the model density slightly different from the actual density calculated with the EOS based on composition, and pressure. The deviation is largest for the experiments with the highest diffusion coefficients, like the C_1-nC_5 at 150 bar and C_1-nC_8 at 180 bar. To check the effect of this deviation, both the model density and the actual density were plotted for the C_1-nC_8 run 91d at 180 bar. Fig. 2.24 gives the density in the vapor phase and Fig. 2.25 the density in the liquid phase for 9 different positions in each phase as a function of time. The density deviation in the vapor phase close to the interface is as large as 20%, while for the liquid phase it is less than 2% at the interface. Note from these plots that the actual density on top of both the vapor and liquid columns are lower than at the bottom. This confirms the assumption of no convection in the cell due to density differences. Because the reduced molar density is used in the extended Sigmund correlation, this is also plotted vs. time for both the vapor and liquid phases in Figs. 2.26 and 2.27. This figures that the deviation between the model and actual reduced molar density is very similar to the deviation in the density. From the plot of the extended Sigmund correlation in Fig. 2.1 it is seen that the 20% error in the vapor reduced molar density at the interface has little effect on the correction factor for $\rho_{mr}<1.0$. The reduced molar density in the vapor phase varied from 0.37 to 0.91 for the methane experiments, and from 0.36 to 0.65 for the nitrogen experiments. In Section 2.4.3 it was shown that using the simplified model had almost no effect on the pressure and liquid level transients except for the first few hours. The deviation between the model and the actual density has therefore little effect on the resulting diffusion correction factor.

The effect of the 10 cm^3 volume in the lines between the pressure transducer and the cell was checked. After reducing this volume to 2 cm^3, a new C_1-nC_{16} experiment (92c) was run at 180 bar. The resulting liquid diffusion correction factor (corrected for the slightly higher pressure) increased by 7%. It is difficult to draw any conclusions based on comparing only two experiments, but this indicates that all the estimated diffusion correction factors may be 5 to 10% too low. To match this

experiment, the total height of the cell had to be reduced slightly to account for the 7 cm^3 in the lines that were removed. The binary interaction coefficient did not change.

Table 2.6 and Figs. 2.25 and 2.27 show that the liquid diffusion coefficient varies significantly both from the interface to the bottom of the cell and also with time. According to Eq. (2.13) the liquid diffusion coefficient is assumed a function of reduced molar density and real molar density only. Figs. 2.28 and 2.29 show how the vapor and liquid diffusion coefficients vary with time for the C_1-nC_8 experiment 91d at 180 bar. Note that the liquid diffusion coefficient varies from 0.45 to 1.37 $\times$ 10^{-4} cm^3/s from the top to the bottom of the liquid column initially. As the methane diffuses down into the liquid column, the liquid diffusion coefficient decreases.

Simulations using a constant liquid diffusion coefficient were made to check if it was possible to get a good match without including a composition dependent diffusion coefficient. This simulation matched the measured pressure and liquid level transients with the same accuracy as when using variable diffusion coefficients. The average diffusion coefficient used was 0.67 $\times$ 10^{-4} cm^3/s. This shows that it is possible to get a good match by using an average diffusion coefficient without knowing the correct correlation between the diffusion coefficient and the concentration and pressure. The same was the case for the C_1-nC_{16} experiment 92c at 180 bar that had a diffusion coefficient varying from 0.12 to 0.81 $\times$ 10^{-4} cm^3/s during the experiment. The average liquid diffusion coefficient used for this match was 0.24 $\times$ 10^{-4} cm^3/s. The C_1-nC_5 experiment 91i at 150 bar also gave a good match with D_L = 1.09 $\times$ 10^{-4} cm^3/s. The pressure drop before stopping these three experiments represented 53% of the total pressure drop for run 91d, 32% for run 92c, and 72% for run 91i. This indicates that using a constant diffusion coefficient may give good match of the measured pressure and liquid level almost all the way to equilibrium conditions. It is, however, difficult to estimate this average diffusion coefficient since it is a function of concentration profiles and reduced molar density profiles.

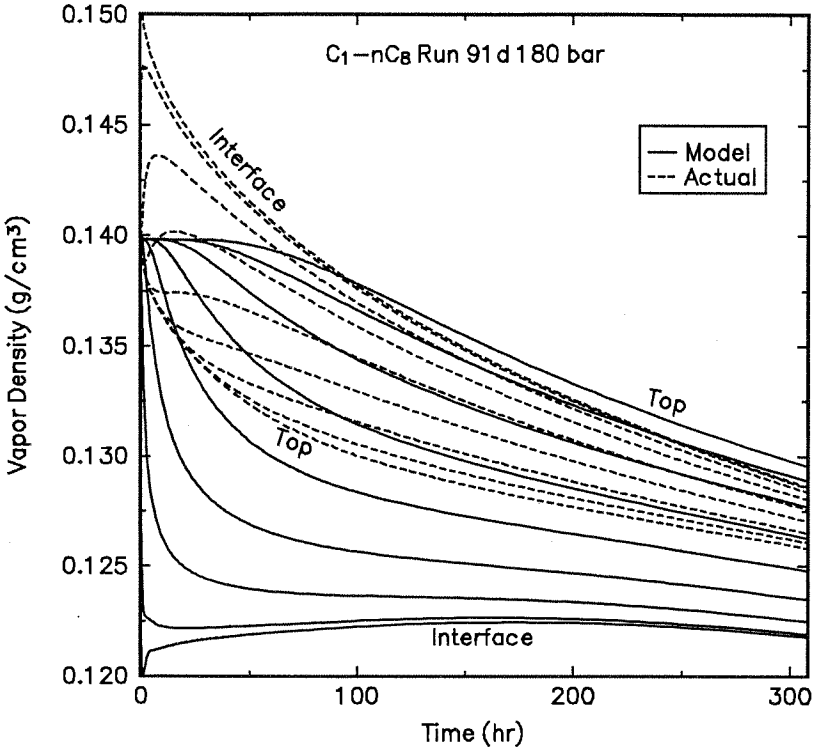

Fig. 2.24 Model and actual density for the vapor phase vs. time

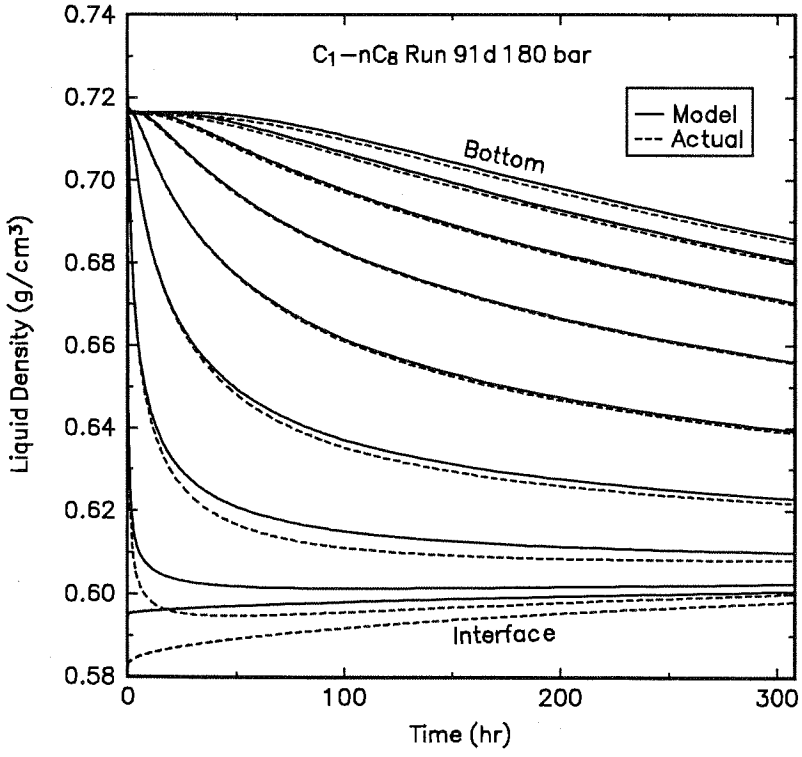

Fig. 2.25 Model and actual density for the liquid phase vs. time

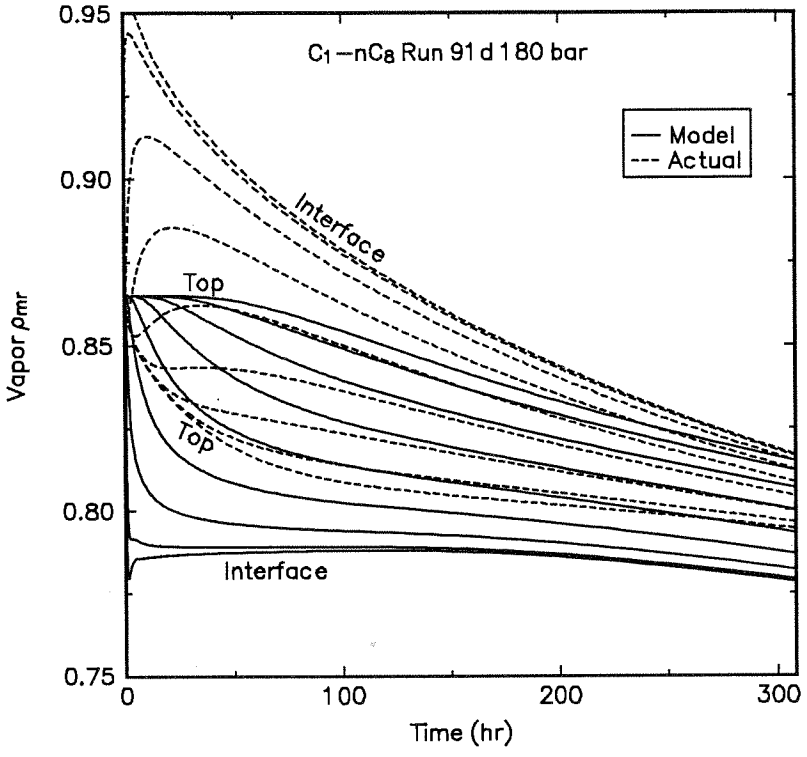

Fig. 2.26 Model and actual reduced molar density for the vapor phase vs. time

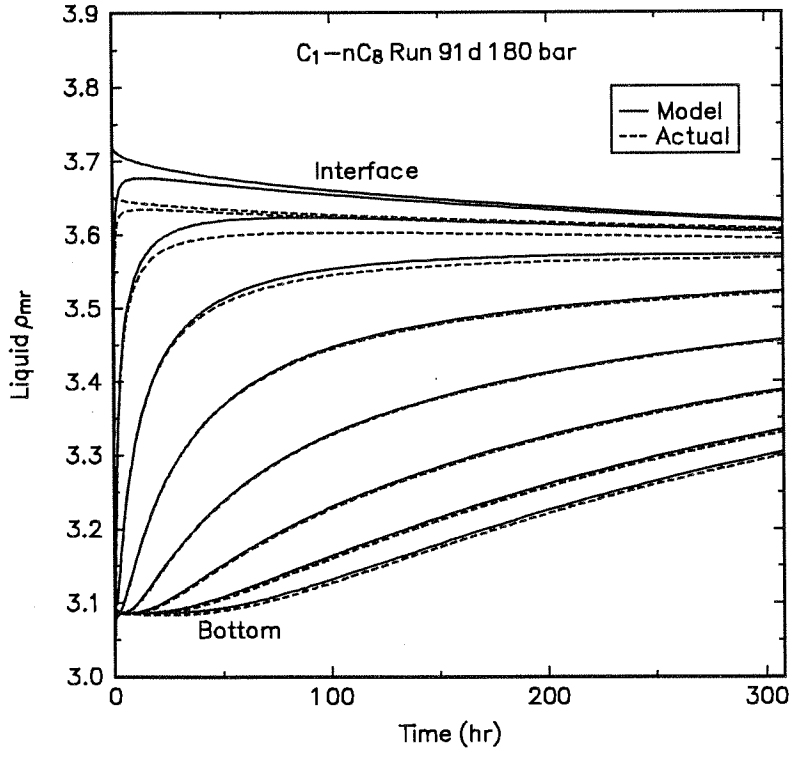

Fig. 2.27 Model and actual reduced molar density for the liquid phase vs. time

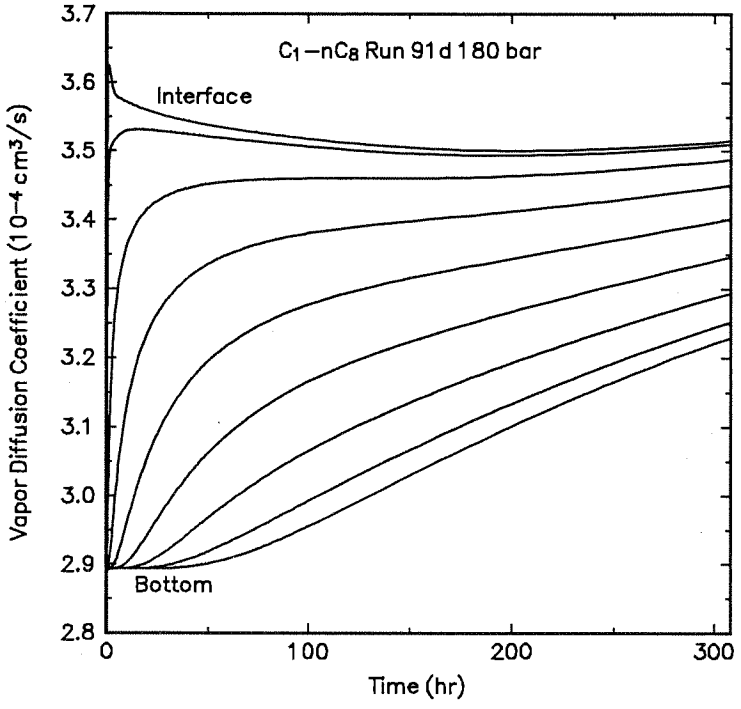

Fig. 2.28 Vapor diffusion coefficient as a function of cell position and time

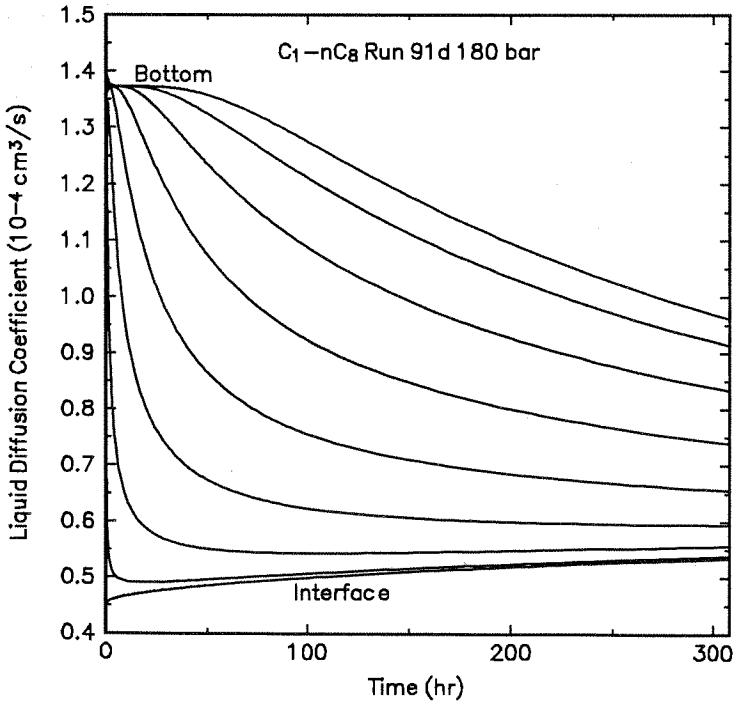

Fig. 2.29 Liquid diffusion coefficient as a function of cell position and time

2.7 Conclusions and Recommendations

The following conclusions have been made from the reported experimental results:

1. A simple method to determine high-pressure liquid diffusion coefficients has been presented, with accurate and reproducible results. The method is based on a constant volume diffusion process, where a vapor diffuses into a liquid with resulting pressure drop and liquid level increasing as a function of time. The liquid diffusion coefficient is determined by simulating the experiment with a numerical simulator using a cubic equation of state.

2. Varying the vapor diffusion coefficient with ± 20% influences the resulting liquid diffusion coefficient by less than 2%. Changing the temperature by 1°C or the pressure by 1 bar influences the results by less than 1%.

3. The accuracy of the measured diffusion coefficient depends on the amount of pressure drop in the system. The fluids used, the initial pressure, and the initial liquid level influences the total pressure drop. For the 27 systems analyzed the accuracy of the liquid diffusion coefficient appeared to be ± 5%.

4. The absolute average deviation by using the extended Sigmund correlation was 22% for the methane experiments and 27% for the nitrogen experiments. No improvements of the extended Sigmund correlation were possible based on the measured diffusion coefficients. At 180 bar, when the methane concentration in the liquid is high, the extended Sigmund correlation underpredicts the diffusion coefficients for nC_8 and nC_{10} by almost 50%. It appears that the deviation between the extended Sigmund correlation and the experimental data is caused by the length or size of the molecules, and not by the reduced molar density alone.

5. One experiment lasts for about one week depending on the diffusion coefficients and the number of pressure and liquid level points needed. A smaller cell would reduce the time but also reduce the accuracy of the measured liquid diffusion coefficient.

6. For the systems with CO_2 there was a large convective mixing that gave an apparent diffusion coefficient 100 to 150 times higher than expected. For these systems it is not possible to measure the diffusion coefficients without modifying the experimental apparatus.

7. For both the methane and nitrogen experiments using water, the pressure drop was too small to obtain reliable diffusion coefficients.

The following recommendations are made for further research:

1. Use the developed method for ternary systems to check the models presently being used to calculate effective diffusion coefficients in multicomponent liquid mixtures; Wilke's formula, Eq. (2.21).

2. The constant volume diffusion method can be used on most binary gas-oil systems that have some swelling effect. Although the method is tested only with binary systems, it can also be used for multicomponent systems, like reservoir oil and gas. Multicomponent systems require accurate tuning of the cubic equation of state with experimental data to give accurate densities for the oil and gas used in the experiments.

3. The underprediction of the diffusion coefficients by the extended Sigmund correlation for high methane concentrations may be important in evaluating gas injection in light oil reservoirs. In the Ekofisk reservoirs the methane mole fraction is as high as 55 to 60% while 16% is C_{10+}. It is difficult to draw any conclusions about underprediction by the extended Sigmund correlation for multicomponent diffusion with high methane fractions based on these binary experiments. The overprediction of the N_2-nC_{16} diffusion coefficients by the extended Sigmund correlation may be important for nitrogen injection. However, the original Ekofisk oil contains about 10 mole% C_{16+} so this overprediction may be of less importance.

2.8 Nomenclature

$c_{\alpha L}$ = liquid diffusion correction factor, dimensionless
C = molar concentration, gmol/cm^3
D = diffusion coefficient, cm^2/s
D_e = effective diffusion coefficient, cm^2/s
f_i = fugacity of component i
F = formation electrical resistivity factor, dimensionless
h = total cell height, cm
ℓ = liquid-gas interface position, cm
k_{12} = binary interaction parameter in the SRK EOS
k_{TL} = temperature correction factor for liquid level, cm/°C
k_{TP} = temperature correction factor for pressure, bar/°C
m = cementation exponent
M = molecular weight, g/gmol
n = number of components
N = total number of moles
p = pressure, Pa
p_r = reduced pressure p/p_c, dimensionless
R = universal gas constant, 8.31438×10^6 Pa cm^3/(K gmol)
s_i = volume translation parameter for component i
t = time, s
T = temperature, K
u = flux per unit area, gmol/(cm^{2}s)
v = molar volume, cm^3/gmol
v = velocity, cm/s
v_{ci} = critical molar volume of component i, cm^3/gmol
x = position, cm
x_i = liquid phase mole fraction of component i
y_i = vapor phase mole fraction of component i
z_{ci} = critical compressibility factor, cm^3/gmol
z_i = phase mole fraction of component i

Greek

α_D = diffusivity product correction factor, dimensionless
β = constant
ϕ = porosity, fraction
ε = Lennard-Jones 12-6 force constant, J
κ = Boltzmann constant, 1.380622×10^{-23} J/K
ρ = density, g/cm^3
ρ_m = molar density, gmol/cm^3
ρ_{mc} = mixture pseudo-critical molar density, dimensionless

ρ_{mr} = mixture reduced molar density, dimensionless
σ_{ij} = Lennard-Jones 12-6 collision diameter, Å
τ = time, s
χ = position, fraction of phase length
ω = Pitzer's acentric factor, dimensionless
Ω_{ij} = binary diffusion collision integral, dimensionless

Subscript

A,B = binary components
0 = at time $t = 0$
c = critical
f = final (at $t = \infty$)
i = component number
j = component number
m = mixture (or molar for ρ)
n = normalized
r = reduced
sim = simulated

Superscript

o = low pressure
L = liquid phase
V = vapor phase

2.9 References

Technical Data Book - Petroleum Refining, third edition, American Petroleum Institute, Washington, DC (1976).

Amyx, J.W., Bass, D.M., Jr., and Whiting, R.L.: *Petroleum Reservoir Engineering - Physical Properties*, McGraw-Hill Book Company, New York (1960).

Beaudoin, J.M. and Kohn, J.P.: "Multiphase and Volumetric Equilibria of the Methane - n-Decane Binary System at Temperatures between -36° and 150°C," *J. Chem. Eng. Data* (1967) **12**, No. 2, 189-191.

Berry, V.J., Jr. and Koeller, R.C.: "Diffusion in Compressed Binary Gaseous Systems," *AIChE J.* (June 1960) 274-280.

Berry, V.M. and Sage, B.H.: "Phase Behavior in Binary And Multicomponent Systems At Elevated Pressures: N-Pentane and Methane - n-Pentane," National Standard Reference Data Series, National Bureau of Standards, Washington, D.C. (1970) **32**.

Bird, R.B., Stewart, W.E., and Lightfoot, E.N.: *Transport Phenomena*, John Wiley & Sons, Inc., New York (1960).

Chung, T.H., *et al.*: "Generalized Multiparameter Correlation for Nonpolar and Polar Fluid Transport Properties," *Ind. Eng. Chem. Res.* (1988) **27**, No. 4, 671-679.

Coats, K.H.: "Implicit Compositional Simulation of Single-Porosity and Dual-Porosity Reservoirs," paper SPE 18427 presented at the SPE Symposium on Reservoir Simulation, Houston, TX, Feb. 6-8 (1989).

Coats, K.H.: "Engineering and Simulation," Fourth International Forum on Reservoir Simulation, Salzburg, Austria, Aug. 31 - Sept. 4 (1992).

Crank, J.: *The Mathematics of Diffusion*, second edition, Oxford University Press, Oxford (1975).

da Silva, F.V. and Belery, P.: "Molecular Diffusion in Naturally Fractured Reservoirs: A Decisive Recovery Mechanism," paper SPE 19672 presented at the 1989 SPE Annual Technical Conference and Exhibition, San Antonio, TX, Oct. 8-11.

Dawson, R., Khoury, F., and Kobayashi, R.: "Self-Diffusion Measurements in Methane by Pulsed Nuclear Magnetic Resonance," *AIChE J.* (1970) **16**, No. 5, 725-729.

Edmister, W.C. and Lee, B.I.: *Applied Hydrocarbon Thermodynamics*, Gulf Publishing Company, Houston, TX (1983).

Erkey, C. and Akgerman, A.: "Translational-Rotational Coupling Parameters for Mutual Diffusion in N-Octane," *AIChE J.* (1989) **35**, No. 3, 443-448.

Fayers, F.J. and Lee, S.T.: "Crossflow Mechanisms by Gas Drive in Heterogeneous Reservoirs," paper 24934 presented at the 1992 Annual Technical Conference and Exhibition, Washington, DC, Oct. 4-7.

Geankoplis, C.J.: *Transport Processes and Unit Operations*, Allyn and Bacon, Inc., Boston (1983).

Glaser, M., *et al.*: "Phase Equilibria of (Methane + n-Hexadecane) and (p, V_m, T) of n-Hexadecane," *J. Chem. Thermodyn.* (1985) **17**, 803-815.

Grogan, A.T., *et al.*: "Diffusion of CO_2 at Reservoir Conditions: Models and Measurements," *SPERE* (Feb. 1988) 93-102.

Grogan, A.T. and Pinczewski, W.V.: "The Role of Molecular Diffusion Processes in Tertiary CO_2 Flooding," *JPT* (May 1987) 591-602.

Helbæk, M.: "Diffusion Coefficient Measurements in Gas/Oil Mixtures at High Pressure by Nuclear Magnetic Resonance," Dr. Ing. Dissertation, The Norwegian Institute of Technology, Laboratory of Physical Chemistry, Trondheim (1992).

Hua, H., Whitson, C.H., and Yuanchang, Q.: "A Study of Recovery Mechanisms in a Nitrogen Diffusion Experiment," *Proc.*, Sixth European Symposium on Improved Oil Recovery, Stavanger, Norway, May 21-23 (1991) 543-553.

Khoury, F. and Kobayashi, R.: "Data by NMR and Representations of Self-Diffusion Coefficients in Carbon Tetrafluoride and the Determination of Intermolecular Force Constants," *J. Chem. Phys.* (1970) **55**, No. 5, 2439-2445.

Killie, S., *et al.*: "High-Pressure Diffusion Measurements by Mach-Zehnder Interferometry," *AIChE J.* (1991) **37**, No. 1, 142-146.

Kohn, J.P. and Bradish, W.F.: "Multiphase and Volumetric Equilibria of the Methane - n-Octane System at Temperatures between -110° and 150°C," *J. Chem. Eng. Data* (1964) **9**, No. 1, 5-8.

Lohrenz, J., Bray, B.G., and Clark, C.R.: "Calculating Viscosities of Reservoir Fluids from Their Compositions," *JPT* (Oct. 1964) 1171-1176; *Trans.*, AIME, **231**.

Marrero, T.R.: "Gaseous Diffusion Coefficients - A Comprehensive Critical Evaluation of Experimental Studies and Correlations of Results," PhD Dissertation, University of Maryland (1970).

Matthews, M.A., Rodden, J.B., and Akgerman, A.: "High-Temperature Diffusion of Hydrogen, Carbon Monoxide, and Carbon Dioxide in Liquid n-Heptane, n-Dodecane. and n-Hexadecane," *J. Chem. Eng. Data* (1987) **32**, No. 3, 319-322.

Michelsen, M.L.: "Note on Constant Volume Diffusion Simulations," Institut for Kemiteknik, Technical University of Denmark (DTH), Lyngby, Denmark (1992).

Morel, D.D., *et al.*: "Diffusion Effects in Gas-Flooded Light Oil Fractured Reservoirs," paper SPE 20516 presented at the 1990 SPE Annual Technical Conference and Exhibition, New Orleans, LA, Sept. 23-26.

Peneloux, A., Rauzy, E., and Freze, R.: "A Consistent Correction for Redlich-Kwong-Soave Volumes," *Fluid Phase Equilibria* (1982) **8**, 7-23.

Press, W.H., *et al.*: *Numerical Recipes - The Art of Scientific Computing*, Cambridge, New York (1986).

Reamer, H.H., Duffy, C.H., and Sage, B.H.: "Diffusion Coefficients in Hydrocarbon Systems: Methane - n-Pentane - Methane in Liquid Phase," *Ind. Eng. Chem.* (1956) **48**, No. 2, 282-284.

Reamer, H.H., Opfell, J.B., and Sage, B.H.: "Diffusion Coefficients in Hydrocarbon Systems: Methane-Decane-Methane in Liquid Phase," *Ind. Eng. Chem.* (1956) **48**, No. 2, 275-282.

Reid, R.C., Prausnitz, J.M., and Poling, B.E.: *The Properties of Gases & Liquids*, fourth edition, McGraw-Hill, New York (1987).

Renner, T.A.: "Measurement and Correlation of Diffusion Coefficients for CO_2 and Rich-Gas Applications," *SPERE* (May 1988) 517-523.

Riazi, M.R. and Whitson, C.H.: "Estimating Diffusion Coefficients of Dense Fluids," *Accepted for publication in Chem. Eng. Comm.* (1989).

Robinson, R.C. and Stewart, W.E.: "Self-Diffusion in Liquid Carbon Dioxide and Propane," *Ind. Eng. Chem. Fund.* (1968) **7**, No. 1, 90-95.

Sigmund, P.M.: "Prediction of Molecular Diffusion At Reservoir Conditions. Part I - Measurement and Prediction of Binary Dense Gas Diffusion Coefficients," *J. Cdn. Pet. Tech.* (Apr.-June 1976a) 48-57.

Sigmund, P.M.: "Prediction of Molecular Diffusion at Reservoir Conditions. Part II - Estimating the Effects of Molecular Diffusion and Convective Mixing In Multicomponent Systems," *J. Cdn. Pet. Tech.* (July-Sept. 1976b) 53-62.

Stiel, L.I. and Thodos, G.: "Lennard-Jones Force Constants Predicted from Critical Properties," *J. Chem. Eng. Data* (1962) **7**, No. 2, 234-236.

Søreide, I.: "Improved Phase Behavior Predictions of Petroleum Reservoir Fluids from a Cubic Equation of State," Dr. Ing. Dissertation, The Norwegian Institute of Technology, Department of Petroleum Engineering, Trondheim (1989).

Villadsen, J. and Michelsen, M.L.: *Solution of Differential Equation Models by Polynomial Approximation*, Prentice-Hall, Inc., Englewood Cliffs, NJ (1978).

Whitson, C.H.: "PVTx - An Equation-of-State Based Program for Simulating & Matching PVT Experiments with Multiparameter Nonlinear Regression," user manual, Pera a/s, Trondheim, Norway (1992).

Whitson, C.H. and Brulé, M.R.: *Phase Behavior*, Monograph Series, SPE, Richardson, TX, to appear (1993).

Wilke, C.R.: "Diffusional Properties of Multicomponent Gases," *Chem. Eng. Progress* (1950) **46**, No. 2, 95-104.

Chapter 3

Gas-Oil Capillary Pressure

3.1 Introduction

One of the primary recovery mechanisms in naturally fractured chalk reservoirs is gravity-capillary drainage. The density difference between gas in the fracture and oil in the matrix causes production of oil until the gravitational forces are equalized by capillary retaining forces. Accurate estimates of the capillary pressure is therefore important for estimating the reservoir performance.

Questions have been raised about the validity of the Young-Laplace equation for scaling low-pressure laboratory capillary pressure curves to reservoir conditions in simulation studies of the Ekofisk reservoir (da Silva, 1989). This work was initiated to determine the effect of gas-oil interfacial tension (IFT) on the gas-oil drainage capillary pressure of chalk.

Laboratory capillary pressure curves are usually measured at standard pressure and temperature and scaled to reservoir conditions by multiplying with the ratio of reservoir-to-laboratory interfacial tension. The most common laboratory methods include the mercury injection method, the porous plate method, and the centrifuge method. The porous plate method is considered the most accurate, while the centrifuge and mercury injection methods are much faster. The disadvantages of the mercury injection are that a the different fluid system is used, the small size of core samples used, and the irreducible wetting phase saturations obtained for high capillary pressures are low compared with other methods (Omoregie, 1988). On the other hand, mercury injection has the advantage that it can be used on irregularly shaped samples, such as drill cuttings. The porous plate method directly measures the capillary pressure curve, as opposed to the centrifuge method where the capillary pressure curve is "back-calculated" by one of several different methods.

Measuring capillary pressure curves on low permeability chalk samples using a standard 6 mm thick porous ceramic plate requires several months. Jennings (1983) described a method for measuring low-pressure capillary pressure curves using 6 μm thick membranes instead of porous plates. This makes the time required for the experiments only dependent on the flow resistance of the core. Using large diameters

and small core lengths, he stated that measuring a complete low-pressure gas-oil capillary pressure curve in twelve steps requires only 100 hr for a 1 md core sample. This is even faster than the centrifuge method.

Use of thin membranes instead of a thick porous plate has become more widely accepted. Hammervold and Skjæveland (1992) compared the use of membranes with ceramic porous plates for measuring water-oil drainage capillary pressure curves on Berea sandstone samples. They found that the time to obtain a drainage capillary pressure curve was reduced by a factor of more than 10. Kalaydjian (1992b) showed the use of oil-wet and water-wet membranes in an experiment measuring three phase capillary pressure. Both drainage and imbibition capillary pressure curves were measured at ambient conditions.

A few results have been published on high-pressure, water-oil capillary pressure measurements, but experimental measurements of gas-oil capillary pressure at high pressure have not been found. Delclaud, Rochon and Nectoux (1987) presented experimental gas-oil displacement results using sandstone for the C_1-nC_5 system at 60°C and pressures from 30 to 135 bar. Interpretation of their data with a numerical simulator suggested that capillary pressure of a high-permeability sandstone can be corrected with IFT only, down to an IFT of about 0.6 mN/m. However, they did not measure directly the capillary pressure at high pressures.

The C_1-nC_5 system at room temperature and pressures from 100 to 170 bar has interfacial tensions on the same order of magnitude as Ekofisk gas and oil at reservoir conditions (0 to 3.5 mN/m). There is also considerable published data available for this binary system, including IFT data. The C_1-nC_5 system was therefore used in this work.

The main purpose of the reported work was to develop and test a method for determining high-pressure, gas-oil drainage capillary pressure curves of chalk samples. The key to success was the application of thin membranes instead of traditional porous plates. With such membranes, the construction and procedure for conducting capillary pressure measurements is relatively simple, making this approach attractive for routine capillary pressure measurements, both at room conditions and reservoir conditions. Use of thin membranes should reduce the time required to achieve a capillary pressure curve by a factor of ten or more.

3.2 Theory and Definitions

The basic theory of capillary pressure and interfacial (surface) tension is outlined in this section. Both the Young equation and the Young-Laplace equation is presented and discussed. Some theories for deviation from these basic equations are also given. The concept of contact angle, spreading coefficient, and wettability are also introduced. Finally the Brooks and Corey equation for relating drainage capillary pressure to the wetting phase saturation is given.

3.2.1 Modelling of Porous Media

A variety of simplified models have been used to model the behavior of the complex network of pores found in porous media. The simplest models consist of a bundle of straight cylindrical capillary tubes of varying diameters. Already in 1941, Leverett stated that this simple model, in many respects, may be misleading. Morrow (1991) lists the factors that a more rigorous model should include:

1. Reservoir pore space should be represented by a network of pores with nonuniform cross sections, generally viewed as consisting of pore bodies interconnected by pore throats.

2. The pores are not circular in cross section, and individual pores may have dual occupancy of liquids with connectivity to neighboring pores.

3. The interaction between contact angle and pore geometry must be taken into account.

4. The surfaces may have non-uniform wetting properties.

5. Various factors, including surface roughness and adsorption, are allowed to cause contact-angle hysteresis.

It is obvious that a model which accounts for all these factors will be complicated and difficult to describe analytically. However, use of such models may give a better understanding of the various phenomena observed during laboratory experiments using a porous medium like sandstone or chalk. The change in wetting properties are particularly important for water flooding experiments. Most equations for converting laboratory capillary pressure curves to reservoir conditions are based on the capillary tube model. The list of factors given here should be kept in mind when reading the remainder of this chapter.

3.2.2 Capillary Pressure

Capillary pressure is caused by interfacial tension between oil, water, gas, and rock, and is usually defined as

$$P_c = p_{nw} - p_w \tag{3.1}$$

where

p_{nw} = nonwetting phase pressure
p_w = wetting phase pressure

For a bundle of capillary tubes, the capillary pressure is always positive. However, the interaction of pore structure and wettability in a porous media allows negative capillary pressures. A very homogenous rock shows an L-shaped capillary pressure curve when plotted vs. the wetting phase saturation. If the pore size distribution is less homogenous, the horizontal part of the capillary pressure curve changes to a curve with a negative slope. A more negative slope indicates a less uniform pore size distribution. High wetting phase saturation represent the largest pores, as illustrated in Fig. 3.1.

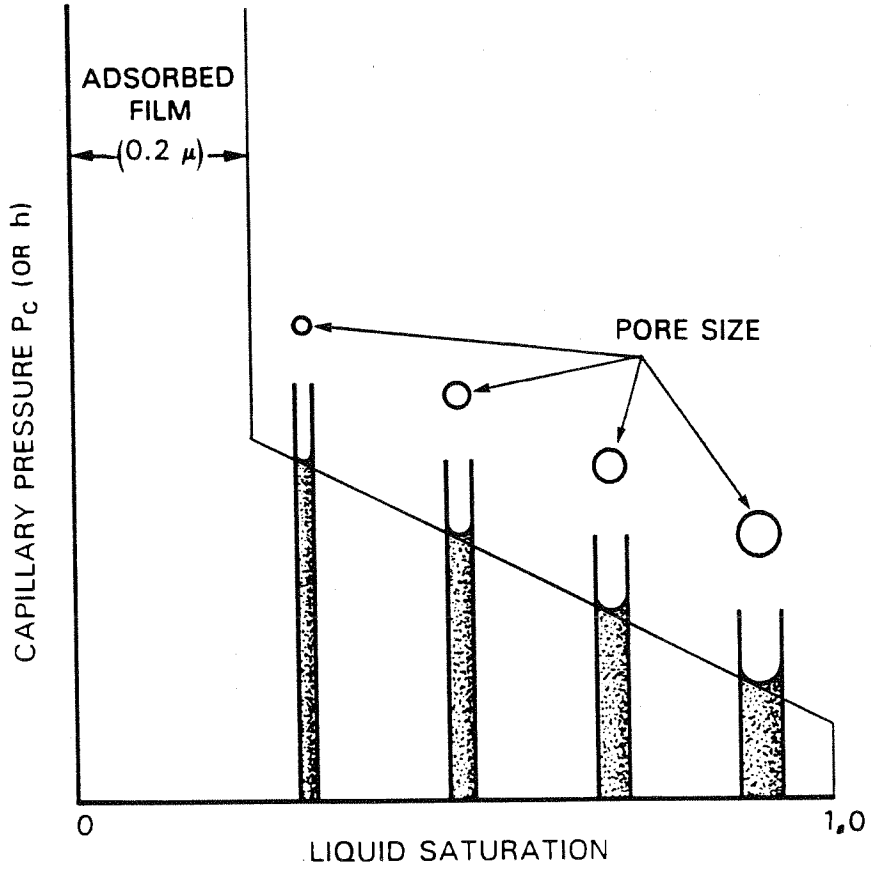

Fig. 3.1 Relation between pore size, liquid saturation, liquid rise, and capillary pressure (Saidi, 1987)

For a water-oil system the capillary pressure is often defined as

$$P_c = P_{cow} = p_o - p_w \tag{3.2}$$

so the capillary pressure can be positive or negative depending on the preferential wettability. The capillary pressure will then be positive for a water wet system, and may be negative for an oil wet system. This is true for a capillary tube, but for a porous media, where the wettability may vary, the capillary pressure is more difficult to predict. Fig. 3.2 shows oil-water capillary pressure curves measured on an intermediate water-wet Berea sandstone core. The drainage curve is obtained when the nonwetting phase is displacing the wetting phase, and the imbibition curve when the wetting phase is displacing the nonwetting phase.

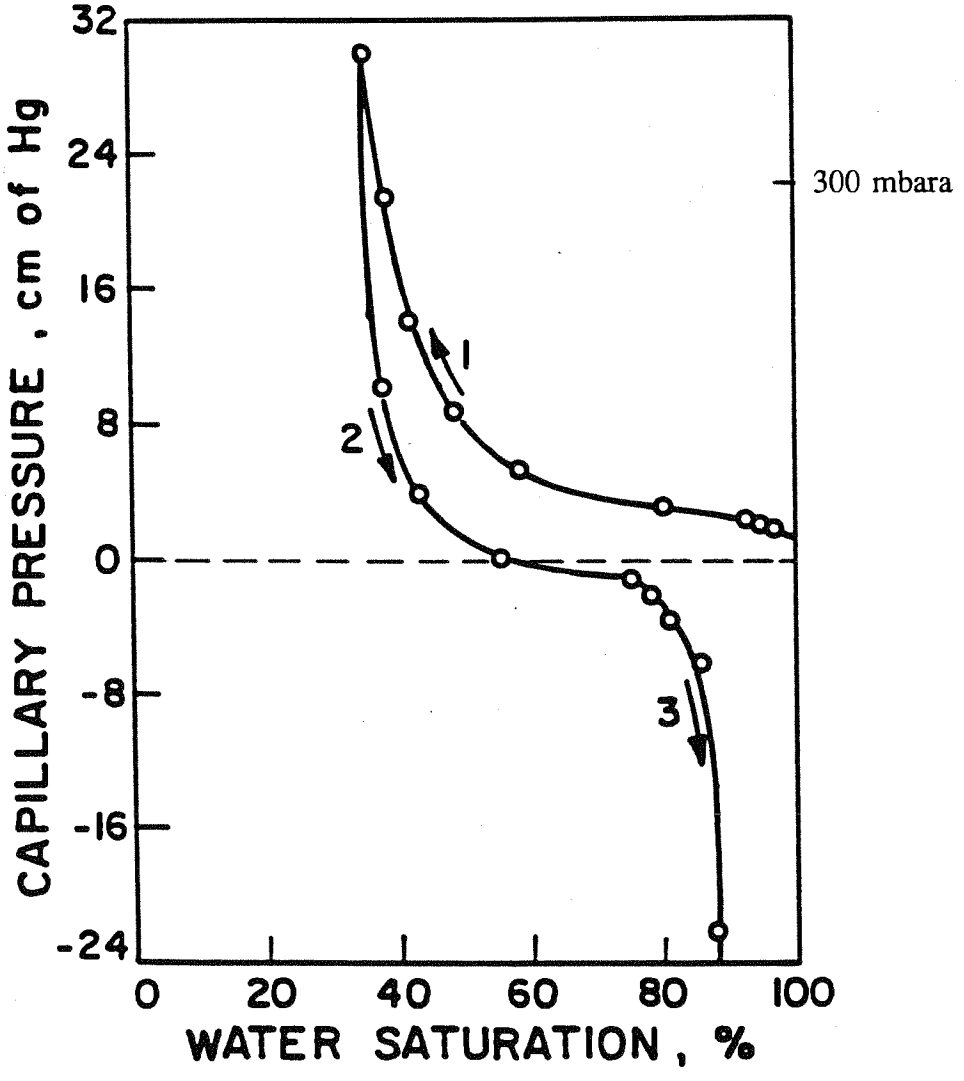

Fig. 3.2 Oil-water capillary pressure curves for an intermediate water-wet Berea sandstone; (1) drainage, (2) imbibition, (3) forced imbibition (Dullien, 1992)

3.2.3 The Young-Laplace Equation

Whenever a gas-liquid or liquid-liquid interface is curved, there will be a differential pressure across the interface to balance the interfacial tension forces. This differential pressure, called capillary pressure, is given by the Young-Laplace equation (Adamson, 1990)

$$P_c = \sigma \left(\frac{1}{R_1} + \frac{1}{R_2} \right) \tag{3.3}$$

where

P_c = capillary pressure, Pa
R = radii of curvature of the interface measured perpendicular to each other
σ = interfacial tension, N/m

This equation is sometimes named the Plateau equation, and is the fundamental equation of capillarity. The radii of curvature of the interface, and hence the capillary pressure, are determined by local pore geometry, wettability, saturation, and saturation history. When the two radii are laying on the opposite side of the meniscus, as seen in Fig. 3.3, one of them is negative. Eq. (3.3) can also be written as

$$p_c = \frac{2\sigma}{R_m} \quad \text{where} \quad \frac{1}{R_m} = \frac{1}{2}\left(\frac{1}{R_1} + \frac{1}{R_2} \right) \tag{3.4}$$

where R_m is the mean radius of curvature. For most porous media, the equations for interfacial curvature are much too complicated to be solved analytically, and capillary pressure must be determined experimentally. In these cases, a simple relationship between contact angle and capillary pressure cannot be derived (Anderson, 1987a; Dullien, 1992).

For a capillary tube or a circular pore with a small radius, the interface may be considered a hemisphere which reduces the Young-Laplace equation to

$$P_c = \frac{2\sigma \cos\theta}{r} \tag{3.5}$$

where

r = radius of capillary tube
θ = liquid-solid contact angle.

Fig. 3.4 describes this relationship schematically. The higher pressure is always on the side of the center of curvature. If the contact angle θ is zero, the radius of the meniscus R equals the pore radius r.

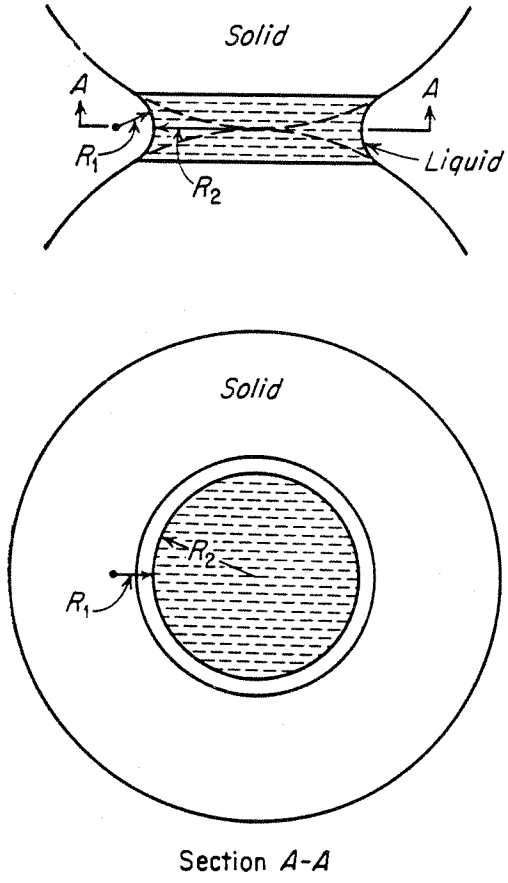

Fig. 3.3 Radii of curvature between particles (Leverett, 1941)

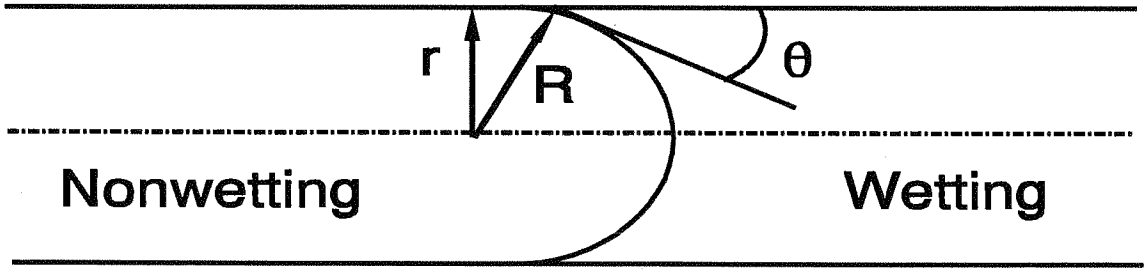

Fig. 3.4 Relationship between contact angle, radius of curvature, and radius of capillary tube

In a porous rock there are converging and diverging pore walls. For a conical capillary pore as shown in Fig. 3.5 the capillary pressure is a function of both the contact angle θ and the conical angle of the capillary α

$$P_c = \frac{2\sigma\cos(\theta+\alpha)}{r} \tag{3.6}$$

The resulting capillary pressure will then be smaller than for a straight cylindrical pore. For a diverging pore, the term $\cos(\theta-\alpha)$ must be used, and the capillary pressure will be larger than for a cylindrical pore. This is true for $(\theta + \alpha) < 90°$ and $(\theta - \alpha) > 0°$.

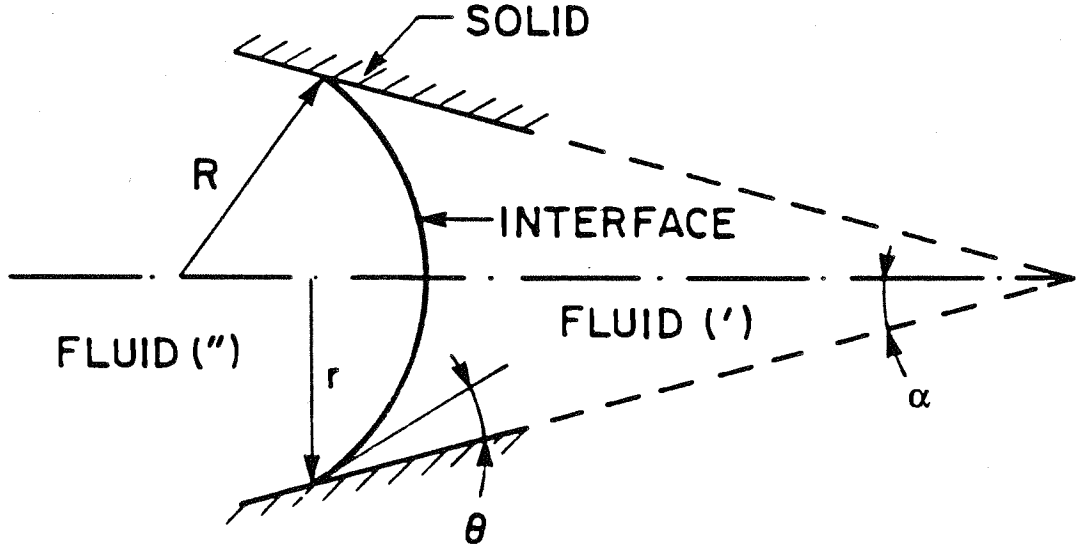

Fig. 3.5 Menisci in a conical capillary pore (Dullien, 1992)

3.2.4 The Young Equation

The Young equation gives the relation between the various surface forces for a vapor-liquid-solid system at equilibrium:

$$\sigma_{LV}\cos\theta = \sigma_{SV} - \sigma_{SL} \tag{3.7}$$

where

σ_{LV} = liquid-vapor interfacial tension, N/m
σ_{SV} = solid-vapor interfacial tension, N/m
σ_{SL} = solid-liquid interfacial tension, N/m
θ = equilibrium contact angle without any gravitational effects

Fig. 3.6 explains the Young equation. The contact angle θ is measured through the liquid phase while for a liquid-liquid-solid system θ is measured through the denser

fluid. In derivation of the Young equation the vertical component of σ_{LV}, given by $\sigma_{LV}\sin\theta$, has been ignored. This is only important for soft surfaces that can be deformed due to the vertical force.

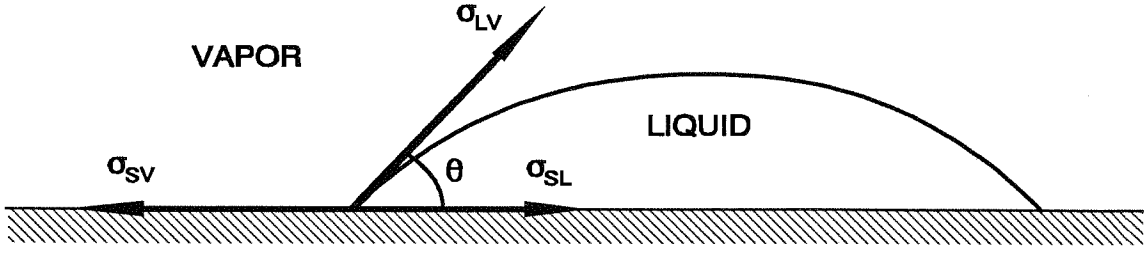

Fig. 3.6 Relationship between interfacial tensions

If the contact angle $\theta = 0$, Eq. (3.7) no longer holds. The imbalance of interfacial tensions is now given by a spreading coefficient (Adamson, 1990; Dullien, 1992)

$$S_{LS} = \sigma_{SV} - \sigma_{LV} - \sigma_{SL} \tag{3.8}$$

A positive spreading coefficient means total spreading of the liquid on the solid. The driving force of spreading is greater for a more positive value of the spreading coefficient. According to Rowlinson and Widom (1982), the *equilibrium* spreading coefficient can never be positive. However, Hirasaki (1991b) shows that for a film in a pore, where the meniscus is curved, the equilibrium spreading coefficient can be positive for a complete wetting system. If the spreading coefficient is negative, Eq. (3.7) is valid and can, combined with Eq. (3.8), be written as

$$\cos\theta = 1 + \frac{S_{LS}}{\sigma_{LV}} \tag{3.9}$$

Table 3.1 gives the interfacial tension for some common fluid systems used for measuring laboratory capillary pressures. Interfacial tension falls linearly as the temperature increases, and as the pressure increases. However, this is not true if the composition of the two fluids change when temperature or pressure is changing, like for oil and gas in equilibrium.

Chalk samples have pores that are much smaller than sandstone and most other reservoir rocks. The largest pores in a chalk are about 1 μm in diameter which is typically the size of the smallest pores in sandstone. Pore sizes in chalks are fairly uniform and vary from about 0.1 to 1.0 μm in diameter. Several articles published on capillary pressure and contact angles in surface chemistry during the past 50 years indicate that for small pores, Young's equation has to be modified (Chattoraj and Birdi, 1984; Adamson, 1990). Several modifications of Young's equation exist, but there is

Table 3.1 Interfacial tension at atmospheric pressure and 20°C (mN/m)

System	Water	Kerosene	Crude Oil	Mercury
Air	72	24	10-35	480
Water		50	10-30	415
Kerosene				380
Crude Oil				380

contradiction between the modifications concerning the net effect of IFT and pore radius on capillary pressure. These modifications state that the contact angle may be a function of the pore radius and the thickness of the adsorbed film. A short review of the suggested modifications to the Young equation follows. To determine the actual effect of the pore size and interfacial tension on chalk, high-pressure capillary pressure experiments have been performed.

3.2.5 Wettability

Wetting indicates a stronger attraction of the solid for one phase than the other. Water wets calcite and silica in the presence of paraffin hydrocarbons. However, addition of small amounts of polar compounds, or deposition of hydrocarbons on the solid surface, will change the wettability. This causes problems when measuring capillary pressure curves on cleaned water-wet cores in the laboratory and then converting the results to reservoir conditions. Restored state cores are often used, where the cleaned core is saturated with crude oil and irreducible water, and aged at reservoir temperature for up to 50 days. This procedure is supposed to reestablish the original wettability found at reservoir conditions. The best approach is to use fresh cores preserved to maintain the original wettability and irreducible water saturation. The capillary pressure is strongly influenced by the wettability of a core sample.

The degree of wetting is often related to the contact angle θ, measured through the denser of the two fluids. If the contact angle is between 0 and 60 to 75° the denser fluid is the wetting phase. A contact angle between 180 and 105 to 120° indicates that the less dense fluid is the wetting phase. In the middle range of contact angles, a system is neutral or intermediate wet (Anderson, 1987a). Fig. 3.7 gives examples of contact angles for some fluids on a silica crystal. Variations in wettability is caused by the interfacial tension between the two fluids and the rock. A core sample may also have a heterogeneous wettability where portions of the surface are strongly water-wet while some are strongly oil-wet. Heterogeneous wettability may occur on the pore scale in actual reservoir media, caused by both mineralogy and asphaltene deposition (Radke, Kovscek, and Wong, 1992). Waterflooding experiments show that oil recovery may be higher for an intermediate or mixed-wet rock than for a strongly water-wet rock.

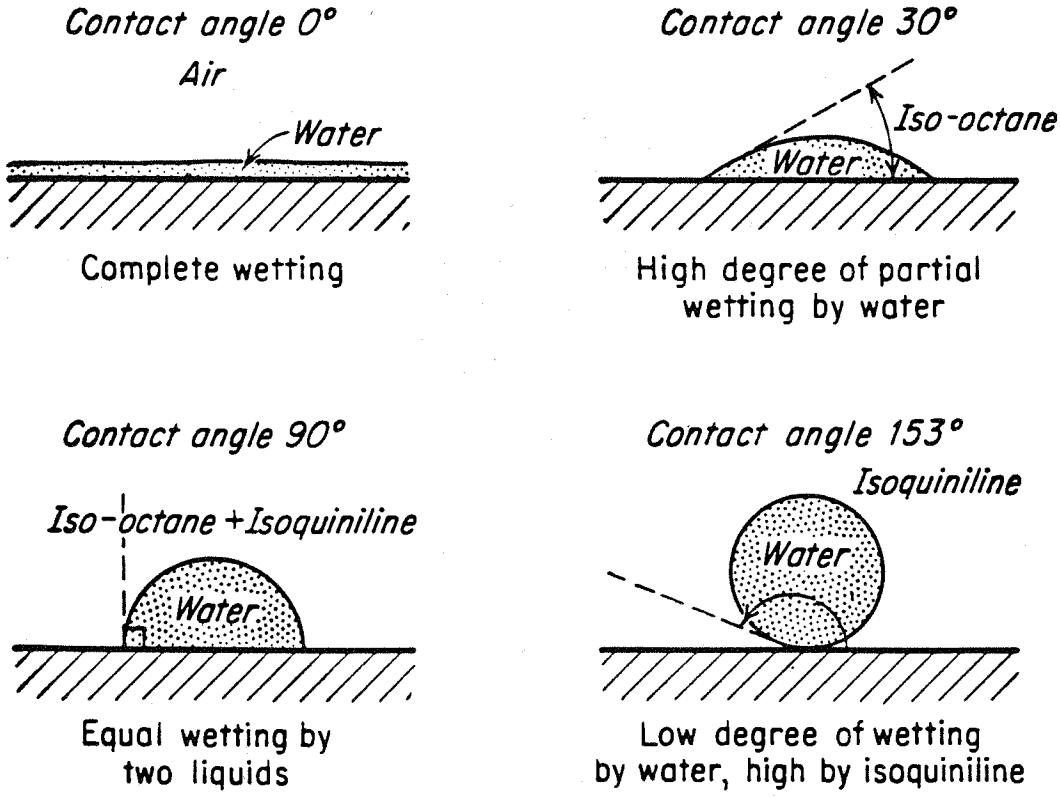

Fig. 3.7 Degree of wetting by contact angles with fluids on silica (Katz *et al.*, 1959)

For a porous media, the effect of wettability is insufficiently represented by the contact angle. Therefore, wettability is often measured using the Amott test (Amott, 1959) or the U.S. Bureau of Mines, USBM test (Donaldson, Thomas, and Lorenz, 1969). In the Amott test, wettability is determined by the amount of oil or water spontaneously imbibed in a core sample compared to the same values when flooded. The Amott wettability index range from +1 for complete water wetting to −1 for complete oil wetting, and is the most widely used wettability index. In the USBM test, wettability index W is the logarithm of the ratio of the areas under centrifuge drainage and imbibition capillary pressure curves. The USBM index W can range from $-\infty$ for oil wet to $+\infty$ for water wet but is usually between −1.5 and +1.0. For both the Amott and the USBM test a sample with wettability index higher than 0.3 is defined as water-wet, while a sample with wettability index lower than −0.3 is defined as oil-wet. Values between −0.3 and 0.3 indicate intermediate wettability.

Fig. 3.8 shows the difference between water displacing oil in a water-wet and an oil-wet rock. Gas displacing oil will be similar to water displacing oil in an oil wet rock. For a water-oil system, most sandstone reservoirs tend to be intermediate wet, whereas most carbonate reservoirs tend to be intermediate wet or oil wet (Lake, 1989).

In a gas-oil system, a contact angle of zero between the liquid and the solid is often

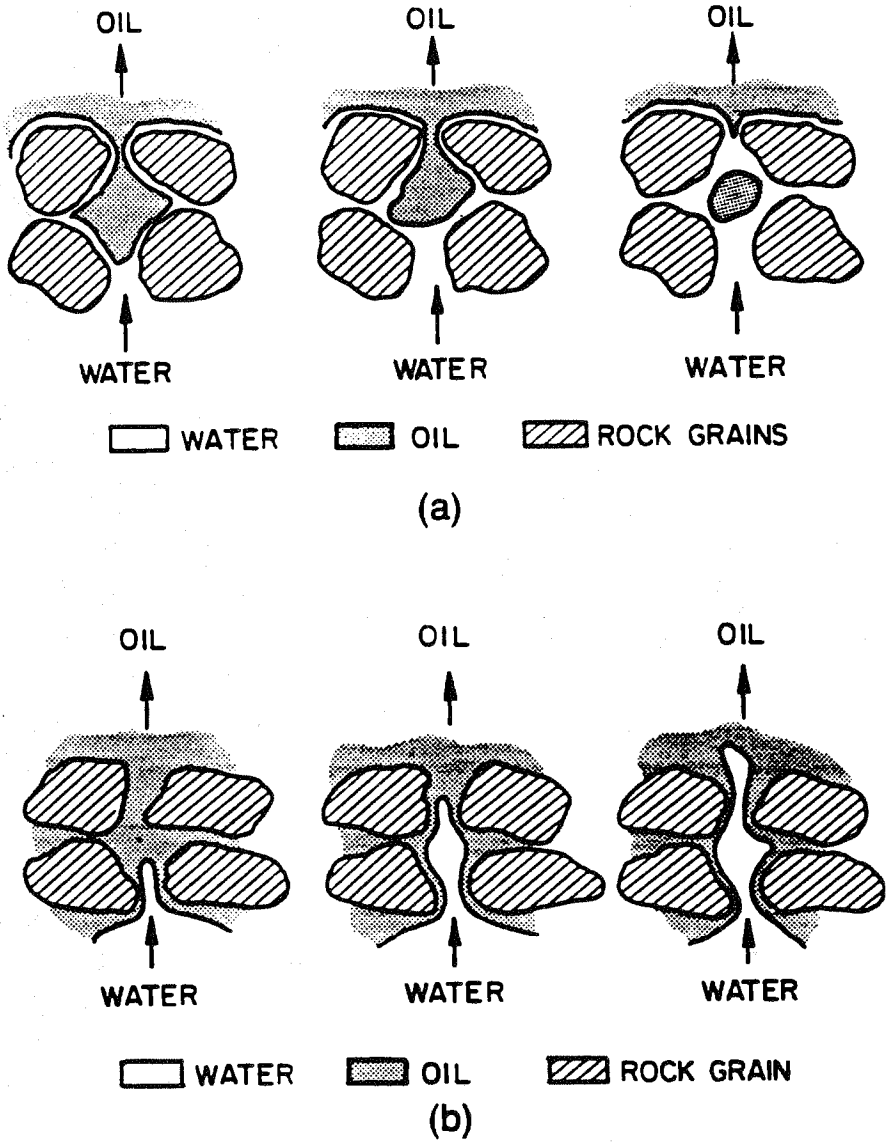

Fig. 3.8 Water displacing oil from a pore during waterflood; (a) strongly water-wet rock, (b) strongly oil-wet rock (Anderson, 1987b)

assumed. This may not be valid at high pressures where the thermodynamic properties of oil and gas approach each other. However, Cahn (1977) showed that in any two-phase mixture of fluids near their critical point, contact angles against any third phase becomes zero. One of the critical phases completely wets the third phase by forming a film that excludes contact between the other critical phase and the third phase. The Cahn transition appears to be an accepted theory and has also been discussed by Rowlinson and Widom (1982). None of these authors quantified how close to the critical point the Cahn transition takes place.

3.2.6 Adsorbed Liquid Film

There is always some degree of adsorption of a gas or vapor at the solid-gas interface. For vapors in equilibrium with a liquid, the amount of adsorption can be quite large and may exceed the point of a monolayer formation. The film pressure or disjoining pressure Π is defined as the difference between the surface tension of the pure solid in vacuum σ_S and that of the film-covered surface σ_{SV}

$$\Pi = \sigma_S - \sigma_{SV} \tag{3.10}$$

Introducing the film pressure in the Young-Laplace equation gives the augmented Young-Laplace equation (Hirasaki, 1991b)

$$P_c = \sigma \left(\frac{1}{R_1} + \frac{1}{R_2} \right) + \Pi(h) \tag{3.11}$$

The film pressure Π is a function of the film thickness h and varies typically as illustrated in Fig. 3.9. For positive values of $d\Pi/dh$, the film is unstable. Therefore, for certain values of film pressure, for example Π_1, there are two possible equilibrium film thicknesses. Thin films are often in the range of 0.1 to 10 nm. For very thick films (>100 nm), the disjoining pressure can usually be neglected. For a complete wetting system, zero contact angle, the film pressure is always positive as shown in Fig. 3.10. This should be the case for most gas-liquid-solid systems. As illustrated in Fig. 3.10, the equilibrium spreading coefficient can be expressed as (Hirasaki, 1991b)

$$S_{LS} = \int_0^{\Pi_{eq}} h \, d\Pi \tag{3.12}$$

The forces that contribute to the film pressure can be divided into long range van der Waal forces, electrostatic forces, and structural forces (related to the molecule structures). Electrostatic forces can be neglected for a system such as C_1-nC_5 . The film pressure from long range or van der Waals forces can be estimated as

$$\Pi = \frac{-A}{6\pi h^3} \tag{3.13}$$

where A is the Hamaker constant (Hirasaki, 1991a). The film pressure from structural forces is given as

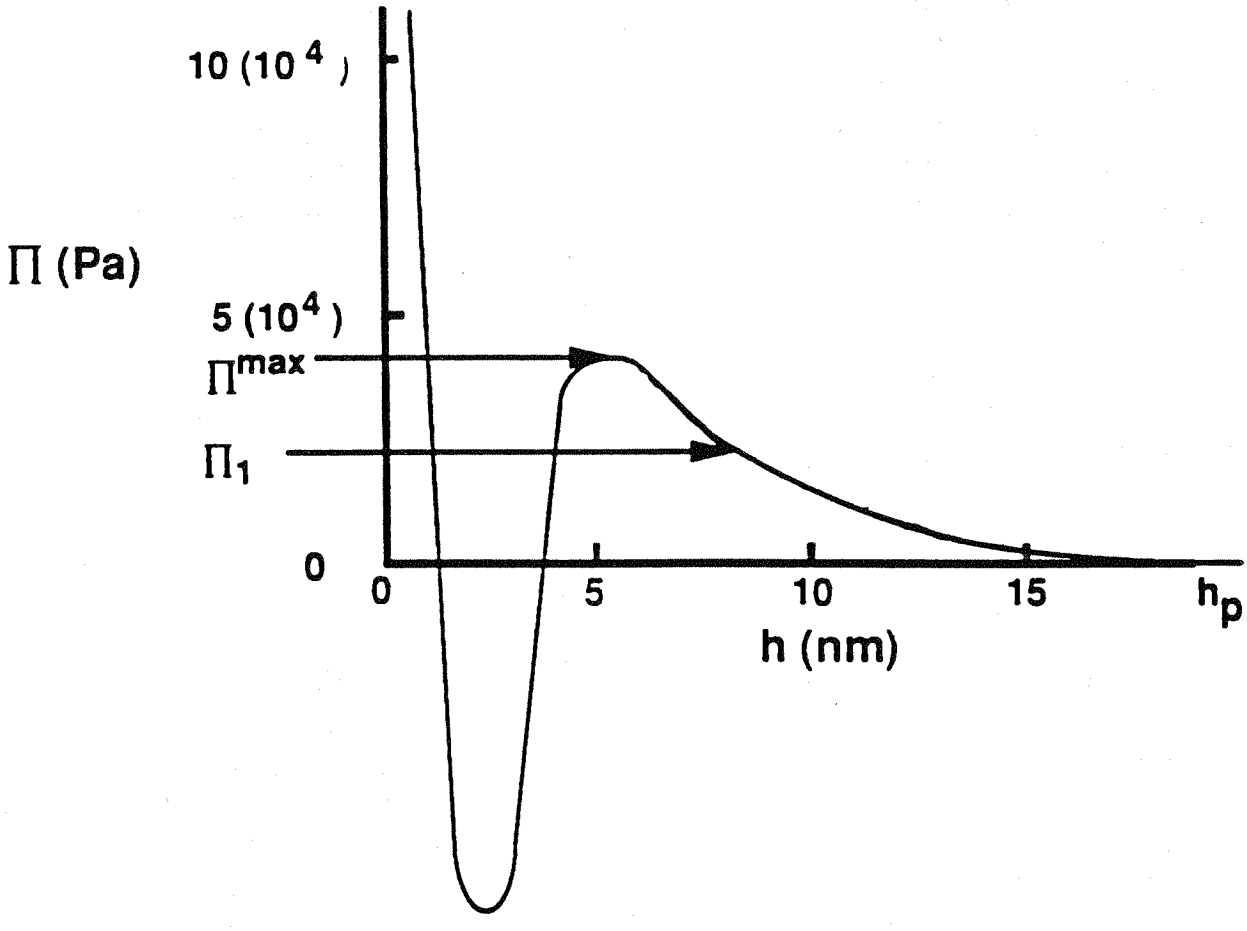

Fig. 3.9 Schematic film pressure isotherm for wetting films on solids fore an intermediate wetting system (Radke, Kovscek, and Wong, 1992)

$$\Pi = A_s \, e^{-h/h_s} \tag{3.14}$$

where A_s and h_s are constants.

The thermodynamic properties of the film differs from the properties of the bulk phase. Therefore, the interfacial tensions of a thin film can be different from the interfacial tensions between bulk phases (Hirasaki, 1991b).

Fig. 3.11 shows a cylindrical pore containing both gas and oil, with a liquid film covering the walls "above" the bulk meniscus. If gravity is neglected, the capillary pressure across the film has to equal the capillary pressure across the bulk meniscus.

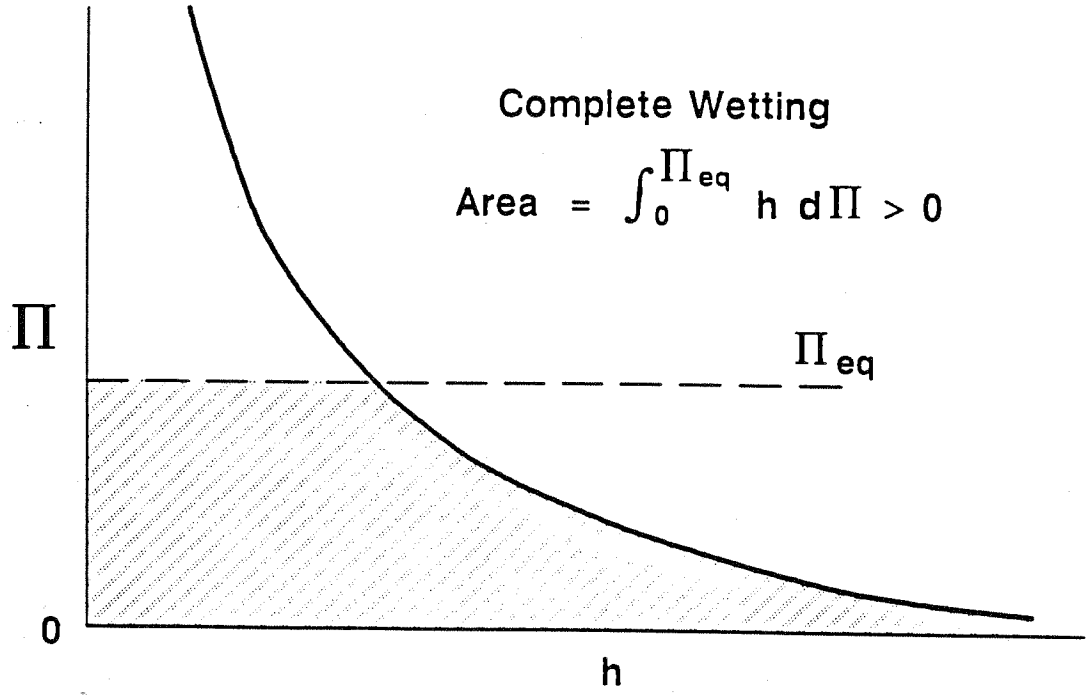

Fig. 3.10 Schematic film pressure isotherm for wetting films on solids for a complete wetting system (Hirasaki, 1991b)

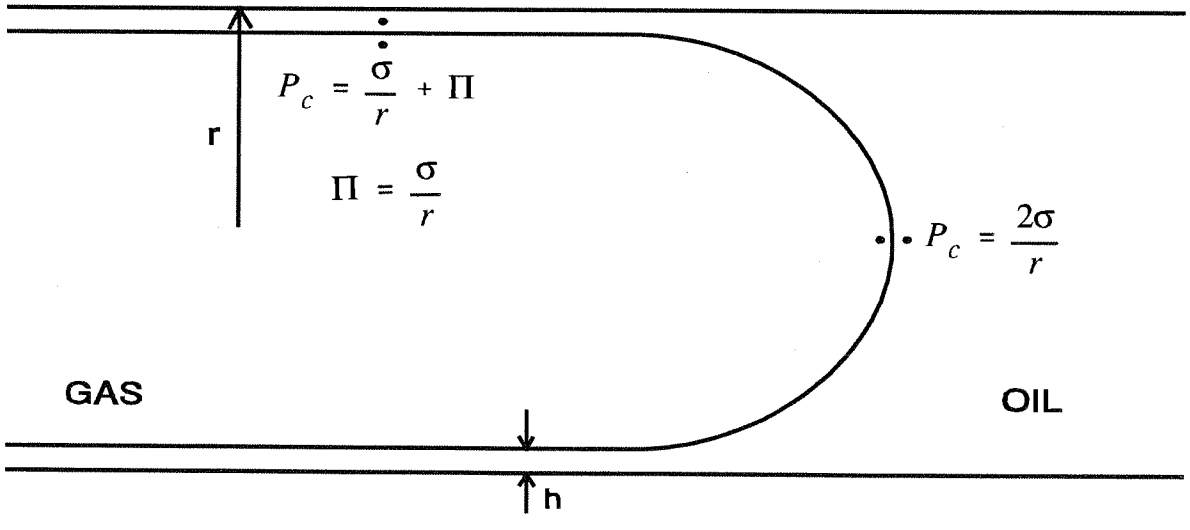

Fig. 3.11 Film pressure in a cylindrical pore with zero contact angle

The film pressure will then be given as

$$\Pi = \frac{\sigma}{r} \tag{3.15}$$

Assuming that only long range forces are important, Eq. (3.13) can be combined with Eq. (3.15) to give

$$h = \sqrt{\frac{-Ar}{6\pi\sigma}} \tag{3.16}$$

A may vary with composition and, therefore, with interfacial tension. However, Eq. (3.16) indicates that the film thickness increases with decreasing interfacial tension.

At the junction of the adsorbed film and the liquid meniscus there will be a transition region, where two contact angles can be defined. The macroscopic contact angle θ_c is governed by the slope of the tangent line of the liquid meniscus, and the microscopic contact angle θ_p is given by the slope of the boundary line of the liquid and the adsorbed film. The macroscopic contact angle θ_c is the thermodynamic contact angle that will obey the Young equation. Fig. 3.12 shows the macroscopic contact angle in a vapor-liquid-solid system. Hirasaki (1991a) stated that for an intermediate wetting system there exists a transition region between the film and the meniscus as shown in Fig. 3.13. This is caused by the shape of the film pressure isotherm given in Fig. 3.9. More information about films and film pressure can be found in the references (Adamson, 1990; 1991a; Hirasaki, 1991b).

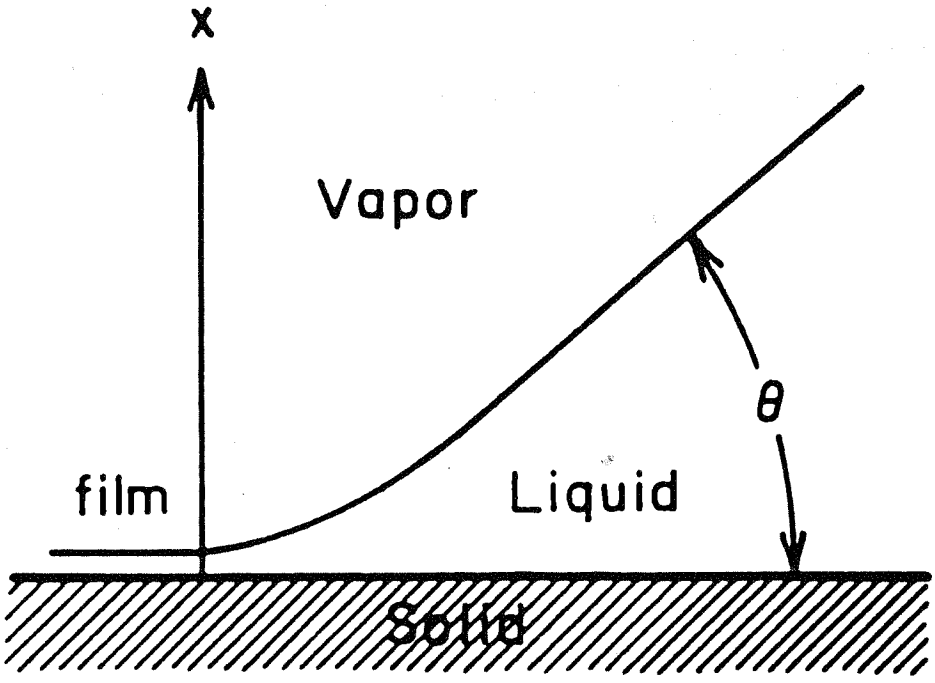

Fig. 3.12 Transition between liquid meniscus and adsorbed film (Adamson, 1990)

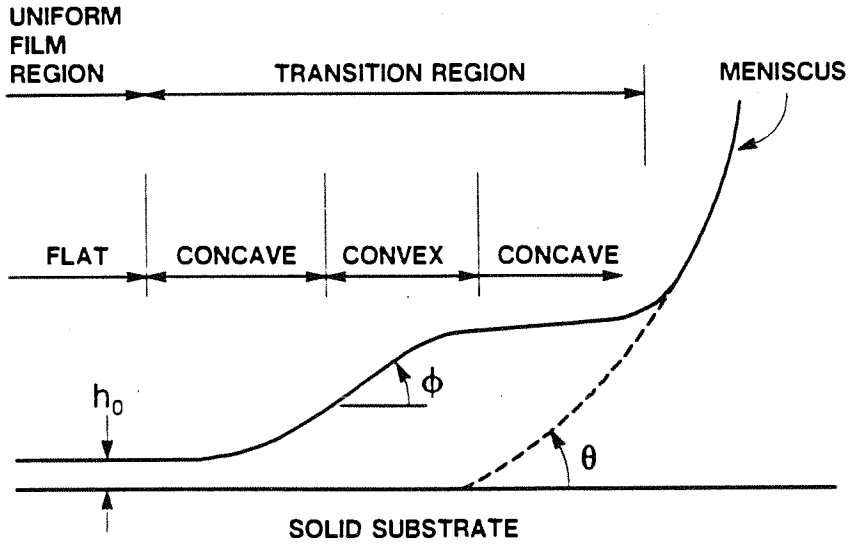

Fig. 3.13 Shape of film-meniscus transition region (Hirasaki, 1991)

3.2.7 Young's Equation with Linear Tension

There have been experimental observations that contact angle varies with the radius of the interface between a droplet and the surface. A modified Young's equation is given by Pethica (1977)

$$\sigma_{LV}\cos\theta = \sigma_{SV} - \sigma_{SL} - \frac{f}{r} \tag{3.17}$$

where

f = linear tension
r = radius of curvature of three phase line

This equation has also been proposed by other researchers, and is referenced by Adamson (1990). Eq. (3.17) shows that the macroscopic contact angle varies with the drop size or pore size, and that θ may increase or decrease as the pore size becomes very small depending on the sign of f. Experimental and theoretical indications are that f should be small and positive. Pethica (1977) states that the ratio of f to σ_{LV} will be on the order of 1 nm for commonly used liquids and solids. This implies that the contact angle increases for a pore radius less than about 0.1 μm. For a membrane with pore size of about 0.1 μm or less, this will reduce the break-through pressure. For a chalk sample with pore diameters larger than 0.1 μm, this will probably have no effect.

For a very small radius Eq. (3.17) will give a negative value for $cos\theta$ which is obviously wrong. This shows that the ratio of f to σ_{LV} given by Pethica can not be generally valid, and has to decrease with decreasing values of r. No conclusions can be drawn about the validity of these results and the effect on capillary pressure.

3.2.8 Effect of Pore Radius on Surface Tension

From thermodynamic considerations it is concluded that with a sufficiently curved surface, the value of the surface tension itself should be affected (Adamson, 1990). Melrose gives the equation

$$\sigma = \sigma^o\left(1 - \frac{\delta}{R_m}\right) \tag{3.18}$$

where

δ = thickness of the interfacial region
σ^o = original interfacial tension
σ = changed interfacial tension
R_m = mean radius of curvature

The thickness of the interfacial region is directly dependent on the size of the molecules (about 0.5 nm for cyclo-hexane). R_m may be positive or negative. Experiments have concluded that for several organic liquids the effective surface tension remained unchanged down to radii of curvature as low as 0.5 nm. For water this was true down to radii of 2 nm even though the molecular size is only 0.15 nm. This may be caused by the polar forces in water. For heavy hydrocarbon components like C_{30} the size of the molecules are about 3 nm. The effect of pore radius on surface tension can therefore be neglected for chalk samples where the smallest pores displaced are about 0.1 μm.

3.2.9 The Kelvin Equation

Together with the Young-Laplace equation, the Kelvin equation gives the second fundamental relationship of surface chemistry, expressing the change in vapor pressure (or saturation pressure) for a curved surface:

$$\ln \frac{p}{p^o} = - \frac{2\sigma M}{\rho_L R T R_m} \tag{3.19}$$

where

M = molecular weight, g/gmol
p = vapor or saturation pressure of liquid in a pore
p^o = vapor or saturation pressure of the bulk liquid
R = universal gas constant, 8.314×10^6 Pa cm^3/(K gmol)
R_m = mean radius of curvature, m
T = temperature, K
ρ_L = density of adsorbed liquid, g/cm^3
σ = interfacial tension, N/m

The reduction in the vapor pressure or saturation pressure of the liquid is due to the liquid's decreased absolute pressure in the pores. This reduction is caused by the capillary pressure across the concave surface which is formed at the gas-liquid interface. The reduction in absolute pressure decreases the molar free energy of the liquid and thereby reduces the vapor or saturation pressure. Consequently, capillary condensation of a vapor to a liquid should occur within a pore at some pressure p determined by the value of R_m for the pore, and less than the saturation pressure of the bulk liquid. This is not true for a liquid like mercury with a contact angle greater than 90°. If the liquid perfectly wets the solid, the contact angle will be 0° and R_m equals the pore radius. This effect is used in some gas bottles by filling it with a porous medium to increase the capacity without increasing the pressure rating of the bottle. Capillary condensation also helps saturating a porous membrane, preventing the liquid in the membrane to be vaporized (Gregg and Sing, 1982; Deetz, 1986). Fig. 3.14 shows the reduction in saturation pressure as a function of pore diameter for a C_1-nC_5

system at 100 bar and water-air at 1 bar, both at 24°C. The Kelvin equation assumes ideal gas behavior and incompressible liquid, so the accuracy at high pressures may be questioned.

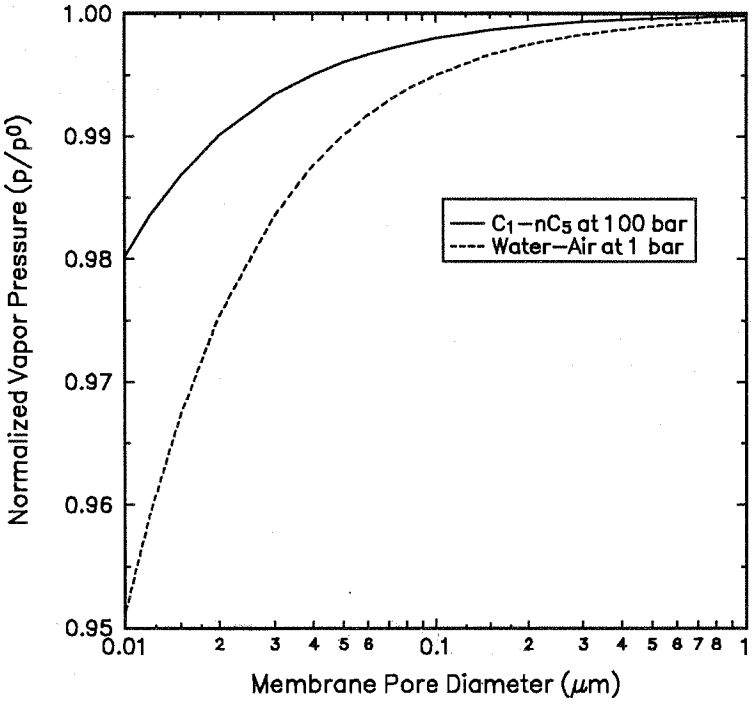

Fig. 3.14 Reduction in saturation pressure for C_1-nC_5 at 100 bar (IFT = 3 mN/m) and water-air at 1 bar (IFT = 72 mN/m) for T = 24°C

Several researchers have proven that the adsorbed layer is thicker in a pore than on an isolated surface, and that the meniscus is deformed by adsorption forces close to the surface (Everett, 1988). The problem of the correction to be applied to the Kelvin radius for the thickness of the adsorbed layer still attracts attention.

3.2.10 Contact Angle in a Porous Medium

For the extremely rough surface in a porous medium, the apparent contact angle is reduced if the true contact angle θ_T is less than 90°. If the true contact angle is larger than 90°, then the apparent contact angle is increased. This has been verified experimentally (Adamson, 1990), and is shown in Fig. 3.15. In a literature survey on wettability, Anderson (1987a) states that the effect of roughness on contact angle, combined with the pore geometry, make the capillary pressure curve insensitive to wettability for small contact angles. (Less than about 50° for drainage and less than about 20° for spontaneous-imbibition).

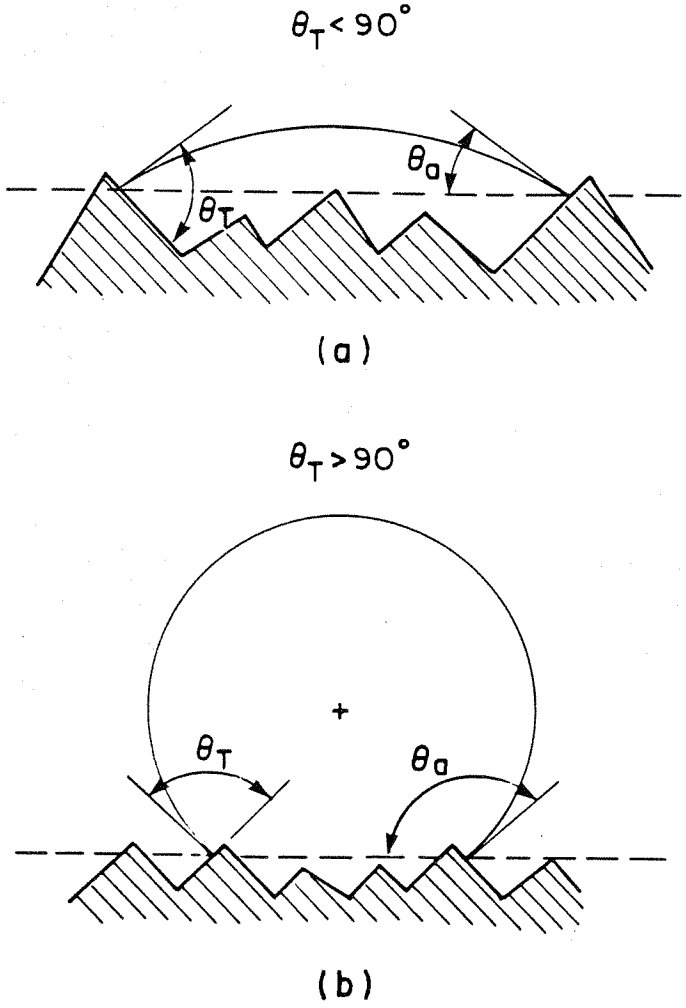

Fig. 3.15 Effects of surface roughness on apparent contact angle. (a) The droplet is the wetting fluid. (b) The droplet is the nonwetting fluid (Dullien, 1992)

3.2.11 Leverett J-Function

Leverett (1941) defined the dimensionless J-function to generalize the drainage capillary pressure-saturation relationship in a porous system:

$$J(S_w) = \frac{P_c}{\sigma}\sqrt{\frac{k}{\phi}} \tag{3.20}$$

where

P_c = capillary pressure, Pa
k = permeability, m^2
ϕ = fractional porosity
σ = interfacial tension, N/m

In deriving this relationship, Leverett assumed that the reservoir behaves like a bundle of capillaries. Later, Rose and Bruce (1949) introduced the contact angle θ into the J-function to account for the wettability of porous media

$$J(S_W) = \frac{P_c}{\sigma \cos\theta \sqrt{\frac{k}{\varphi}}} \tag{3.21}$$

Dumoré and Schols (1974) found that capillary pressure curves from mercury injection and porous plate experiments can be transformed into one curve without including the contact angle. Amyx, Bass, and Whiting (1960) and Saidi (1987) also state that the contact angle should be neglected, while Lake (1989) and O'Meara, Hirasaki and Rohan (1992) recommend Eq. (3.21).

The J-function is useful for scaling drainage capillary pressure for varying k and ϕ within the same reservoir, or for comparing capillary pressure curves from different fluid systems. This scaling assumes that all samples have the same pore size distribution and tortuosity, so it can not be used to scale P_c between different lithologic types or formations.

3.2.12 The Brooks and Corey Equation

Brooks and Corey (Bear, 1988) proposed the following relationship for the drainage capillary pressure based on experimental data:

$$P_c = P_{ce}\, S_w^{*\,-\frac{1}{\lambda}} \tag{3.22}$$

where

P_{ce} = capillary entry pressure or threshold pressure
S_w^* = normalized wetting phase saturation
λ = pore size distribution index

A small value for λ (0.5) indicates a wide range of pore sizes, while a large value (4.0) indicates a narrow range. The normalized wetting phase saturation is defined as

$$S_w^* = \frac{S_w - S_{wi}}{1 - S_{wi}} \tag{3.23}$$

where S_{wi} is the irreducible wetting phase saturation. Fig. 3.16 shows examples of the capillary curve for varying values of the pore size distribution index λ. Fig. 3.17 shows the effect of varying the capillary entry pressure P_{ce}.

Eq. (3.22) can be rearranged to

$$\log P_c = \log P_{ce} - \frac{1}{\lambda} \log S_w^* \tag{3.24}$$

Plotting P_c vs. S_w^* on a log-log scale should give a straight line with slope = λ^{-1}. The Brooks and Corey model is used in interpretation of the centrifuge capillary pressure measurements given in this study. Other more complicated models could have been used, but the Brooks and Corey model gave a good match of the measured capillary pressure data. The pore size distribution index is also used in Corey's relative permeability correlations (Standing, 1975):

$$k_{rw} = S_w^{*\frac{2+3\lambda}{\lambda}} \qquad k_{rnw} = k_r^o \left(1 - S_w^*\right)^2 \left[1 - S_w^{*\frac{2+\lambda}{\lambda}}\right] \tag{3.25}$$

Fig. 3.18 gives a plot of the Corey relative permeability correlations for various values of the pore size distribution index λ.

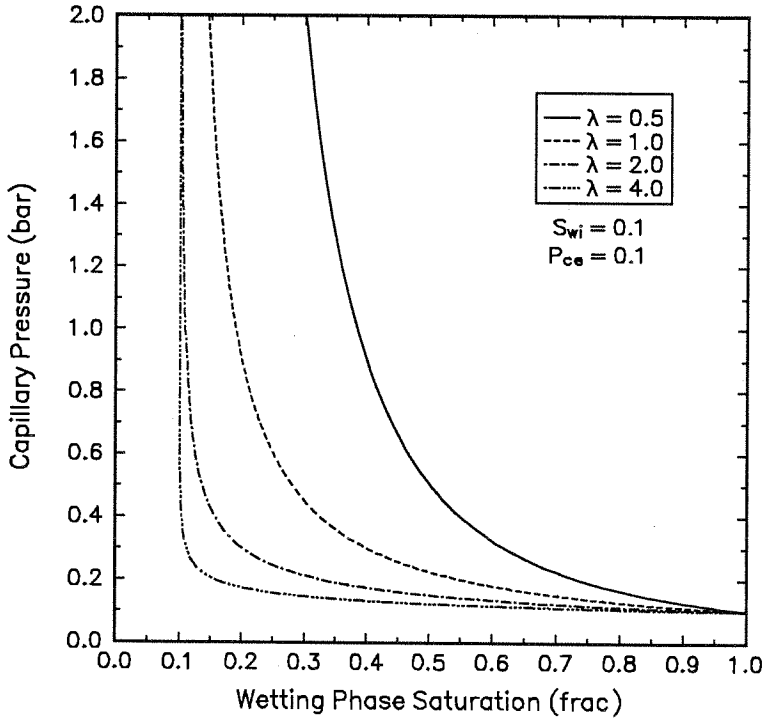

Fig. 3.16 Corey capillary pressure function for various values of λ

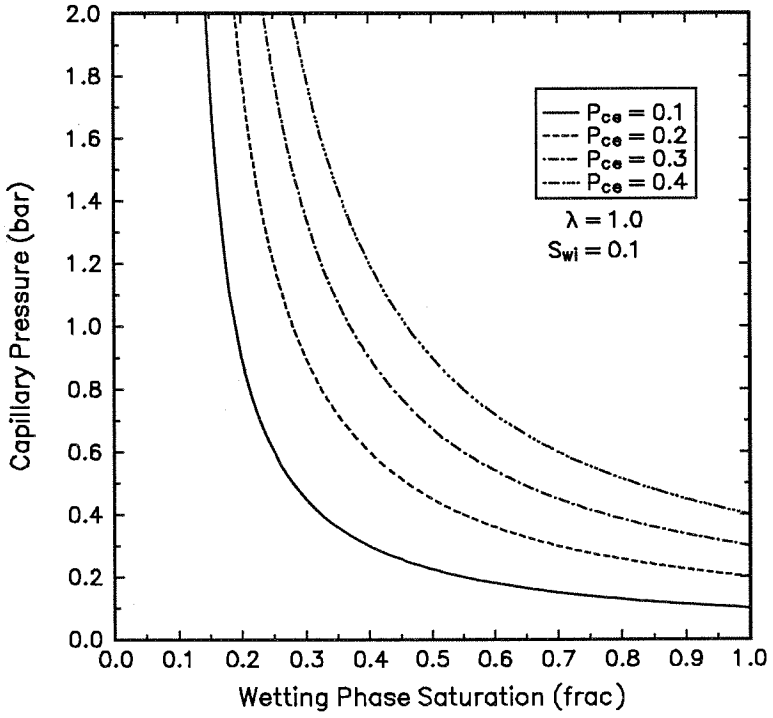

Fig. 3.17 Corey capillary pressure function for various values of P_{ce}

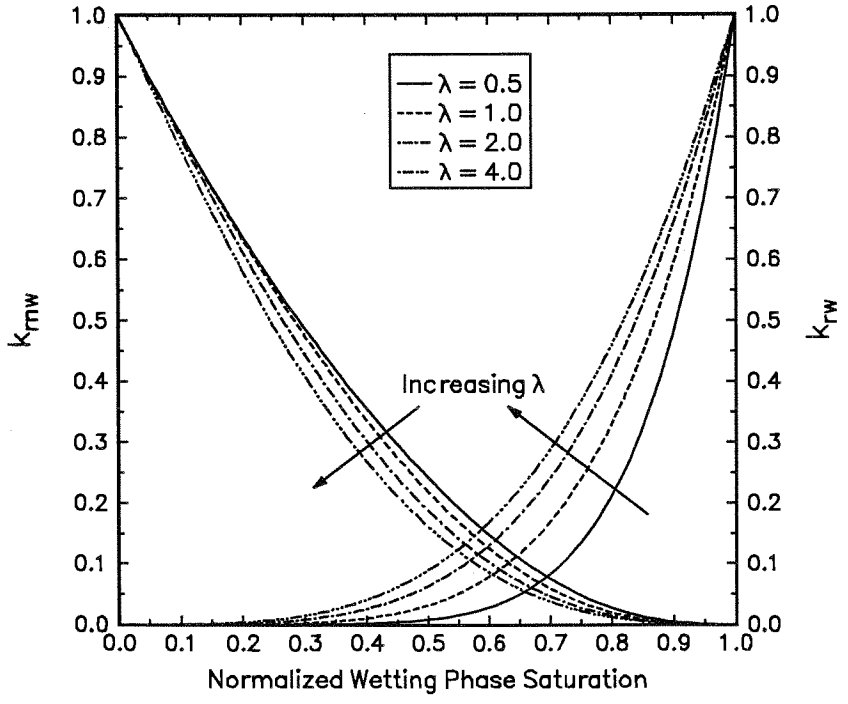

Fig. 3.18 Corey relative permeability correlations for various values of λ

3.3 Methods for Measuring Capillary Pressure Curves

This review will examine and compare the three most common procedures used to determine capillary pressure curves on small core samples; (1) the porous plate or restored state method, (2) the centrifuge method, and (3) the mercury injection method. Two other less common methods will also be mentioned; (4) the dynamic capillary-pressure method and (5) the evaporation method. The last section in this chapter deals with the conversion of laboratory capillary pressure curves to reservoir conditions.

3.3.1 Porous Plate/Membrane Method

In the porous plate or diaphragm method, a core sample with known pore volume is saturated with the wetting liquid, and put on a porous plate saturated with the same liquid. Fig. 3.19 shows a schematic drawing of the apparatus. Other names for this method is diaphragm method or semipermeable membrane method. The porous plate is permeable to the wetting phase only, up to a certain differential pressure. To assure capillary contact between the core sample and the porous plate, a sheet of kleenex paper or some kind of paste is often used. A spring on top of the core also helps maintaining capillary contact with the porous plate. Increasing the pressure in the nonwetting phase in steps, while keeping a constant pressure in the wetting phase, gives a stepwise increase of the capillary pressure. It is important to wait for equilibrium conditions at each differential pressure step to obtain the capillary pressure curve. The saturation at each equilibrium capillary pressure is determined from weighing the core sample or from measuring the produced volume of the wetting fluid. Both drainage and imbibition capillary curves can be measured. The porous plate method is also referred to as the *restored state* method because it is possible to use restored core samples; The core is given an irreducible water saturation and aged with crude oil at reservoir temperature for up to 50 days to simulate the conditions found in a reservoir.

The porous plate method is a direct method for measuring the capillary pressure, and is considered to be the most exact method. The disadvantage with the porous plate method is the time needed to obtain a complete capillary pressure curve. Older porous plates also had a limited break-through pressure. For high permeable sandstone it may take a few weeks to obtain a capillary pressure curve. For low permeable chalk it may require several months. Gas-oil capillary pressure curve measurements require less time than liquid-liquid measurements. The porous plate method is often used as a reference method for the faster and less accurate methods.

By using thin membranes instead of the porous plates, the time required to measure a capillary pressure curve can be reduced by a factor of ten or more (Jennings, 1983;

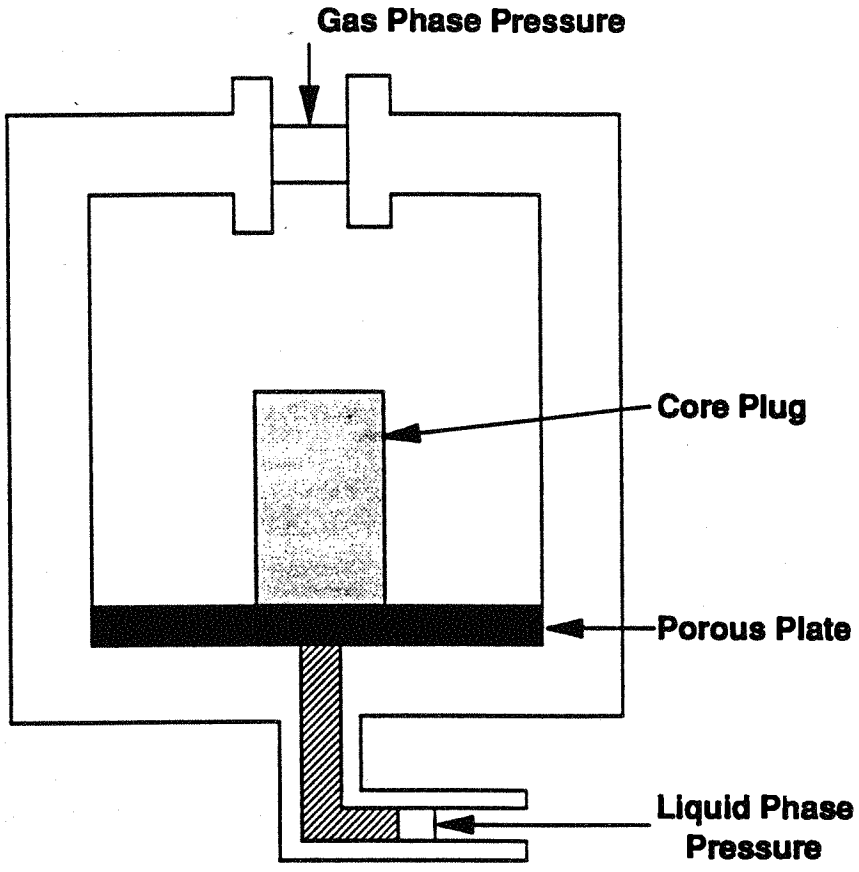

Fig. 3.19 Schematic drawing of the porous plate drainage capillary pressure apparatus (Melrose, 1990)

Jennings, McGregor, and Morse, 1988; Hammervold and Skjæveland, 1992). This makes the time required for the experiments only dependent on the flow resistance of the core, and is therefore the same as for the centrifuge method. Newer membranes are 6 to 150 μm thick, while the standard porous plate is 6,000 μm thick. The upper limit for the air-water capillary pressure may be increased to above 50 bar when using these membranes. The disadvantage with the use of thin membranes is the increased diffusion rate through the membrane for gas-liquid measurements, especially around the core sample. However, this diffusion rate can be measured and corrected for or separated from the liquid production rate (Jennings, 1983; Delclaud, Rochon, and Nectoux, 1987). For a water-oil system, diffusion through the membrane is negligible due to the low solubility of water in oil.

By using large core diameters (10 cm) and small core lengths (1 cm) Jennings states that measuring a complete low-pressure gas-oil capillary pressure curve in twelve steps requires only about 100 hr for a 1 md core sample. It may, however, be difficult to obtain core samples with this diameter.

Advantages of the porous plate/membrane method are:

- Measures the capillary pressure directly.
- The most accurate of the methods.
- The only method that can use large samples.
- Can be run at elevated pressure and temperature.
- Reservoir fluids can be used.
- The only method recommended for slightly clayey samples.
- Relative permeability can be measured together with the capillary pressure.
- The equipment is not expensive even if automated.

Disadvantages

- Time consuming if porous plates are used instead of thin membranes.

3.3.2 Centrifuge Method

This approach to measuring capillary pressure is an indirect method which is faster than the traditional porous plate method, but about as fast as the membrane method. Both drainage and imbibition capillary curves can be measured. Capillary pressure measured in the centrifuge was first adopted by Hassler and Brunner (1945). A multi-speed test is performed in the centrifuge, and the fluid production at equilibrium for each rotational speed is used to generate the capillary pressure curve. At each speed, the capillary pressure and the saturation in the plug represents a portion of the capillary pressure curve. The capillary pressure at the outlet of the core plug is assumed equal to zero and the capillary pressure increases towards the inner side of the core as shown in Fig. 3.20. The height h^* represents the capillary entry pressure P_{ce}.

Small core samples give reduced accuracy due to low pore volume and small volumes of produced liquid. A common problem both for manual and automated liquid volume readings is noise. For gas-liquid measurements, the pressure in the liquid phase in the sample becomes less than the atmospheric pressure (or the pressure in the gas phase in the core holder). This may create cavitation or boiling in the liquid phase at the inner end of the core, especially if the solubility of the gas in the liquid is high. One of the advantages (or disadvantages) with the centrifuge method is the possibility to measure high capillary pressures. The assumption of 100% wetting phase saturation and $P_c = 0$ at the end of the core does not hold if the capillary pressure is too high. The very high gravitational forces used often permanently deforms the core sample and changes the properties of the core. At a speed of 10,000 RPM the gravitational force is 10,000 g for the Beckman L8M ultracentrifuge.

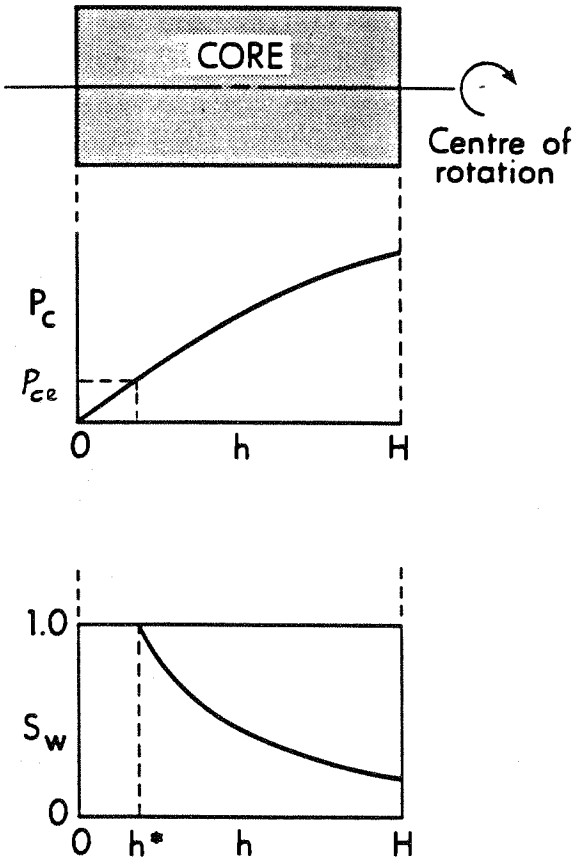

Fig. 3.20 Capillary pressure distribution and saturation profile in a core sample during centrifuging (Bentsen and Anli, 1977)

The capillary pressure at any point in the core is, if we assume $P_c = 0$ at r_e, given by

$$P_c = \frac{1}{2}\Delta\rho\,\omega^2(r_e^2 - r^2) \tag{3.26}$$

where

r_e = radius to the external end of the core, cm
ω = angular velocity, rad/s
$\Delta\rho$ = density difference, kg/m^3

The average saturation in the core sample is given by the produced volume at each angular velocity and is related to the local saturation by

$$\bar{S} = \frac{1}{r_e - r_i}\int_{r_i}^{r_e} S_w(r)\,dr \tag{3.27}$$

where r_i is the radius to the inner end of the core.

Because capillary pressure varies along the core at each rotational speed, this method does not give a direct or point-value measure on the capillary pressure curve. At each speed a segment of the capillary pressure curve is applied to the core sample with the segment increasing at higher rotational speeds, where the one end of the segment is always $P_c = 0$ at $S_w = 1$. As a result of the method not giving point values on the capillary pressure curve, various methods are used to interpret (back-calculate) the actual capillary pressure curve from production data.

The Hassler and Brunner Method

The oldest, and still a widely used method, is the Hassler and Brunner procedure (Hassler and Brunner, 1945; Slobod, Chambers, and Prehn, 1951), which calculates the capillary pressure at the inner end of the core. Changing variables in Eq. (3.27) and using Eq. (3.26) gives

$$\bar{S} = \frac{1}{2P_c(r_i)}\left(1 + \frac{r_i}{r_e}\right) \int_0^{P_c(r_i)} \frac{S\left(P_c(r)\right)}{\sqrt{1 - \frac{P_c(r)}{P_c(r_i)}\left(1 - \frac{r_i^2}{r_e^2}\right)}}\, dP_c(r) \tag{3.28}$$

This integral can not be solved directly since $S(P_c(r))$ is unknown. Hassler and Brunner assumed that $r_e - r_i << r_e$ which gives

$$P_c(r_i)\,\bar{S} = \int_0^{P_c(r_i)} S\left(P_c(r)\right)\, dP_c(r) \tag{3.29}$$

This equation should hold for $r_i/r_e > 0.7$. A more complicated method can be used if $r_i/r_e < 0.7$. Based on Eq. (3.29), the saturation at the inner end of the core sample is given as

$$S(r_i) = \frac{d}{dP_c}\left(P_c(r_i)\,\bar{S}\right) \tag{3.30}$$

This method neglects the variation in acceleration with length along the core ($g = \omega^2 r$). For the Beckman L8M centrifuge using a 4 cm long core plug $r_i = 5.4$ and $r_e = 9.4$ cm giving $r_i/r_e = 0.57$. This gives a large variation in the acceleration along the core and makes the Hassler and Brunner method inaccurate. The main problem with the Hassler and Brunner method is that it involves numerical integration, derivation, and successive substitution. This causes numerical problems when using experimental data points that

always have some noise included. Using a large number of data points, and smoothing the date before use, is often necessary.

Several modifications to the Hassler and Brunner method exist (Skuse, Firoozabadi, and Ramey, 1992). All these modifications give the capillary pressure at the inner end of the core sample by assuming zero capillary pressure at the outer end of the core. Fig. 3.21 gives an example of the repeatability of the centrifuge method for three runs on the same sandstone core sample using the Hassler and Brunner method. The fluids used were air-brine and air-decane. Core plugs with 1" length and 1" in diameter were used with permeabilities of about 10 md and with porosities of about 8%. The repeatability is bad and the shape of the capillary pressure curves is varying between the runs. Total pore volumes of the core samples were about 1.0 cm^3 and may explain the bad repeatability.

Parameter Estimation Methods

Several authors have used a parameter estimation technique to avoid the numerical problems in the Hassler and Brunner related methods. This gives a stable method that requires fewer data points and gives estimates of both the irreducible wetting phase saturation and the threshold pressure. All these methods assumes a function for the capillary pressure. This was first used by Bentsen and Anli (1977) together with a model for the capillary pressure as a function of saturation. The same was done by van Domselaar (1984) that used another equation combined with parameter estimation. Nordtvedt and Kolltveit (1991) also used a parameter estimation technique but fitted a spline function that is more flexible than using a fixed model for the capillary pressure. However, problems with noise in the measured produced liquid volume may give unrealistic capillary pressure curves when using a spline model. O'Meara, Hirasaki and Rohan (1992) used the Brooks and Corey equation given in Section 3.2.12. All the parameter estimation methods history match the production data as a function of the angular velocity and should therefore give better results than the Hassler and Brunner method. These methods include the capillary pressure distribution in the core and not only at the inner end.

The volume resolution in a manually operated centrifuge is often as low as $\pm$ 0.25 cm^3. Munkvold and Torsæter (1990) presented a method for measuring relative permeabilities using an automated centrifuge with a volume resolution of $\pm$ 0.06 cm^3. Using smaller diameter receiving tubes increases the resolution to $\pm$ 0.03 cm^3. Hirasaki, Rohan, and Dudley (1992) also described an automated centrifuge with a volume resolution of 0.04 cm^3 for measuring relative permeability. They discussed the recent improvements and potential pitfalls in the design of equipment, design of experiment, and interpretation. Omoregie (1988) states that centrifuge equilibration times may be greater than 15 hours for high-permeability rocks, and as long as 30 hours for low-permeability rocks. This makes a complete centrifuge capillary pressure

measurement last for about one week. A critical discussion of the interpretation methods of centrifuge capillary pressure data has been presented by Melrose (1988) and by Wunderlich (1985).

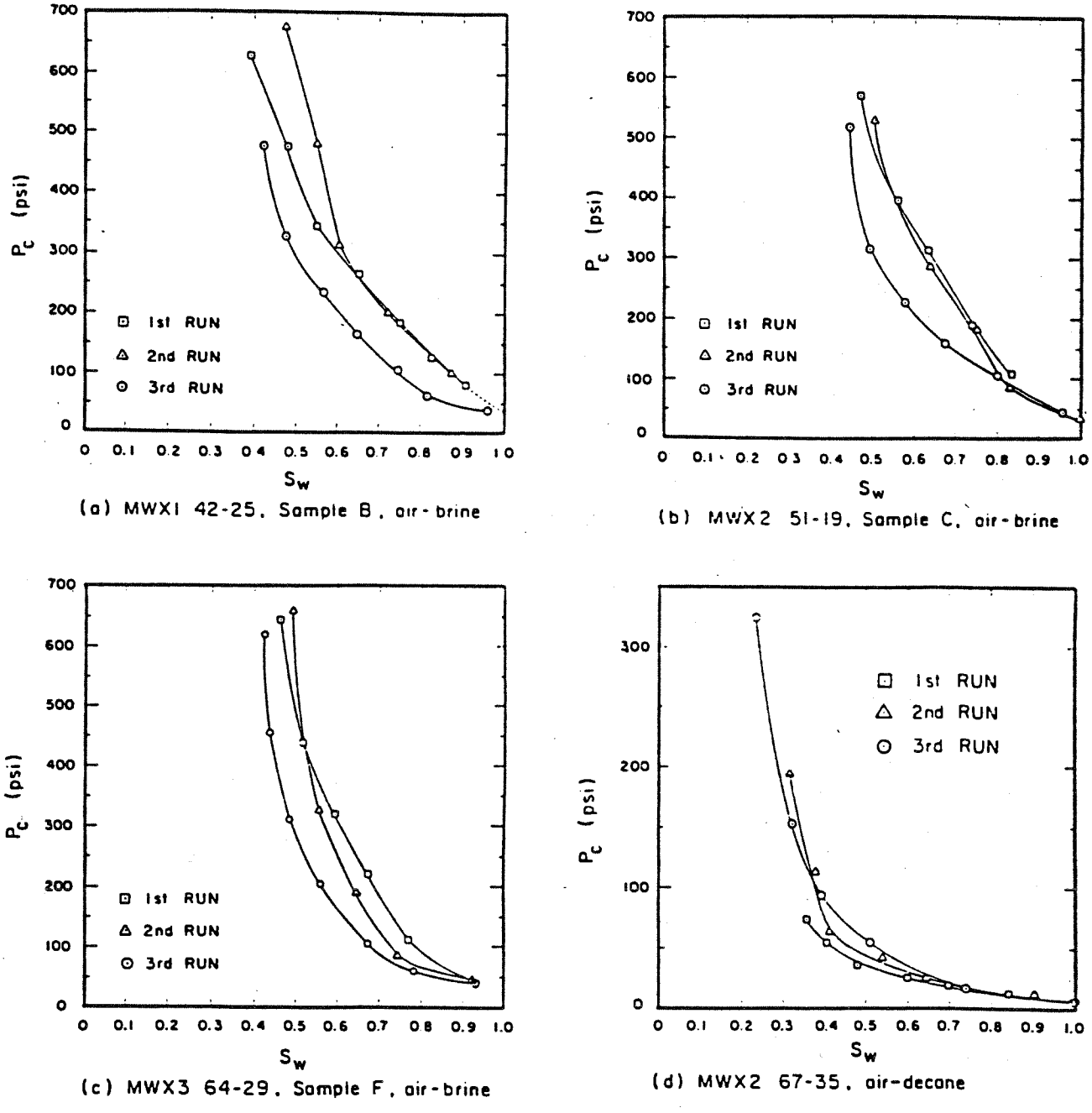

Fig. 3.21 Capillary pressure curves for repeated runs on a given core using the Hassler and Brunner method on centrifuge data (Ward and Morrow, 1987)

Advantages of the centrifuge method are:

- A relatively fast method compared with the porous plate method.
- Relative permeability can be measured together with the capillary pressure (can also be measured for the porous plate method).
- Can be run at reservoir temperature.
- Reservoir fluids can be used, but at low pressure only.
- Several samples can be run simultaneously.
- A robust and simple method to use.

Disadvantages

- Not recommended for samples with high clay content or loosely consolidated sandstone.
- Difficult to measure low capillary pressure on high permeability samples.
- Gives only an indirect measurement of the capillary pressure by angular velocity, radius and density difference.
- Limited sample size gives small pore volume and inaccurate volume readings.
- Results depend on the interpretation method used.
- Not possible to measure the positive part of the imbibition curve.
- The very high gravitational force may permanently deform the sample.
- Very low residual saturations can be obtained that are outside the range defined as capillary pressure (King, *et al.*, 1986).
- Expensive equipment, when automated.

3.3.3 Mercury Injection Method

This method is also known as the Purcell method (Purcell, 1949). A sample with known pore volume is evacuated, and mercury which is the nonwetting phase, is injected in steps while recording the pressure and the volume of the injected mercury. The mercury vapor, together with any residual gas, corresponds to the wetting phase. Saturation is determined from the volume of mercury injected at each pressure. The mercury injection method is the fastest method available for measuring capillary pressure curves. Pressures up to 4000 bar can be used with the risk of accessing closed pores by micro fractures, and permanently deforming the sample.

The mercury injection method is an indirect method and the resulting capillary pressure curve has to be converted to the fluid system of interest (gas-oil, water-gas, or water-oil). In measuring air-mercury capillary pressure, care should be taken to allow sufficient time (20-30 min) for the interface to reach equilibrium for each pressure (Dumoré and Schols, 1974; Saidi, 1987). Fig. 3.22 shows the mercury-air interfacial tension as a function of time. However, usual procedure is to wait only 1 to 5 minutes

for equilibrium which will give a too high capillary pressure. In addition, there is discrepancy in the literature about which interfacial tension and contact angle to use for the mercury-air system. Pure mercury has an IFT of 480 mN/m while Dumoré and Schols (1974) recommended an IFT of 375 mN/m and sufficient time to reach equilibrium IFT. The mercury-air contact angle used is 140°, or 40° if measured through the wetting phase. However, some authors claim that the effective contact angle is close to zero due to the roughness of the porous media. A combination of an IFT of 480 mN/m and a contact angle of 40° gives an effective IFT ($\sigma \cos\theta$) of 368 mN/m. This gives about the same result as using an IFT of 375 mN/m and $\theta = 0°$. An IFT of 375 mN/m and $\theta = 40°$ gives $\sigma\cos\theta = 287$ mN/m which results in a capillary pressure that is 40% lower than for an IFT of 480 mN/m and $\theta = 0°$.

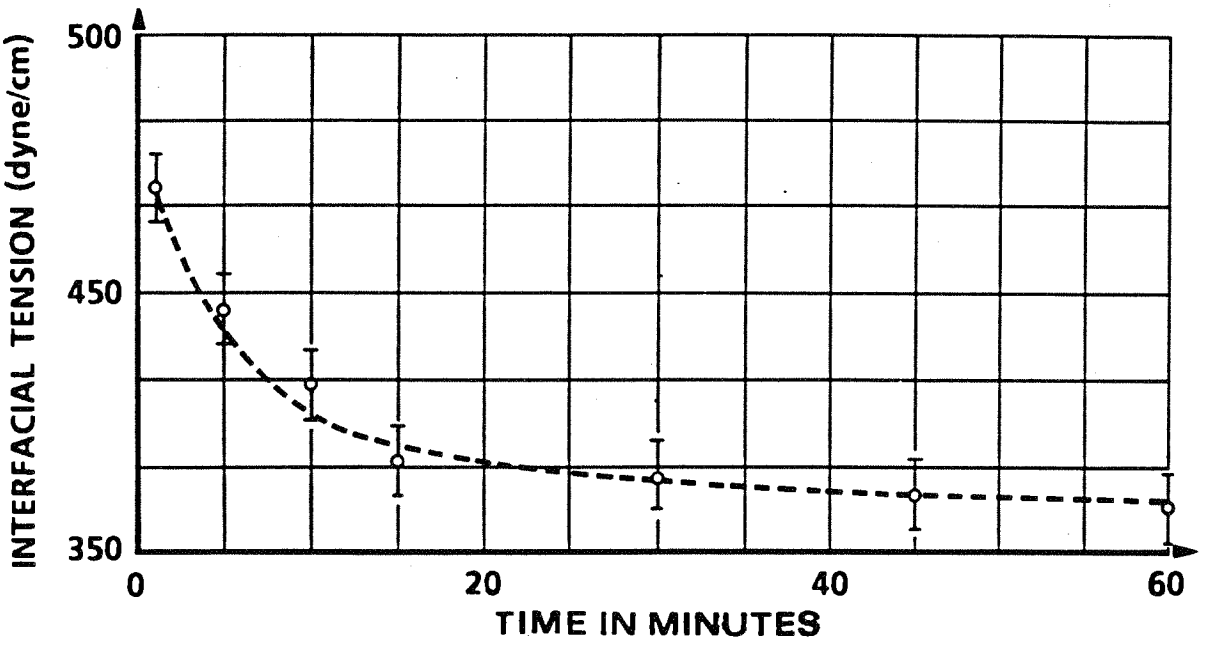

Fig. 3.22 Mercury-air interfacial tension as a function of age of interface (Dumoré and Schols, 1974)

Mercury Porosimetry

The mercury injection method was originally developed to determine pore sizes in the macropore range. IUPAC divides pores roughly into the following groups (Everett, 1988)

Micropores	$d < 0.2$ nm
Mesopores	$d = 2.0 - 50$ nm
Macropores	$d > 50$ nm

Pore sizes down to $d = 2.5$ nm can be measured by using a pressure of up to 4000 bar. The smallest pore size invaded at a given pressure is calculated using the Washburn

equation (Gregg and Sing, 1982) given as

$$d = -\frac{4\sigma\cos\theta}{\Delta p} \tag{3.31}$$

The mercury injection method gives the size of the pore entrance, and not the actual size of the pore body. Therefore, the volume of a big pore with a small pore entrance will be registered as if it was a pore with a small uniform radius.

Micropore volumes are usually determined by nitrogen adsorption having an upper limit for the pore diameters measured of 10 to 20 nm. Usually the mercury injection method and the nitrogen adsorption method are used in conjunction to obtain the complete curve of total pore volume against pore radius. However, for oil recovery calculations there is no need for the pore distribution below the macropore range.

When using the mercury injection method on core samples, one should not use pressure up to 4000 bar. A common upper limit is 200 bar which represents a pore throat diameter of 70 nm. If too high pressure is used, there may be an increase in pore volume caused by fracturing of pore walls that gives access to pores previously closed. There may also be elastic deformation which opens up cracks and passageways, or a permanent compacting effect of the grain structure in the core (Gregg and Sing, 1982).

Advantages of the mercury injection method are:

- Very fast even if waiting 30 minutes at each pressure.
- Can be applied to irregularly-shaped samples, like drill cuttings.

Disadvantages

- Results must be converted to reservoir fluid systems
- Not recommended for samples with high clay content (Monicard, 1980)
- Gives usually a more flat capillary pressure curve than the other methods
- Gives lower irreducible wetting phase saturation than most other methods
- The mercury injection method is a destructive method, as the core material is contaminated with mercury

3.3.4 Dynamic Capillary Pressure Method

Dynamic capillary pressure is the capillary pressure during displacement of fluids in porous media. The effect of the movement of fluids may cause some difference between the static and dynamic capillary pressure.

To investigate this question, Brown (1951) compared steady-state dynamic and static capillary pressure measurements. For the steady-state dynamic capillary pressure method, oil and gas is injected through a special wetted disk into a Hassler type core holder with a fixed differential pressure. This pressure difference is the capillary pressure. The pressure drop for the gas flowing through the core is adjusted to match the pressure drop of the oil phase. When this condition is attained, a constant capillary pressure and saturation is assumed to exist throughout the core. In approaching this equilibrium condition, the pressure drop in the gas phase is higher than in the oil phase. This makes the oil in the core being displaced to a region of higher saturation. The capillary pressure data obtained should, therefore, correspond to the drainage curve obtained by static methods. The saturation at each differential pressure is determined by weighing. By varying the quantity of each fluid entering the core, the saturation can be varied. Brown found no difference between the steady-state dynamic and static capillary pressure curves for the gas-oil system in the 1,000 md sandstone and limestone samples used. This may be caused by the high permeability of the cores.

Kalaydjian (1992a) presented a waterflooding experiment where both saturation and capillary pressure were measured locally. This experiment measured the unsteady-state dynamic capillary pressure. Water-wet and oil-wet membranes were used to measure the pressure in each phase along the core sample. The saturation was measured using ultrasonic transducers. A limestone and a sandstone sample were used, both with a permeability of about 170 md. The imbibition capillary pressure was found to increase with the flow rate, especially for the limestone sample. Kalaydjian found that it appears difficult to split viscous effects and capillary effects in two separate terms.

3.3.5 Evaporation Method

This method can be used to determine the irreducible wetting phase saturation, and will not give a complete capillary pressure curve. The core sample is saturated with water or toluene and then put in a current of dry air. The weight loss as a function of time is used to determine the irreducible saturation. When the irreducible saturation is reached there is evaporation only by diffusion so the slope is much smaller. A method measuring low-temperature nitrogen adsorption/desorption isotherms can also be used to measure the capillary pressure curve for low wetting phase saturations (Melrose, 1990; Melrose, 1991). However, the accuracy and validity of this method has been questioned (Saidi, 1987).

3.3.6 Comparing the Methods

Based on the evaluation of the various methods for measuring the capillary pressure, the following conclusions and recommendations can be made:

- The porous plate method is most accurate if allowing sufficient time to reach hydrodynamic equilibrium.
- By using thin membranes instead of ceramic disks, the porous plate method is almost as fast as the centrifuge method.
- The porous plate method should be used if the samples have a high clay content or if the permeability is high (>1000 md).
- The porous plate method is the only method that can be used at elevated pressure and temperature with reservoir fluids.
- The parameter estimation methods are much more stable than the Hassler and Brunner related methods for interpreting centrifuge experiments.
- Some interpretation methods for centrifuge experiments can be questioned.
- The assumption of 100% saturation of the wetting phase during a centrifuge run may not hold if the speed is above a critical limit. The resulting capillary pressure curve will then be incorrect for high values of the capillary pressure.
- The mercury injection method is useful as a preliminary method to determine the capillary entry pressure for the slower centrifuge and porous plate methods, but may give a different shape of the capillary pressure curve.
- It is important to wait for equilibrium for the porous plate method, the centrifuge method, and the mercury injection method.
- The unsteady-state dynamic capillary pressure method should be used to measure the increase in capillary pressure with flow rate.
- The evaporation method can be used to determine the irreducible wetting phase saturation and to measure the capillary pressure curve for low wetting phase saturations.

3.3.7 Conversion of P_c to Reservoir Conditions

Measuring capillary pressure at reservoir conditions requires complicated equipment and is also difficult to perform. Capillary pressure curves are therefore measured at laboratory conditions and scaled to reservoir conditions. Since the capillary pressure is a function of local pore geometry, interfacial tension, wettability, saturation, and saturation history, this conversion is very difficult. The models usually applied neglects the effect of local pore geometry, and uses the contact angle to represent the wetting of the fluid-rock system. Both the Young-Laplace equation using the mean pore radius and the contact angle, and the Leverett J-function may be used. For scaling the capillary pressure curve of a core sample, both the permeability and the porosity is constant, so both equations gives the following relationship:

$$P_{cR} = \frac{\sigma_R \cos\theta_R}{\sigma_L \cos\theta_L} P_{cL} \tag{3.32}$$

R and L indicates reservoir and laboratory conditions respectively. The interfacial tension can be measured both at laboratory and at reservoir conditions with reasonable accuracy. However, the contact angle is difficult to measure for a rock and the wettability is insufficiently represented by the contact angle. The effect of the converging and diverging pore walls is also neglected in this model. For gas-oil systems it is often assumed that the contact angle $\theta = 0$, and for water-oil systems the contact angle is sometimes assumed constant. This gives a simplified relationship between the laboratory and reservoir capillary pressure.

$$P_{cR} = \frac{\sigma_R}{\sigma_L} P_{cL} \tag{3.33}$$

For water-oil systems this equation may give incorrect results as the wettability, and thereby the contact angle, is changing at elevated temperature (Søndenå, *et al.*, 1990; Søndenå, 1991; Søndenå, *et al.*, 1992). One of the main purposes of this work is to check Eq. (3.33) for gas-oil drainage capillary pressure curves on chalk samples at both high and low pressure (low and high interfacial tensions, respectively).

3.4 Apparatus and Methods

Development of the apparatus and the operating procedure were the most time-consuming parts of this work. Several problems were encountered and solved during the development of the method. Most of the important details will be explained in the following sections.

3.4.1 Apparatus

The apparatus consists of the following elements:

- A Millipore filter holder modified to be used as a core holder
- Two hand pumps (one 250 cm^3 and one 10 cm^3)
- Two 30 cm^3 motorized pumps with accurate volume transducers
- A circulation pump (0 to 20 cm^3/min)
- Two 1000 cm^3 high-pressure containers
- A differential pressure transducer
- Two pressure transducers
- A sapphire sight glass
- Two temperature transducers
- A temperature controller
- A PC with a data acquisition card
- 30 m high-pressure tubing and 40 valves

A drawing of the apparatus is given in Fig. 3.23. The main parts are the core holder, the manual and automated gas and oil pumps, the high-pressure reservoirs, the circulation pump, and the differential and absolute pressure transducers. Most of the valves are used during the initialization of the apparatus, and for isolation and evacuation after dismounting equipment for calibration and maintenance. Valve 14 is a needle valve that allows slow opening. This is important when filling the evacuated core holder with equilibrium oil. Leaks are also a common problem with high-pressure equipment. Isolating parts of the equipment by closing valves, makes leaks easier to locate. A brief description of the function of some of the main parts follows:

- The manual gas pump is used to adjust the absolute pressure in the system during initialization. It is also used to inject gas into the core holder when starting an experiment.

- The manual oil pump is used to inject overpressured equilibrium oil into the evacuated core holder and the lines in the lower system (below valves 9, 12, 15, and 16). This pump is also used to withdraw oil from the core holder when

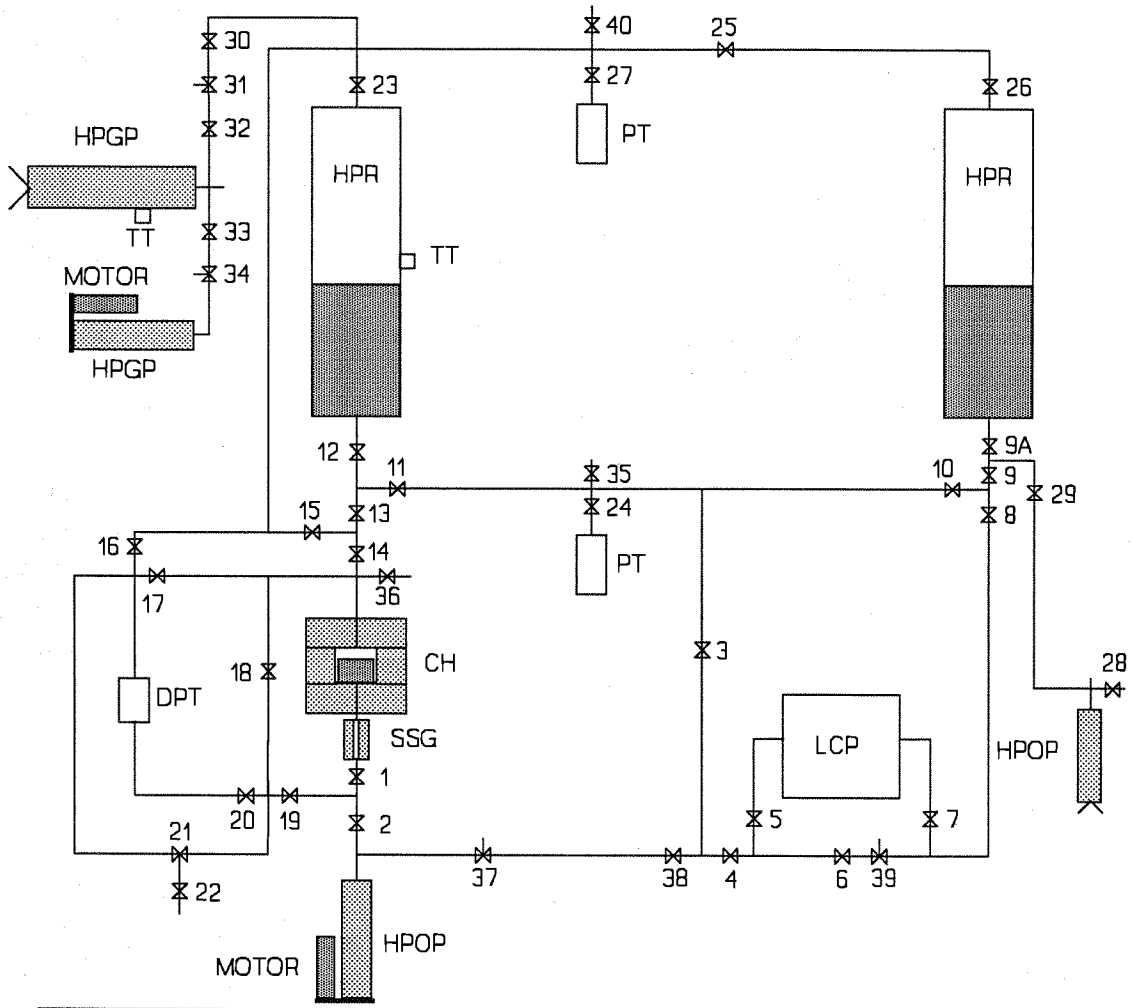

Fig. 3.23 The high-pressure capillary pressure apparatus

displacing the dead volume around the core during the start of an experiment.

- The two containers are mounted so that they can be shaken to create equilibrium gas and oil before charging the automatic gas pump and the core holder. Only one container is necessary.

- The circulation pump is used to circulate overpressured equilibrium oil through the core holder and the lines in the lower system before starting an experiment. This dissolves any free gas in the system and reduces the problem of concentration gradients in the lines, that cause diffusion and pressure drop after starting the experiment.

- The automatic oil pump is connected to the differential pressure transducer by a PC. This pump withdraws the produced oil from the core holder and keeps the selected differential pressure constant at each step of the capillary pressure curve. The accuracy of this pump is crucial for being able to keep the differential pressure within ± 5 mbar at an absolute pressure of about 100 bar. The differential pressure is checked and adjusted every 5 seconds.

- The automatic gas pump is connected to the absolute pressure transducer by the PC and injects gas into the top of the core holder to keep a constant pressure below the core holder. A high resolution pressure transducer is needed to avoid fluctuations in the differential pressure. The gas pump must be slow enough so that the oil pump will always be able to keep a constant differential pressure. It is more important to maintain a constant differential pressure than a constant absolute pressure.

Fig. 3.24 gives a drawing of the core holder. The top and bottom part of the core holder is a Millipore high-pressure 316 stainless filter holder, and the middle part is also made of stainless steel with the same type of seals as the filter holder. Viton o-rings were used in all seals. Use of the Millipore filter holder has the advantage of being well tested and specially designed for good sealing around the membrane. Fig. 3.25 gives details about the seals between the Millipore cap and the middle part of the core holder. A ring of a thin teflon sheet was used below the perforated screen to prevent any gas from diffusing through the outer part of the membrane and flow around the screen. This reduces the amount of diffusion through the membranes.

Fig. 3.26 shows details of the membranes, the core, and the perforated membrane support plate. The original Millipore membrane support plate was used. This is smooth and does not damage the membranes. The upper drawing is a top view and the lower drawing is a side view. Note that the vertical to horizontal ratio in the side view is 30 to 1. Figs. 3.27 and 3.28 show two photographs of the coreholder; disassembled and assembled. Details of the spring with the grooved washer and the double o-ring seal can be seen.

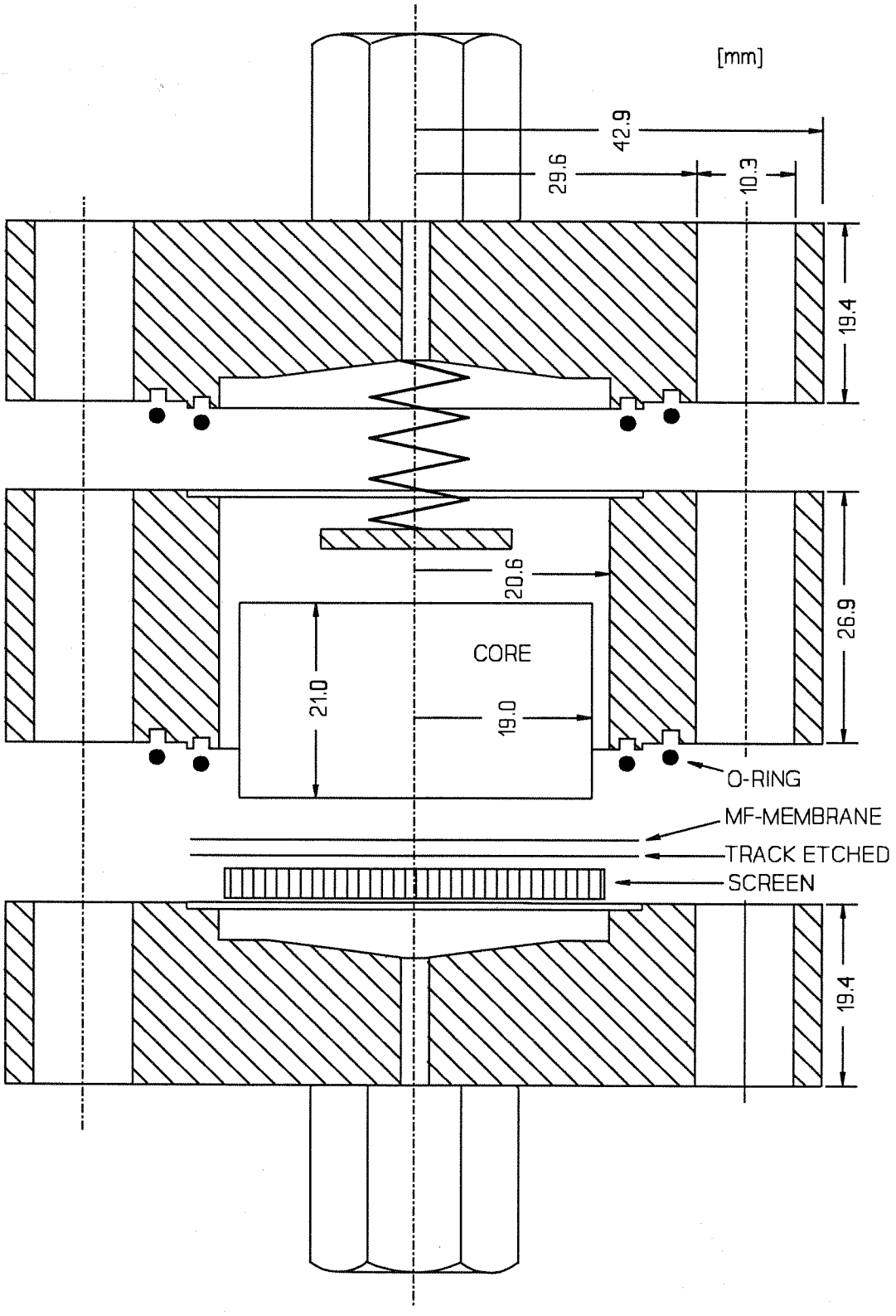

Fig. 3.24 Dimensions of the core holder

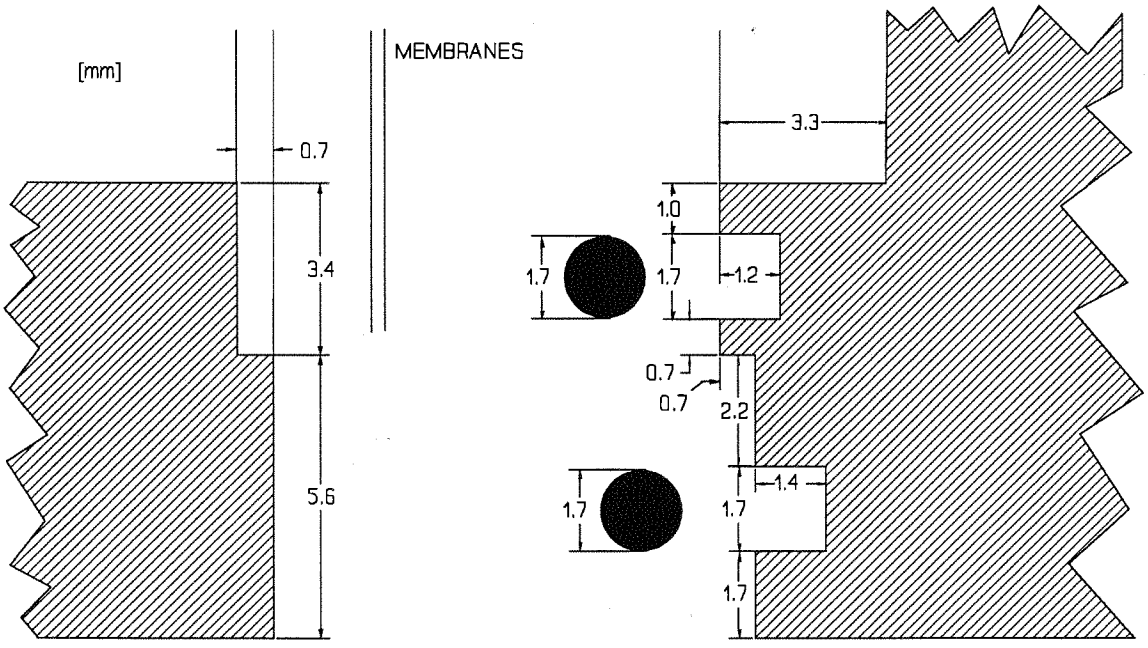

Fig. 3.25 Details of coreholder seals

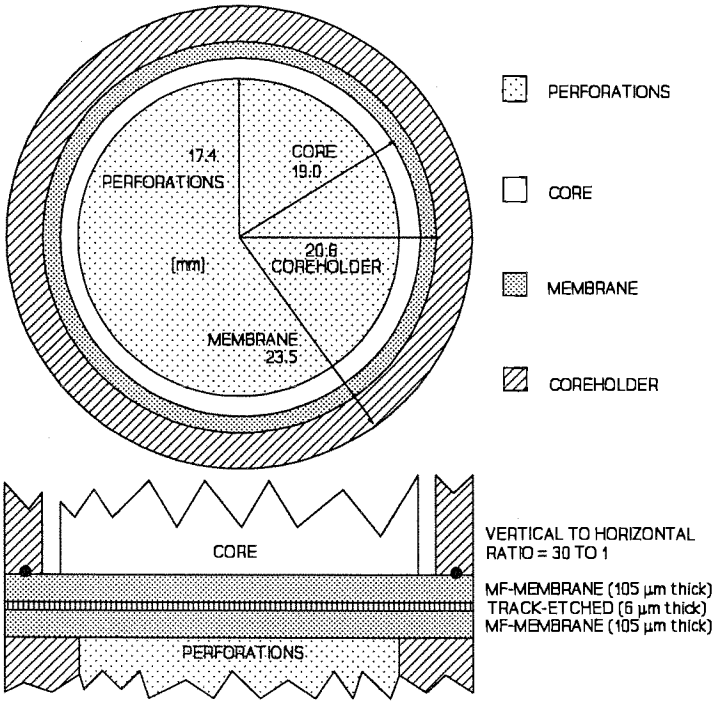

Fig. 3.26 Top view and side view of membranes inside coreholder

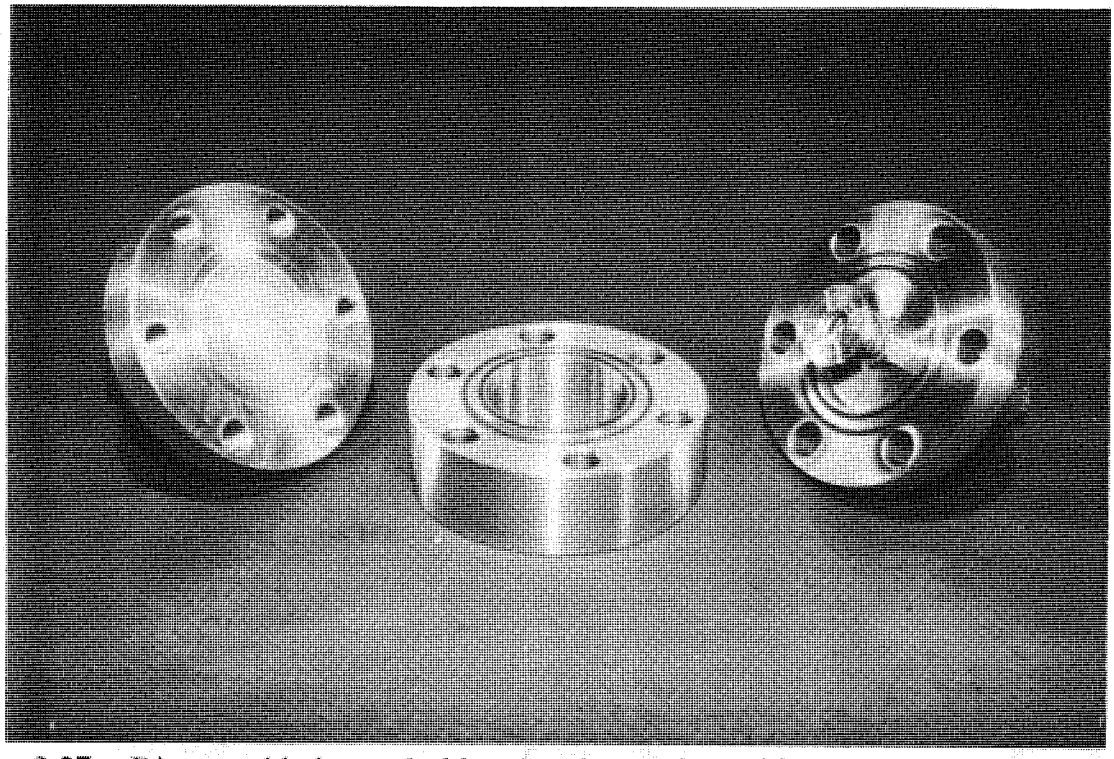

Fig. 3.27 Disassembled core holder showing spring with grooved washer

Fig. 3.28 Assembled high-pressure capillary pressure core holder

To keep the differential and absolute pressures constant, two computer controlled positive displacement pumps were used, making it possible to determine accurately the core oil saturation by material balance (also accounting for gas diffusion through the membrane). The oil pump keeps the differential pressure constant, while the gas pump keeps the absolute pressure constant. The automated pumps can handle a production rate from 0.0 to 2.0 cm^3/hr. A photo of the automated pump is given in Fig. 3.29 including motor, gearheads, and displacement transducer. Two planetary gearheads were used, giving a total reduction of 30,000:1 for the gas pump and 40,000:1 for the oil pump. Due to the small volume and low compressibility of the oil, the oil pump has the largest effect on the differential pressure. However, the oil pump must not be too slow compared with the gas pump. The positive displacement pumps were low cost pumps from HiP. Fig. 3.30 shows the computer control of the apparatus, including only the active parts used during an experiment. The apparatus was designed to measure differential pressures in the range of 0 to 1,000 mbar with fluctuations less than ± 5 mbar (caused by temperature variations). More details about the computer control is given in Appendix E, while Appendix F gives details about the equipment used.

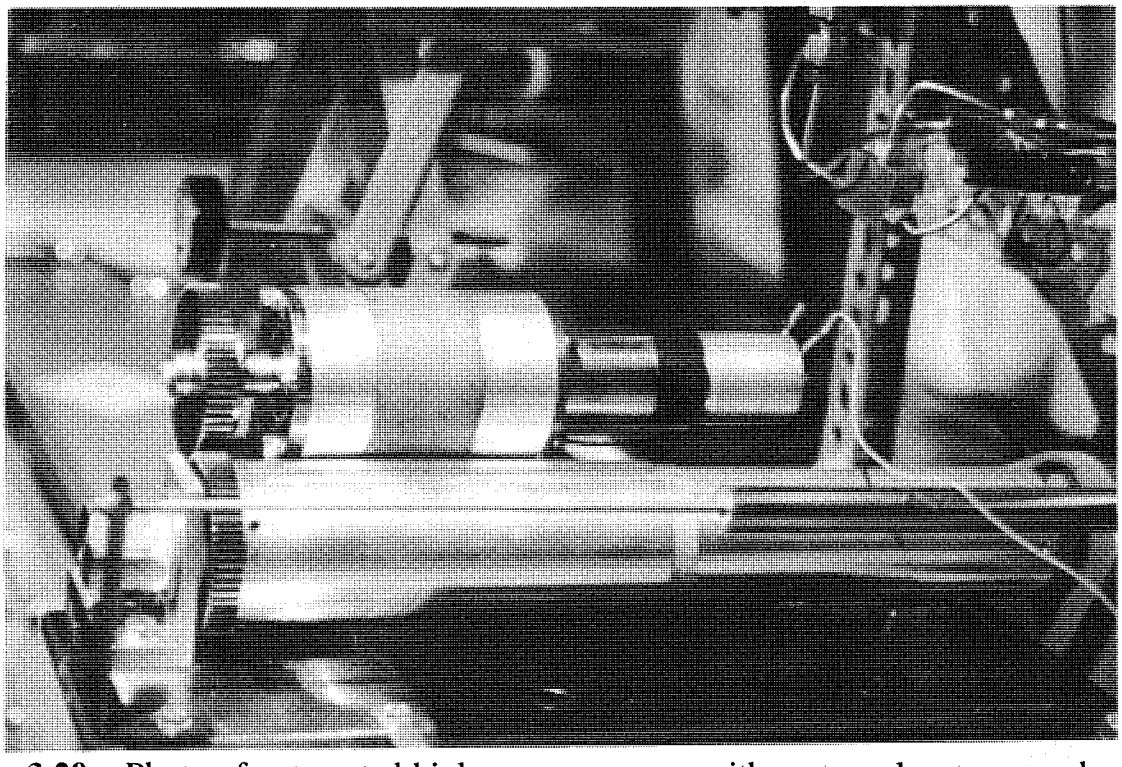

Fig. 3.29 Photo of automated high-pressure pump with motor, planetary gearheads, and displacement transducer for volume measurement

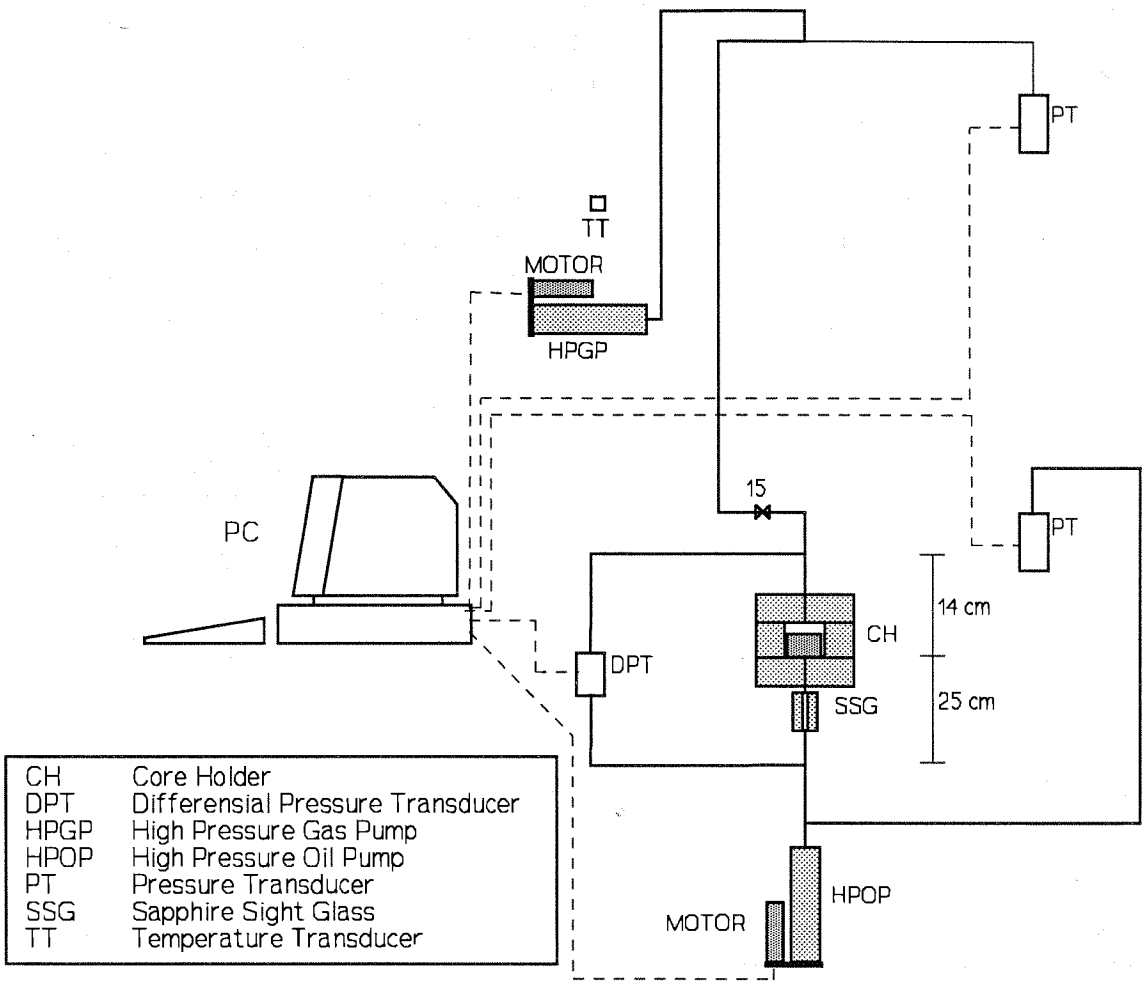

Fig. 3.30 Main parts of apparatus with computer control

A separate proportional temperature controller connected to an electrical heater keeps the temperature in the room constant to 24.0 ± 0.05°C. A fan is mounted above the heater to get good mixing of the air in the room. A constant temperature is very important to be able to keep the differential pressure constant, and to maintain thermodynamic equilibrium in the system.

Very low flow rates and produced volumes make it important to have accurate volume measurements. The low differential pressure compared with the absolute pressure in the system made it necessary to use accurate absolute and differential pressure transducers. Table 3.2 gives the accuracy and resolution for the transducers.

Table 3.2 Transducer accuracy and resolution

Transducer	Unit	Range	Accuracy	Resolution
Differential Pressure	(mbar)	0 - 1000	1.0	0.20
Pressure	(bar)	0 - 200	0.3	0.04
Temperature	(°C)	0 - 50	0.2	0.01
Volume Produced	(cm^3)	0 - 30	0.2	0.01

3.4.2 Membranes

The use of membranes instead of traditional porous plates speeds up the capillary pressure experiment significantly. The time needed to measure a capillary pressure curve becomes almost independent of the flow resistance from the membrane itself, and depends only on the flow resistance from the core sample. This is true if the pore size of the membrane is not selected smaller than necessary (close to the diameter of the smallest pore drained during a capillary pressure experiment). The time required for a capillary pressure curve will be much shorter at lower pressures, where the interfacial tension and thereby the differential pressures are higher. For a one dimensional capillary pressure experiment, Jennings (1981) gives the following analytical relationship for the time required to reach equilibrium at each differential pressure step:

$$t \propto \frac{\phi L^2 \Delta S_W}{k \Delta P_c} \tag{3.34}$$

where

L = core length
ΔP_c = incremental change in capillary pressure
ΔS_w = incremental change in saturation

Eq. (3.34) shows that the time required is proportional to the square of the core sample

length, and inversely proportional to the differential pressure and the permeability of the core. The viscosities of the two fluids and the relative permeabilities will also be important for the equilibrium time, and these effects are more difficult to estimate. Eq. (3.34) should overpredict the time for stabilization when all sides of the core are open.

Both cellulosic and track-etched membranes from Millipore and Costar-Nuclepore were compared, to find the most appropriate membranes for the experiments. The flow rates and pore sizes were also compared with data for porous ceramic plates from Coors and Soilmoisture. The results from these comparisons follow.

Cellulosic Membranes

The membranes are made of mixtures of cellulose acetate and cellulose nitrate, and have no clearly defined or regular pore structure. High porosity make the flow rate high taken into account the thickness of the membrane (100 to 150 μm). The structure of a cellulosic membrane is shown in Fig. 3.31.

Track-Etched Membranes

The track-etch process is a two-step process involving a nuclear reactor (or a cyclotron) and an etch bath. In the first step, a thin film (10 μm) of polycarbonate or polyester is bombarded with neutrons (or argon molecules). These particles leave damage tracks in the film that are more vulnerable to chemical attack than the bulk of the film. The film is then run through an etch bath, and strength and time in the bath controls the pore size. This process results in membranes where pore sizes are produced with great precision, varying no more than 0 to -20% of rated pore sizes. This assures a narrow pore size distribution, and thereby a distinct break-through pressure. Pores are close to perfectly round cylinders, with random dispersion over the surface of the membrane. In general, porosities above 15% result in low-strength membranes. The porosity is usually decreased with the pore size to maintain the strength of the membranes. The structure of a track-etched membrane is shown in Fig. 3.32. Break-through pressure will be reduced by the overlapping pores. If we assume two overlapping pores where the resulting pore has radii of r and $2r$, the break-through pressure will be reduced by 25%. This follows from the Young-Laplace equation.

The etching starts at the surface and eats its way through the membrane from both sides. For very small pore sizes (below 0.1 μm), this can result in a *diabolo* shaped hole. Pore sizes are determined by use of a scanning electron microscope (SEM). The minimum pore size that can be determined using SEM is about 0.05 μm. Therefore, both pore size and shape are difficult to determine for pore sizes below 0.05 μm.

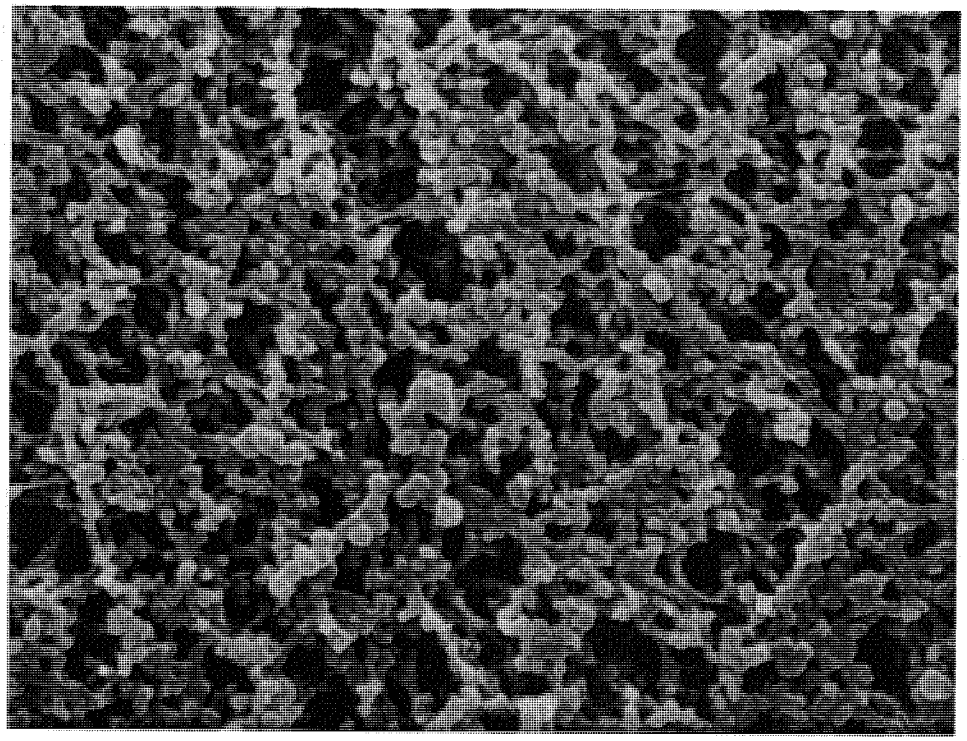

Fig. 3.31 Structure of the Millipore MF cellulosic membrane (5,000X, 0.45 μm)

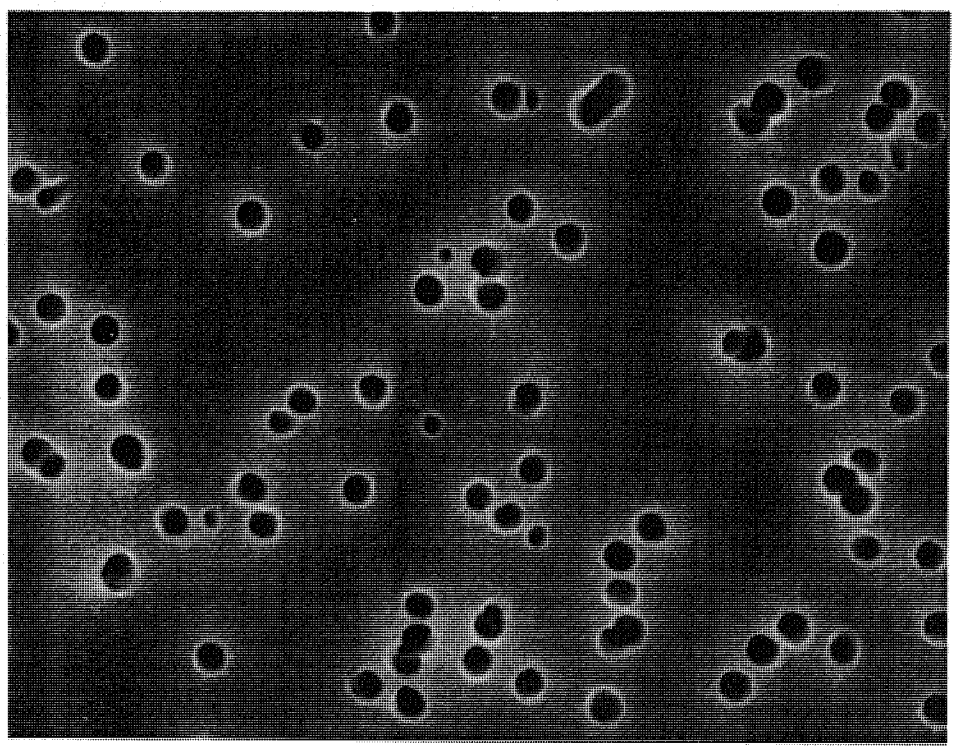

Fig. 3.32 Structure of the Millipore track-etched membrane (15,000X, 0.2 μm)

Comparing the Membranes

Table 3.3 compares properties for the cellulosic and the track-etched membranes available from Millipore and Costar-Nuclepore. It appears that there are only minor differences between the membranes from Millipore and Costar-Nuclepore. Available pore sizes and technical assistance may be important. Both cellulosic and track-etched membranes are water wet, but can be made oil wet by special treatment. A disadvantage with the track-etched membranes in core analysis, is that it clogs rapidly by impurities in the fluids or by particles from the core sample. The cellulosic membranes have no clearly defined pore size and have a less distinct break-through pressure than the track-etched membranes.

Table 3.3 Comparing properties of two membrane types from Millipore and Nuclepore

	Mixed Esters of Cellulose		Track-Etched Membranes	
Properties	Millipore MF	Nuclepore MF	Millipore Isopore	Nuclepore Polycarbonate
Max. temperature, °C	120	120	140	140
Pore size*, µm	0.025-8	0.10-5	0.1-10	0.015-12
Diameter, mm	13-293	13-293	13-47	13-142
Thickness, µm	100-150	125	10	6-10
Porosity, %	70-84	72-88	5-15	0.1-12
Burst strength**, bar		0.35	>1.0	>0.7
Comment	Thick, Soft, Brittle		Thin, Strong, Elastic	

* Other pore sizes may be ordered
** For unsupported membrane. Differential pressures above 100 bars may be used.

Use of both cellulosic membranes and track-etched membranes instead of the thick porous plates have become more widely accepted. Jennings (1983) used track-etched membranes measuring low-pressure capillary pressures curves for a kerosene-air system. Hammervold and Skjæveland (1992) compared the use of water-wet track-etched membranes with ceramic porous plates for measuring water-oil drainage capillary pressure curves on Berea sandstone samples at ambient conditions. They found that the time to obtain a drainage capillary pressure curve was reduced by a factor of more than 10. Kalaydjian (1992b) used both water- and oil-wet cellulosic membranes to measure three-phase capillary pressure. Both drainage and imbibition capillary pressure curves were measured at ambient conditions.

To further compare the cellulosic and track-etched membranes, data from catalogs and correspondence with the manufacturers were used together with estimated values for flow rates and break-through pressures. Permeability was calculated from the given flow rates using Darcy's law

$$k = \frac{q\mu L}{A\Delta p} \tag{3.35}$$

Poiseuille's law was also used to calculate the permeability for the track-etched membranes

$$k = \frac{n\pi r^4}{8} \tag{3.36}$$

where n is the number of pores per unit area. To estimate the break-through pressures, the Young-Laplace equation for cylindrical tubes was used

$$P_c = \alpha \frac{2\sigma \cos\theta}{r} \tag{3.37}$$

where α is a pore-shape correction factor. According to Millipore, the contact angle for a polycarbonate-water-air system is 60°. To obtain a match between the catalog and estimated break-through pressures for the track-etched membranes, a shape factor of 0.75 had to be used. This could be caused by the overlapping pores mentioned earlier. The match was good for both the Millipore and Nuclepore track-etched membranes. For the cellulosic membranes, an apparent contact angle of 73° gave a match of the catalog break-through pressures. This is equivalent to a shape factor of 0.29 assuming a contact angle of 0°.

Tables 3.4 to 3.7 give catalog and estimated properties for the cellulosic and track-etched membranes from Millipore and Costar-Nuclepore. A water viscosity of 1.0 cp and a water-air IFT = 72 mN/m were used in the calculations. For the track-etched membranes, uneven variations in pore density cause uneven variations in flow rates as a function of pore size. Poiseuille's equation gives lower permeabilities than measured for small pore diameters. Tables 3.8 and 3.9 give the properties for porous ceramic plates from Coors and Soilmoisture.

Fig. 3.33 plots catalog and estimated break-through pressures for cellulosic and track-etched membranes, and ceramic plates. Track-etched membranes give a higher break-through pressure than the cellulosic membranes for a given pore diameter. The pore diameters in the catalog for the ceramic plates are probably calculated from break-through pressures assuming a contact angel of 0° and cylindrical pores. This results in a higher break-through pressure, compared with the membranes, for a given pore diameter.

Flow rates are compared in Fig. 3.34. Note the drastic reduction in flow rate as the pore diameter decreases. It is therefore important to not use a membrane with smaller

pores than necessary. According to Millipore, the flow rates given by Costar-Nuclepore for track-etched membranes above 2.0 μm, are too high. Comparing the flow rates for the membranes with the ceramic plates, shows a reduction of several orders of magnitude. The higher break-through pressure for the ceramic plates makes it possible to use a plate with pore size that is 2 to 3 times larger than for the membranes. However, the flow rate for the ceramic plates is several orders of magnitude lower than for a membrane with the same break-through pressure. Cellulosic and track-etched membranes give almost the same flow rate.

To check the effect of using membranes instead of porous plates, the flowrates obtained together with a core sample were calculated. Both a 5 md chalk sample and a 300 md Sandstone sample were used, with a height of 2 cm. The flow was one dimensional and flowrates are calculated from permeabilities and thickness using a viscosity of 1 cp and a differential pressure of 100 mbar. Darcy's law was used to calculate the flow rates with permeability $\bar{k}$ given by a harmonic average:

$$q = \frac{\bar{k} A \Delta p}{\mu (L_c + L_m)} \quad \text{and} \quad \bar{k} = \frac{(L_c + L_m)}{\frac{L_c}{k_c} + \frac{L_m}{k_m}} \tag{3.38}$$

where

k_c = core permeability
k_m = membrane permeability
L_c = core length
L_m = membrane thickness

Fig. 3.35 gives flow rates for the 5 md chalk sample for different membranes and porous plates as a function of membrane or porous plate pore diameter. The flow rate is not influenced by the membrane permeability down to a membrane pore diameter of 0.1 μm. For chalk samples with pore sizes down to 0.1 μm, membranes with a pore size of 0.1 μm or lower must be used. A smaller membrane pore diameter will significantly increase the time required to measure a capillary pressure curve. Using the 0.16 μm ceramic plate reduces the flow rate through the core sample by a factor of 10 compared with a 0.05 μm or larger membrane.

Fig. 3.36 gives flow rates for the 300 md sandstone sample. The flow rate is unaffected by the membrane permeability down to a membrane pore diameter of 0.4 μm. Using a membrane with a smaller pore size reduces the flow rate significantly. For a Berea sandstone, pores with a diameter smaller than 1 μm will not be displaced during a capillary pressure experiment. Using a 1 μm ceramic plate reduces the flow rate with a factor of 10 or more compared with a 0.4 μm membrane. However, if a Soilmoisture ceramic plate with a 2.1 μm pore diameter could be used, this would give close to the same flow rate as using membranes.

Table 3.4 Catalog and estimated properties for Millipore track-etched membranes

Catalog Properties					Estimated Properties			
d (μm)	L (μm)	Pore Density (1/cm^2)	Water q^* (cm^3/min/cm^2)	P_{cb}** (bar)	ϕ (%)	Poiseuille k (md)	Darcy k (md)	P_{cb}† (bar)
10.0	10	1.0E+05	520	<0.07	8	249	13	0.11
8.0	12	1.0E+05	370	0.15	5	102	11	0.14
5.0	15	4.0E+05	400	0.21	8	62	15	0.22
3.0	7	2.0E+06	375	0.48	14	40	6.0	0.36
2.0	8	2.0E+06	180	0.56	6	8.0	3.5	0.54
1.0	9	2.0E+07	190	0.77	16	5.0	4.2	1.1
0.8	9	3.0E+07	100	1.1	15	3.1	2.2	1.4
0.6	9	3.0E+07	55	1.8	9	0.97	1.2	1.8
0.4	10	1.0E+08	60	2.5	13	0.64	1.5	2.7
0.2	10	4.5E+08	20	5.1	14	0.18	0.49	5.4
0.1	10	6.0E+08	3	>6.9	5	0.015	0.073	11

d = pore diameter, L = thickness, ϕ = porosity, k = permeability
* Water flow rate for Δp = 10 psi = 0.69 bar, μ = 1.0 cp
** Air break-through pressure in water saturated membrane (gauge limit = 6.9 bar)
† Using water-polycarbonate contact angle of 60° and a shape factor of 0.75

Table 3.5 Catalog and estimated properties for Millipore cellulosic MF membranes

Catalog Properties					Estimated	
d (μm)	L (μm)	Water q^* (cm^3/min/cm^2)	P_{cb}** (bar)	ϕ (%)	Darcy k (md)	P_{cb}† (bar)
8	135	620	0.42	84	205	0.11
5	135	580	0.42	84	192	0.17
3	150	320	0.70	83	118	0.28
1.2	150	270	0.77	82	99	0.70
0.8	150	190	0.98	82	70	1.1
0.65	150	140	1.2	81	51	1.3
0.45	150	60	2.1	79	22	1.9
0.30	150	32	2.5	77	12	2.8
0.22	150	18	3.5	75	6.6	3.8
0.10	105	1.5	14	74	0.4	8.4
0.05	105	0.74	18	72	0.19	17
0.025	105	0.15	21	70	0.04	34

d = pore diameter, L = thickness, ϕ = porosity, k = permeability
* Water flow rate for Δp = 10 psi = 0.69 bar, μ = 1.0 cp
** Air break-through pressure in water saturated membrane
† Using water-solid contact angle of 73° ($\cos\theta$ = 0.3) to match given data

Table 3.6 Catalog and estimated properties for Nuclepore track-etched membranes

Catalog Properties					Estimated Properties			
d (μm)	L (μm)	Pore Density (1/cm^2)	Water q^* (cm^3/min/cm^2)	P_{cb}** (bar)	ϕ (%)	Poiseuille k (md)	Darcy k (md)	P_{cb}† (bar)
10	10	1.0E+05	2500	>0.07	8	249	61	0.11
8	7	1.0E+05	2000	0.21	5	102	34	0.14
5	10	4.0E+05	2000	0.21	8	62	49	0.22
3	9	2.0E+06	1500	0.48	14	40	33	0.36
2	10	2.0E+06	350	0.62	6	8.0	8.6	0.54
1	11	2.0E+07	250	0.96	16	5.0	6.7	1.1
0.8	9	3.0E+07	215	1.2	15	3.1	4.7	1.4
0.6	10	3.0E+07	115	2.0	9	0.97	2.8	1.8
0.4	10	1.0E+08	70	2.9	13	0.64	1.7	2.7
0.2	10	3.0E+08	20	5.7	9	0.12	0.49	5.4
0.1	6	3.0E+08	4	>6.9	2.4	0.0075	0.059	11
0.08	6	3.0E+08	2	>6.9	1.5	0.0031	0.029	14
0.05	6	6.0E+08	0.7	>6.9	1.2	0.00093	0.010	22
0.03	6	6.0E+08	0.15	>6.9	0.4	0.00012	0.0022	36
0.015	6	6.0E+08	0.015	>6.9	0.1	0.00001	0.00022	72

d = pore diameter, L = thickness, ϕ = porosity, k = permeability
* Water flow rate for Δp = 10 psi = 0.69 bar, μ = 1.0 cp
** Air break-through pressure in water saturated membrane (gauge limit = 6.9 bar)
† Using water-polycarbonate contact angle of 60° and a shape factor of 0.75

Table 3.7 Catalog and estimated properties for Nuclepore cellulosic MF membranes

Catalog Properties					Estimated	
d (μm)	L (μm)	Water q^* (cm^3/min/cm^2)	P_{cb}** (bar)	ϕ (%)	Darcy k (md)	P_{cb}† (bar)
5	125	700	0.42	84	214	0.17
3	125	400	0.62	83	122	0.28
1.2	125	300	0.76	82	92	0.70
0.8	125	240	0.97	82	73	1.1
0.65	125	120	1.3	81	37	1.3
0.45	125	68	2.1	79	21	1.9
0.30	125	34	2.7	77	10	2.8
0.22	125	20	3.5	75	6.1	3.8
0.10	125	5	–	74	1.5	8.4

d = pore diameter, L = thickness, ϕ = porosity, k = permeability
* Water flow rate for Δp = 10 psi = 0.69 bar, μ = 1.0 cp
** Air break-through pressure in water saturated membrane
† Using water-solid contact angle of 73° ($\cos\theta$ = 0.3) to match given data

Table 3.8 Catalog and estimated properties for Coors porous ceramic plates

Catalog Properties						Estimated	
		Water				Darcy	
d (μm)	L (μm)	q^* ($cm^3/min/cm^2$)	P_{cb}^{**} (bar)	ϕ (%)	k (md)	k (md)	$P_{cb}^{\dagger}$ (bar)
10.6	6000	19	0.28	39	250	273	0.27
8.75	6000	9.5	0.34	46	120	140	0.33
5.25	6000	5.8	0.55	38	75	85	0.55
1.85	6000	2.6	1.62	42	31.5	38	1.56
0.50	6000	0.0093	5.72	34	0.135	0.14	5.76

d = pore diameter, L = thickness, ϕ = porosity, k = permeability
* Water flow rate for Δp = 10 psi = 0.69 bar, μ = 1.0 cp
** Air break-through pressure in water saturated plate
† Using water-solid contact angle of 0° gives same value as catalog data. This shows that pore diameter probably is calculated from break-through pressure.

Table 3.9 Catalog and estimated properties for Soilmoisture porous ceramic plates

Catalog Properties					Estimated	
		Water			Darcy	
d (μm)	L (μm)	q^* ($cm^3/min/cm^2$)	P_{cb}^{**} (bar)	ϕ (%)	k (md)	$P_{cb}^{\dagger}$ (bar)
6	6350	122	0.48	50	1904	0.48
2.5	6350	34	1.31	45	529	1.15
2.1	6350	1.4	1.38	34	21	1.37
1.2	6350	0.68	2.41	38	11	2.40
0.8	6350	0.68	3.17	34	11	3.60
0.5	6350	0.48	5.52	31	7.4	5.76
0.16	6350	0.010	15.17	32	0.16	18.0

d = pore diameter, L = thickness, ϕ = porosity, k = permeability
* Water flow rate for Δp = 10 psi = 0.69 bar, μ = 1.0 cp
** Air break-through pressure in water saturated plates
† Using water-solid contact angle of 0° gives same value as catalog data. This shows that pore diameter probably is calculated from break-through pressure.

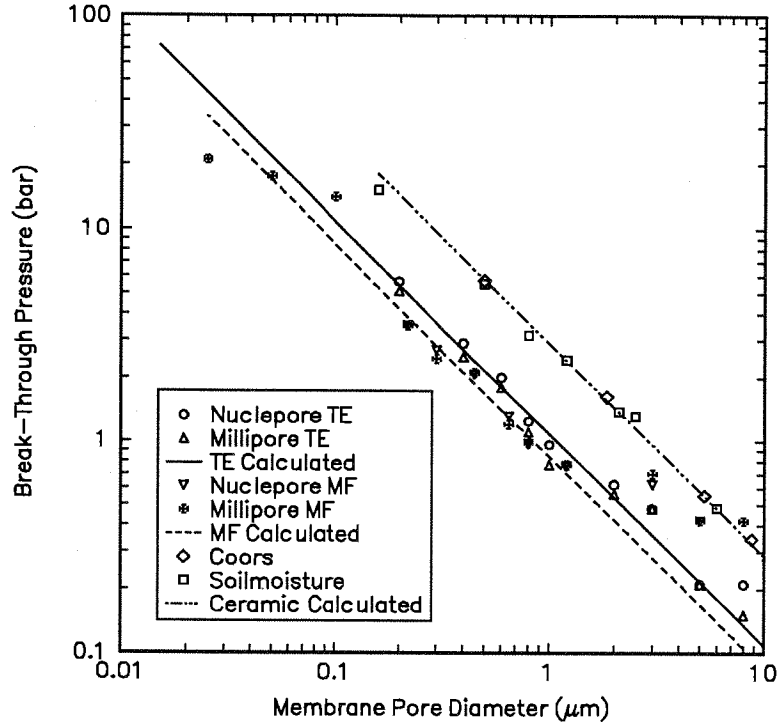

Fig. 3.33 Measured and estimated air-water break-through pressure for cellulosic (MF) and track-etched (TE) membranes, and ceramic plates

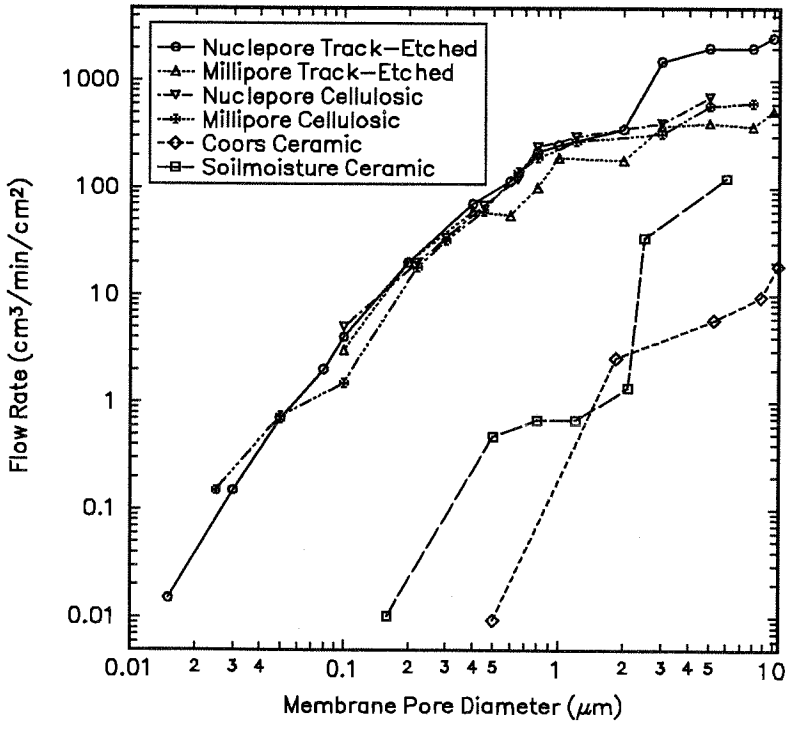

Fig. 3.34 Measured flow rates for cellulosic and track-etched membranes, and porous ceramic plates (μ = 1 cp, Δp = 100 mbar)

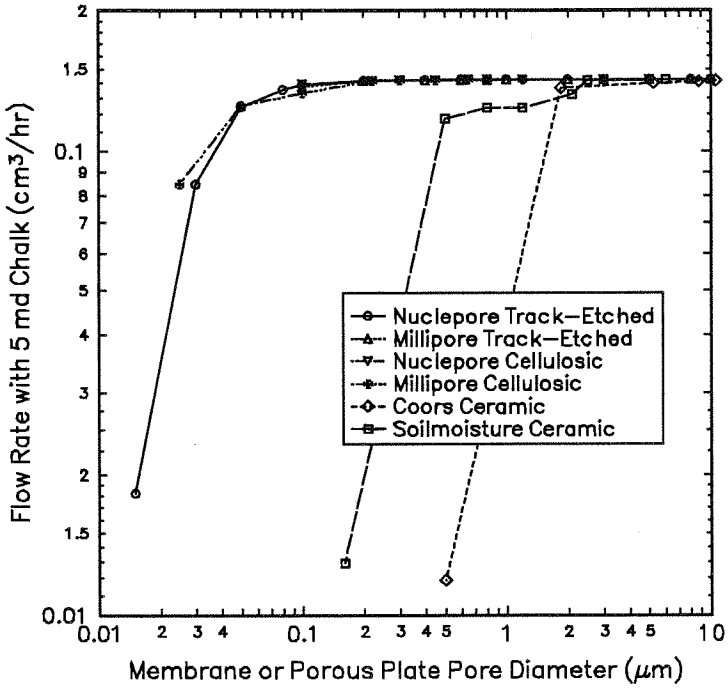

Fig. 3.35 Comparing flow rates for a 5 md chalk core as a function of membrane pore size and porous plate pore size (μ = 1 cp, Δp = 100 mbar, L_c = 2 cm)

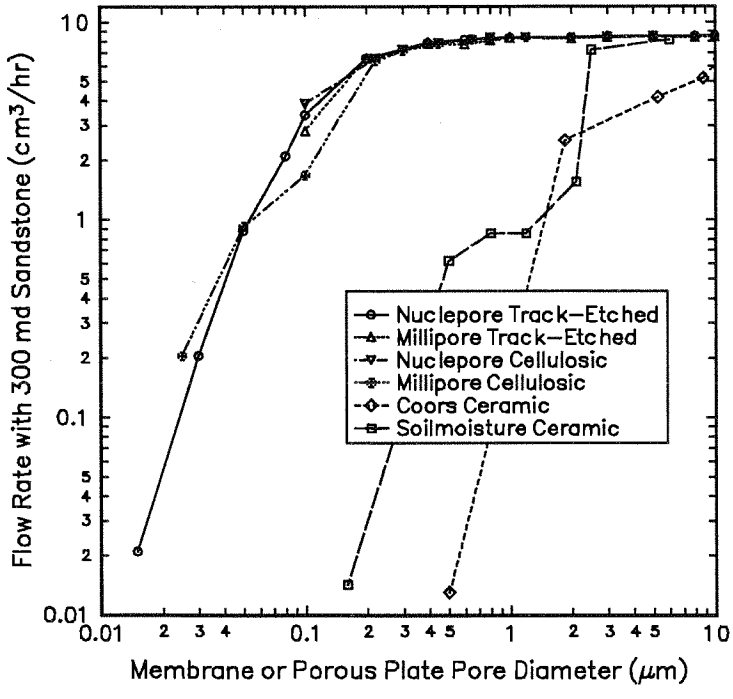

Fig. 3.36 Comparing flow rates for a 300 md sandstone as a function of membrane pore size and porous plate pore size (μ = 1 cp, Δp = 100 mbar, L_c = 2 cm)

Diffusion Problems

A problem when using thin membranes in measuring gas-liquid capillary pressure is the diffusion through the membrane. The rate of diffusion can be approximated by

$$u_A = -(D_{AB})_e \frac{\Delta C_A}{L} \tag{3.39}$$

where

ΔC_A = molar concentration difference of A across membrane, gmol/cm^3
$(D_{AB})_e$ = effective diffusion coefficient in the porous membrane, cm^2/s
u_A = flux of species A per unit area, gmol/(cm^{2}s)
L = membrane thickness, cm

This is valid for a thin membrane where the concentration gradient can be approximated by the concentration difference ΔC divided by the thickness of the membrane L. The effective diffusion coefficient is a function of porosity and tortuosity of the membrane. The diffusion flux will be approximately proportional to the porosity of the membrane and inversely proportional to the membrane thickness. Diffusion rate will decrease as the tortuosity of the membrane increases. Both the porosity and the tortuosity of the cellulosic membranes are much higher than for the track-etched membranes. However, the tortuosity should at most reduce the diffusion flux with a factor of 2.

The diffusion rate through the cellulosic membranes may be smaller than for the track-etched membranes for pore diameters above 0.1 μm. In this range the ratio ϕ/L is smaller for the cellulosic membranes compared with the track-etched membranes. For pore diameters below 0.1 μm, the porosity of the track-etched membranes is significantly reduced, while the porosity of the cellulosic membranes is almost constant. This will reduce the rate of diffusion through the track-etched membranes compared with the cellulosic membranes.

Another difference between the two types of membranes is the direction of diffusion. For the track-etched membranes, molecules can only diffuse vertically through the pores of the membrane and not horizontally inside the membrane. This may be important when using a core holder arrangement as shown in Fig 3.26. Gas outside the core sample has to diffuse horizontally inside the membranes to get through the smaller diameter perforated part of the membrane support plate. Overall diffusion may then be reduced significantly.

Membranes Used in the Experiments

A 6 μm thick Nuclepore polycarbonate track-etched membrane is used as the main membrane in the system. On top of the track-etched membrane is a 105 μm thick Millipore cellulosic MF membrane. A cellulosic membrane was also used below the track-etched membrane, however, this membrane may not be necessary and will only slow down the experiments. All the membranes had a pore diameter of 0.1 μm. The cellulosic membrane on top serves several purposes:

1. Improves capillary contact because it is soft
2. Protects the thin track-etched membrane from the rough core surface
3. Acts as a prefilter to avoid plugging of the track-etched membrane

Use of both track-etched and cellulosic membranes appeared to give a sandwich effect that reduced diffusion by a factor of 10 or more. The pore size of the membrane is selected based on the pore size distribution of the core, and is independent of the IFT of the fluid system. Capillary contact is achieved using a spring that pushes the core directly onto the membranes. The spring force is 2.0 kg on a core area of 11 cm^2 making a contact pressure of 170 mbar.

3.4.3 Experimental Procedure

Clean gloves should be used when handling the core and the membranes. Any trace of fat or grease can change the wetting characteristics, thus altering the break-through pressure of the membrane.

The use of equilibrium gas and oil at high pressure makes the experiments much more difficult to run compared with low-pressure air-oil experiments. This increases the time needed to initialize the experiments. To avoid swelling of the oil, and gas coming out of solution during the experiment, it is important to achieve thermodynamic equilibrium in all parts of the system. Initialization of the system may require several days with circulation and flushing the coreholder with equilibrium oil. Another problem with high-pressure experiments is leaks. Therefore the system must equalize for about 12 hours before starting the experiment to make sure there is no pressure drop. A linear pressure drop indicates a leak and not diffusion.

The following procedure is used to run the experiments:

1. Evacuate all parts of the system and fill some "dead" oil into the containers. Continue to evacuate for some time to remove any air dissolved in the oil. Raise the pressure by injecting gas into the containers and shake the containers to create equilibrium gas and oil. Make sure the valves are shut before shaking the containers to avoid liquid in the lines between the gas pump and the

containers. Repeat gas injection and shaking until the desired pressure is reached. Fill the manual oil pump with equilibrium oil, and the gas pumps with equilibrium gas, by withdrawing fluid from the container. Make sure all the lines are filled with equilibrium oil or gas.

2. Mount the core on top of the membrane, and assemble the core holder.

3. Evacuate the core holder and fill the lower system including the core holder slowly with saturated oil from the manual oil pump. Circulate until all free gas is out of the lower system.

4. Raise the pressure in the lower system 30 to 50 bar above bubblepoint pressure and circulate through the core holder to make sure any trapped gas inside the core is dissolved, and replaced by equilibrium oil. This step is very important, and several hours with circulation at high pressure is required. Lower the pressure slowly using the automatic oil pump while circulating through the coreholder from the top side. Any gas that may be released will accumulate above the core, causing no problems for achieving a 100% oil saturated core.

5. Displace the dead volume surrounding the core by injecting gas into the top of the core holder, displacing the oil through the membrane. Calculate the dead volume based on the volume of the core holder and the core before starting the displacement. Make sure the differential pressure does not exceed the capillary entry pressure of the core during the displacement. Set the first differential pressure below the entry pressure of the core and start the automated oil and gas pumps. Let the system stabilize for 12 hours.

6. Determine the capillary pressure curve by increasing the differential pressure in steps. Make sure the system has stopped producing oil and reached capillary equilibrium before increasing the differential pressure. Continue until gas breaks through the membranes or until the desired capillary pressure is reached.

A more detailed experimental procedure is given in Appendix D. The experimental apparatus is fully automated making it possible to measure a capillary pressure curve unattended after initialization. All the chalk experiments used the same core sample without remounting it, thereby preventing experimental uncertainty by changing core properties, variation in core mounting, and possible leaks.

3.4.4 Problems During the Experiments

Because the differential pressure was extremely temperature dependent, the apparatus had to be redesigned and modified. After installing an accurate temperature controller and two automated high-pressure pumps, the results were both accurate and reproducible.

Millipore cellulosic membranes were used in the beginning, but they were very brittle and easily damaged during the initialization of the experiments. When using track-etched membranes alone, the rough surface of the core pushing the membrane directly down on the perforated steel plate created holes in the membrane. Using a cellulosic membrane on top of the track-etched membrane solved this problem.

The diffusion through the membrane also caused some unexpected problems in calculating the saturation in the core. After using a cellulosic membrane above and below the track-etched membrane, diffusion rate was reduced by a factor of 10 or more.

There were some problems in maintaining capillary contact if the bottom of the core was slightly rounded. The best way to assure a flat and smooth surface was using a fine diamond saw when cutting the cores.

3.5 Core Description and Fluid Properties

A homogenous and well characterized chalk was chosen for the experiments with the same pore size as the Ekofisk chalk. Accurate interfacial tension estimates are essential to check the effect of interfacial tension on the capillary pressure, and a methane - normal-pentane binary system was chosen. High-pressure interfacial tension data is available for this system, and the pressure required to reduce the interfacial tension to values found in the Ekofisk reservoir, is only 150 bar.

This section gives the results of the preliminary study of the Stevens chalk, including porosity and permeability measurements, mercury injection, and low-pressure centrifuge experiments.

3.5.1 Stevens Chalk

The cores were drilled from the Danish chalk outcrop Stevens in the Faxe area from Upper Danian, which is a part of the Ekofisk formation found in the Greater Ekofisk Area fields. The Stevens outcrop has almost no macro fractures and is fairly homogenous in contrast to the heavily fractured Ekofisk formation.

A preliminary study determined the rock properties of the Stevens chalk. The following experiments were conducted:

- Mercury injection
- Helium porosity
- Brine porosity (saturation method)
- Air permeability (Klinkenberg corrected)
- Liquid permeability using brine
- Centrifuge capillary pressure curves (air-brine, air-oil and water-oil)

Eleven 1" and seven 1½" cores were drilled for use in measurements of the properties of the Stevens chalk. Helium porosity and air permeability were measured on all cores, while liquid permeability was measured on three of the 1½" samples. Tables 3.10 and 3.11 give the results.

These results show that the helium porosity ranges from 46.5 to 48.5% with an average of 47.6%. Porosity from the saturation method is lower, with an average of 45.7% for the 1" cores, and 42.6% for the 1½" cores. Short saturation time at atmospheric pressure is probably the reason why the larger cores had lower brine porosities. Air permeability ranged from 4.5 to 6.3 md, the same as measured with brine. Both the 1" and the 1½" cores gave the same average porosity and average air permeability.

The conclusion from these measurements is that the Stevens chalk outcrop used in this study is reasonably homogenous. The composition of the brine used in the experiments is given in Table 3.12.

Table 3.10 Porosity and permeability for the 1" Stevens core samples

1 Inch Core Number	Length (cm)	Helium Porosity (%)	Brine Porosity (%)	Air Permeability (md)
1	4.33	47.6	-	6.3
2	4.14	47.5	46.5	5.1
3	4.01	47.2	45.0	4.8
4	3.96	47.1	-	5.7
5	4.38	47.4	-	4.9
6	4.45	48.5	-	4.5
7	2.57	47.9	45.9	4.8
8	2.73	47.8	45.3	4.7
9	2.72	47.9	46.3	4.8
10	3.82	47.0	45.4	4.8
11	3.29	47.8	-	4.8
Average		47.6	45.7	5.0

Table 3.11 Porosity and permeability for the 1½" Stevens core samples

1½ Inch Core Number	Length (cm)	Helium Porosity (%)	Brine Porosity (%)	Air Permeability (md)	Liquid Permeability (md)
1A	4.19	47.9	42.4	4.6	4.3
2A	4.34	46.5	43.4	5.2	-
3A	4.47	46.8	42.1	Crushed	-
4A	4.55	47.4	-	5.3	5.3
5A	4.13	47.0	-	4.7	-
6A	3.57	46.9	-	5.4	5.7
7A	3.77	46.9	-	5.0	-
Average		47.1	42.6	5.0	5.1

Table 3.12 Synthetic brine composition

Component	ppm
Sodium chloride	38,100
Calcium chloride	4,860
Magnesium chloride	220
Density (g/cm^3 @ 21 °C)	1.0421

3.5.2 Mercury Injection

A Carlo Erba Porosimeter was used for mercury injection on the Stevens outcrop using a pressure up to 200 bar, penetrating pores down to a minimum pore throat diameter of 70 nm. The two samples used for the mercury injection had a bulk volume of 1.0 to 1.5 cm^3, which was the maximum possible for the equipment used. This gives a pore volume of only 0.5 and 0.75 cm^3 which reduces the accuracy of the measurements. Table 3.13 gives a summary of the results. Porosity was measured using another helium porosimeter, with results that were the same as for our measurements.

Table 3.13 Results from mercury injection on the Stevens chalk outcrop

Sample Number	Mass (g)	Sample Density (g/cm^3)	Helium Grain Density (g/cm^3)	Specific Pore Volume (cm^3/g)	Macro Pore Volume* (cm^3/g)	Micro Pore Volume* (cm^3/g)	Helium Porosity (%)
1	2.109	1.43	2.73	0.333	-	-	47.7
2	1.470	1.43	2.73	0.333	0.315	0.018	47.7

* Micropores are pores with diameter less than 10 nm.

The pore size distribution for the two Stevens chalk samples are given in Figs. 3.37 and 3.38. The figures shows that 95% of the pore volume is in pores with a pore throat diameter of less than 1.0 μm, and about 10% of the pore volume is in pores with a pore throat diameter less than 0.2 μm. A contact angle of 140° and an interfacial tension of 480 mN/m were used to calculate the pore diameter. The mean pore diameter was 0.6 μm compared to the rage of 0.4 to 1.0 μm found in Ekofisk. In contrast, the pore sizes of Berea sandstone ranges from 1 to 100 μm as seen in Fig. 3.41.

Sample 1 of the Stevens chalk appears to give a too low irreducible wetting saturation, and therefore the results from sample 2 are used to compare with the other capillary pressure measurements. To avoid too low irreducible wetting phase saturations, the last point measured at a pressure of 200 bar was not included. Fig. 3.39 gives a plot of the capillary pressure curve for sample 2 on logarithmic axes using normalized saturation, and verifies the straight line given by Eq. (3.24). The slope of the straight line gives a pore size distribution index $\lambda = 3.4$ with an irreducible wetting phase saturation $S_{wi} = 0.10$. Fig. 3.40 shows the capillary pressure data together with the Corey curve based on Eq. (3.22). This curve was used to estimate the entry pressure for the centrifuge and high-pressure capillary pressure runs.

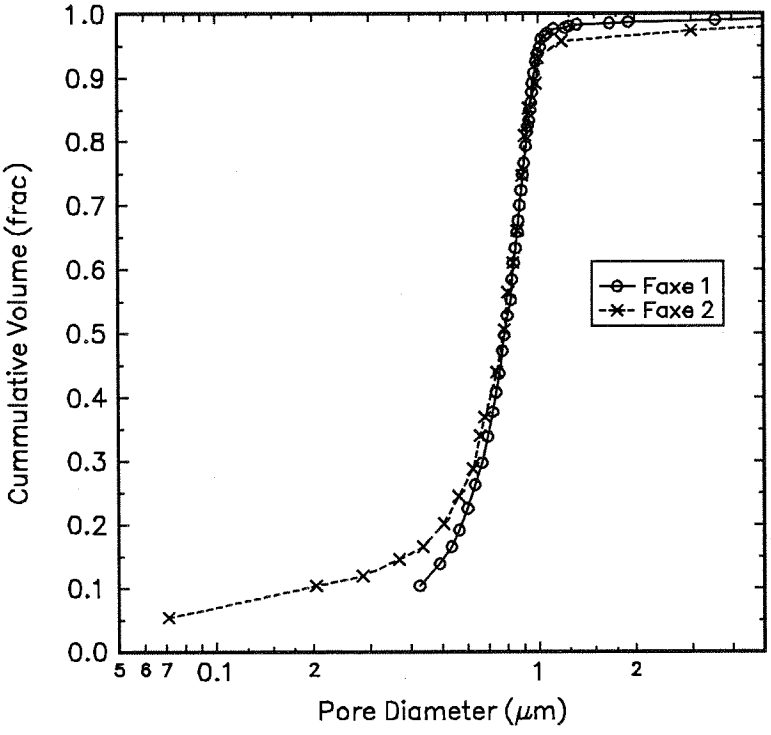

Fig. 3.37 Cumulative pore size distribution from mercury injection on Stevens chalk

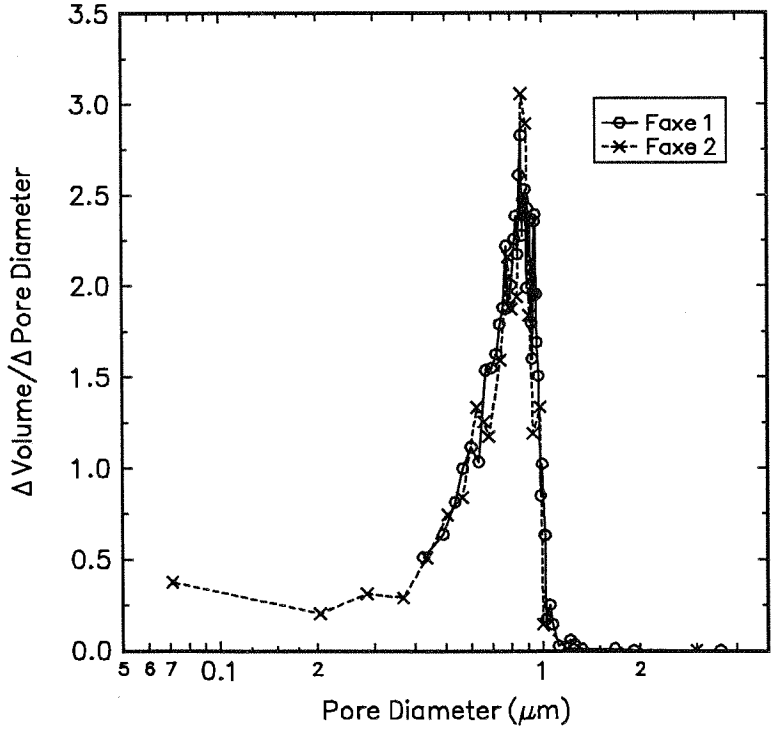

Fig. 3.38 Pore size distribution from mercury injection on Stevens chalk

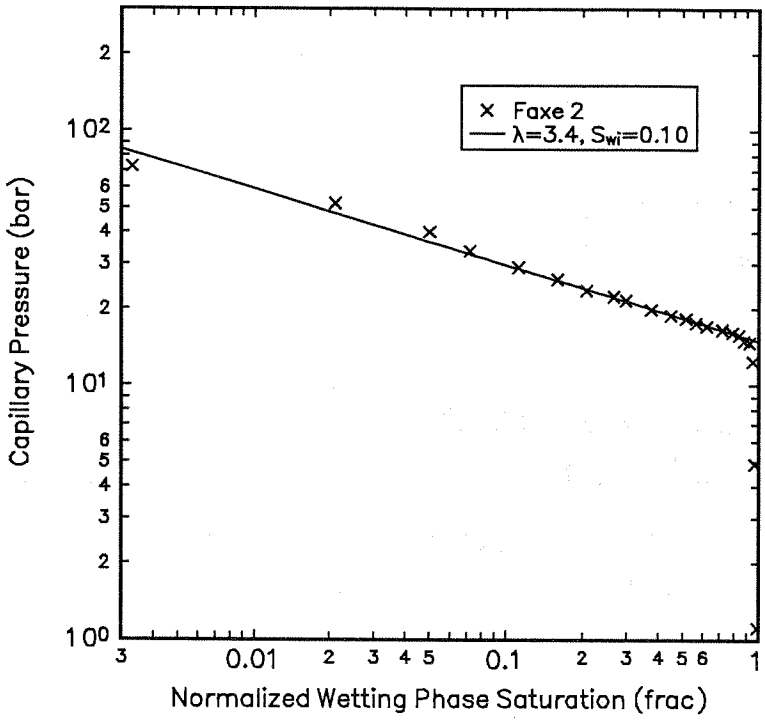

Fig. 3.39 Corey log-log curve fit for mercury injection on Stevens chalk

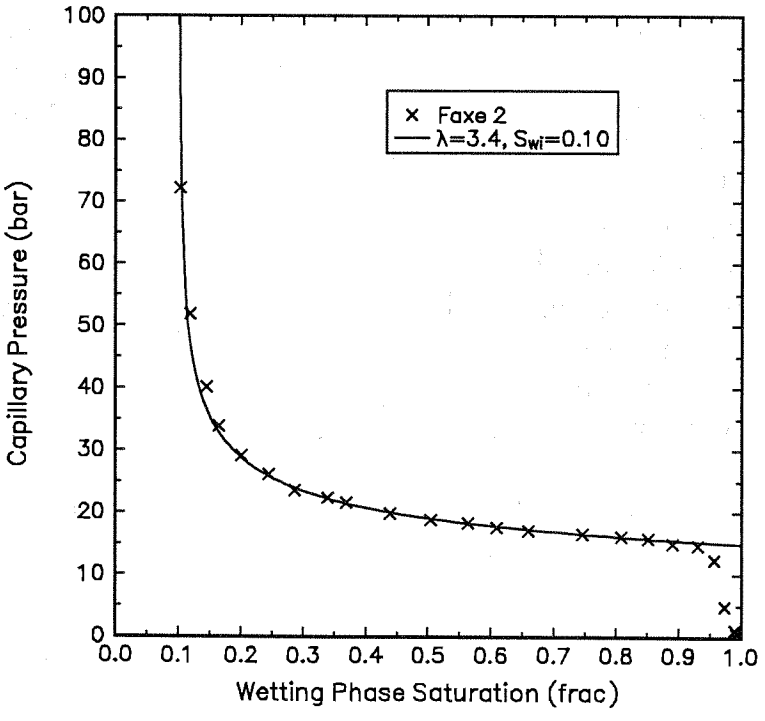

Fig. 3.40 Capillary pressure curve from mercury injection on Stevens chalk with Corey curve

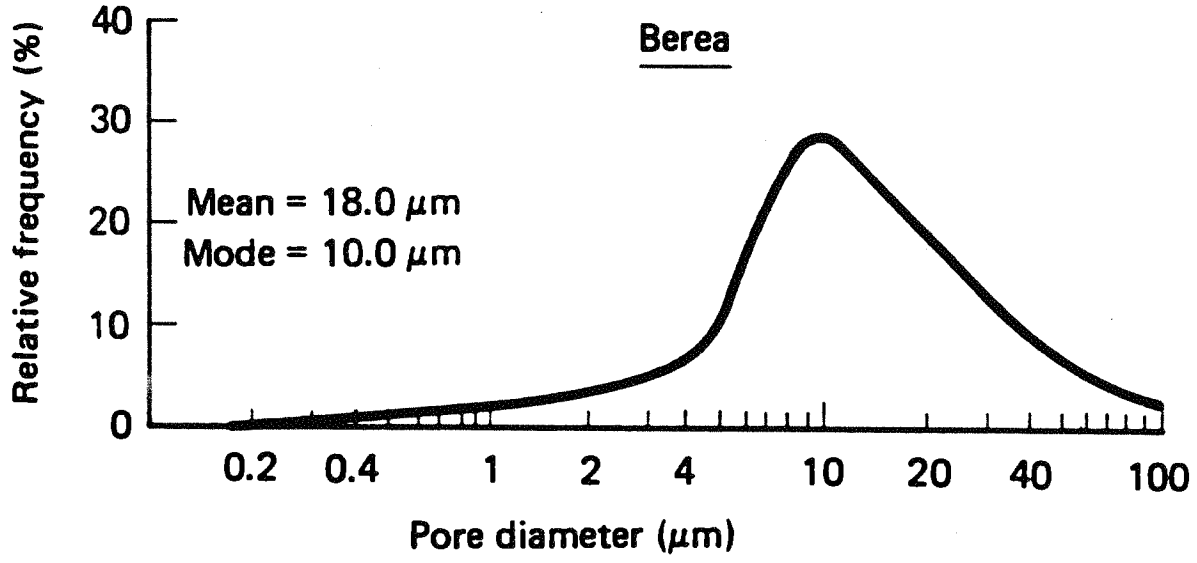

Fig. 3.41 Pore size distribution for a Berea sandstone (Lake, 1989)

3.5.3 Centrifuge Capillary Pressure Curves

Centrifuge experiments using both Berea samples and Stevens chalk samples were run using a Beckman L8M ultracentrifuge. A parameter estimation method was used for interpretation of the centrifuge experiments. The saturation distribution in the core is assumed to follow the Brooks and Corey equation described in Section 3.2.12. The capillary pressure is given directly by the centrifuge speed, the density difference of the fluids, and the radius to each position in the core. The measured liquid volume produced at each centrifuge speed is then matched by the use of parameter estimation. Use of parameter estimation avoids the numerical problems in the Hassler and Brunner related methods. O'Meara, Hirasaki and Rohan (1992) also used the Brooks and Corey equation together with parameter estimation in interpretation of centrifuge experiments. Table 3.14 gives an overview of the experiments including some of the results obtained. The last column gives maximum centrifuge speed (RPM) and shows if epoxy coated core sample was used to force one-dimensional displacement.

Fig. 3.42 shows an example of the match of the produced volume as a function of the centrifuge speed. The capillary pressure distribution and the saturation in the core sample as a function of centrifuge speed is given in Figs. 3.43 and 3.44. Note that at each centrifuge speed the capillary pressure varies from zero at the outer end of the core, and up to the value at the inner end of the core sample. The resulting centrifuge capillary pressure curve is given in Fig. 3.45. The symbols indicate the capillary pressure at the inner end of the core sample for each centrifuge speed.

Table 3.14 Overview of centrifuge experiments on Stevens chalk and Berea sandstone

Sample	System	k (md)	ϕ (%)	IFT (mN/m)	S_{wc} (%)	λ	P_{ce} (bar)	Comments
2A	Air-Oil	5.2	46.5	24	11.0	2.7	1.03	3D, 7000 rpm
5A	Air-Brine	4.9	46.9	72	3.2	2.3	2.55	3D, 7000 rpm
7A	Air-Oil	5.1	46.9	24	12.0	2.2	0.97	3D, 7000 rpm
E09	Oil-Brine	4.9	44.0	25	11.0	1.9	1.24	1D, 9000 rpm
E10	Air-Brine	5.0	43.8	72	3.8	2.4	2.41	1D, 7500 rpm
E23	Air-Oil	4.2	45.3	24	15.0	1.5	0.76	1D, 10000 rpm
E25	Air-Oil	3.5	42.6	24	10.5	1.6	0.90	1D, 10000 rpm
E26	Air-Oil	4.6	47.7	24	18.0	1.9	0.83	1D, 10000 rpm
Berea 1	Air-Ker	313	20.8	24	32.8	0.9	0.033	3D, 5000 rpm
Berea 2	Air-Oil	313	21.0	24	34.1	1.0	0.033	3D, 4000 rpm

Brine = 50,000 ppm Oil = Tor stock tank oil Ker = Kerosene

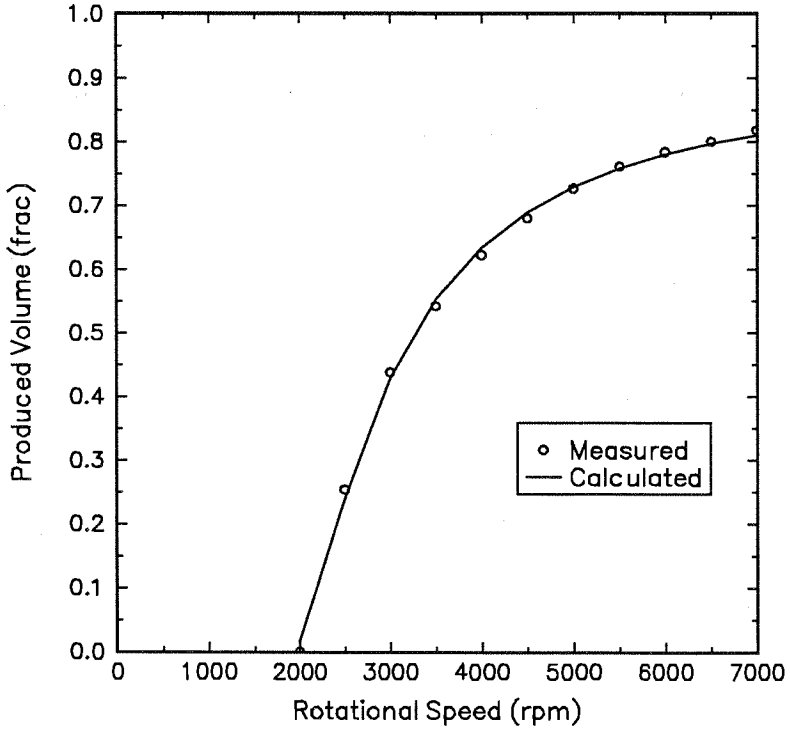

Fig. 3.42 Match of produced volume as a function of centrifuge speed for Stevens chalk sample 2A using air-oil

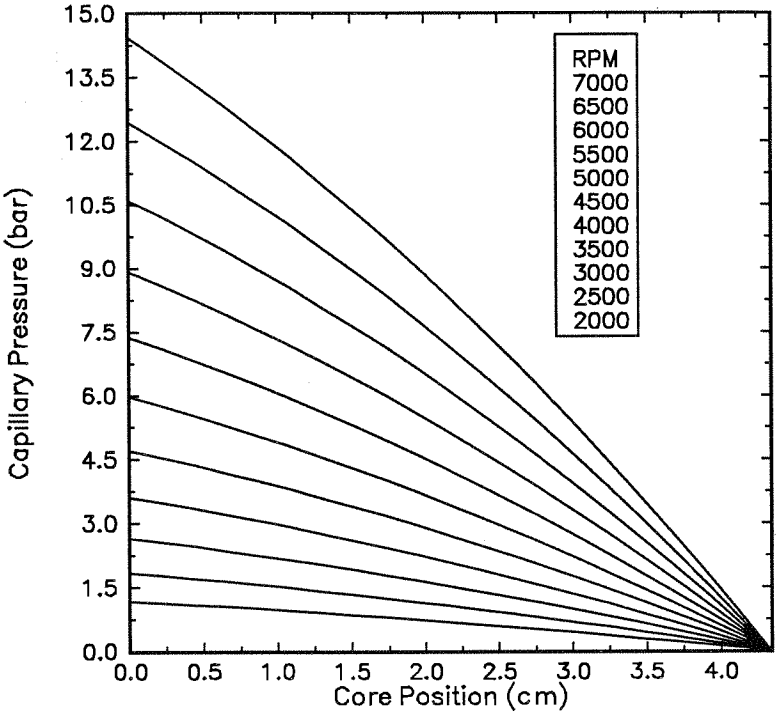

Fig. 3.43 Capillary pressure distribution in the core sample as a function of centrifuge speed for Stevens chalk sample 2A using air-oil

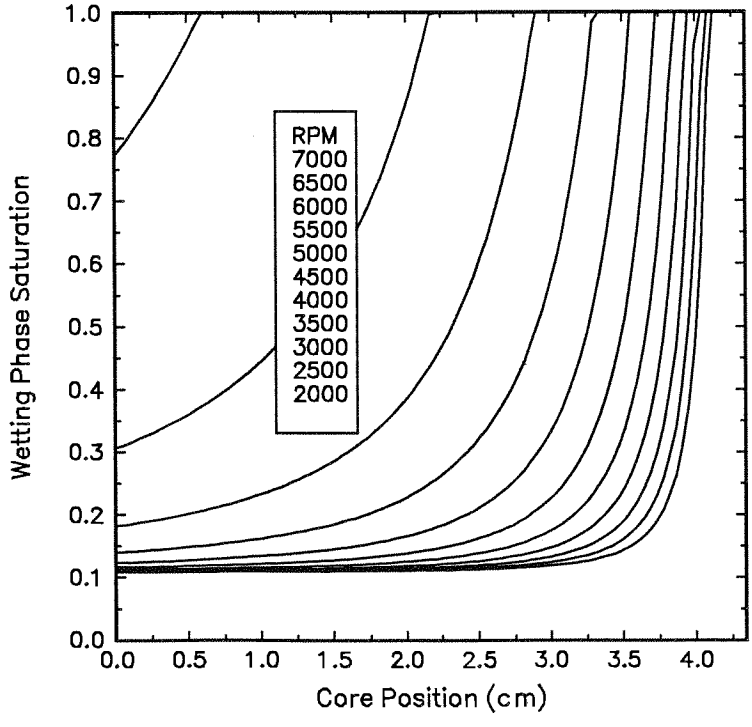

Fig. 3.44 Saturation distribution in the core sample as a function of centrifuge speed for Stevens chalk sample 2A using air-oil

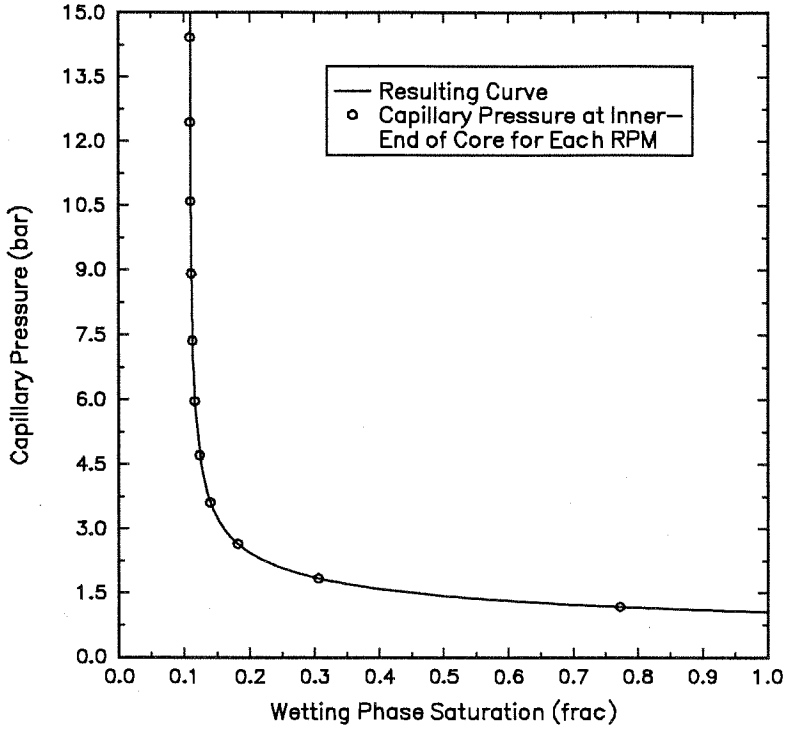

Fig. 3.45 Resulting centrifuge air-oil capillary pressure curve for Stevens chalk sample 2A using parameter estimation

Fig. 3.46 shows all the capillary pressure curves from the air-oil centrifuge experiments. The three experiments E23, E25, and E26 were run with fewer speeds and also a smaller pore volume caused by the epoxy coating. This results in less reliable results. However, the two three-dimensional air-oil capillary pressure curves 2A and 7A almost overlay. Fig. 3.47 shows the capillary pressure from the two air-brine centrifuge experiments. The repeatability is good but the irreducible wetting phase saturation is significantly lower than for the air-oil system. A very low S_{wi} value is often seen in air-brine centrifuge experiments. Fig. 3.48 shows the capillary pressure from the oil-brine experiment. For the oil-brine experiment, the maximum speed of 9000 rpm was too low to obtain a reliable capillary pressure curve.

To compare the centrifuge capillary pressure curves for the Stevens chalk using different fluid systems, the Leverett J-function is plotted in Fig. 3.49. There are some variation in the capillary entry pressure, even if excluding the 1D experiments. Even for these homogenous chalk samples there is a large variation in the centrifuge capillary pressure curves.

The centrifuge capillary pressure curves from the two Berea core samples are given in Fig. 3.50. The curves almost overlay even if light oil (kerosene) was used for the first run and Ekofisk stock-tank oil for the second run. Capillary pressures up to 6.5 bar were used, but the plot is scaled to show the most important part of the curves.

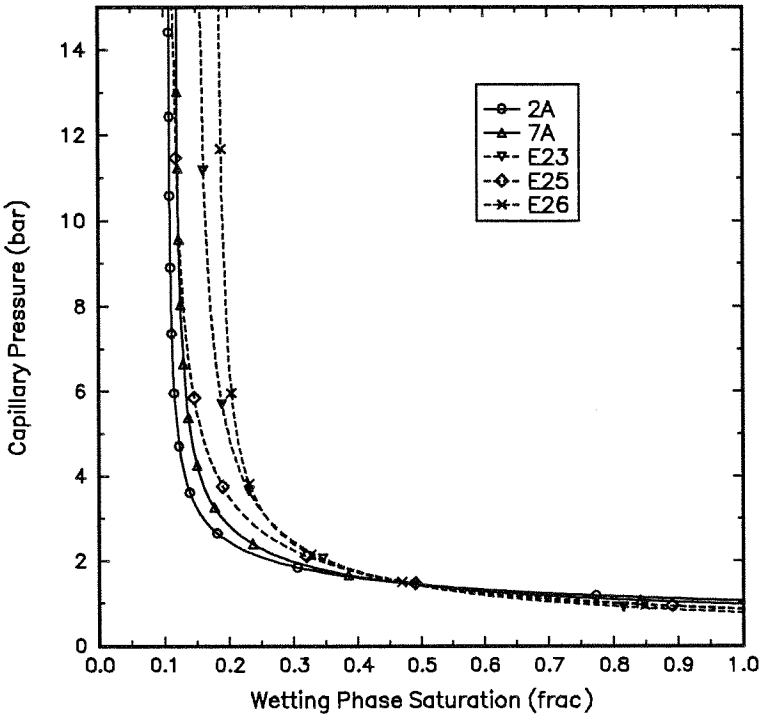

Fig. 3.46 Centrifuge air-oil capillary pressure curves for Stevens chalk samples using parameter estimation. Symbols give P_c at inner end of core for each RPM.

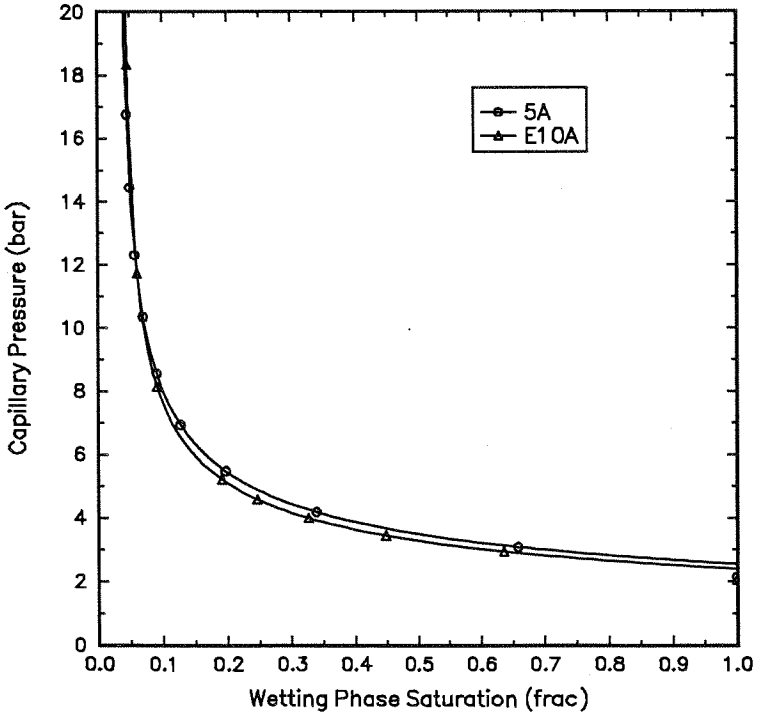

Fig. 3.47 Centrifuge air-brine capillary pressure curves for Stevens chalk using parameter estimation. Symbols give P_c at inner end of core for each RPM.

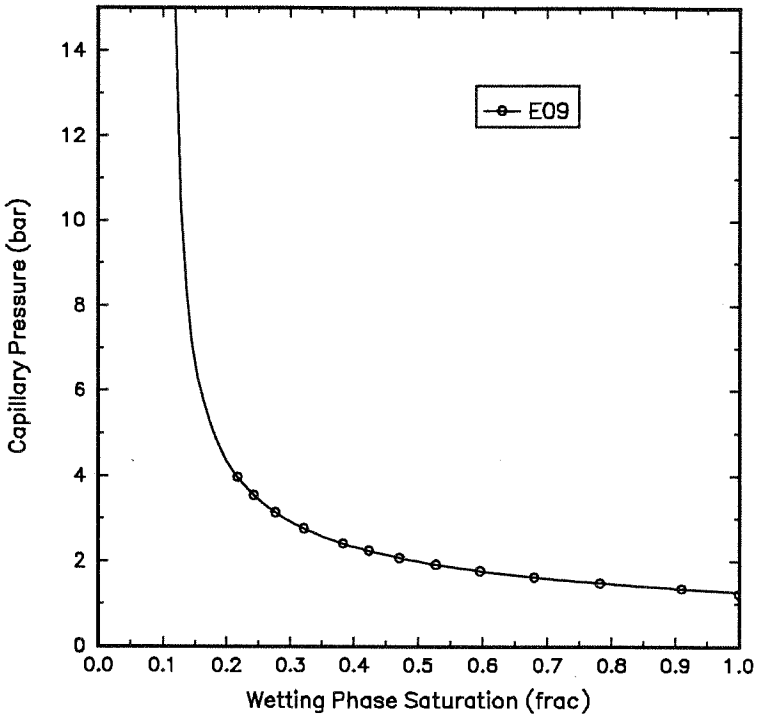

Fig. 3.48 Centrifuge oil-brine capillary pressure curves for Stevens chalk using parameter estimation. Symbols give P_c at inner end of core for each RPM.

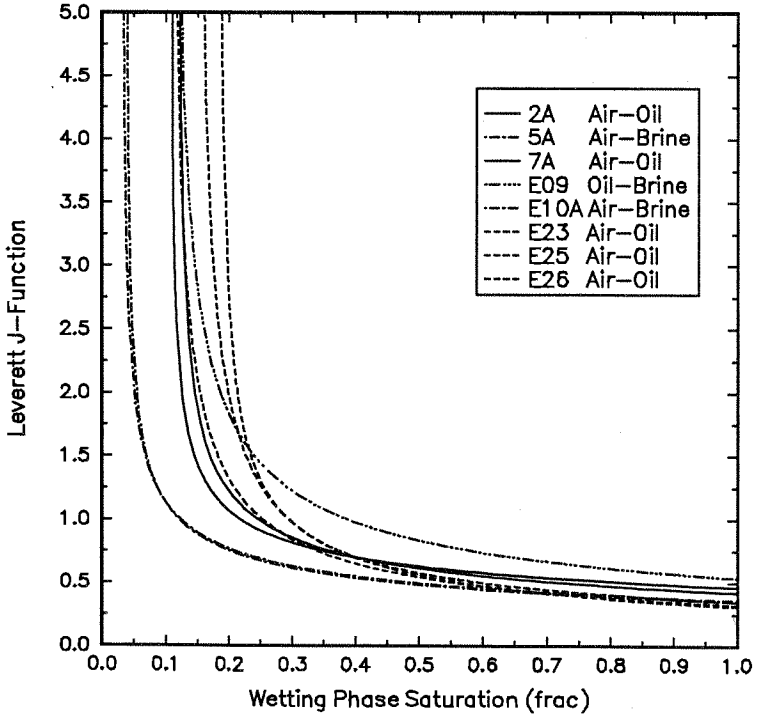

Fig. 3.49 Comparing air-oil, air-brine, and oil-brine P_c curves for Stevens chalk by plotting the Leverett J-function (corrected for IFT, k, and ϕ).

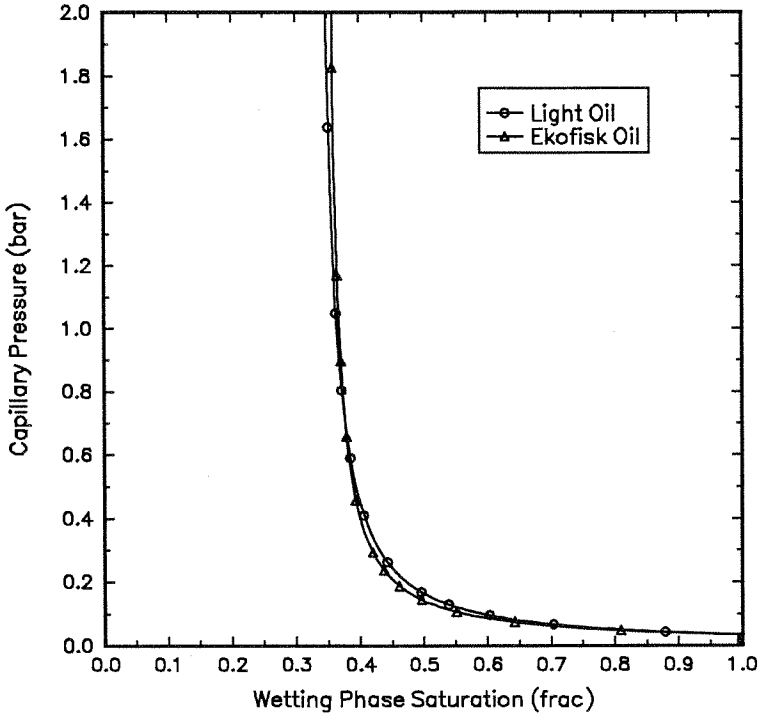

Fig. 3.50 Centrifuge air-oil capillary pressure curves for Berea sandstone using parameter estimation. Symbols give P_c at inner end of core for each RPM.

3.5.4 Interfacial Tensions

Accurate values for the interfacial tension (IFT) are essential for determining the effect of IFT on capillary pressure, and thereby check the validity of the Young-Laplace equation. The most widely used correlation is the Weinaug and Katz extension to the Macleod correlation (Reid, Prausnitz, and Poling, 1987):

$$\sigma_{go}^{1/4} = \sum_{i=1}^{N} P_i \left(x_i \rho_{mo} - y_i \rho_{mg} \right) \tag{3.40}$$

with

x_i = liquid mole fraction of component i
y_i = vapor mole fraction of component i
P_i = parachor for estimating IFT
ρ_m = molar density, gmol/cm^3
σ = interfacial tension, mN/m

This correlation estimates interfacial tension accurately for normal paraffins if the densities and compositions are accurate.

Stegemeier measured the interfacial tension of C_1-nC_5 at high pressures in 1959. These data were the basis for the paper by Hough and Stegemeier (1961), where they modified Eq. (3.40) slightly by using 3/11 as the exponent and modified parachor values. The experimental data that were the basis for this modification are shown in Fig. 3.51, where the interfacial tension is given as a function of pressure and temperature. Fig. 3.52 shows IFT values for both the original and modified Weinaug and Katz correlation together with data from the paper by Hough and Stegemeier. The three values used in our calculations are also shown. The near-critical interfacial tension values for the C_1-nC_5 system reported by Stegemeier have later been verified by other researchers (Willhite, 1986). The interfacial tension values used in our calculations should therefore be accurate to within a few percent.

Viscosities and densities were calculated using a phase behavior program, PVTx (Whitson, 1992), using the Peng-Robinson equation of state including volume translation. The EOS was tuned by regression on the C_1-nC_5 binary interaction parameter using composition and density of the vapor and liquid phases from the NSRDS data book on C_1-nC_5 systems by Berry and Sage (1970). A pressure-composition diagram based on these data is plotted in Fig. 3.53 and shows that the liquid composition is nearly a linear function of pressure. Experimental data reported by several researchers were the basis for their work, so the data should be accurate. Table 3.15 gives calculated PVT data together with interfacial tension values used in our study.

For the air-brine, air-oil and brine-oil systems used in the centrifuge experiments, the interfacial tension was measured using a Krüss ring tensiometer. The measured values shown in Table 3.16 were used when comparing the low-pressure centrifuge capillary pressure curves with the high-pressure measurements.

Table 3.15 Interfacial tension, compositions, viscosities and densities for each pressure at 24°C

Pressure (bara)	Interfacial Tension* (mN/m)	Gas C_1 (mol%)	Oil C_1 (mol%)	Gas Viscosity** (cp)	Oil Viscosity** (cp)	Gas Density** (kg/m3)	Oil Density** (kg/m3)
70.0	6.3	96.77	32.87	0.013	0.11	60	548
105.7	3.2	95.81	47.07	0.015	0.09	101	502
130.0	1.5	94.49	56.25	0.017	0.07	136	465

* IFT data from interpolation in Hough and Stegemeier (1961) chart.
** Used PVTx with Peng-Robinson 79 including volume translation tuned on data from the NSRDS data book by Berry and Sage (1970) using C_1-C_5 BIPS = 0.024.

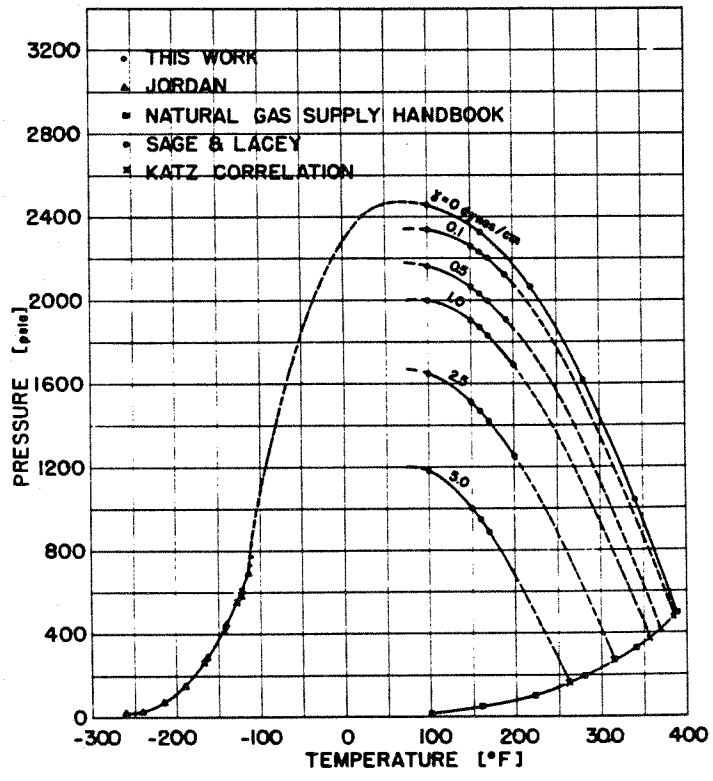

Fig. 3.51 Experimental interfacial tension data for C_1-nC_5 (Hough and Stegemeier, 1961)

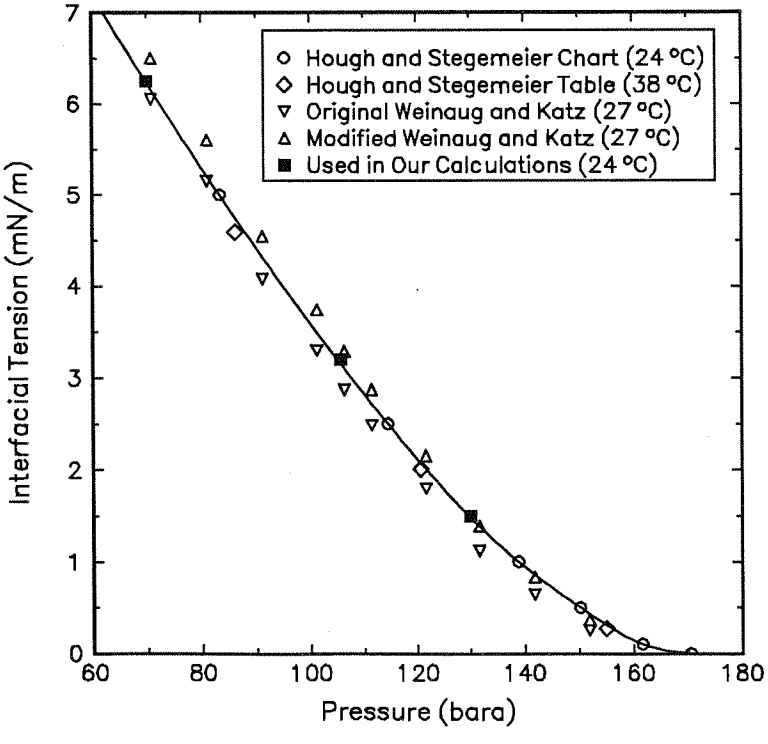

Fig. 3.52 IFT data for the C_1-nC_5 system

Table 3.16 Measured interfacial tensions at 20°C

Fluid System	IFT (mN/m)
Air - Brine	74
Air - Oil	24
Brine - Oil	25
Oil = Tor stock-tank oil (well 2/4 E-12)	

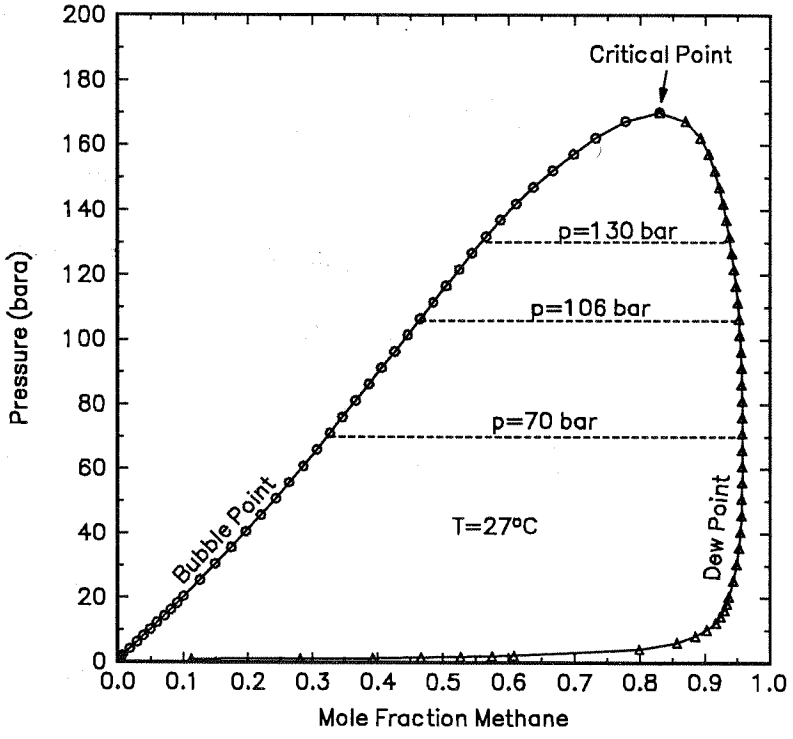

Fig. 3.53 Pressure-composition diagram for the C_1-nC_5 system (Berry and Sage, 1970)

3.6 Data and Results

3.6.1 Low-Pressure Centrifuge Experiments

A Beckman L8M automated centrifuge was used to measure capillary pressure curves for air-oil, air-water and water-oil at ambient conditions. Details about these experiments were given in Section 3.5.3. The two 3D air-oil experiments using the Stevens chalk and the two experiments using Berea sandstone will be used to compare the low-pressure centrifuge experiments with the high-pressure membrane experiments. Tor stock-tank oil (STO) from the Ekofisk area was used in all experiments except for the first Berea sample where kerosene was used. No epoxy coating or sleeve was used to cover the outside of the cores. The centrifuge data were interpreted with a method which uses parameter estimation to avoid the problems related to numerical derivatives. This method is described by O'Meara, Hirasaki and Rohan (1992) and is not influenced by fluctuations in the produced liquid volume readings in centrifuge runs. The Corey equation, Eq. (3.22), was used as the model equation in the interpretation method.

Table 3.17 gives the permeability and porosity for the selected centrifuge core samples together with the calculated Corey pore size distribution index, the irreducible wetting phase saturation, and the entry pressure. This table shows about the same pore size distribution index determined from low- and high-pressure experiments for both the Stevens chalk and the Berea sandstone cores.

Table 3.17 Measured and calculated data for the centrifuge experiments

Run	Permeability (md)	Porosity (%)	Corey Pore Size Distribution Index λ	Irreducible Saturation S_{Wi} (%)	Entry Pressure p_{ce} (mbar)
Stevens 2A	5.2	46.5	2.7	11.0	1034
Stevens 7A	5.1	46.9	2.2	12.0	966
Berea 1	313	20.8	0.9	32.8	33
Berea 2	313	21.0	1.0	34.1	33

3.6.2 High-Pressure Capillary Pressure Experiments

Both Berea sandstone and Stevens chalk samples were used in the high-pressure experiments. Table 3.18 gives an overview of the high-pressure membrane capillary pressure experiments performed at 24 °C with a binary system of C_1 (99.5% purity) and nC_5 (99% purity).

Table 3.18 Overview of high pressure capillary pressure experiments

Number of Experiments	Core Sample	Permeability (md)	Pressure (bara)	IFT (mN/m)
1	Berea Sandstone	300	105	3.2
1	Stevens Chalk	5	70	6.3
2	Stevens Chalk	5	105	3.2
2	Stevens Chalk	5	130	1.5

Berea Sandstone

One run was performed using a 1½" diameter 313 md Berea sandstone with epoxy coating at 105 bara with IFT = 3.2 mN/m. The epoxy coating was used to eliminate diffusion in the annulus by forcing one dimensional flow through the core sample. The only problem was keeping the differential pressure constant in the range of 0 to 50 mbar; the apparatus was designed to run 0 to 1000 mbar with an accuracy of ± 5 mbar. Few data points and fluctuations in the differential pressure make this run less accurate than for the chalk samples. The main purpose of this run was to test the apparatus and calculation procedure.

Fig. 3.54 gives the Corey log-log plot of the data from the Berea sandstone, and Fig. 3.55 gives the capillary pressure curve with the Corey curve. This match gave a pore size distribution index $\lambda = 1.6$ with an irreducible wetting phase saturation $S_{wi} = 0.37$.

Stevens Chalk

Five runs were performed using a 1½" diameter 5 md Stevens chalk sample with no epoxy coating. Pressures of 70, 105.6, and 130 bar were used, giving interfacial tensions of 6.3, 3.2, and 1.5 mN/m, respectively. The core sample data are: $l = 2.12$ cm, $d = 3.78$ cm, $\phi = 48\%$, $k \approx 5$ md, $V_{pore} = 11.42$ cm^3. All runs used the same core plug, without remounting the core for each new experiment. The core was evacuated and resaturated for each new experiment, thereby minimizing the change in conditions between each experiment. The two experiments at 105 and 130 bar had excellent repeatability. Only one run was performed at 70 bar.

A log-log plot of the capillary pressure curve for the Stevens chalk with C_1-nC_5 at 70 bar and IFT = 6.3 mN/m is given in Fig. 3.56, and the Corey curve together with the measured data are shown in Fig. 3.57. This gave a pore size distribution index $\lambda = 2.1$ and an irreducible wetting phase saturation $S_{wi} = 0.11$. The measured points give a good match of the Corey curve. Table 3.19 gives the measured and calculated data, including diffusion rates, time run at each differential pressure, and the time before a stable production/diffusion was reached.

The results of the two experiments at 105 bar and IFT = 3.2 mN/m are shown in Figs. 3.58 and 3.59. The Corey curve gave a pore size distribution index $\lambda = 2.0$ and $S_{wi} = 0.11$. For the last two points in the first experiment, the differential pressure was increased too early, and the saturation was therefore slightly higher than for the second experiment. The rest of the measured points show very good repeatability, and the Corey curve matches all parts of the capillary pressure curve. Tables 3.20 and 3.21 give detailed results.

The results from the capillary pressure experiment for the Stevens chalk with C_1-nC_5 at 130 bar is given as a log-log plot in Fig. 3.60, together with the Corey curve in Fig. 3.61. The logarithmic plot gave a straight line with $\lambda = 1.7$ and $S_{wi} = 0.11$. These two runs also show excellent repeatability, confirming the high accuracy of the high-pressure capillary pressure apparatus. The data does not, however, match the Corey curve at high wetting phase saturations. Tables 3.22 and 3.23 give the details.

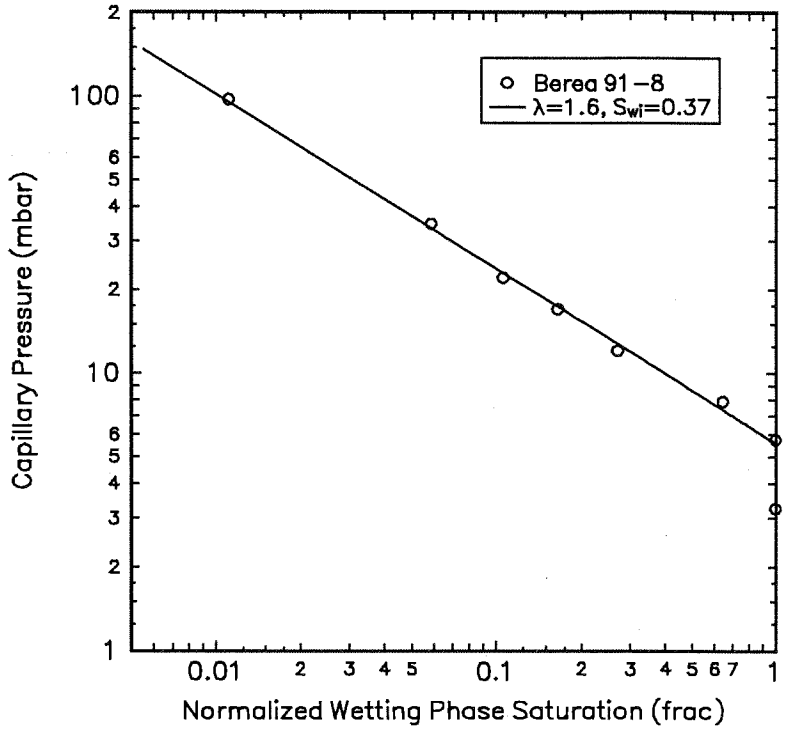

Fig. 3.54 Corey log-log curve fit for Berea sandstone at 105 bara (IFT = 3.2 mN/m)

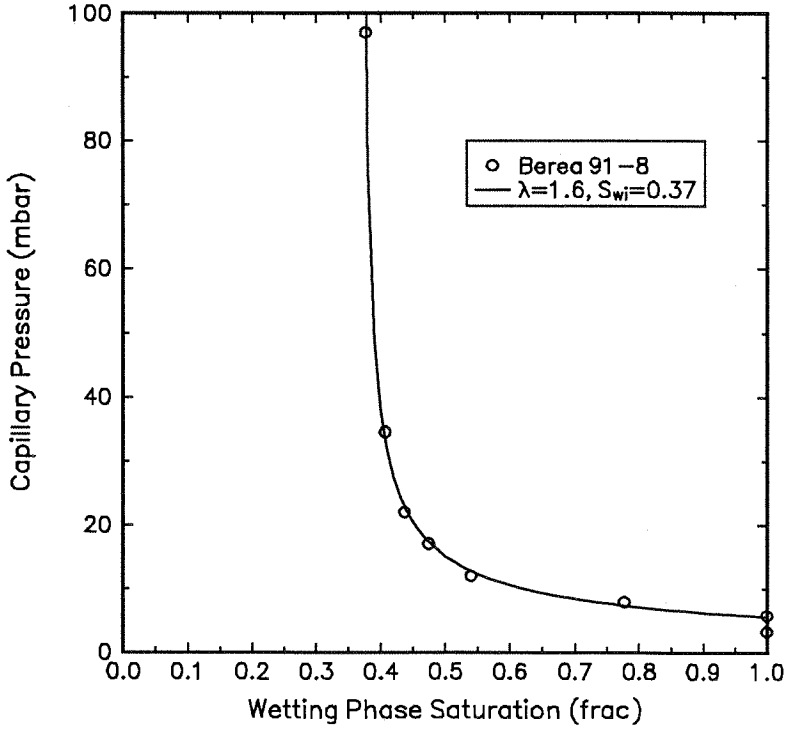

Fig. 3.55 Capillary pressure curve for Berea sandstone at 105 bara with Corey curve (IFT=3.2 mN/m)

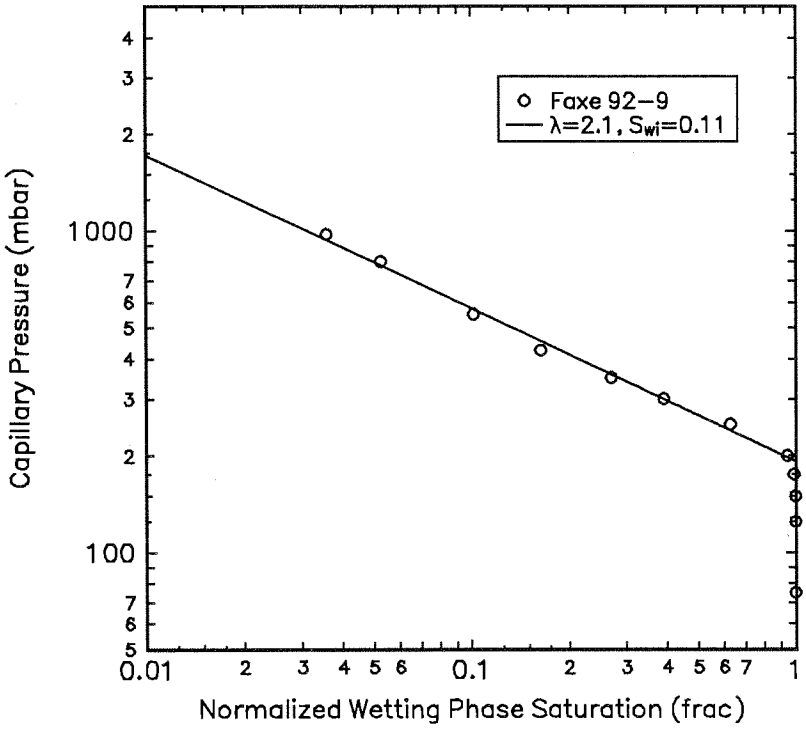

Fig. 3.56 Corey log-log curve fit for Stevens chalk at 70 bara (IFT = 6.3 mN/m)

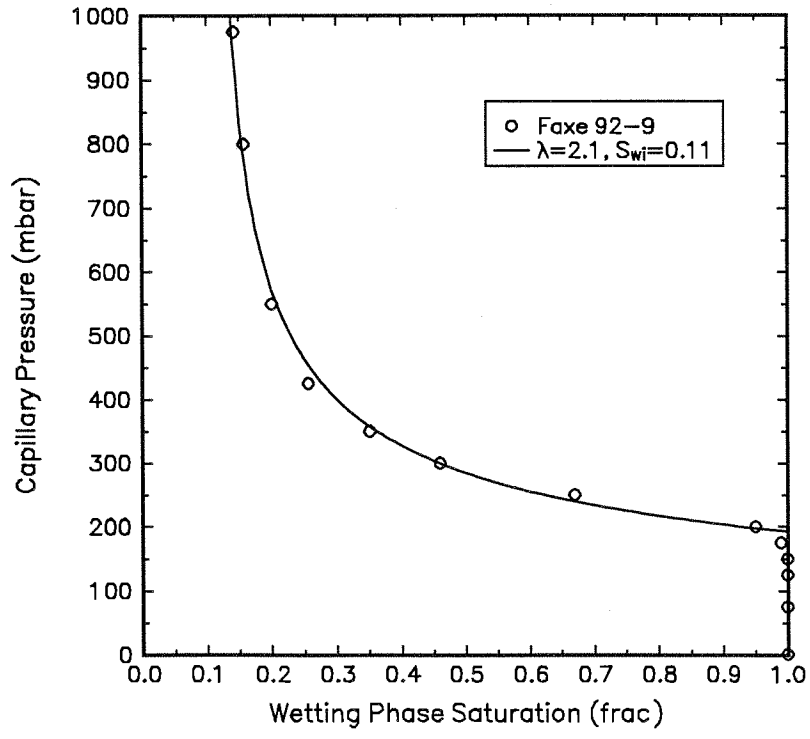

Fig. 3.57 Capillary pressure curve for Stevens chalk at 70 bara with Corey curve (IFT = 6.3 mN/m)

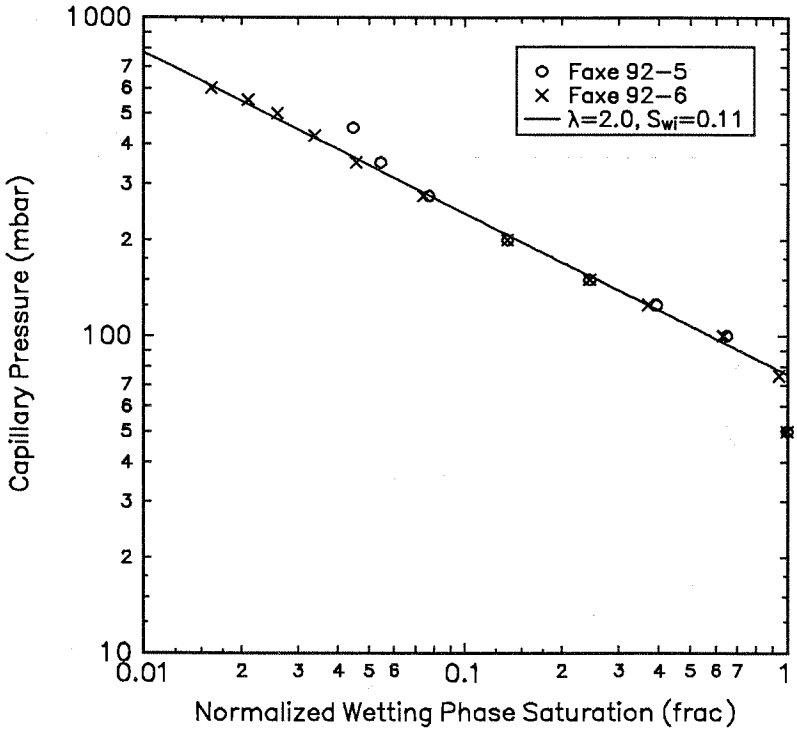

Fig. 3.58 Corey log-log curve fit for Stevens chalk at 105 bara (IFT = 3.2 mN/m)

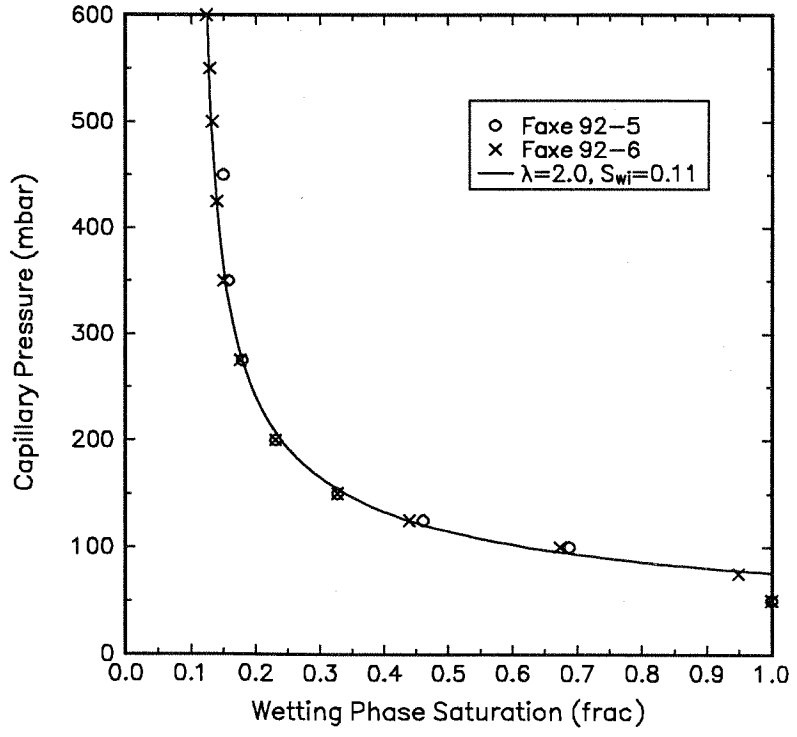

Fig. 3.59 Capillary pressure curve for Stevens chalk at 105 bara with Corey curve (IFT = 3.2 mN/m)

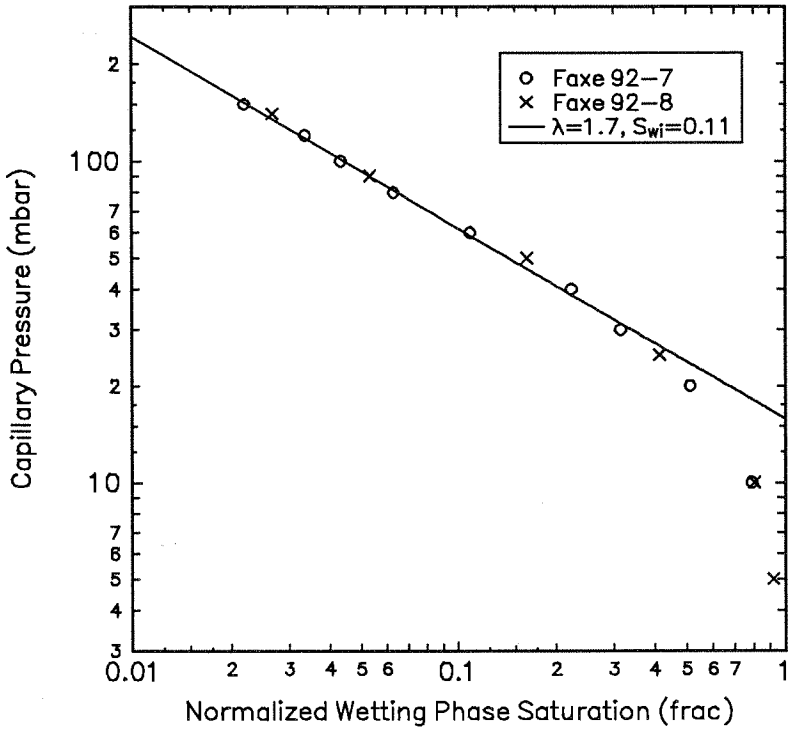

Fig. 3.60 Corey log-log curve fit for Stevens chalk at 130 bara (IFT = 1.5 mN/m)

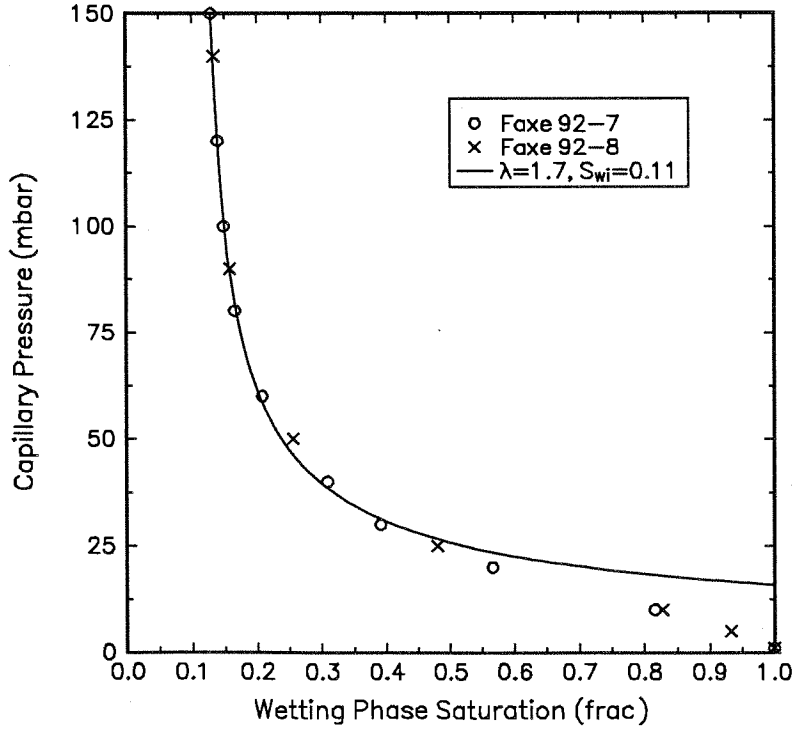

Fig. 3.61 Capillary pressure curve for Stevens chalk at 130 bara with Corey curve (IFT = 1.5 mN/m)

Table 3.19 Capillary pressure data for the 5 md Stevens chalk run 92-9 at 70 bar, IFT = 6.3 mN/m

Δp (mbar)	t_{run} (hr)	t_{stable} (hr)	q_{diff} (cm^3/hr)	ΔV_{diff} (cm^3)	V_{prod} (cm^3)	S_o (frac.)
75	53	30	0.008	0.000	0.00	1.000
125	34	1	0.009	0.000	0.00	1.000
150	24	1	0.012	0.000	0.00	1.000
175	30	2	0.013	0.390	0.11	0.990
200	52	15	0.013	0.676	0.56	0.951
250	37	15	0.015	0.555	3.77	0.670
300	47	30	0.018	0.846	6.17	0.460
350	49	30	0.022	1.078	7.41	0.351
425	51	30	0.027	1.377	8.50	0.256
550	44	30	0.034	1.496	9.13	0.200
800	38	30	0.048	1.824	9.63	0.157
975	25		0.065	1.625	9.80	0.142
Total	484	214		9.867		

Table 3.20 Capillary pressure data for the 5 md Stevens chalk run 92-5, 105.7 bar, IFT = 3.2 mN/m

Δp (mbar)	t_{run} (hr)	t_{stable} (hr)	q_{diff} (cm^3/hr)	ΔV_{diff} (cm^3)	V_{prod} (cm^3)	S_o (frac.)
50	18	14	0.0100	0.000	0.00	1.000
100	20	18	0.0060	0.120	3.56	0.688
125	14	16	0.0060	0.084	6.16	0.461
150	26	23	0.0060	0.156	7.68	0.327
200	34	30	0.0060	0.204	8.78	0.231
275	30	24	0.0070	0.210	9.38	0.179
350	27	22	0.0050	0.135	9.61	0.158
450	19	10	0.0090	0.171	9.71	0.150
Total	188	157		1.080		

Table 3.21 Capillary pressure data for the 5 md Stevens chalk run 92-6, 105.7 bar, IFT = 3.2 mN/m

Δp (mbar)	t_{run} (hr)	t_{stable} (hr)	q_{diff} (cm^3/hr)	ΔV_{diff} (cm^3)	V_{prod} (cm^3)	S_o (frac.)
50	37	20	0.0060	0.000	0.00	1.000
75	25	15	0.0028	0.075	0.58	0.949
100	35	25	0.0030	0.105	3.72	0.674
125	37	30	0.0020	0.074	6.40	0.440
150	38	35	0.0024	0.076	7.68	0.327
200	48	40	0.0022	0.144	8.78	0.231
275	58	45	0.0020	0.116	9.41	0.176
350	53	40	0.0011	0.053	9.70	0.151
425	48	30	0.0018	0.096	9.82	0.140
500	46	25	0.0012	0.046	9.90	0.133
550	38	20	0.0010	0.038	9.95	0.129
600	34	10	0.0008	0.034	10.00	0.124
Total	497	335		0.839		

Table 3.22 Capillary pressure data for the 5 md Stevens chalk run 92-7 at 130 bar, IFT = 1.5 mN/m

Δp (mbar)	t_{run} (hr)	t_{stable} (hr)	q_{diff} (cm^3/hr)	ΔV_{diff} (cm^3)	V_{prod} (cm^3)	S_o (frac.)
0				0.000	0.00	1.000
10	48	30	0.0051	0.240	2.10	0.816
20	47	30	0.0028	0.132	4.95	0.567
30	56	38	0.0013	0.073	6.95	0.391
40	44	30	0.0011	0.048	7.89	0.309
60	67	50	0.0011	0.074	9.05	0.208
80	76	50	0.0007	0.053	9.52	0.166
100	74	48	0.0000	0.046	9.72	0.149
120	97	40	0.0000	0.041	9.82	0.140
150	48	30	0.0003	0.014	9.94	0.130
Total	557	346		0.639		

Table 3.23 Capillary pressure data for the 5 md Stevens chalk run 92-8 at 130 bar, IFT = 1.5 mN/m

Δp (mbar)	t_{run} (hr)	t_{stable} (hr)	q_{diff} (cm^3/hr)	ΔV_{diff} (cm^3)	V_{prod} (cm^3)	S_o (frac.)
0				0.000	0.00	1.000
5	60	35	0.0031	0.186	0.77	0.933
10	45	30	0.0030	0.135	1.96	0.828
25	72	50	0.0002	0.014	5.94	0.480
50	62	60	0.0000	0.000	8.50	0.256
90	110	70	0.0001	0.011	9.62	0.158
140	90	30	0.0140	1.260	9.89	0.134
Total	439	275		1.606		

The diffusion rate was measured at each differential pressure for all experiments. Diffusion rate was determined by plotting the produced oil volume vs. time, and measuring the slope after a constant rate was reached. The first four experiments (run 92-5 to 8) had a very low diffusion rate that was independent of the differential pressure. The total volume of diffusion during each experiment was about 10% of the total volume of oil produced. For some of the experiments, the diffusion rate decreased with increasing differential pressure. The diffusion rate was about 0.007 cm^3/hr for the first experiment at 105 bara and about 0.002 cm^3/hr for the second experiment. For the two experiments at 130 bara, the diffusion rates were less than 0.005 cm^3/hr and decreased significantly with increasing differential pressure. Fig. 3.62 compares the diffusion rates for the four experiments at 105 and 130 bara (run 92-5 to 8). Due to different initialization procedures, the diffusion rate through the membrane was significantly higher during the experiment at 70 bar (0.01 to 0.07 cm^3/hr), which may reduce the accuracy slightly. For all experiments the volume of oil produced was corrected for the diffusion rate. The diffusion rate was assumed constant at each differential pressure step. This appeared to be a valid assumption based on earlier experiments using only a membrane (no core).

The diffusion coefficients for the C_1-nC_5 system used in the experiments were estimated using the Sigmund correlation together with the data in Table 3.15, and were 1.04, 1.01, and 1.06 × 10^{-4} cm^3/s for pressures of 70, 105.7 and 130 bar, respectively. The diffusion rate should therefore be reduced as the pressure is increased and the differential pressure reduced (see Section 3.4.2 for diffusion through membranes). The lower concentration gradient across the membrane at higher pressures and lower differential pressures will also reduce the diffusion rate.

Fig. 3.63 gives an example of produced volume vs. time for run 92-8 at Δp = 10 mbar (p = 130 bar, IFT = 1.5 mN/m). Estimated diffusion rate was 0.0030 cm^3/hr and the produced oil volume corrected for diffusion is also included in the plot. The

differential pressure is also given and it is slightly lower than 10 mbar for the first 10 hours before the production slows down. The variation in the differential pressure is less than ± 0.2 mbar which is very good taking into account the absolute pressure of 130 bar. This represents a variation in absolute pressure of less than 0.0002% between the oil and gas side of the apparatus.

After increasing the differential pressure to 25 mbar, the diffusion rate decreased to 0.0002 cm^3/hr as shown in Fig. 3.64. The differential pressure varied slightly more at this step and was about 24 mbar for the first 15 hours when the production rate was high. A semilog plot of the produced volume vs. time at 25 mbar is given in Fig. 3.65. High sampling rate gives a smooth production curve also in the beginning of each differential pressure step.

A complete plot of produced volume vs. time for run 92-6 (p = 105 bar, IFT = 3.2 mN/m) is given in Fig. 3.66. Differential pressure vs. time is also included. The produced volume is not corrected for diffusion rate, and therefore, the slope of the curve at the end of each differential pressure is not zero. This, combined with the large time scale, may give the impression that equilibrium is not reached at each differential pressure.

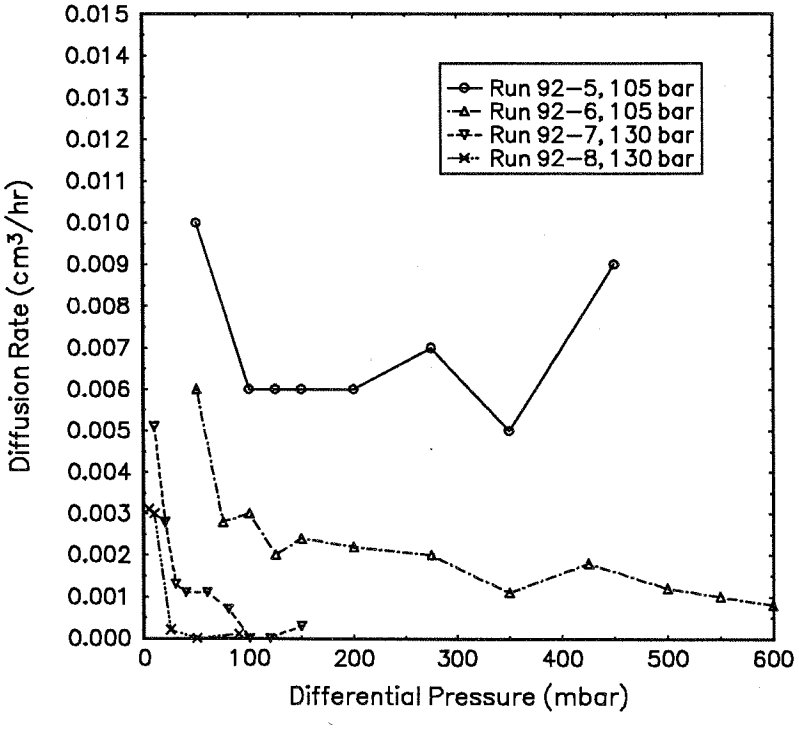

Fig. 3.62 Diffusion rates as a function of differential pressure for run 92-5 to 8

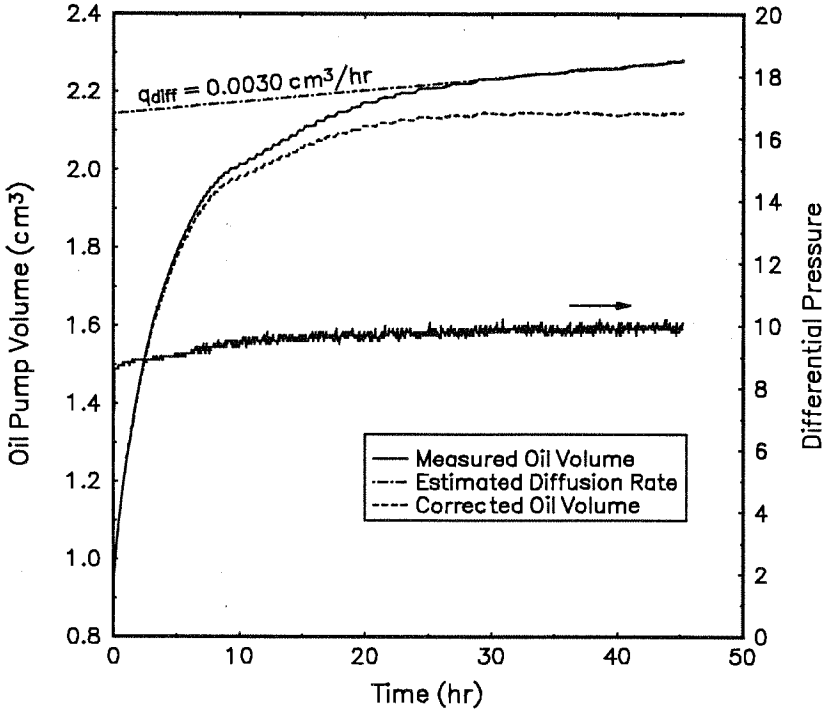

Fig. 3.63 Example of produced oil volume vs. time for run 92-8 at Δp = 10 mbar (p = 130 bar and IFT = 1.5 mN/m)

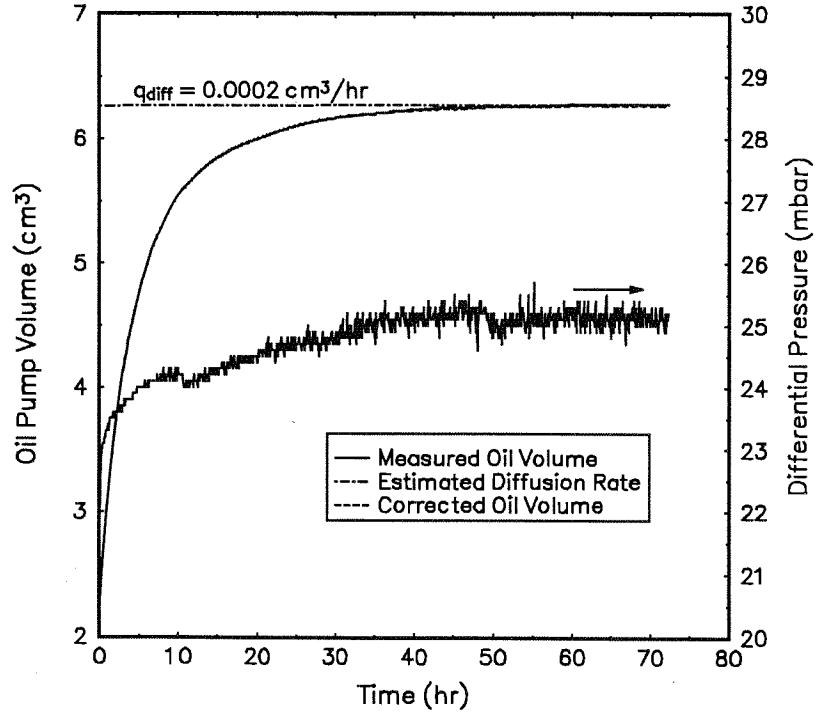

Fig. 3.64 Example of produced oil volume vs. time for run 92-8 at Δp = 25 mbar (p = 130 bar and IFT = 1.5 mN/m)

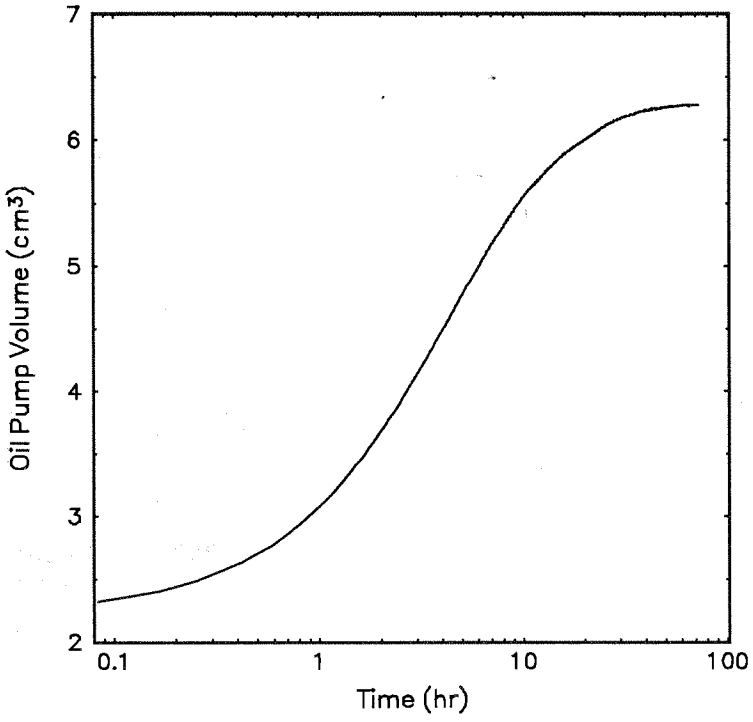

Fig. 3.65 A semilog plot of produced oil volume vs. time for run 92-8 at Δp = 25 mbar (p = 130 bar and IFT = 1.5 mN/m)

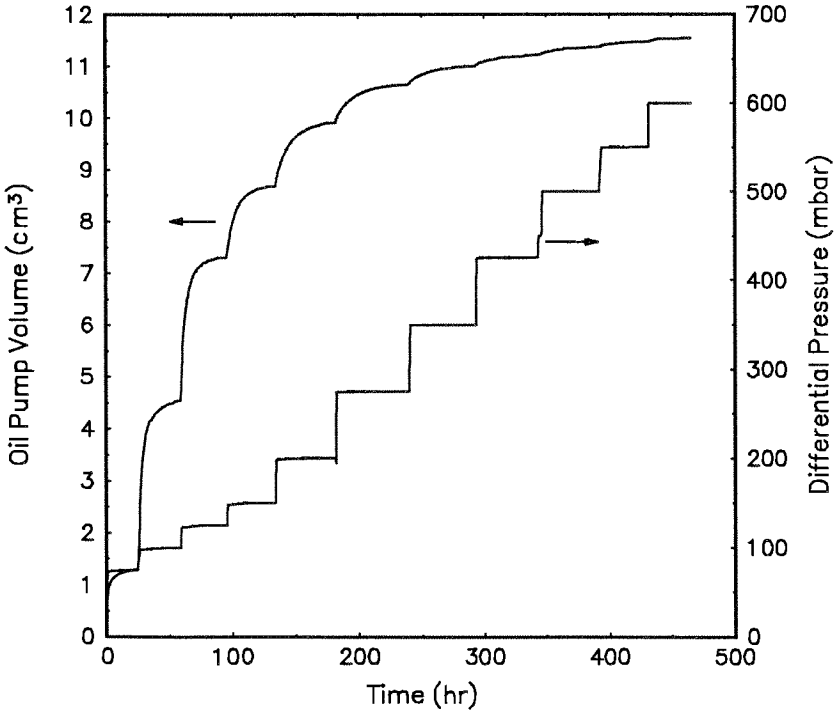

Fig. 3.66 Example of cumulative produced oil volume vs. time for run 92-6 for all the differential pressures used (p = 105.7 bar and IFT = 3.2 mN/m)

3.7 Interpretation and Discussion

The accuracy of the transducers and the precision of the automated pumps make the high-pressure capillary pressure apparatus very accurate compared with centrifuge experiments. The only uncertainty is the difference between the measured and the real differential pressure applied to the core. This is caused by gas in the lines on top of the membrane and up to the connection to the differential pressure transducer (see Fig. 3.30). The lines around the differential pressure transducer should be oil filled causing the measured differential pressure to be about 5 mbar higher than the applied differential pressure for the height of 14 cm and the densities given in Table 3.15. This should be negligible for differential pressures above 50 mbar, and was only relevant for the Berea sandstone and the 130 bar Stevens chalk experiment.

The time required to measure one high-pressure capillary pressure curve was about two weeks for the 5 md Stevens chalk at 70 and 105 bar, and about three weeks for the longest experiment at 130 bar. The longer time required for the capillary pressure run at 130 bar with an IFT = 1.5 mN/m can be explained by Eq. (3.34). This equation shows that the time required for equilibrium is inversely proportional to the differential pressure increase at each capillary pressure step. The experiment at 70 bar was slightly faster than at 105 bar. Therefore we can conclude that using the developed apparatus at low pressures should allow a complete capillary pressure curve to be measured on a chalk sample in about one week. These results are consistent with the findings of Jennings, McGregor, and Morse (1988) and Hammervold and Skjæveland (1992) mentioned in Sections 3.1 and 3.4.2.

Fig. 3.67 compares the high-pressure Berea gas-oil capillary pressure curve with the low-pressure air-oil centrifuge data by plotting the Leverett J-function. The high- and low-pressure data are close for entry pressure and irreducible saturation. However, the calculated pore size distributions are slightly lower for the centrifuge experiments giving $\lambda = 0.9$ and 1.0 compared with $\lambda = 1.6$ for the high pressure experiment. The Berea 1 centrifuge experiment ran 2 to 4 hours at each of the 18 differential pressure steps, while the Berea 2 experiment ran 4 to 8 hours at each step. This explains the difference between the two curves around $S_w = 0.5$. The total time used for the high-pressure run was the same as for the centrifuge runs (about 5 days) using only 8 differential pressure steps. If a membrane with a pore diameter of 1 μm had been used instead of the 0.1 μm membrane, the high-pressure experiment would have been faster. The one dimensional flow caused by the epoxy coating also increased the time needed for stabilization at each differential pressure step. It is not possible to draw a general conclusion based on only one experiment, but the results indicate that the Young-Laplace equation is valid for Berea sandstone for IFT values between 3.2 and 24 mN/m using a contact angle $\theta = 0$.

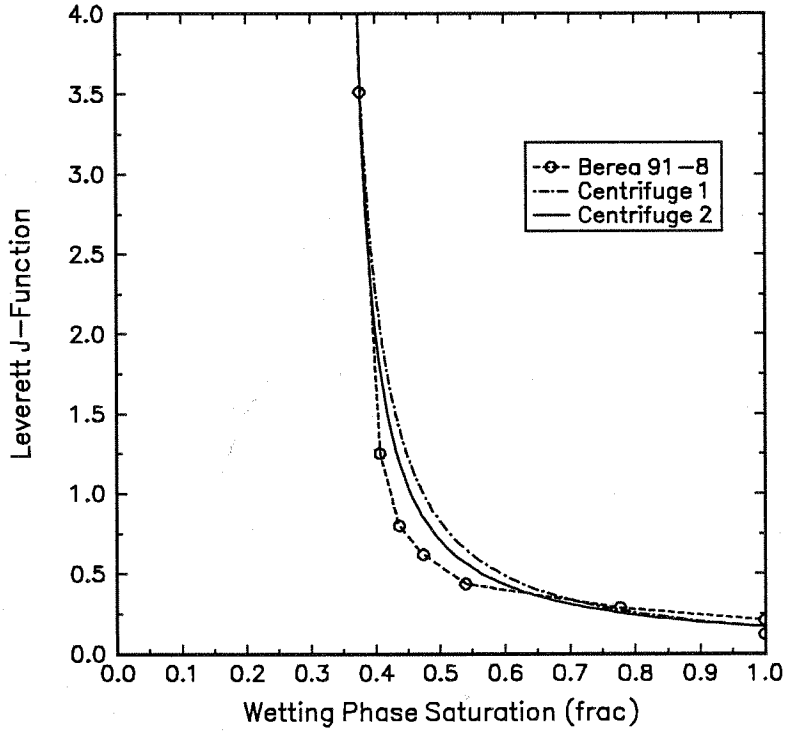

Fig. 3.67 Leverett J-Function for Berea sandstone at 105 bara and from centrifuge runs

The five high-pressure capillary pressure curves for the Stevens chalk are shown in Fig. 3.68 together with the two best low-pressure air-oil centrifuge capillary pressure curves. To check if the Young-Laplace equation is valid for scaling the measured capillary pressure curves, the Leverett J-function is plotted in Fig. 3.69 for these runs. All the curves should overlay if scaling with interfacial tension and a constant contact angle is valid. The three different interfacial tension values for the high-pressure experiments do not give the same J-curve when assuming an equal contact angle (θ = 0°), even though they were measured on the same core sample. The curves for 6.3 and 3.2 mN/m is fairly close. The J-function for the lowest interfacial tension is much lower than the other data, especially for high values of the wetting phase saturation, which corresponds to the largest pores. It can also be seen in Fig. 3.61 that the Corey curve does not match the capillary pressure at high wetting phase saturation for IFT = 1.5 mN/m. This indicates that something is happening in the largest pores.

Different core samples and interpretation method may be part of the reason for the deviation between the low-pressure centrifuge curves and the high-pressure curves. The wide spread in the air-oil centrifuge capillary pressure curves in Fig. 3.46 indicate that the accuracy of the centrifuge capillary curves are low. It is therefore difficult to draw any conclusions about the deviation between the 6.3 and 24 mN/m Leverett J-function curves.

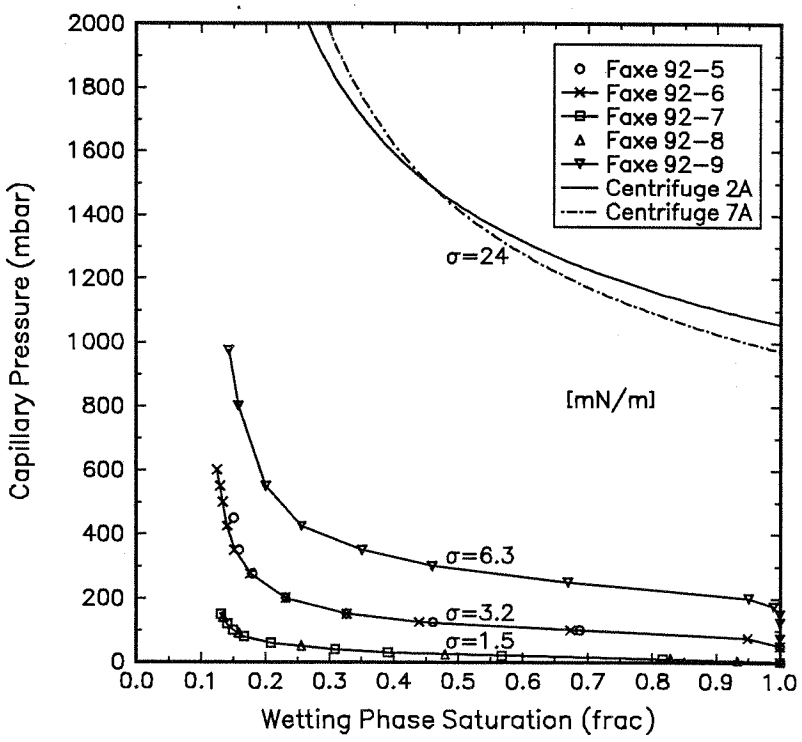

Fig. 3.68 Capillary pressure curves for the three IFT values and centrifuge runs with air-oil

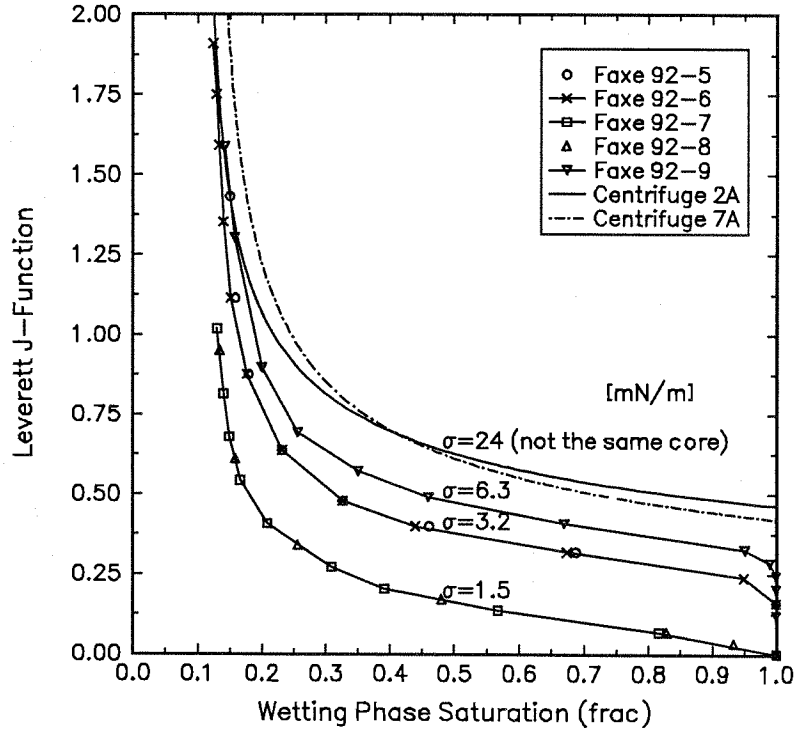

Fig. 3.69 Leverett J-function for the three IFT values and centrifuge runs with air-oil

For scaling the mercury capillary pressure curves, the contact angle can be included or neglected when using Eq. (3.32). In Fig. 3.70, the mercury Leverett J-function for $\theta_{Hg} = 0°$ and $\theta_{Hg} = 40°$ match fairly well with the 3.2 and 6.3 mN/m capillary pressure curves even though the interfacial tension of mercury is about 100 times higher than for the C_1-nC_5 system. Note that the mercury capillary pressure curve is more flat than the gas-oil capillary pressure curves, and that the irreducible wetting phase saturation is lower for the mercury experiments. This difference is seen in most comparisons of mercury and gas-oil capillary pressure curves using either porous plate or centrifuge. The pore volume of the sample used for the mercury injection was only 0.5 cm^3 compared with the pore volume of 11.5 cm^3 for the high-pressure experiments, and 21.7 cm^3 for the centrifuge experiments.

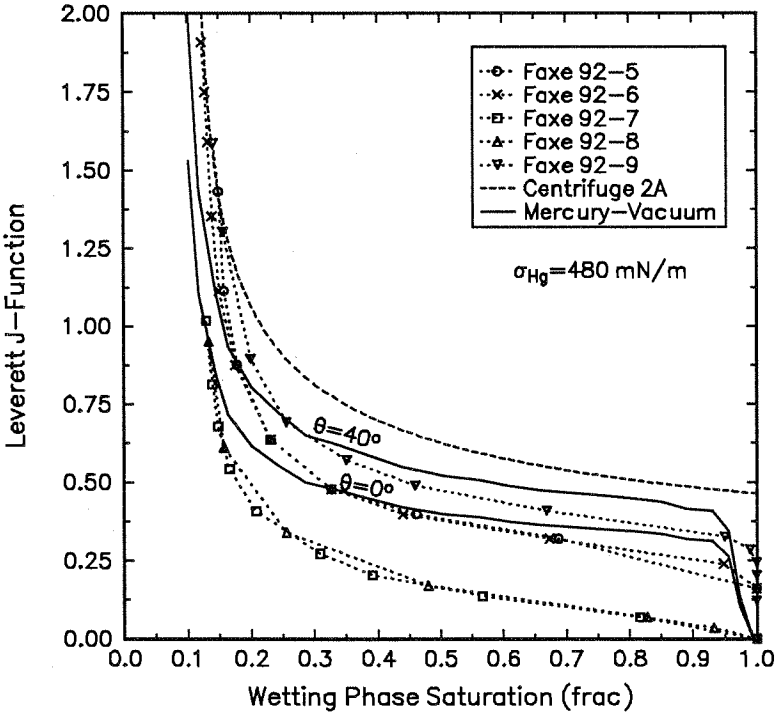

Fig. 3.70 Leverett J-function for the mercury penetration compared with the three IFT values and the centrifuge runs with air-oil

The high-pressure capillary pressure experiments indicate that capillary pressure is almost linear with interfacial tension down to an IFT of about 5 mN/m. For interfacial tensions less than 5 mN/m the capillary pressure is lower than predicted by the Young-Laplace equation if the contact angle is assumed constant. The recovery of oil by gravity-capillary drainage will be underestimated if low-pressure capillary pressure curves are scaled by interfacial tension only. As the interfacial tension is reduced below 2 mN/m, this underestimation of the oil recovery by linear IFT scaling becomes even worse. Results from these experiments indicate a much more effective gas-oil gravity-capillary drainage process for shorter effective core (matrix block) heights in chalk than would be predicted by applying linear scaling by interfacial tension to low-

pressure capillary pressure data.

Two different explanations on what happens for low values of interfacial tension can be found in the literature:

Increasing Contact Angle as IFT Decreases

Asar and Handy (1988) measured steady-state relative permeabilities for a C_1-C_3 system using a Berea sandstone core sample for interfacial tensions between 0.03 and 0.82 mN/m. They found that as the IFT approaches zero, the relative permeabilities for both gas and oil become straight lines, and the residual oil and gas saturations are reduced. They also found two factors indicating that the oil-wet character of the system decreases as the IFT decreases: (1) the gas saturation at which the gas and oil relative permeability curves intersect was higher as the IFT decreased, and (2) the ratio of the relative permeability of the oil phase at residual gas saturation to the relative permeability of the gas phase at residual oil saturation, increased as IFT decreased. This may be represented by an increasing contact angle as the interfacial tension decreases. No other references have been found mentioning anything about increasing contact angles for high pressure gas-oil-solid systems.

Cahn Transition and Redistribution of Phases

Ronde (1992b; 1992a) explain the results of Asar and Handy by the Cahn transition (Rowlinson and Widom, 1982). Sufficiently close to the critical point one of the two phases completely wets the solid, which gives a redistribution of phases in the pores. This causes a core-annular flow regime (film-flow) starting in the larger pores and then, as the interfacial tension is reduced, also in the finer pores. Fig. 3.71 explains this theory. Ronde stated that this transition starts at an IFT = 0.3 mN/m for the C_1-C_3-Berea system used by Asar and Handy. Other authors referenced by Ronde noted a cross-over from capillary to gravity driven imbibition at an interfacial tension of about 1 mN/m. In a plot of density difference vs. IFT, there is a distinct change in slope at about 1 mN/m.

Rowlinson and Widom (1982) stated that in a gravitational field, if enough liquid is available to form a film, any excess liquid sinks to the bottom. They stated that typical film thickness is 20 to 30 nm, which is the same as the film thickness for vapor-liquid-solid systems mentioned in Section 3.2.6. Cahn (1977) described the Cahn transition, and said that it is the transition between a finite contact angle and zero contact angle with perfect wetting. Neither Rowlinson and Widom or Cahn mentions anything about how close to the critical point this transition should occur.

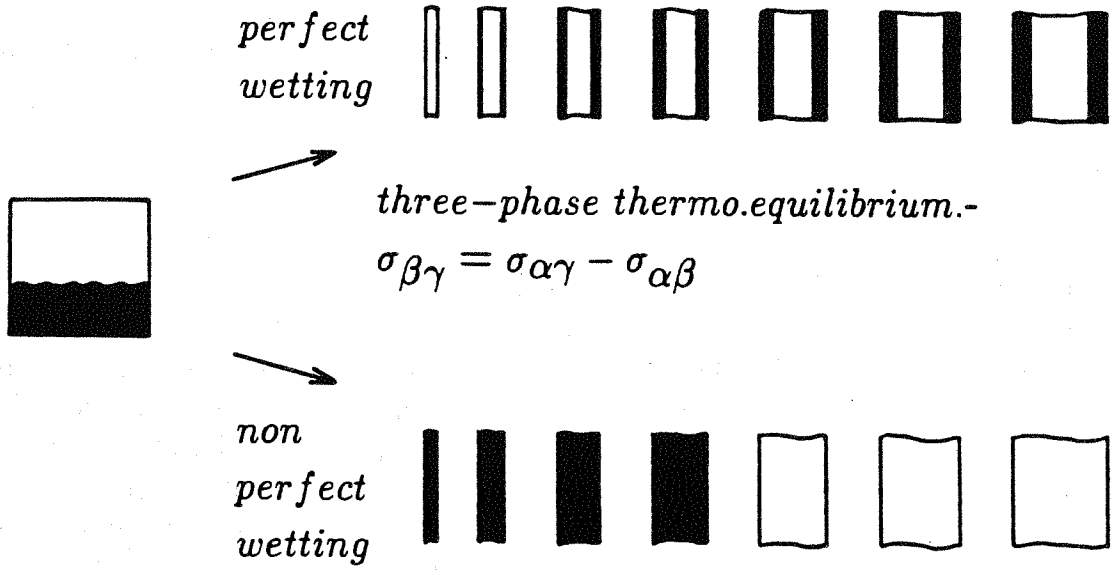

Fig. 3.71 The difference between a perfect and a nonperfect wetting system

The theory of an increasing contact angle as the properties of the gas and oil approach each other near critical conditions was checked. This gives a way of quantifying the lower capillary pressure measured at low interfacial tensions, even if the contact angle does not approach 90°.

Fig. 3.72 shows a plot of the Leverett J-function for the five high-pressure capillary pressure experiments where the contact angle was adjusted to make the curves as close as possible in the low saturation range. The apparent contact angles that gave these results are given in Table 3.24, together with IFT values and $\sigma\cos\theta$ values. This table also compares the Corey pore size distribution index which decreases slightly as IFT decreases. The decreasing λ should, according to Eq. (3.25), affect the relative permeabilities for these low interfacial tension values.

The shape of the capillary pressure curve at IFT = 3.2 and 6.3 mN/m is almost identical, where the Leverett J-function is consistent with the centrifuge data using $\sigma\cos\theta$ to scale, where σ and θ are functions of IFT. However, the shape of the capillary pressure curve for IFT = 1.5 mN/m is significantly different than curves at higher IFTs, and particularly at high wetting phase saturations (large pores). This can also be seen in Fig. 3.61, showing that the Corey curve does not match the measured capillary pressure curve at high wetting phase saturations.

Fig. 3.73 shows a plot of the apparent contact angle vs. interfacial tension. Three sets of contact angles that all give the overlaying curves seen in Fig. 3.72 are given. The ratios between $\sigma\cos\theta$ for IFT = 1.5, 3.2, and 6.3 mN/m are constant, while the threshold IFT value is varied. As seen in this plot, the apparent contact angle may start to increase somewhere in the range of 5 to 10 mN/m. As the interfacial tension

is further reduced, the contact angle may approach 90° or may decrease to 0° going through a Cahn transition.

In Fig. 3.72, the data from the 3.2 and 6.3 mN/m experiments fall on top of each other, while the data for the 1.5 mN/m experiment is much lower for the highest wetting phase saturation. This could be caused by a redistribution of phases caused by the Cahn transition starting in the largest pores.

Table 3.24 Experimental Corey pore size distribution index and apparent contact angle

Pressure (bara)	σ (IFT) (mN/m)	Corey Pore Size Distribution Index λ	Irreducible Saturation S_{Wi} (%)	Apparent* Contact Angle $\hat{\theta}$ (deg.)	σ cos$\hat{\theta}$ (mN/m)
70.0	6.3	2.1	11	0	6.3
105.7	3.2	2.0	11	37	2.6
130.0	1.5	1.7	11	64	0.6

* Apparent contact angle gives overlapping Leverett J-functions for $S_w < 0.35$.

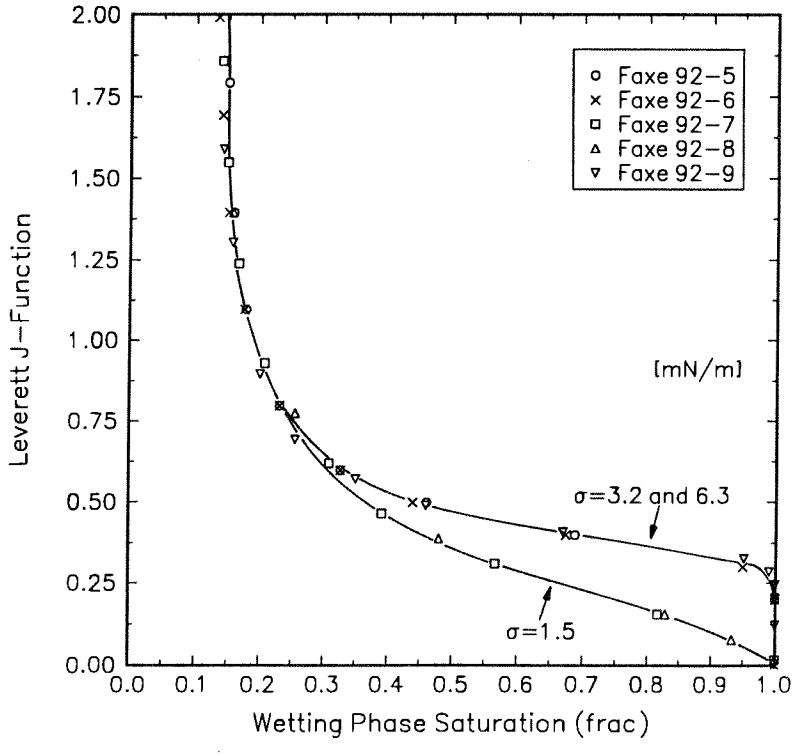

Fig. 3.72 Leverett J-function for the three IFT values with contact angle adjusted to match the curves for $S_w < 0.35$

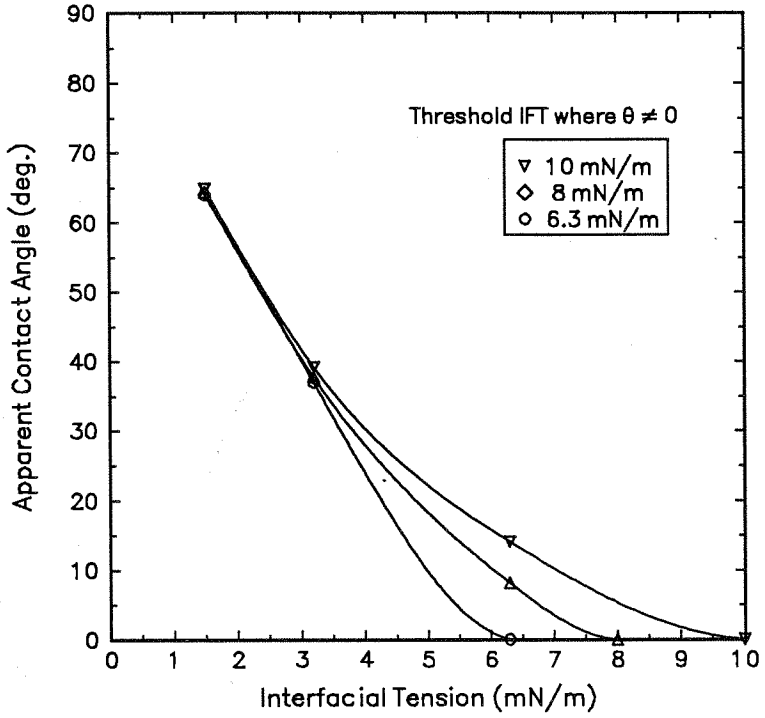

Fig. 3.73 Adjusted apparent contact angles to match the P_c curves for $S_w < 0.35$. The ratios between $\sigma\cos\theta$ for IFT = 1.5, 3.2, and 6.3 mN/m are constant, while the threshold IFT value is varied.

3.8 Conclusions and Recommendations

The following conclusions have been made from the reported experimental results:

1. A relatively simple and fast method to determine high-pressure gas-oil drainage capillary pressure curves has been presented, with accurate and reproducible results. The method is based on a modified porous plate method using thin membranes instead of a porous plate.

2. One high-pressure run using a 300 md Berea sandstone core is presented, and compared with a low-pressure centrifuge capillary pressure curve. Results indicate that scaling the low-pressure capillary pressure curve with interfacial tension gives almost the same results as the high-pressure experiment. The apparent gas-oil contact angle appears to be constant for IFT values between 3 and 24 mN/m for this particular sandstone sample.

3. Drainage gas-oil capillary pressure curves using a 5 md Stevens chalk at gas-oil interfacial tensions of 1.5, 3.2, and 6.3 mN/m for a high-pressure C_1-nC_5 system have been measured (using the same core sample), and compared with mercury injection and centrifuge runs at low pressure.

   The capillary pressure curves were not a linear function of interfacial tension. It appears that the deviation starts at an IFT of about 5 mN/m, and increases at increasing pressures, and as the interfacial tension decreases. The nonlinearity may be explained as an increasing apparent contact angle as IFT decreases, and/or as a redistribution of phases caused by the Cahn transition, starting in the larger pores and then, as IFT decreases, also in the finer pores. For values of IFT below about 2 mN/m, it appears that another effect changes the shape of the capillary pressure curve for high wetting phase saturations. This effect could be the Cahn transition. The capillary pressure is further reduced, and becomes very low compared to scaling low pressure measurements by IFT only.

4. The recovery of oil by gravity-capillary drainage will be underestimated if low-pressure capillary pressure curves are scaled by interfacial tension only. This underestimation of the oil recovery starts at about 5 mN/m and becomes even worse as the interfacial tension is reduced below 2 mN/m. Results from these experiments indicate a much more effective gas-oil gravity-capillary drainage process for shorter effective core (matrix block) heights in chalk than would be predicted by applying linear scaling by interfacial tension to low-pressure capillary pressure data.

5. For the chalk studied, the shape of the capillary pressure curve, and thereby the Corey pore size distribution index, appears to be affected by low interfacial tension (IFT < 2 mN/m). Accordingly, relative permeabilities may also be affected by interfacial tension in this range of IFT. The presence of irreducible water may effect this result.

6. The time required to achieve a capillary pressure curve varied from two to three weeks for the 5 md chalk cores, with IFT values between 1.5 and 6.3 mN/m. For low-pressure experiments it should be possible to measure a capillary pressure curve of chalk in about one week.

7. It appears that the Brooks & Corey equation gives a good match of the measured capillary pressure curves of the chalk samples both for mercury injection, low-pressure air-oil centrifuge experiments, and high-pressure gas-oil measurements. This is not true for values of IFT below about 2 mN/m.

The following recommendations are made for further research:

1. The developed experimental procedure can be used for all types of drainage capillary pressure measurements at both high and low pressures and temperatures.

2. The time required for measuring one capillary pressure curve can be reduced by reducing the core length and maintaining the volume by increasing the core diameter. The time required should be proportional to the square of the core length.

3. To improve the accuracy of the high-pressure capillary pressure apparatus for low IFT values, the height between the connections to the differential pressure transducer should be made as small as possible for gas-liquid measurements. Both the differential pressure transducer and the absolute pressure transducers should be replaced with transducers with higher resolution. A high precision temperature cabinet should also be used, both to allow a more constant temperature, and to allow measurements at reservoir temperature. If C_1 - C_3 is used instead of C_1 - nC_5, the bubble point pressure at 24°C is reduced from 170 to about 95 bara. This makes it easier to maintain a constant differential pressure.

4. More experiments should be performed to determine the most efficient way to eliminate the diffusion through the membrane around the core. This may be done using a membrane that is permeable only for a given diameter that is slightly smaller than the core diameter. Diffusion may also be reduced by forcing one dimensional displacement through the core, but this will slow down the experiment.

5. The indications that gas-oil gravity-capillary drainage in chalk will be much more effective for small matrix block heights at low interfacial tensions than predicted by scaling low-pressure capillary pressure curves, should be examined further. This is the major justification for continuing research in this area. The effect of low interfacial tension on gas-oil gravity-capillary drainage should also be examined for sandstone.

6. The effect of irreducible water saturation in a water wet core sample should be examined. This may change the behavior seen for IFT below 2 mN/m where the shape of the capillary pressure curve is changed for high wetting phase saturations. Also the effect of using reservoir oil and gas should be examined. It is then important to filter the oil using a membrane before starting the experiment to avoid plugging of the membrane during the displacement of the oil during the experiments.

3.9 Nomenclature

A = Hamaker constant, J
C = molar concentration, gmol/cm^3
d = pore diameter, μm
D = diffusion coefficient, cm^2/s
f = linear tension, mN
h = film thickness, nm
J = Leverett J-function
k = permeability, μm^2
k_{rw} = wetting phase relative permeability
L_c = core length, cm
L_m = thickness of membrane, μm
M = molecular weight, g/gmol
n = number of pores per unit area
p = pressure, Pa
P_c = capillary pressure, Pa
P_{ce} = capillary entry pressure, Pa
p_{nw} = pressure in nonwetting phase, Pa
p_w = pressure in wetting phase, Pa
P_i = parachor for IFT correlation
r = pore radius, m
R = universal gas constant, 8.31438×10^6 Pa cm^3/(K gmol)
R = radius of interface curvature, m
R_m = mean radius of interface curvature, m
S_{LS} = liquid-solid spreading coefficient
S_w = wetting phase saturation
S_{wi} = irreducible wetting phase saturation
S_W^* = normalized wetting phase saturation
t = time to equilibrium, s
T = temperature, K
u = flux per unit area, gmol/(cm^{2}s)
v_L = molar volume of adsorbed liquid, cm^3/gmol
W = U.S. Bureau of Mines wettability index
x = position, cm
x_i = liquid phase mole fraction
y_i = vapor phase mole fraction

Greek

α = pore-shape correction factor
δ = thickness of interfacial region, m
Δ = incremental change
λ = Corey pore size distribution index
Π = film pressure or disjoining pressure, N/m
ϕ = porosity, frac.
ρ = density, kg/m^3
σ = interfacial tension, N/m
θ = contact angle

Subscript

c = core
g = gas phase
L = liquid phase
L = laboratory conditions
m = mean or membrane
nw = nonwetting
o = oil phase
R = reservoir conditions
S = solid phase
V = vapor phase
w = wetting

Superscript

o = equilibrium or original

3.10 References

Adamson, A.W.: *Physical Chemistry of Surfaces*, fifth edition, John Wiley & Sons, New York (1990).

Amott, E.: "Observations Relating to the Wettability of Porous Rock," *Trans.*, AIME (1959) **216**, 156-162.

Amyx, J.W., Bass, D.M., Jr., and Whiting, R.L.: *Petroleum Reservoir Engineering - Physical Properties*, McGraw-Hill Book Company, New York (1960).

Anderson, W.G.: "Wettability Literature Survey - Part 4: Effects of Wettability on Capillary Pressure," *JPT* (Oct. 1987a) 1283-1300.

Anderson, W.G.: "Wettability Literature Survey - Part 5: The Effects of Wettability on Relative Permeability," *JPT* (Nov. 1987b) 1453-1468.

Asar, H. and Handy, L.L.: "Influence of Interfacial Tension on Gas/Oil Relative Permeability in a Gas-Condensate System," *SPERE* (Feb. 1988) 257-264.

Bear, J.: *Dynamics of Fluids in Porous Media*, reprint, originally published by Elsevier, 1972, Dover Publications, Inc., New York (1988).

Bentsen, R.G. and Anli, J.: "Using Parameter Estimation Techniques to Convert Centrifuge Data Into a Capillary Pressure Curve," *SPEJ* (Feb. 1977) 57-64; *Trans.*, AIME, **263**.

Berry, V.M. and Sage, B.H.: "Phase Behavior in Binary And Multicomponent Systems At Elevated Pressures: N-Pentane and Methane - n-Pentane," National Standard Reference Data Series, National Bureau of Standards, Washington, D.C. (1970) **32**.

Brown, H.W.: "Capillary Pressure Investigations," *Trans.*, AIME (1951) **192**, 67-74.

Cahn, J.W.: "Critical Point Wetting," *J. Chem. Phys.* (1977) **66**, No. 8, 3667-3672.

Chattoraj, D.K. and Birdi, K.S.: *Adsorption and the Gibbs Surface Excess*, Plenum Press, New York (1984).

da Silva, F.V.: "Primary and Enhanced Recovery of Ekofisk Field: A Single- and Double-Porosity Numerical Simulation Study," paper SPE 19840 presented at the 1989 SPE Annual Technical Conference and Exhibition, San Antonio, TX, Oct. 8-11.

Deetz, D.W.: "Stabilized Ultrathin Liquid Membranes for Gas Separation," *Proc.*, Liquid Membranes - Theory and Applications, Denver, Colorado, June 8-12, ACS Symposium Series (1986) **347**, 152-165.

Delclaud, J., Rochon, J., and Nectoux, A.: "Investigation of Gas/Oil Relative Permeabilities: High-Permeability Oil Reservoir Application," paper SPE 16966 presented at the 1987 SPE Annual Technical Conference and Exhibition, Dallas, TX, Sept. 27-30.

Donaldson, E.C., Thomas, R.D., and Lorenz, P.B.: "Wettability Determination and Effect on Recovery Efficiency," *SPEJ* (Mar. 1969) 13-20.

Dullien, F.A.L.: *Porous Media - Fluid Transport and Pore Structure*, second edition, Academic Press, Inc., San Diego, CA (1992).

Dumoré, J.M. and Schols, R.S.: "Drainage Capillary Pressure Functions and the Influence of Connate Water," *SPEJ* (Oct. 1974) 437-444.

Everett, D.H.: "Pore Systems and Their Characteristics," *Proc.*, Characterization of Porous Solids, Elsevier, Amsterdam (1988) 1-21.

Gregg, S.J. and Sing, K.S.W.: *Adsorption, Surface Area and Porosity*, second edition, Academic Press, London (1982).

Hammervold, W.L. and Skjæveland, S.M.: "Improvement of Diaphragm Method for Drainage Capillary Pressure Measurement With Micro Pore Membrane," Advances in Core Evaluation, EUROCAS III, Paris (1992).

Hassler, G.L. and Brunner, E.: "Measurement of Capillary Pressure in Small Core Samples," *Trans.*, AIME (1945) **160**, 114-123.

Hirasaki, G.J.: "Shape of Meniscus/Film Transition Region," *Interfacial Phenomena in Petroleum Recovery*, N.R. Morrow (ed.), Marcel Dekker, Inc., New York (1991a) 77-99.

Hirasaki, G.J.: "Thermodynamics of Thin Films and Three-Phase Contact Regions," *Interfacial Phenomena in Petroleum Recovery*, N.R. Morrow (ed.), Marcel Dekker, Inc., New York (1991b) 23-76.

Hirasaki, G.J., Rohan, J.A., and Dudley, J.W., II: "Interpretation of Oil/Water Relative Permeabilities From Centrifuge Displacement," paper 24879 presented at the 1992 Annual Technical Conference and Exhibition, Washington, DC, Oct. 4-7.

Hough, E.W. and Stegemeier, G.L.: "Correlation of Surface and Interfacial Tension of Light Hydrocarbons in the Critical Region," *SPEJ* (Dec. 1961) 259-263; *Trans.*, AIME, **222**.

Jennings, J.W., Jr.: "A Method for Producing a Rapid Experiment for the Measurement of Capillary Pressure," MS Thesis, Texas A&M University (1981).

Jennings, J.W., Jr.: "A Method for Measuring Capillary Pressure and Relative Permeabilities Based Upon a Transient Analysis of a Rapid Restored-State," PhD Dissertation, Texas A&M University (1983).

Jennings, J.W., Jr., McGregor, D.S., and Morse, R.A.: "Simultaneous Determination of Capillary Pressure and Relative Permeability by Automatic History Matching," *SPEFE* (June 1988) 322-328.

Kalaydjian, F.J.-M.: "Dynamic Capillary Pressure Curve for Water/Oil Displacement in Porous Media: Theory vs. Experiment," paper 24813 presented at the 1992 Annual Technical Conference and Exhibition, Washington, DC, Oct. 4-7.

Kalaydjian, F.J.-M.: "Performance and Analysis of Three-Phase Capillary Pressure Curves for Drainage and Imbibition in Porous Media," paper 24878 presented at the 1992 Annual Technical Conference and Exhibition, Washington, DC, Oct. 4-7.

Katz, D.L., *et al.*: *Handbook of Natural Gas Engineering*, McGraw Hill Book Co., Inc., New York (1959).

King, M.J., *et al.*: "Simultaneous Determination of Residual Saturation and Capillary Pressure Curves Utilizing the Ultracentrifuge," paper SPE 15595 presented at the 1986 SPE Annual Technical Conference and Exhibition, New Orleans, LA, Oct. 5-8.

Lake, L.W.: *Enhanced Oil Recovery*, Prentice Hall, New Jersey (1989).

Leverett, M.C.: "Capillary Behavior in Porous Solids," *Trans.*, AIME (1941) **142**, 152-169.

Melrose, J.C.: "Interpretation of Centrifuge Capillary Pressure Data," *The Log Analyst* (Jan.-Feb. 1988) 40-47.

Melrose, J.C.: "Valid Capillary Pressure Data at Low Wetting-Phase Saturations," *SPERE* (Feb. 1990) 95-99.

Melrose, J.C.: "Scaling Procedures for Capillary Pressure Data at Low Wetting-Phase Saturations," *SPEFE* (June 1991) 227-232.

Monicard, R.P.: *Properties of Reservoir Rocks: Core Analysis*, Editions Technip, Paris (1980).

Morrow, N.R.: "Introduction to Interfacial Phenomena in Oil Recovery," *Interfacial Phenomena in Petroleum Recovery*, N.R. Morrow (ed.), Marcel Dekker, Inc., New York (1991) 1-21.

Munkvold, F.R. and Torsæter, O.: "Relative Permeability From Centrifuge and Unsteady-State Experiments," paper SPE 21103 presented at the 1990 SPE Latin American Petroleum Engineering Conference, Rio de Janeiro, Oct. 14-19.

Nordtvedt, J.E. and Kolltveit, K.: "Capillary Pressure Curves From Centrifuge Data by Use of Spline Functions," *SPERE* (Nov. 1991) 497-501.

O'Meara, D.J., Jr., Hirasaki, G.J., and Rohan, J.A.: "Centrifuge Measurements of Capillary Pressure: Part 1 - Outflow Boundary Condition," *SPERE* (Feb. 1992) 113-142.

Omoregie, Z.S.: "Factors Affecting the Equivalency of Different Capillary Pressure Measurement Techniques," *SPEFE* (Mar. 1988) 147-155.

Pethica, B.A.: "The Contact Angle Equilibrium," *J. Colloid Interface Sci.* (1977) **62**, No. 3, 567-569.

Purcell, W.R.: "Capillary Pressures - Their Measurement Using Mercury and the Calculation of Permeability Therefrom," *Trans.*, AIME (1949) **186**, 39-48.

Radke, C.J., Kovscek, A.R., and Wong, H.: "A Pore-Level Scenario for the Development of Mixed Wettability in Oil Reservoirs," paper 24880 presented at the 1992 Annual Technical Conference and Exhibition, Washington, DC, Oct. 4-7.

Reid, R.C., Prausnitz, J.M., and Poling, B.E.: *The Properties of Gases & Liquids*, fourth edition, McGraw-Hill, New York (1987).

Ronde, H.: "Effect of Low Interfacial Tensions on Relative Permeabilities in Some Gas Condensate Systems," paper SPE 25072 presented at the European Petroleum Conference, Cannes, France, Sept. 16-18 (1992a).

Ronde, H.: "Relative Permeability at Low Interfacial Tensions," paper SPE 24877 presented at the 1992 Annual Technical Conference and Exhibition, Washington, DC, Oct. 4-7.

Rose, W. and Bruce, W.A.: "Evaluation of Capillary Character in Petroleum Reservoir Rock," *Trans.*, AIME (1949) **186**, 127-142.

Rowlinson, J.S. and Widom, B.: *Molecular Theory of Capillarity*, International Series of Monographs on Chemistry, Clarendon Press, Oxford (1982) **8**.

Saidi, A.M.: *Reservoir Engineering of Fractured Reservoirs (Fundamental and Practical Aspects)*, TOTAL Edition Press, Paris (1987).

Skuse, B., Firoozabadi, A., and Ramey, H.J., Jr.: "Computation and Interpretation of Capillary Pressure From a Centrifuge," *SPEFE* (1992) 17-24.

Slobod, R.L., Chambers, A., and Prehn, W.L., Jr.: "Use of Centrifuge for Determining Connate Water, Residual Oil, and Capillary Pressure Curves of Small Core Samples," *Trans.*, AIME (1951) **192**, 127-134.

Standing, M.B.: "Notes on Relative Permeability Relationships," The Norwegian Institute of Technology, Department of Petroleum Engineering, Trondheim (1975).

Søndenå, E.: "Studies of Capillary Pressure and Electrical Resistivity in Porous Rock Samples at Reservoir Conditions," Dr. Scient. Dissertation, Univeristy of Bergen, Department of Physics, Norway (1991).

Søndenå, E., *et al.*: "A Comparison Between Capillary Pressure Data and Saturation Exponent Obtained at Ambient Conditions and at Reservoir Conditions," *SPEFE* (1992) 34-40.

Søndenå, E., *et al.*: "The Effect of Reservoir Conditions on Saturation Exponent and Capillary Pressure Curve for Water-Wet Samples," *Proc.*, Advances in Core Evaluation, EUROCAS I, London, Gordon and Breach, London (1990) 411-426.

van Domselaar, H.R.: "An Exact Equation to Calculate Actual Saturations From Centrifuge Capillary Pressure Measurements," *Rev. Tec. Intevep* (1984) **4**, 55-62.

Ward, J.S. and Morrow, N.R.: "Capillary Pressures and Gas Relative Permeabilities of Low-Permeability Sandstone," *SPEFE* (Sept. 1987) 345-356.

Whitson, C.H.: "PVTx - An Equation-of-State Based Program for Simulating & Matching PVT Experiments with Multiparameter Nonlinear Regression," user manual, Pera a/s, Trondheim, Norway (1992).

Willhite, G.P.: *Waterflooding*, Textbook Series, SPE, Richardson, TX (1986) **3**.

Wunderlich, R.W.: "Imaging of Wetting and Nonwetting Phase Distributions: Application to Centrifuge Capillary Pressure Measurements," paper SPE 14422presented at the 1985 Annual Technical Conference and Exhibition, Las Vegas, NV, Sept. 22-25.

Appendix A

Diffusion Data Bank

This appendix gives high pressure binary and self diffusion data for both vapor and liquid hydrocarbons collected from several published papers. These data were used to check the accuracy of the Sigmund correlation and the Riazi and Whitson correlation given in Chapter 2. First a table with the critical properties is given, and then several tables comparing the experimental and estimated diffusion coefficients. These tables should be useful for anyone trying to develop a better correlation for estimating high pressure binary diffusion coefficients for vapor and liquid hydrocarbons. The vertical line in the tables separate the published data from the calculated values. α_D is the density-diffusivity correction factors based on the experimental diffusion data, the extended Sigmund correlation, and the Riazi and Whitson correlation. The Jossi, Stiel, and Thodos correlation was used to estimate the mixture viscosity μ. More details about the equations used are given in Chapter 2. At the end of each table the average deviation (AD) and the average absolute deviation (AAD) between the experimental and estimated diffusion coefficients are given.

Table A.1 Critical properties used in diffusion data bank calculations

Component	M	v_c ($cm^3/gmol$)	T_c (K)	Z_c	ω	p_c (bara)
N2	28.01	90.09	126.3	0.2916	0.0450	33.99
CO2	44.01	94.28	304.2	0.2742	0.2310	73.56
C1	16.04	99.27	190.6	0.2884	0.0115	46.04
C2	30.07	148.00	305.4	0.2843	0.0908	48.77
C3	44.10	202.90	369.8	0.2804	0.1454	42.49
C4	58.12	254.70	425.2	0.2736	0.1928	37.97
C5	72.15	304.00	469.9	0.2623	0.2510	33.71
C6	86.18	370.10	507.4	0.2643	0.2957	30.13
C7	100.20	432.30	540.3	0.2633	0.3506	27.36
C8	114.23	492.10	568.8	0.2587	0.3978	24.86
C9	128.26	547.70	594.6	0.2536	0.4437	22.89
C10	142.29	603.10	617.6	0.2462	0.4902	20.96
nC12	170.34	713.00	658.2	0.2400	0.5750	18.42
nC14	198.40	830.00	693.0	0.2300	0.5810	15.97
nC16	226.45	931.54	722.0	0.2200	0.7420	14.18

Table A.2 Binary diffusion data for C_1-C_3 from Sigmund (1976a)

T (°C)	p (psia)	$\rho_m \times 10^3$ (gmol/cm^3)	x_1	$D \times 10^5$ (cm^2/s)	ρ_{mr}	$(\rho_m D)^0 \times 10^6$ (gmol/cm/s)	Expr. α_D	Sigm. α_D	Sigm. Dev. (%)	μ (cp)	Riazi α_D	Ria. Dev. (%)
38.1	203	0.551	0.896	88.300	0.06	5.126	0.949	1.001	-5.5	0.0113	1.059	11.6
38.1	400	1.138	0.901	46.000	0.13	5.126	1.021	1.005	1.6	0.0115	1.053	3.1
38.1	600	1.769	0.899	31.500	0.20	5.126	1.087	1.007	7.4	0.0118	1.043	-4.0
38.1	806	2.450	0.904	18.800	0.28	5.126	0.898	1.006	-12.0	0.0122	1.030	14.7
38.1	1002	3.140	0.903	16.400	0.36	5.126	1.005	1.003	0.1	0.0127	1.015	1.0
38.1	1003	11.100	0.100	2.230	2.18	5.126	0.483	0.499	-3.4	0.0703	0.487	0.8
38.1	1250	10.960	0.280	2.360	2.00	5.126	0.505	0.568	-12.7	0.0519	0.545	8.1
38.1	1253	4.090	0.904	13.200	0.47	5.126	1.053	0.996	5.4	0.0135	0.989	-6.1
38.1	1500	5.060	0.904	10.400	0.58	5.126	1.027	0.984	4.1	0.0146	0.958	-6.7
38.1	1500	11.320	0.285	2.240	2.06	5.126	0.495	0.544	-10.1	0.0551	0.518	4.8
38.1	1500	9.780	0.465	3.010	1.63	5.126	0.574	0.710	-23.6	0.0347	0.640	11.4
38.1	1504	11.430	0.104	1.870	2.24	5.126	0.417	0.475	-13.9	0.0762	0.443	6.2
38.1	2000	11.680	0.108	2.250	2.29	5.126	0.513	0.457	10.9	0.0812	0.405	-21.1
38.1	2000	11.840	0.247	2.440	2.19	5.126	0.564	0.493	12.6	0.0653	0.453	-19.6
38.1	2000	11.060	0.472	2.250	1.83	5.126	0.485	0.633	-30.5	0.0412	0.571	17.6
38.1	2000	9.031	0.702	4.850	1.28	5.126	0.854	0.828	3.1	0.0249	0.732	-14.4
38.1	2000	7.026	0.902	5.660	0.81	5.126	0.776	0.947	-22.1	0.0172	0.883	13.8
38.1	2250	11.990	0.267	2.180	2.20	5.126	0.510	0.489	4.0	0.0652	0.441	-13.5
38.1	2500	11.800	0.090	1.700	2.32	5.126	0.391	0.442	-12.9	0.0873	0.365	-6.6
38.1	2500	12.160	0.258	2.090	2.24	5.126	0.496	0.473	4.5	0.0690	0.416	-16.0
38.1	2500	10.590	0.703	3.200	1.50	5.126	0.661	0.757	-14.5	0.0297	0.654	-1.0
38.1	2500	12.040	0.441	2.320	2.03	5.126	0.545	0.557	-2.2	0.0498	0.496	-8.9
38.1	3000	10.220	0.904	4.220	1.17	5.126	0.841	0.859	-2.2	0.0231	0.739	-12.2
38.1	3000	12.020	0.091	1.690	2.37	5.126	0.396	0.425	-7.2	0.0933	0.330	-16.6
71.4	202	0.493	0.886	119.600	0.06	5.605	1.052	1.001	4.9	0.0122	1.061	0.8
71.4	405	1.010	0.885	53.100	0.12	5.605	0.957	1.004	-4.9	0.0124	1.055	10.2
71.4	600	1.552	0.880	34.700	0.18	5.605	0.961	1.006	-4.7	0.0126	1.047	9.0
71.4	805	2.116	0.881	26.200	0.25	5.605	0.989	1.007	-1.8	0.0129	1.037	4.9
71.4	1001	2.678	0.890	20.500	0.31	5.605	0.980	1.005	-2.6	0.0133	1.027	4.8
71.4	1500	9.810	0.135	2.870	1.90	5.605	0.502	0.608	-21.1	0.0510	0.545	8.5
71.4	1500	4.246	0.881	12.200	0.50	5.605	0.924	0.993	-7.4	0.0147	0.983	6.4
71.4	1750	10.250	0.117	3.180	2.00	5.605	0.582	0.570	2.0	0.0570	0.506	-13.0
71.4	2000	5.794	0.883	8.910	0.68	5.605	0.921	0.970	-5.3	0.0165	0.928	0.7
71.4	2000	10.410	0.137	2.390	2.02	5.605	0.444	0.563	-26.9	0.0574	0.493	11.0
71.4	2475	10.810	0.133	2.360	2.10	5.605	0.455	0.532	-16.8	0.0630	0.448	-1.5
71.4	3000	8.462	0.901	5.190	0.97	5.605	0.784	0.911	-16.3	0.0206	0.814	3.9
71.4	3000	11.020	0.406	2.790	1.90	5.605	0.549	0.610	-11.2	0.0453	0.513	-6.5
71.4	3000	11.110	0.150	2.160	2.14	5.605	0.428	0.514	-20.1	0.0657	0.415	-3.2
104.8	198	0.454	0.900	126.700	0.05	6.067	0.948	1.000	-5.5	0.0131	1.062	12.0
104.8	202	0.469	0.485	130.000	0.08	6.067	1.005	1.002	0.3	0.0119	1.056	5.1
104.8	220	0.477	0.285	121.000	0.09	6.067	0.951	1.003	-5.4	0.0115	1.053	10.7
104.8	410	0.909	0.867	67.000	0.11	6.067	1.004	1.004	0.0	0.0132	1.057	5.2
104.8	600	1.394	0.870	41.300	0.17	6.067	0.949	1.006	-6.0	0.0134	1.050	10.7
104.8	610	2.124	0.088	26.200	0.42	6.067	0.917	1.000	-9.0	0.0135	0.978	6.6
104.8	800	1.871	0.864	33.500	0.22	6.067	1.033	1.007	2.6	0.0136	1.043	0.9
104.8	893	2.095	0.867	28.500	0.25	6.067	0.984	1.007	-2.3	0.0138	1.039	5.5
104.8	904	2.498	0.484	22.500	0.41	6.067	0.926	1.000	-8.0	0.0139	0.998	7.7
104.8	1000	2.365	0.887	25.100	0.28	6.067	0.979	1.006	-2.8	0.0140	1.035	5.7
104.8	1000	5.926	0.109	9.430	1.16	6.067	0.921	0.862	6.4	0.0269	0.751	-18.5
104.8	1500	3.638	0.891	16.600	0.42	6.067	0.995	1.000	-0.4	0.0150	1.005	0.9
104.8	1500	4.777	0.510	12.170	0.77	6.067	0.958	0.953	0.5	0.0180	0.894	-6.8
104.8	1500	7.930	0.124	4.410	1.54	6.067	0.576	0.740	-28.4	0.0377	0.637	10.5
104.8	2000	6.901	0.469	6.990	1.15	6.067	0.795	0.866	-8.9	0.0247	0.765	-3.8
104.8	2000	4.931	0.881	11.400	0.58	6.067	0.927	0.984	-6.2	0.0163	0.962	3.8
104.8	2000	9.162	0.088	4.090	1.81	6.067	0.618	0.645	-4.3	0.0483	0.548	-11.2
104.8	2450	9.628	0.116	3.650	1.88	6.067	0.579	0.617	-6.5	0.0512	0.514	-11.2
104.8	2500	6.168	0.881	8.960	0.73	6.067	0.911	0.962	-5.6	0.0180	0.912	0.1
								AD	-6.0			0.3
								AAD	8.4			8.1

Table A.3 Binary diffusion data for C_1-C_4 from Sigmund (1976a)

T (°C)	p (psia)	$\rho_m \times 10^3$ (gmol/cm^3)	x_1	$D \times 10^5$ (cm^2/s)	ρ_{mr}	$(\rho_m D)^0 \times 10^6$ (gmol/cm/s)	Expr. α_D	Sigm. α_D	Sigm. Dev. (%)	μ (cp)	Riazi α_D	Ria. Dev. (%)
38.1	1010	10.350	0.147	1.433	2.50	4.345	0.341	0.372	-9.0	0.1091	0.387	13.4
38.1	1444	10.470	0.142	1.520	2.53	4.345	0.366	0.359	2.0	0.1167	0.352	-3.9
38.1	1494	4.820	0.958	10.190	0.54	4.345	1.130	0.989	12.5	0.0142	0.972	-14.0
38.1	1752	5.730	0.959	7.485	0.63	4.345	0.987	0.976	1.1	0.0152	0.942	-4.6
38.1	1990	6.770	0.946	5.579	0.77	4.345	0.869	0.953	-9.7	0.0167	0.897	3.2
38.1	2150	7.300	0.945	4.199	0.84	4.345	0.706	0.941	-33.4	0.0175	0.875	24.0
38.1	2520	8.540	0.945	5.042	0.98	4.345	0.991	0.910	8.2	0.0196	0.820	-17.2
71.4	200	0.490	0.973	101.700	0.05	4.753	1.049	1.000	4.6	0.0125	1.062	1.2
71.4	200	0.490	0.927	96.200	0.06	4.753	0.992	1.001	-0.9	0.0122	1.061	6.9
71.4	992	2.620	0.972	17.390	0.28	4.753	0.959	1.006	-5.0	0.0134	1.033	7.8
71.4	1010	9.410	0.124	2.169	2.29	4.753	0.429	0.453	-5.6	0.0815	0.448	4.4
71.4	1220	9.540	0.125	2.266	2.32	4.753	0.455	0.441	3.0	0.0851	0.429	-5.7
71.4	1256	9.510	0.163	3.148	2.28	4.753	0.630	0.458	27.3	0.0772	0.447	-29.0
71.4	1484	4.180	0.932	10.660	0.49	4.753	0.938	0.994	-6.0	0.0146	0.988	5.4
71.4	1484	9.630	0.125	1.933	2.35	4.753	0.392	0.433	-10.4	0.0879	0.409	4.3
71.4	1500	9.660	0.161	3.080	2.32	4.753	0.626	0.443	29.3	0.0815	0.424	-32.3
71.4	1746	9.700	0.118	2.498	2.37	4.753	0.510	0.423	17.0	0.0918	0.387	-24.2
71.4	1964	9.810	0.126	1.634	2.39	4.753	0.337	0.416	-23.2	0.0938	0.372	10.4
71.4	2500	6.850	0.971	6.299	0.74	4.753	0.908	0.960	-5.8	0.0174	0.905	-0.3
104.8	200	0.450	0.971	122.100	0.05	5.147	1.067	1.000	6.3	0.0133	1.062	-0.5
104.8	200	0.450	0.973	127.500	0.05	5.147	1.115	1.000	10.3	0.0134	1.062	-4.7
104.8	1008	8.310	0.113	3.069	2.03	5.147	0.495	0.556	-12.2	0.0602	0.521	5.2
104.8	1245	8.500	0.115	3.285	2.08	5.147	0.542	0.538	0.8	0.0632	0.499	-8.1
104.8	1500	8.800	0.121	2.686	2.15	5.147	0.459	0.511	-11.4	0.0682	0.470	2.4
104.8	1764	8.860	0.134	2.639	2.15	5.147	0.454	0.510	-12.2	0.0678	0.459	0.9
104.8	1960	8.990	0.124	2.682	2.19	5.147	0.468	0.494	-5.5	0.0718	0.436	-6.9
								AD	-1.1			-2.4
								AAD	10.5			10.5

Table A.4 Binary diffusion data for C_1-N_2 from Sigmund (1976a)

T (°C)	p (psia)	$\rho_m \times 10^3$ (gmol/cm^3)	x_1	$D \times 10^5$ (cm^2/s)	ρ_{mr}	$(\rho_m D)^0 \times 10^6$ (gmol/cm/s)	Expr. α_D	Sigm. α_D	Sigm. Dev. (%)	μ (cp)	Riazi α_D	Ria. Dev. (%)
40.0	204	0.548	0.500	187.000	0.05	9.059	1.131	1.000	11.6	0.0156	1.063	-6.1
40.0	507	1.380	0.500	71.700	0.13	9.059	1.092	1.005	8.0	0.0158	1.056	-3.3
40.0	757	2.080	0.500	49.200	0.20	9.059	1.130	1.007	10.9	0.0161	1.048	-7.2
40.0	1012	2.810	0.500	34.500	0.27	9.059	1.070	1.006	6.0	0.0165	1.038	-3.0
40.0	1265	3.550	0.500	26.600	0.34	9.059	1.042	1.004	3.6	0.0170	1.025	-1.7
40.0	1500	4.230	0.500	22.900	0.40	9.059	1.069	1.001	6.4	0.0175	1.011	-5.5
40.0	1506	4.230	0.500	22.500	0.40	9.059	1.051	1.001	4.7	0.0175	1.011	-3.8
40.0	1770	4.990	0.500	18.500	0.47	9.059	1.019	0.995	2.3	0.0181	0.993	-2.6
40.0	2000	5.710	0.500	16.400	0.54	9.059	1.034	0.988	4.4	0.0188	0.973	-5.9
40.0	2020	5.710	0.500	16.000	0.54	9.059	1.009	0.988	2.0	0.0188	0.973	-3.6
65.6	202	0.499	0.500	209.200	0.05	9.631	1.084	1.000	7.7	0.0165	1.063	-1.9
65.6	501	1.249	0.500	84.300	0.12	9.631	1.093	1.004	8.1	0.0167	1.058	-3.3
65.6	752	1.887	0.500	57.500	0.18	9.631	1.127	1.006	10.7	0.0170	1.051	-6.7
65.6	1001	2.525	0.500	41.300	0.24	9.631	1.083	1.007	7.0	0.0173	1.043	-3.7
65.6	1268	3.221	0.500	31.700	0.31	9.631	1.060	1.006	5.1	0.0177	1.032	-2.6
65.6	1506	3.826	0.500	26.500	0.36	9.631	1.053	1.003	4.7	0.0181	1.021	-3.0
65.6	1760	4.520	0.500	22.900	0.43	9.631	1.075	0.999	7.0	0.0186	1.006	-6.4
65.6	2008	5.107	0.500	19.700	0.48	9.631	1.045	0.994	4.8	0.0192	0.991	-5.1
93.3	208	0.473	0.500	239.800	0.04	10.232	1.109	1.000	9.8	0.0174	1.064	-4.0
93.3	506	1.157	0.500	93.100	0.11	10.232	1.053	1.004	4.6	0.0176	1.059	0.6
93.3	762	1.748	0.500	63.500	0.17	10.232	1.085	1.006	7.3	0.0179	1.053	-2.9
93.3	1000	2.302	0.500	48.700	0.22	10.232	1.096	1.007	8.1	0.0181	1.047	-4.4
93.3	1256	2.893	0.500	38.200	0.27	10.232	1.080	1.006	6.8	0.0185	1.039	-3.8
93.3	1508	3.477	0.500	33.100	0.33	10.232	1.125	1.005	10.7	0.0188	1.029	-8.5
93.3	1762	4.063	0.500	26.800	0.39	10.232	1.064	1.002	5.8	0.0193	1.017	-4.4
93.3	1999	4.586	0.500	23.200	0.43	10.232	1.040	0.999	4.0	0.0197	1.005	-3.3
								AD	6.6			-4.1
								AAD	6.6			4.1

Table A.5 Binary diffusion data for C_1-C_5 from Reamer, Duffy, and Sage (1956)

T (°C)	p (psia)	$\rho_m \times 10^3$ (gmol/cm^3)	x_1	$D \times 10^5$ (cm^2/s)	ρ_{mr}	$(\rho_m D)^0 \times 10^6$ (gmol/cm/s)	Expr. α_D	Sigm. α_D	Sigm. Dev. (%)	μ (cp)	Riazi α_D	Ria. Dev. (%)
4.4	250	7.420	0.119	0.966	2.16	3.393	0.211	0.505	-139.0	0.0664	0.461	118.4
4.4	500	8.414	0.214	1.000	2.36	3.393	0.248	0.427	-72.2	0.0773	0.434	75.2
4.4	750	9.160	0.295	1.050	2.47	3.393	0.283	0.382	-34.9	0.0817	0.421	48.6
4.4	1000	9.756	0.369	1.096	2.53	3.393	0.315	0.360	-14.2	0.0805	0.418	32.6
4.4	1250	10.280	0.435	1.143	2.56	3.393	0.346	0.348	-0.6	0.0774	0.418	20.6
4.4	1500	11.070	0.496	1.198	2.64	3.393	0.391	0.317	18.9	0.0802	0.404	3.5
4.4	1750	11.920	0.551	1.263	2.73	3.393	0.444	0.286	35.5	0.0840	0.389	-12.4
4.4	2000	12.570	0.612	1.328	2.72	3.393	0.492	0.288	41.4	0.0784	0.393	-20.1
4.4	2250	12.740	0.692	1.412	2.53	3.393	0.530	0.362	31.8	0.0598	0.440	-17.0
37.8	250	8.317	0.084	1.338	2.46	3.758	0.296	0.389	-31.4	0.1084	0.396	33.7
37.8	500	8.917	0.165	1.366	2.55	3.758	0.324	0.351	-8.4	0.1127	0.386	19.1
37.8	750	9.439	0.239	1.394	2.62	3.758	0.350	0.327	6.8	0.1115	0.382	9.2
37.8	1000	9.819	0.311	1.421	2.63	3.758	0.371	0.322	13.3	0.1015	0.390	5.2
37.8	1250	10.190	0.376	1.449	2.63	3.758	0.393	0.321	18.4	0.0929	0.397	1.2
37.8	1500	10.670	0.437	1.477	2.66	3.758	0.419	0.312	25.5	0.0883	0.398	-5.0
37.8	1750	10.890	0.506	1.505	2.58	3.758	0.436	0.341	21.9	0.0742	0.423	-3.1
37.8	2000	11.080	0.582	1.542	2.47	3.758	0.455	0.386	15.2	0.0611	0.455	0.1
37.8	2250	11.109	0.679	1.598	2.24	3.758	0.472	0.476	-0.7	0.0470	0.512	8.3
71.1	250	7.947	0.064	1.812	2.36	4.109	0.350	0.425	-21.4	0.0961	0.426	21.6
71.1	500	8.406	0.137	1.812	2.43	4.109	0.371	0.398	-7.3	0.0970	0.420	13.3
71.1	750	8.853	0.205	1.812	2.49	4.109	0.390	0.375	4.0	0.0966	0.415	6.2
71.1	1000	9.047	0.273	1.812	2.47	4.109	0.399	0.384	3.8	0.0851	0.430	7.7
71.1	1250	9.320	0.336	1.812	2.46	4.109	0.411	0.386	6.0	0.0782	0.438	6.5
71.1	1500	9.502	0.400	1.812	2.42	4.109	0.419	0.403	3.8	0.0693	0.453	8.2
71.1	1750	9.700	0.468	1.812	2.36	4.109	0.428	0.426	0.5	0.0612	0.472	10.4
71.1	2000	9.673	0.550	1.820	2.21	4.109	0.428	0.485	-13.2	0.0502	0.512	19.5
71.1	2250	9.030	0.666	1.830	1.85	4.109	0.402	0.629	-56.4	0.0358	0.600	49.2
104.4	250	5.290	0.044	2.462	1.59	4.447	0.293	0.725	-147.7	0.0400	0.608	107.5
104.4	500	7.508	0.119	2.415	2.19	4.447	0.408	0.495	-21.3	0.0708	0.487	19.4
104.4	750	7.945	0.185	2.378	2.26	4.447	0.425	0.468	-10.2	0.0720	0.478	12.6
104.4	1000	8.021	0.253	2.341	2.21	4.447	0.422	0.486	-15.2	0.0638	0.496	17.4
104.4	1250	8.265	0.316	2.313	2.21	4.447	0.430	0.487	-13.4	0.0602	0.501	16.6
104.4	1500	8.366	0.383	2.276	2.15	4.447	0.428	0.509	-18.9	0.0542	0.518	21.1
104.4	1750	8.379	0.456	2.239	2.06	4.447	0.422	0.546	-29.5	0.0475	0.544	29.0
104.4	2000	8.205	0.547	2.202	1.88	4.447	0.406	0.615	-51.4	0.0394	0.590	45.2
137.8	250	5.874	0.022	4.970	1.77	4.773	0.612	0.657	-7.4	0.0492	0.576	-5.8
137.8	500	5.790	0.088	4.543	1.71	4.773	0.551	0.681	-23.5	0.0445	0.595	7.9
137.8	750	7.026	0.158	4.134	2.02	4.773	0.608	0.562	7.6	0.0571	0.536	-11.9
137.8	1000	7.064	0.230	3.744	1.97	4.773	0.554	0.582	-5.0	0.0517	0.553	-0.1
137.8	1250	7.072	0.306	3.382	1.90	4.773	0.501	0.609	-21.4	0.0463	0.575	14.7
137.8	1500	6.602	0.411	3.066	1.67	4.773	0.424	0.694	-63.8	0.0365	0.636	50.0
								AD	-14.0			19.1
								AAD	26.4			22.8

Table A.6 Binary diffusion data for C_1-C_{10} from Reamer, Opfell, and Sage (1956)

T (°C)	p (psia)	$\rho_m \times 10^3$ (gmol/cm^3)	x_1	$D \times 10^5$ (cm^2/s)	ρ_{mr}	$(\rho_m D)^0 \times 10^6$ (gmol/cm/s)	Expr. α_D	Sigm. α_D	Sigm. Dev. (%)	μ (cp)	Riazi α_D	Ria. Dev. (%)
4.4	500	5.666	0.173	0.373	3.25	2.153	0.098	0.147	-49.7	0.4111	0.159	62.4
4.4	1000	6.573	0.295	0.345	3.59	2.153	0.105	0.104	1.3	0.5131	0.147	39.6
4.4	1500	7.234	0.400	0.307	3.75	2.153	0.103	0.089	14.1	0.4022	0.160	54.9
4.4	2000	7.995	0.482	0.259	3.94	2.153	0.096	0.073	23.6	0.3730	0.157	63.1
4.4	2500	8.738	0.552	0.203	4.08	2.153	0.082	0.064	22.4	0.3289	0.156	88.8
4.4	3000	9.477	0.610	0.150	4.19	2.153	0.066	0.057	13.1	0.2928	0.152	130.9
4.4	3500	10.230	0.656	0.106	4.29	2.153	0.050	0.052	-2.7	0.2774	0.144	185.8
4.4	4000	10.880	0.700	0.075	4.30	2.153	0.038	0.051	-35.1	0.2299	0.147	286.9
37.8	500	5.538	0.153	0.595	3.20	2.386	0.138	0.155	-12.1	0.3970	0.167	21.0
37.8	1000	6.217	0.270	0.551	3.44	2.386	0.144	0.122	15.2	0.3966	0.170	18.2
37.8	1500	6.962	0.362	0.494	3.69	2.386	0.144	0.095	34.3	0.4323	0.159	10.1
37.8	2000	7.530	0.449	0.428	3.80	2.386	0.135	0.085	37.0	0.3316	0.171	26.7
37.8	2500	8.154	0.523	0.355	3.90	2.386	0.121	0.077	36.9	0.2727	0.177	45.8
37.8	3000	8.876	0.581	0.288	4.04	2.386	0.107	0.067	37.7	0.2599	0.169	57.4
37.8	3500	9.568	0.637	0.223	4.11	2.386	0.089	0.062	30.3	0.2221	0.170	90.4
37.8	4000	10.270	0.687	0.166	4.14	2.386	0.071	0.060	15.5	0.1880	0.173	142.7
71.1	500	5.427	0.140	0.967	3.15	2.611	0.201	0.163	19.0	0.3701	0.178	-11.5
71.1	1000	6.020	0.249	0.901	3.36	2.611	0.208	0.132	36.5	0.3641	0.181	-12.7
71.1	1500	6.600	0.340	0.808	3.53	2.611	0.204	0.110	46.0	0.3426	0.182	-11.0
71.1	2000	7.079	0.422	0.701	3.63	2.611	0.190	0.101	47.1	0.2716	0.194	1.9
71.1	2500	7.648	0.494	0.593	3.74	2.611	0.174	0.090	48.2	0.2346	0.197	13.2
71.1	3000	8.187	0.561	0.491	3.79	2.611	0.154	0.085	44.7	0.1888	0.207	34.2
71.1	3500	8.827	0.621	0.390	3.86	2.611	0.132	0.080	39.4	0.1620	0.211	59.7
71.1	4000	9.478	0.680	0.297	3.86	2.611	0.108	0.080	25.8	0.1310	0.224	107.4
104.4	500	5.030	0.133	1.354	2.92	2.827	0.241	0.215	10.7	0.2182	0.232	-3.6
104.4	1000	5.625	0.238	1.257	3.15	2.827	0.250	0.162	35.1	0.2367	0.227	-9.4
104.4	1500	6.164	0.327	1.132	3.32	2.827	0.247	0.137	44.7	0.2305	0.225	-8.9
104.4	2000	6.664	0.408	0.987	3.44	2.827	0.233	0.121	48.0	0.2036	0.229	-1.4
104.4	2500	7.127	0.479	0.844	3.52	2.827	0.213	0.112	47.4	0.1726	0.237	11.3
104.4	3000	7.612	0.550	0.711	3.56	2.827	0.191	0.108	43.8	0.1395	0.251	31.0
104.4	3500	8.257	0.612	0.582	3.64	2.827	0.170	0.099	41.7	0.1256	0.252	48.1
104.4	4000	8.938	0.678	0.461	3.65	2.827	0.146	0.099	32.3	0.1036	0.268	83.5
137.8	500	4.595	0.126	1.747	2.68	3.035	0.264	0.305	-15.4	0.1338	0.298	12.5
137.8	1000	5.285	0.227	1.623	2.97	3.035	0.283	0.198	29.9	0.1713	0.270	-4.6
137.8	1500	5.837	0.318	1.461	3.16	3.035	0.281	0.161	42.8	0.1749	0.263	-6.4
137.8	2000	6.204	0.404	1.281	3.21	3.035	0.262	0.152	41.8	0.1405	0.283	8.0
137.8	2500	6.752	0.476	1.104	3.34	3.035	0.246	0.134	45.6	0.1334	0.279	13.4
137.8	3000	7.243	0.547	0.930	3.40	3.035	0.222	0.127	42.9	0.1141	0.289	30.1
137.8	3500	7.795	0.618	0.771	3.42	3.035	0.198	0.124	37.3	0.0957	0.305	53.8
137.8	4000	8.398	0.684	0.632	3.40	3.035	0.175	0.127	27.6	0.0807	0.323	84.5
								AD	26.1			46.2
								AAD	31.9			49.7

Table A.7 Binary diffusion data for C_2-N_2, C_1-N_2, and C_1-C_2 from Berry and Koeller (1960)

T (°C)	p (psia)	$\rho_m \times 10^3$ (gmol/cm^3)	x_1	$D \times 10^5$ (cm^2/s)	ρ_{mr}	$(\rho_m D)^0 \times 10^6$ (gmol/cm/s)	Expr. α_D	Sigm. α_D	Sigm. Dev. (%)	μ (cp)	Riazi α_D	Ria. Dev. (%)
C_2 - N_2												
40.0	500	1.439	0.800	37.000	0.20	6.071	0.877	1.007	-14.8	0.0125	1.038	18.3
40.0	1000	3.126	0.800	16.600	0.44	6.071	0.855	0.999	-16.8	0.0143	0.984	15.1
40.0	1500	4.993	0.800	9.850	0.69	6.071	0.810	0.967	-19.4	0.0175	0.901	11.2
40.0	2000	6.853	0.800	6.690	0.95	6.071	0.755	0.916	-21.2	0.0221	0.805	6.6
40.0	2500	8.457	0.800	5.220	1.18	6.071	0.727	0.857	-17.9	0.0270	0.720	-1.0
								AD	-18.0			10.1
C_1 - N_2								AAD	18.0			10.5
40.0	500	1.350	0.800	68.000	0.13	9.059	1.014	1.005	0.9	0.0141	1.055	4.1
40.0	1000	2.739	0.800	32.700	0.27	9.059	0.989	1.006	-1.8	0.0147	1.036	4.8
40.0	1500	4.131	0.800	21.100	0.40	9.059	0.962	1.001	-4.0	0.0156	1.008	4.8
40.0	2000	5.493	0.800	15.500	0.54	9.059	0.940	0.989	-5.2	0.0168	0.971	3.4
40.0	2500	6.817	0.800	12.200	0.66	9.059	0.918	0.972	-5.9	0.0183	0.927	0.9
								AD	-3.2			3.6
C_1 - C_2								AAD	3.6			3.6
40.0	1000	3.116	0.800	21.000	0.35	6.423	1.019	1.004	1.4	0.0128	1.015	-0.4
40.0	2000	7.159	0.800	8.400	0.80	6.423	0.936	0.949	-1.4	0.0175	0.879	-6.1
40.0	4000	12.582	0.800	4.300	1.40	6.423	0.842	0.789	6.4	0.0288	0.623	-26.0
40.0	8000	16.763	0.800	3.000	1.87	6.423	0.783	0.622	20.6	0.0422	0.345	-55.9
40.0	1000	17.896	0.800	2.700	1.99	6.423	0.752	0.573	23.8	0.0476	0.254	-66.2
60.0	1000	2.826	0.800	23.300	0.31	6.776	0.972	1.005	-3.5	0.0131	1.024	5.3
60.0	2000	6.240	0.800	9.900	0.69	6.776	0.912	0.967	-6.1	0.0167	0.916	0.5
60.0	4000	11.408	0.800	5.000	1.27	6.776	0.842	0.830	1.4	0.0265	0.672	-20.2
60.0	8000	15.908	0.800	3.400	1.77	6.776	0.798	0.658	17.6	0.0394	0.382	-52.2
60.0	1000	17.087	0.800	3.100	1.90	6.776	0.782	0.608	22.2	0.0442	0.287	-63.2
77.2	1000	2.611	0.800	24.900	0.29	7.074	0.919	1.006	-9.5	0.0135	1.029	12.0
77.2	2000	5.605	0.800	11.300	0.62	7.074	0.895	0.978	-9.2	0.0164	0.941	5.1
77.2	4000	10.524	0.800	5.800	1.17	7.074	0.863	0.859	0.5	0.0250	0.711	-17.6
77.2	8000	15.189	0.800	3.900	1.69	7.074	0.837	0.688	17.9	0.0374	0.413	-50.7
77.2	1000	16.422	0.800	3.600	1.83	7.074	0.836	0.636	23.9	0.0419	0.316	-62.2
								AD	7.1			-26.5
								AAD	11.0			29.6

Table A.8 Self diffusion data for C_1 from Dawson, Koury, and Kobayashi (1970)

T (°C)	p (psia)	$\rho_m \times 10^3$ (gmol/cm^3)	x_1	$D \times 10^5$ (cm^2/s)	ρ_{mr}	$(\rho_m D)^0 \times 10^6$ (gmol/cm/s)	Expr. α_D	Sigm. α_D	Sigm. Dev. (%)	μ (cp)	Riazi α_D	Ria. Dev. (%)
-118.7	141	0.891	1.000	57.610	0.09	4.877	1.053	1.003	4.7	0.0064	1.049	-0.4
-118.7	175	1.166	1.000	42.720	0.12	4.877	1.021	1.004	1.7	0.0065	1.044	2.2
-118.7	216	21.889	1.000	1.655	2.17	4.877	0.743	0.501	32.5	0.0530	0.566	-23.8
-118.7	3460	24.277	1.000	1.194	2.41	4.877	0.594	0.408	31.4	0.0777	0.275	-53.8
-99.8	199	1.120	1.000	48.748	0.11	5.451	1.002	1.004	-0.2	0.0072	1.047	4.5
-99.8	241	1.412	1.000	38.190	0.14	5.451	0.989	1.005	-1.6	0.0073	1.043	5.4
-99.8	299	1.896	1.000	29.135	0.19	5.451	1.013	1.006	0.7	0.0075	1.034	2.0
-99.8	341	2.317	1.000	24.079	0.23	5.451	1.024	1.007	1.7	0.0077	1.026	0.2
-99.8	368	2.646	1.000	21.230	0.26	5.451	1.031	1.007	2.3	0.0079	1.018	-1.2
-99.8	407	18.834	1.000	2.506	1.87	5.451	0.866	0.620	28.4	0.0374	0.634	-26.8
-99.8	1464	20.916	1.000	1.961	2.08	5.451	0.753	0.540	28.3	0.0473	0.507	-32.6
-99.8	3958	23.092	1.000	1.560	2.29	5.451	0.661	0.454	31.3	0.0642	0.299	-54.8
-86.1	251	1.307	1.000	46.876	0.13	5.857	1.046	1.005	4.0	0.0078	1.046	0.0
-86.1	349	1.984	1.000	30.861	0.20	5.857	1.045	1.007	3.7	0.0081	1.035	-1.0
-86.1	448	2.875	1.000	22.468	0.29	5.857	1.103	1.006	8.8	0.0086	1.016	-7.8
-86.1	536	4.084	1.000	15.817	0.41	5.857	1.103	1.001	9.2	0.0094	0.987	-10.5
-86.1	1380	18.809	1.000	2.735	1.87	5.857	0.878	0.621	29.3	0.0378	0.575	-34.5
-86.1	4530	22.344	1.000	1.830	2.22	5.857	0.698	0.484	30.8	0.0579	0.304	-56.5
-82.3	230	1.143	1.000	55.974	0.11	5.968	1.072	1.004	6.3	0.0079	1.049	-2.1
-82.3	280	1.445	1.000	42.537	0.14	5.968	1.030	1.005	2.4	0.0080	1.044	1.4
-82.3	335	1.803	1.000	34.025	0.18	5.968	1.028	1.006	2.1	0.0082	1.038	1.0
-82.3	390	2.208	1.000	27.950	0.22	5.968	1.034	1.007	2.7	0.0083	1.031	-0.3
-82.3	455	2.773	1.000	23.022	0.28	5.968	1.070	1.006	5.9	0.0086	1.019	-4.7
-82.3	532	3.621	1.000	18.233	0.36	5.968	1.106	1.003	9.3	0.0092	1.000	-9.6
-82.3	595	4.627	1.000	14.174	0.46	5.968	1.099	0.997	9.3	0.0099	0.973	-11.4
-82.3	625	5.348	1.000	12.544	0.53	5.968	1.124	0.990	12.0	0.0106	0.953	-15.2
-82.3	857	16.085	1.000	3.488	1.60	5.968	0.940	0.721	23.3	0.0294	0.672	-28.6
-82.3	3950	21.590	1.000	2.053	2.14	5.968	0.743	0.513	30.9	0.0523	0.355	-52.2
-75.5	112	0.499	1.000	131.586	0.05	6.165	1.066	1.000	6.2	0.0080	1.058	-0.8
-75.5	198	0.923	1.000	71.014	0.09	6.165	1.063	1.003	5.6	0.0081	1.053	-1.0
-75.5	303	1.500	1.000	42.685	0.15	6.165	1.038	1.005	3.2	0.0083	1.044	0.6
-75.5	419	2.256	1.000	28.718	0.22	6.165	1.051	1.007	4.2	0.0086	1.031	-1.9
-75.5	555	3.428	1.000	19.222	0.34	6.165	1.069	1.004	6.0	0.0093	1.006	-5.9
-75.5	644	4.528	1.000	14.760	0.45	6.165	1.084	0.998	8.0	0.0101	0.978	-9.8
-75.5	1101	15.493	1.000	3.992	1.54	6.165	1.003	0.742	26.0	0.0281	0.674	-32.9
-75.5	1991	18.498	1.000	2.979	1.84	6.165	0.894	0.633	29.2	0.0371	0.551	-38.4
-51.3	279	1.152	1.000	62.716	0.11	6.851	1.055	1.004	4.8	0.0090	1.051	-0.3
-51.3	384	1.653	1.000	42.965	0.16	6.851	1.036	1.006	3.0	0.0092	1.044	0.7
-51.3	511	2.323	1.000	31.320	0.23	6.851	1.062	1.007	5.2	0.0095	1.033	-2.7
-51.3	646	3.144	1.000	23.379	0.31	6.851	1.073	1.005	6.3	0.0100	1.016	-5.3
-51.3	803	4.284	1.000	17.157	0.43	6.851	1.073	0.999	6.8	0.0108	0.989	-7.9
-51.3	941	5.503	1.000	13.617	0.55	6.851	1.094	0.988	9.7	0.0119	0.955	-12.7
-51.3	1108	7.293	1.000	10.344	0.72	6.851	1.101	0.962	12.6	0.0139	0.899	-18.3
-51.3	1304	10.050	1.000	7.438	1.00	6.851	1.091	0.905	17.1	0.0179	0.812	-25.5
-51.3	1720	13.273	1.000	5.237	1.32	6.851	1.015	0.815	19.7	0.0240	0.707	-30.3
-51.3	2407	16.035	1.000	4.024	1.59	6.851	0.942	0.723	23.2	0.0304	0.603	-36.0
-51.3	3398	18.055	1.000	3.356	1.79	6.851	0.884	0.649	26.6	0.0364	0.500	-43.4
-51.3	4557	19.520	1.000	2.887	1.94	6.851	0.823	0.594	27.8	0.0420	0.405	-50.7
-16.5	322	1.150	1.000	69.414	0.11	7.794	1.024	1.004	1.9	0.0102	1.053	2.9
-16.5	451	1.603	1.000	50.370	0.16	7.794	1.036	1.006	2.9	0.0104	1.047	1.1
-16.5	598	2.197	1.000	36.351	0.22	7.794	1.025	1.007	1.8	0.0106	1.038	1.3
-16.5	731	2.775	1.000	29.409	0.28	7.794	1.047	1.006	3.9	0.0109	1.028	-1.8
-16.5	928	3.696	1.000	22.280	0.37	7.794	1.057	1.003	5.1	0.0115	1.008	-4.6
-16.5	1115	4.651	1.000	17.826	0.46	7.794	1.064	0.996	6.3	0.0123	0.984	-7.5
-16.5	1447	6.494	1.000	12.644	0.64	7.794	1.053	0.975	7.4	0.0141	0.928	-11.9
-16.5	1816	8.596	1.000	9.516	0.85	7.794	1.049	0.938	10.6	0.0168	0.854	-18.6
-16.5	2270	10.873	1.000	7.317	1.08	7.794	1.021	0.884	13.4	0.0205	0.769	-24.7
-16.5	3100	13.778	1.000	5.448	1.37	7.794	0.963	0.799	17.0	0.0262	0.649	-32.6
-16.5	4350	16.347	1.000	4.191	1.62	7.794	0.879	0.712	19.0	0.0324	0.523	-40.5
-16.5	5935	18.323	1.000	3.613	1.82	7.794	0.849	0.639	24.7	0.0385	0.402	-52.7

Continued on next page....

Table A.8 .....continued from last page

T (°C)	p (psia)	$\rho_m \times 10^3$ (gmol/cm^3)	x_1	$D \times 10^5$ (cm^2/s)	ρ_{mr}	$(\rho_m D)^0 \times 10^6$ (gmol/cm/s)	Expr. α_D	Sigm. α_D	Sigm. Dev. (%)	μ (cp)	Riazi α_D	Ria. Dev. (%)
23.9	771	2.365	1.000	38.387	0.23	8.827	1.028	1.007	2.1	0.0120	1.038	1.0
23.9	982	3.082	1.000	29.531	0.31	8.827	1.031	1.006	2.5	0.0124	1.025	-0.6
23.9	1386	4.539	1.000	20.533	0.45	8.827	1.056	0.997	5.5	0.0134	0.991	-6.2
23.9	1846	6.253	1.000	14.756	0.62	8.827	1.045	0.978	6.4	0.0151	0.938	-10.2
23.9	2370	8.152	1.000	11.242	0.81	8.827	1.038	0.947	8.8	0.0174	0.868	-16.4
23.9	3020	10.228	1.000	8.808	1.02	8.827	1.021	0.901	11.8	0.0206	0.781	-23.5
23.9	4161	12.986	1.000	6.577	1.29	8.827	0.968	0.824	14.9	0.0258	0.651	-32.7
23.9	5996	15.829	1.000	5.018	1.57	8.827	0.900	0.730	18.8	0.0323	0.494	-45.1
49.4	709	1.936	1.000	50.064	0.19	9.450	1.026	1.006	1.9	0.0125	1.046	2.0
49.4	945	2.628	1.000	36.646	0.26	9.450	1.019	1.007	1.2	0.0129	1.035	1.6
49.4	1185	3.351	1.000	28.781	0.33	9.450	1.021	1.005	1.6	0.0133	1.021	0.1
49.4	1489	4.287	1.000	22.833	0.43	9.450	1.036	0.999	3.5	0.0140	0.999	-3.5
49.4	1851	5.413	1.000	18.049	0.54	9.450	1.034	0.989	4.3	0.0149	0.967	-6.4
49.4	2264	6.678	1.000	14.488	0.66	9.450	1.024	0.972	5.0	0.0163	0.924	-9.7
49.4	2975	8.706	1.000	10.963	0.86	9.450	1.010	0.936	7.4	0.0190	0.843	-16.6
80.7	993	2.452	1.000	42.560	0.24	10.187	1.024	1.007	1.7	0.0137	1.040	1.5
80.7	1256	3.133	1.000	33.150	0.31	10.187	1.020	1.005	1.4	0.0140	1.027	0.8
80.7	1680	4.240	1.000	23.860	0.42	10.187	0.993	1.000	-0.7	0.0148	1.002	0.9
80.7	2138	5.432	1.000	18.910	0.54	10.187	1.008	0.989	1.9	0.0158	0.968	-4.0
80.7	2640	6.694	1.000	15.370	0.66	10.187	1.010	0.972	3.8	0.0172	0.924	-8.5
80.7	3498	8.673	1.000	11.670	0.86	10.187	0.994	0.936	5.8	0.0198	0.840	-15.4
80.7	4699	10.981	1.000	8.760	1.09	10.187	0.944	0.881	6.7	0.0236	0.725	-23.2
80.7	6025	12.961	1.000	7.215	1.29	10.187	0.918	0.825	10.2	0.0274	0.613	-33.2
								AD	10.2			-14.1
								AAD	10.2			14.9

Table A.9 Self diffusion data for CO_2 and C_3 from Robinson and Stewart (1968)

T (°C)	p (psia)	$\rho_m \times 10^3$ (gmol/cm^3)	x_1	$D \times 10^5$ (cm^2/s)	ρ_{mr}	$(\rho_m D)^0 \times 10^6$ (gmol/cm/s)	Expr. α_D	Sigm. α_D	Sigm. Dev. (%)	μ (cp)	Riazi α_D	Ria. Dev. (%)
CO_2												
0.5	1070	21.780	1.000	1.170	2.05	4.082	0.624	0.549	12.1	0.0960	0.506	-19.0
0.5	1070	21.780	1.000	1.180	2.05	4.082	0.630	0.549	12.9	0.0960	0.506	-19.6
0.5	2140	22.730	1.000	1.000	2.14	4.082	0.557	0.513	7.8	0.1077	0.458	-17.8
22.5	1016	17.600	1.000	1.970	1.66	4.380	0.792	0.699	11.7	0.0644	0.608	-23.2
22.5	1605	19.320	1.000	1.860	1.82	4.380	0.821	0.638	22.2	0.0753	0.559	-31.9
22.5	2143	20.240	1.000	1.590	1.91	4.380	0.735	0.605	17.6	0.0823	0.527	-28.3
22.5	2680	20.920	1.000	1.560	1.97	4.380	0.745	0.580	22.1	0.0883	0.500	-32.9
								AD	15.2			-24.7
C_3								AAD	15.2			24.7
23.0	213	11.340	1.000	1.220	2.30	2.464	0.562	0.451	19.7	0.0905	0.477	-15.1
23.0	1233	11.780	1.000	1.200	2.39	2.464	0.574	0.415	27.6	0.1055	0.390	-32.0
85.7	2470	10.310	1.000	1.820	2.09	2.950	0.636	0.533	16.1	0.0684	0.433	-31.9
								AD	21.2			-26.3
								AAD	21.2			26.3

Table A.10 Binary infinite dilution diffusion data for C_n-C_8 from Erkey and Akgerman (1989)

T (°C)	p (psia)	$\rho_m \times 10^3$ (gmol/cm^3)	x_1	$D \times 10^5$ (cm^2/s)	ρ_{mr}	$(\rho_m D)^0 \times 10^6$ (gmol/cm/s)	Expr. α_D	Sigm. α_D	Sigm. Dev. (%)	μ (cp)	Riazi α_D	Ria. Dev. (%)
C_1 - C_8												
31	250	6.091	0.000	0.667	3.00	2.758	0.147	0.189	-28.5	0.4943	0.161	9.2
62	250	5.878	0.000	0.975	2.89	3.009	0.190	0.226	-18.4	0.3598	0.192	0.6
88	250	5.693	0.000	1.271	2.80	3.213	0.225	0.258	-14.7	0.2781	0.220	-2.1
114	250	5.496	0.000	1.629	2.70	3.412	0.262	0.294	-12.1	0.2159	0.253	-3.7
138	250	5.300	0.000	1.975	2.61	3.591	0.291	0.331	-13.5	0.1716	0.286	-2.0
162	250	5.086	0.000	2.404	2.50	3.766	0.325	0.371	-14.4	0.1369	0.322	-0.8
								AD	-16.9			0.2
C_2 - C_8								AAD	16.9			3.1
31	250	6.091	0.000	0.489	3.00	1.739	0.171	0.189	-10.6	0.4943	0.161	-6.1
62	250	5.878	0.000	0.714	2.89	1.906	0.220	0.226	-2.4	0.3598	0.192	-13.0
88	250	5.693	0.000	0.923	2.80	2.043	0.257	0.258	-0.4	0.2781	0.220	-14.3
114	250	5.496	0.000	1.200	2.70	2.176	0.303	0.294	3.0	0.2159	0.253	-16.6
138	250	5.300	0.000	1.477	2.61	2.296	0.341	0.331	3.0	0.1716	0.286	-16.2
162	250	5.086	0.000	1.797	2.50	2.414	0.379	0.371	1.9	0.1369	0.322	-15.0
								AD	-0.9			-13.5
C_3 - C_8								AAD	3.5			13.5
31	250	6.091	0.000	0.400	3.00	1.325	0.184	0.189	-3.0	0.4943	0.161	-12.5
62	250	5.878	0.000	0.592	2.89	1.454	0.239	0.226	5.8	0.3598	0.192	-20.0
88	250	5.693	0.000	0.779	2.80	1.560	0.284	0.258	9.2	0.2781	0.220	-22.5
114	250	5.496	0.000	1.001	2.70	1.663	0.331	0.294	11.1	0.2159	0.253	-23.6
138	250	5.300	0.000	1.232	2.61	1.757	0.372	0.331	11.0	0.1716	0.286	-23.1
162	250	5.086	0.000	1.516	2.50	1.849	0.417	0.371	11.0	0.1369	0.322	-22.8
								AD	7.5			-20.8
C_5 - C_8								AAD	8.5			20.8
31	250	6.091	0.000	0.319	3.00	0.935	0.208	0.189	8.9	0.4943	0.161	-22.6
62	250	5.878	0.000	0.479	2.89	1.026	0.275	0.226	17.8	0.3598	0.192	-30.2
88	250	5.693	0.000	0.630	2.80	1.100	0.326	0.258	20.8	0.2781	0.220	-32.4
114	250	5.496	0.000	0.815	2.70	1.173	0.382	0.294	23.0	0.2159	0.253	-33.8
138	250	5.300	0.000	0.999	2.61	1.239	0.427	0.331	22.6	0.1716	0.286	-33.1
162	250	5.086	0.000	1.227	2.50	1.304	0.479	0.371	22.4	0.1369	0.322	-32.7
								AD	19.2			-30.8
C_7 - C_8								AAD	19.2			30.8
31	250	6.091	0.000	0.266	3.00	0.738	0.220	0.189	13.8	0.4943	0.161	-26.8
62	250	5.878	0.000	0.385	2.89	0.811	0.279	0.226	19.2	0.3598	0.192	-31.4
88	250	5.693	0.000	0.498	2.80	0.871	0.326	0.258	20.7	0.2781	0.220	-32.3
114	250	5.496	0.000	0.622	2.70	0.930	0.368	0.294	20.0	0.2159	0.253	-31.3
138	250	5.300	0.000	0.812	2.61	0.983	0.438	0.331	24.5	0.1716	0.286	-34.7
162	250	5.086	0.000	1.007	2.50	1.035	0.495	0.371	24.9	0.1369	0.322	-34.9
								AD	20.5			-31.9
C_{10} - C_8								AAD	20.5			31.9
31	250	6.091	0.000	0.218	3.00	0.572	0.232	0.189	18.4	0.4943	0.161	-30.7
62	250	5.878	0.000	0.328	2.89	0.628	0.307	0.226	26.5	0.3598	0.192	-37.6
88	250	5.693	0.000	0.422	2.80	0.674	0.357	0.258	27.5	0.2781	0.220	-38.2
114	250	5.496	0.000	0.538	2.70	0.719	0.411	0.294	28.5	0.2159	0.253	-38.6
138	250	5.300	0.000	0.707	2.61	0.759	0.493	0.331	33.0	0.1716	0.286	-42.1
162	250	5.086	0.000	0.917	2.50	0.799	0.583	0.371	36.3	0.1369	0.322	-44.8
								AD	28.4			-38.7
C_{12} - C_8								AAD	28.4			38.7
31	250	6.091	0.000	0.192	3.00	0.505	0.232	0.189	18.3	0.4943	0.161	-30.6
62	250	5.878	0.000	0.290	2.89	0.554	0.308	0.226	26.7	0.3598	0.192	-37.8
88	250	5.693	0.000	0.384	2.80	0.594	0.368	0.258	29.8	0.2781	0.220	-40.1
114	250	5.496	0.000	0.499	2.70	0.634	0.433	0.294	32.0	0.2159	0.253	-41.6
138	250	5.300	0.000	0.631	2.61	0.670	0.499	0.331	33.8	0.1716	0.286	-42.8
162	250	5.086	0.000	0.823	2.50	0.705	0.594	0.371	37.5	0.1369	0.322	-45.8
								AD	29.7			-39.8
C_{14} - C_8								AAD	29.7			39.8
31	250	6.091	0.000	0.176	3.00	0.447	0.240	0.189	21.0	0.3598	0.192	-20.1
62	250	5.878	0.000	0.261	2.89	0.490	0.313	0.226	27.9	0.2781	0.220	-29.5
88	250	5.693	0.000	0.353	2.80	0.526	0.382	0.258	32.4	0.2159	0.253	-33.9
114	250	5.496	0.000	0.446	2.70	0.560	0.438	0.294	32.8	0.1716	0.286	-34.7
138	250	5.300	0.000	0.566	2.61	0.591	0.507	0.331	34.8	0.1369	0.322	-36.5
162	250	5.086	0.000	0.748	2.50	0.622	0.612	0.371	39.3	0.4943	0.161	-73.7
								AD	31.4			-38.1
								AAD	31.4			38.1

Appendix B

Diffusion Experiments

This appendix gives the match of each of the constant volume diffusion experiments. Details about each experiment are given in Tables 2.6 and 2.7. About half of the experiments has no experimental liquid level measured, only pressure.

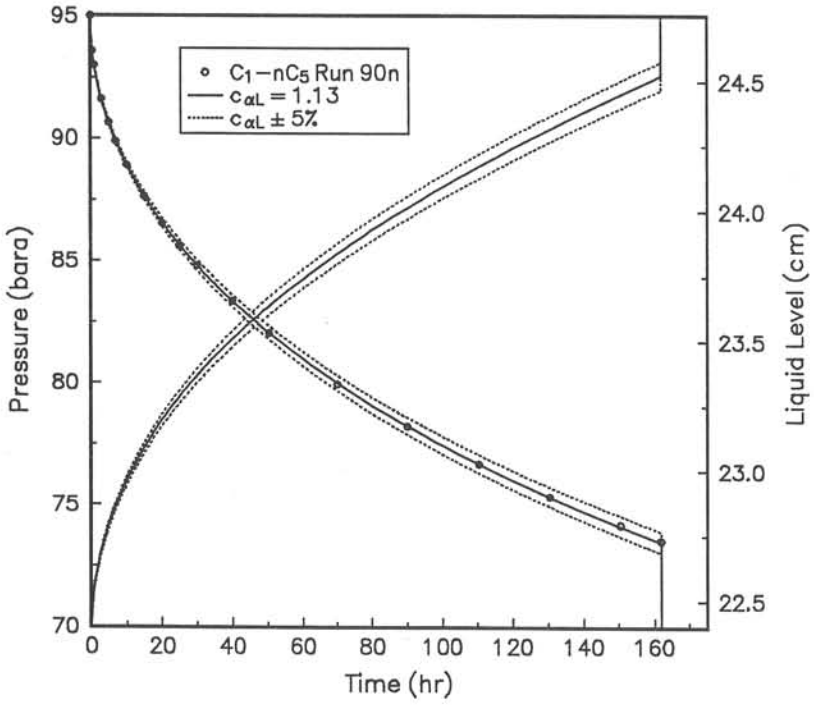

Fig. B.1 Results from matching CVD experiment 90n, C_1-nC_5 at 100 bar

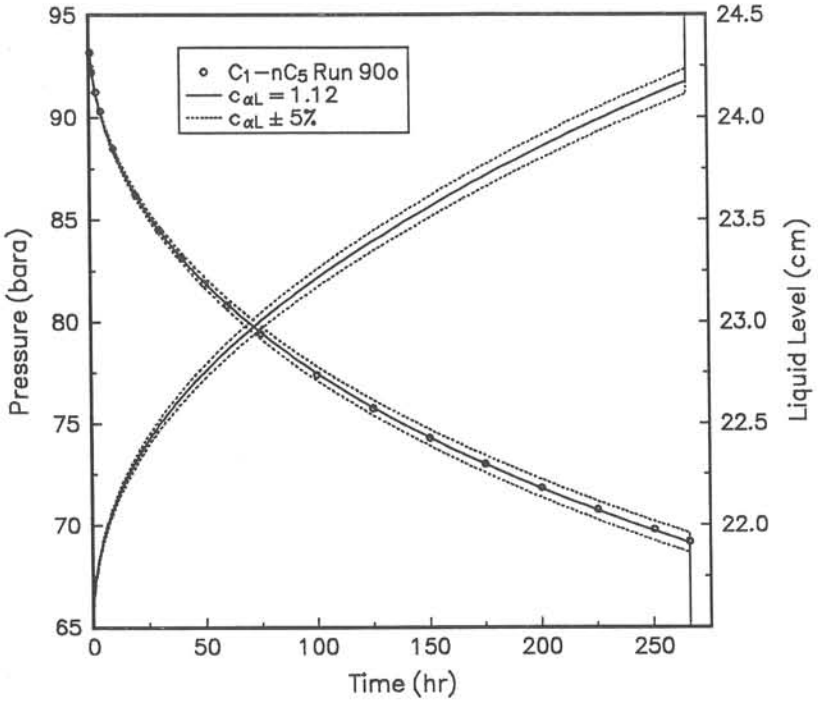

Fig. B.2 Results from matching CVD experiment 90o, C_1-nC_5 at 100 bar

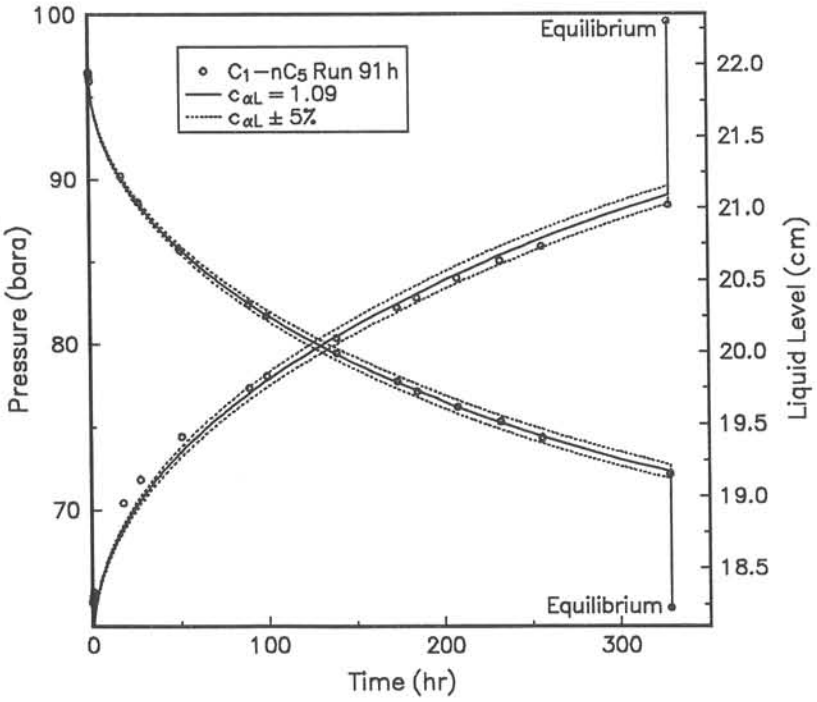

Fig. B.3 Results from matching CVD experiment 91h, C_1-nC_5 at 100 bar

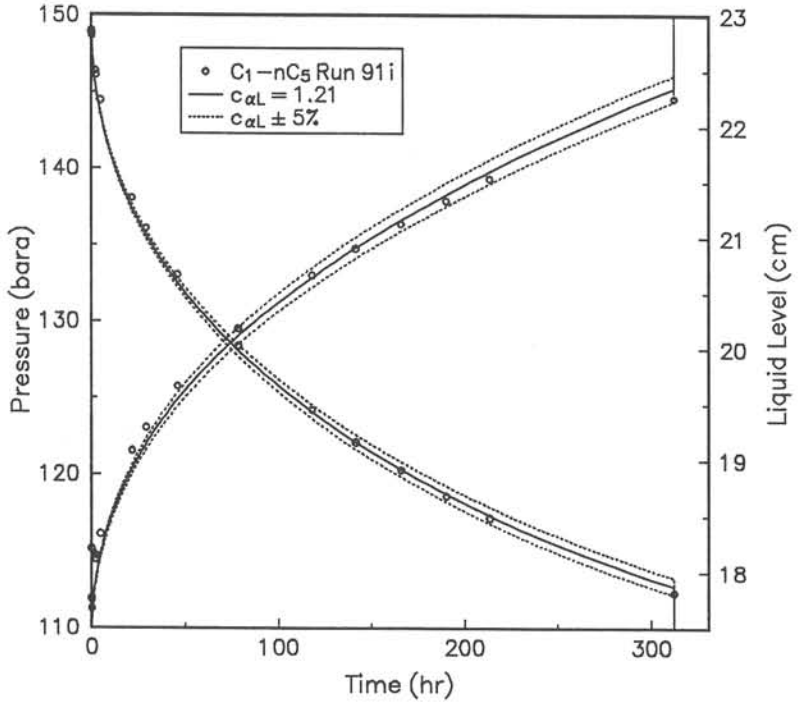

Fig. B.4 Results from matching CVD experiment 91i, C_1-nC_5 at 150 bar

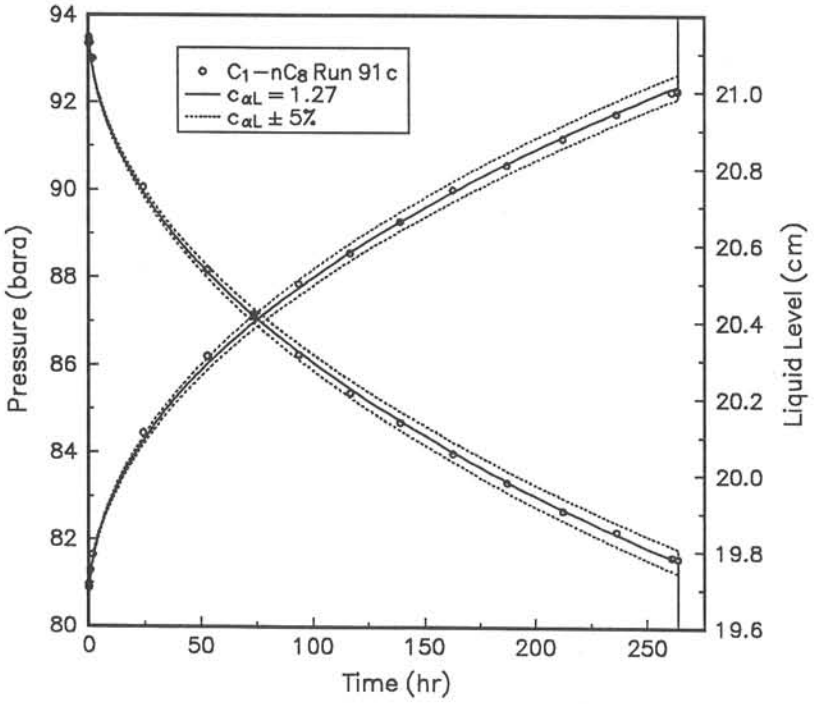

Fig. B.5 Results from matching CVD experiment 91c, C_1-nC_8 at 100 bar

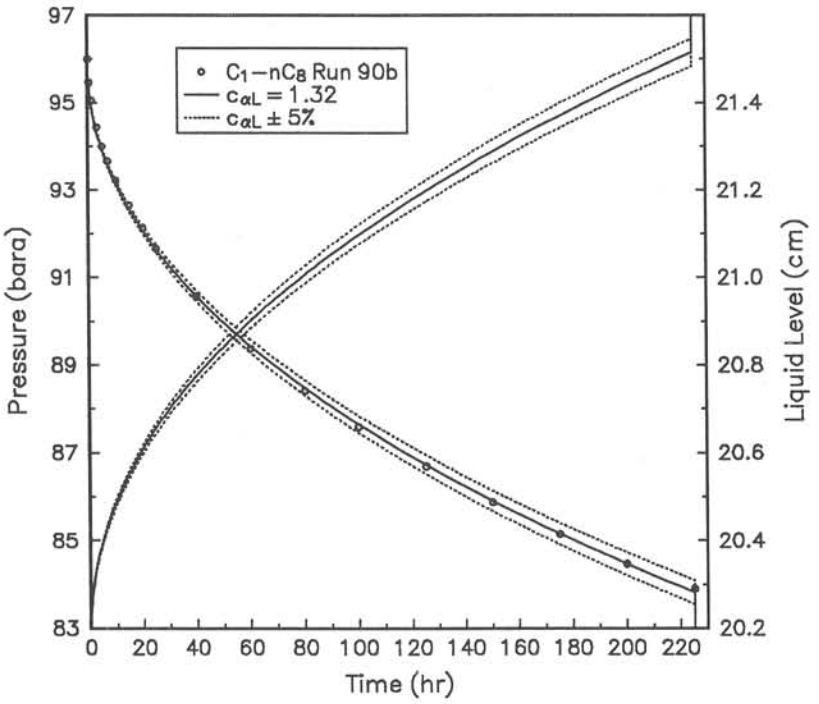

Fig. B.6 Results from matching CVD experiment 90b, C_1-nC_8 at 100 bar

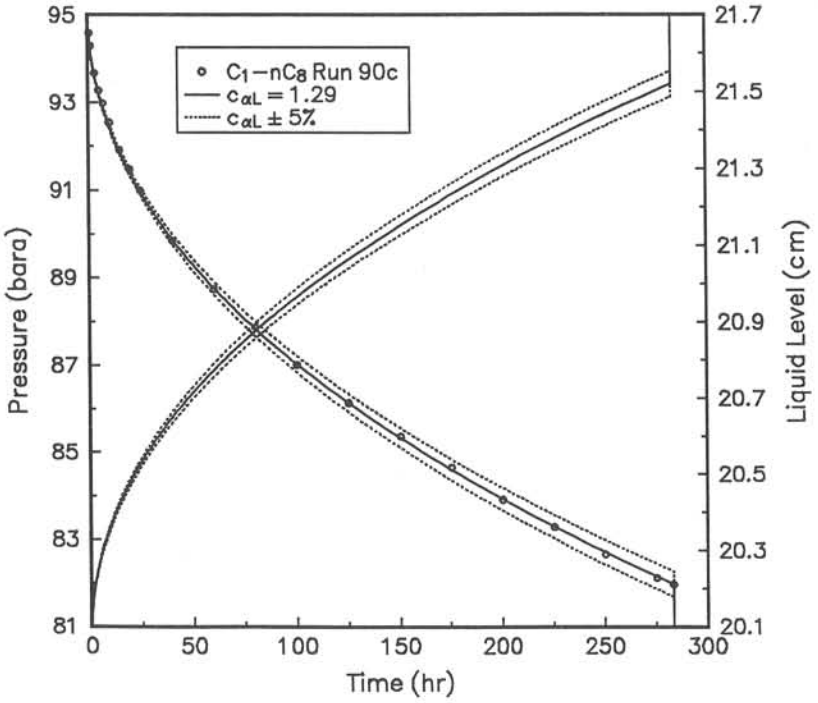

Fig. B.7 Results from matching CVD experiment 90c, C_1-nC_8 at 100 bar

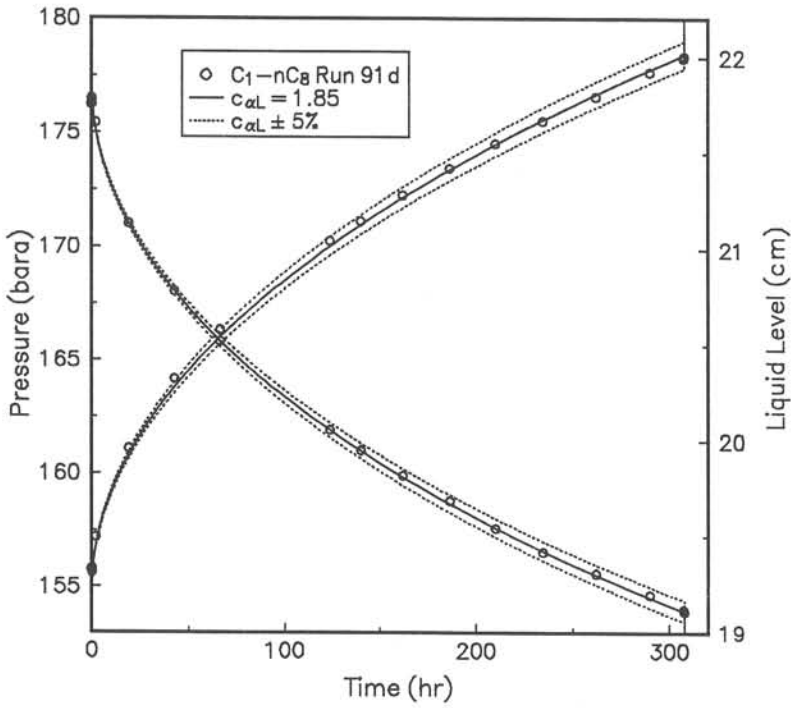

Fig. B.8 Results from matching CVD experiment 91d, C_1-nC_8 at 180 bar

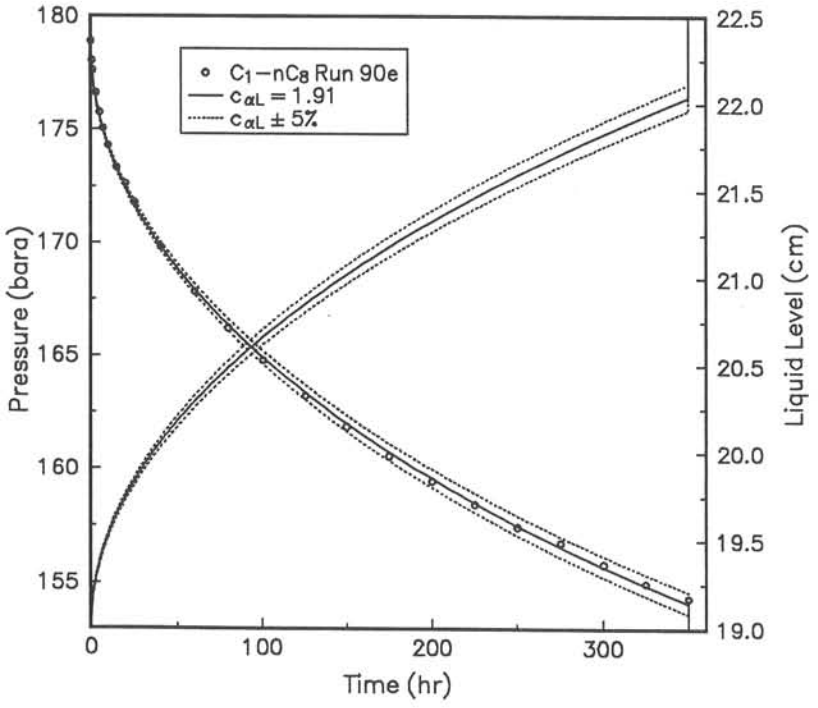

Fig. B.9 Results from matching CVD experiment 90e, C_1-nC_8 at 180 bar

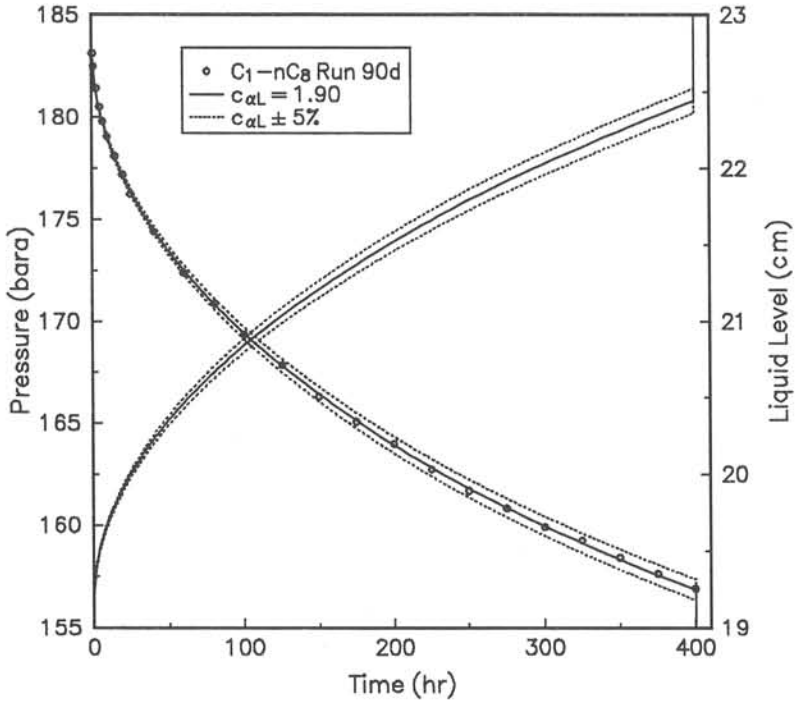

Fig. B.10 Results from matching CVD experiment 90d, C_1-nC_8 at 180 bar

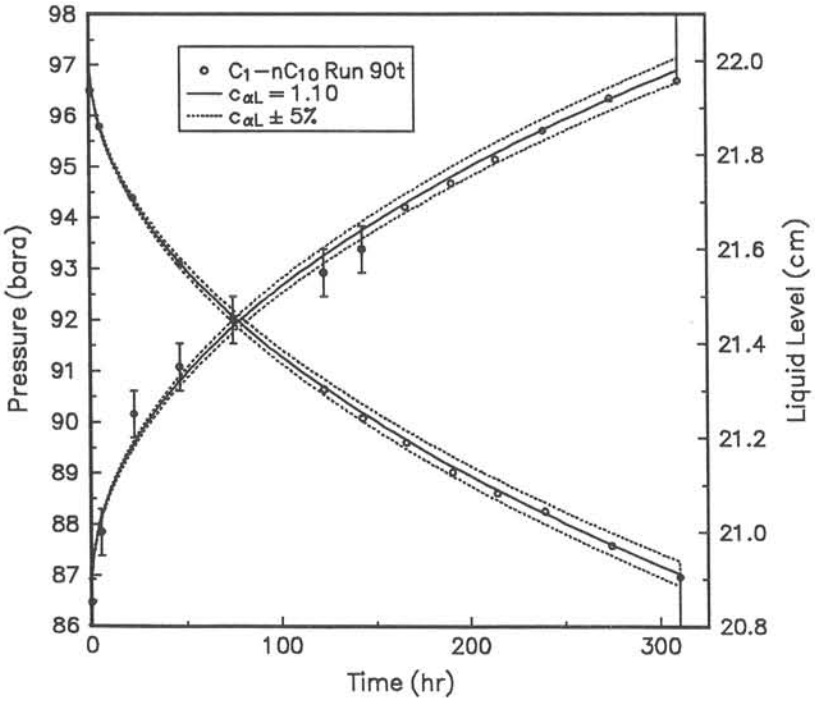

Fig. B.11 Results from matching CVD experiment 90t, C_1-nC_{10} at 100 bar

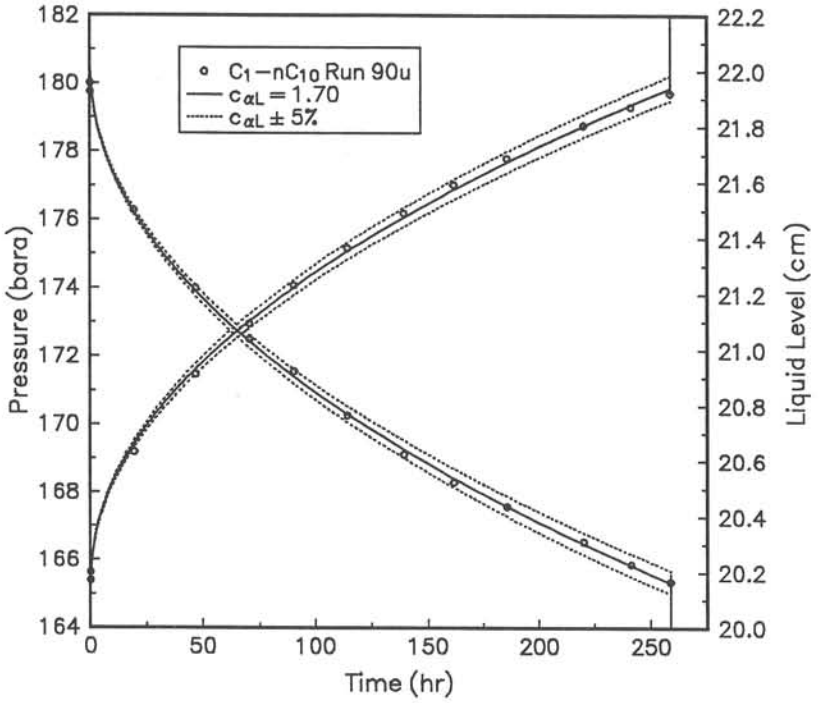

Fig. B.12 Results from matching CVD experiment 90u, C_1-nC_{10} at 180 bar

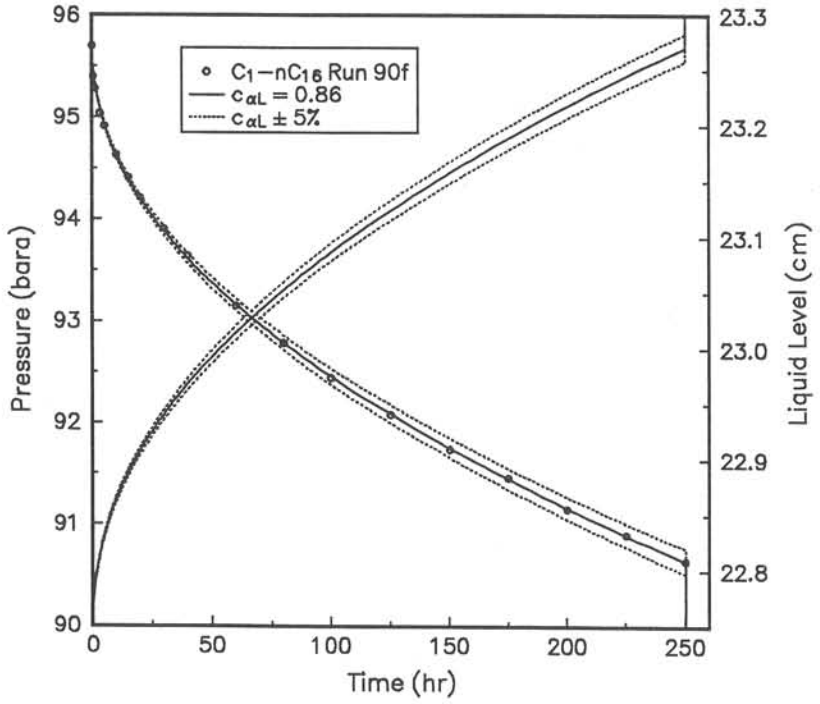

Fig. B.13 Results from matching CVD experiment 90f, C_1-nC_{16} at 100 bar

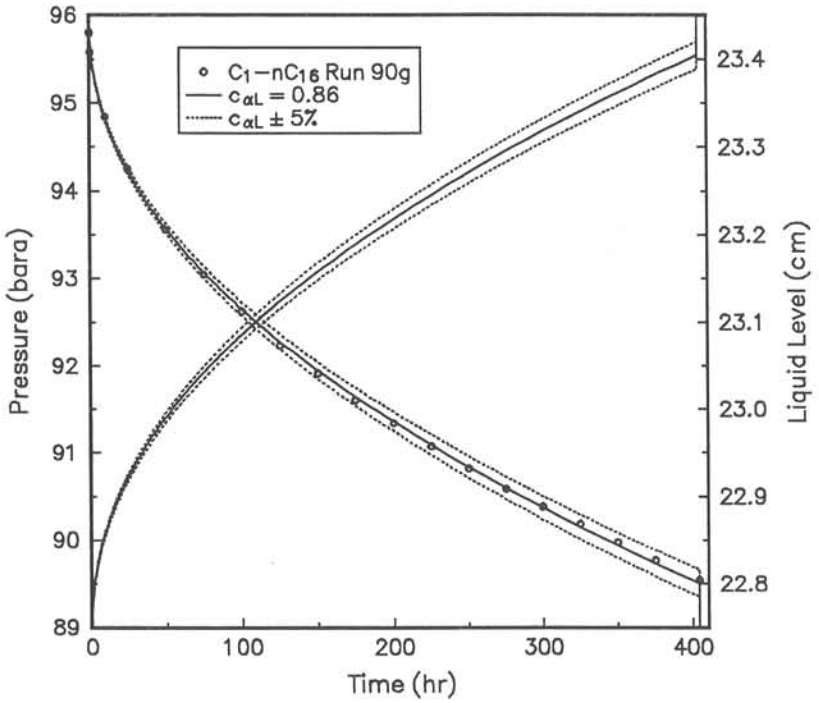

Fig. B.14 Results from matching CVD experiment 90g, C_1-nC_{16} at 100 bar

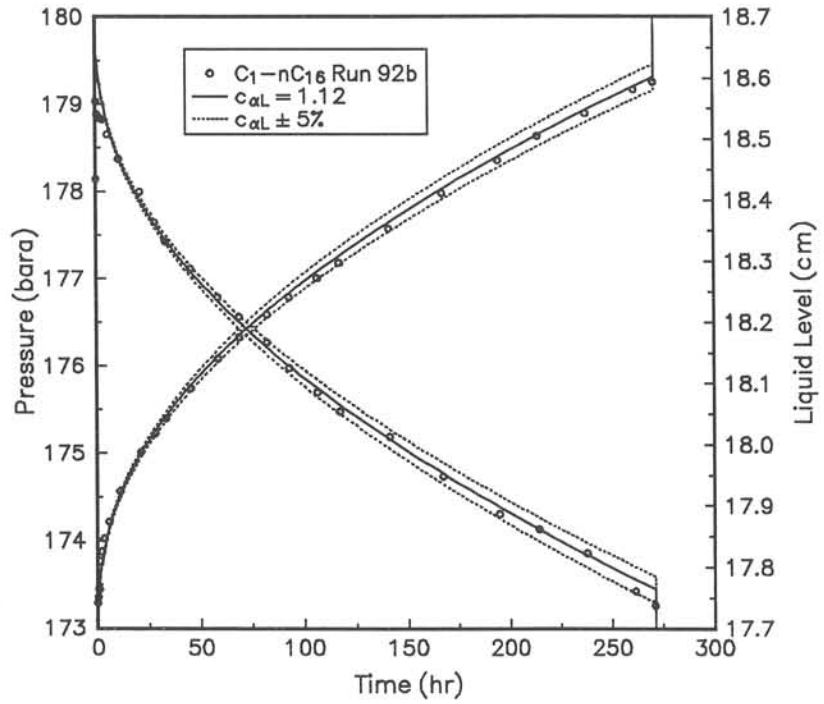

Fig. B.15 Results from matching CVD experiment 92b, C_1-nC_{16} at 180 bar

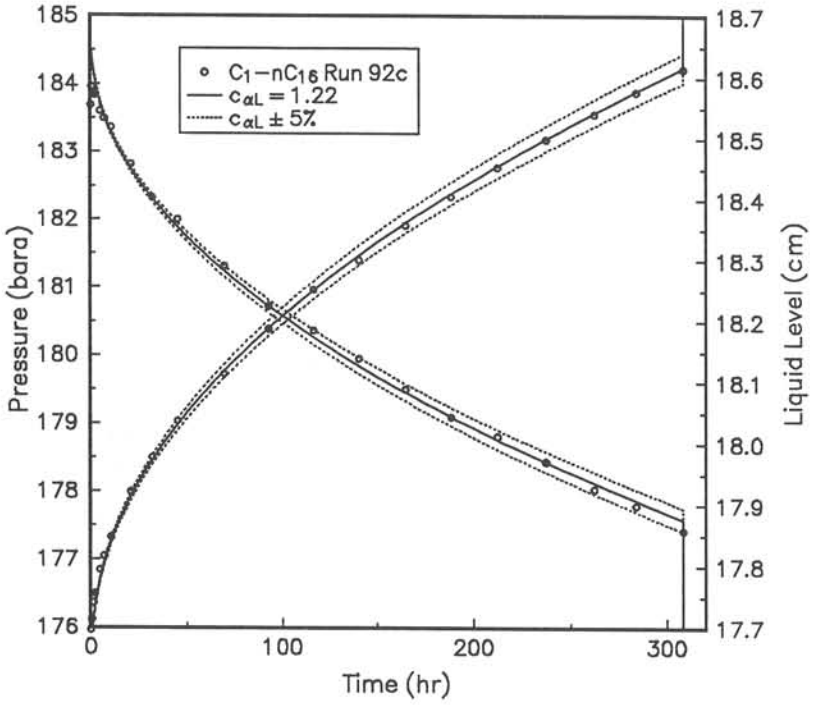

Fig. B.16 Results from matching CVD experiment 92c, C_1-nC_{16} at 180 bar

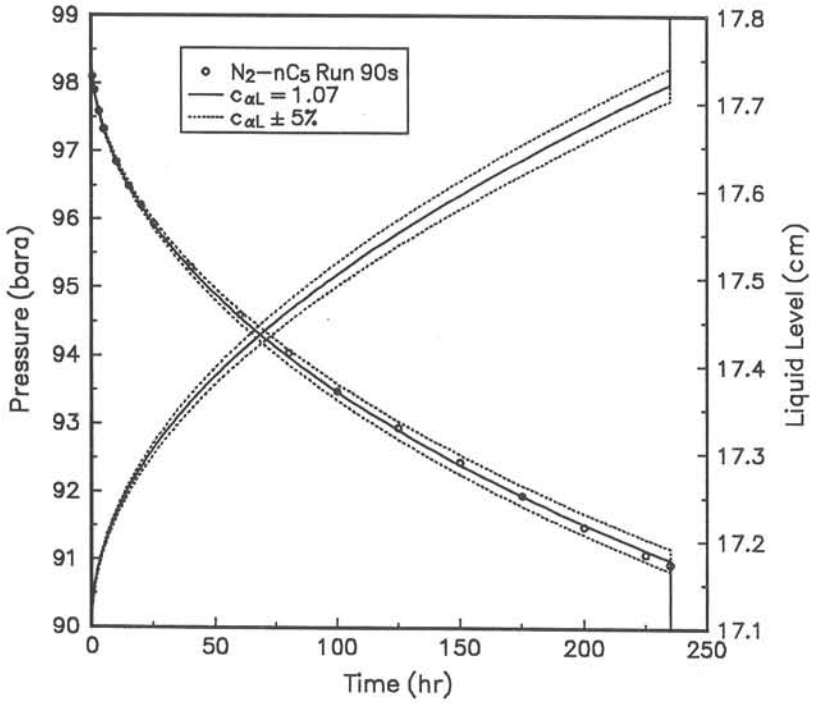

Fig. B.17 Results from matching CVD experiment 90s, N_2-nC_5 at 100 bar

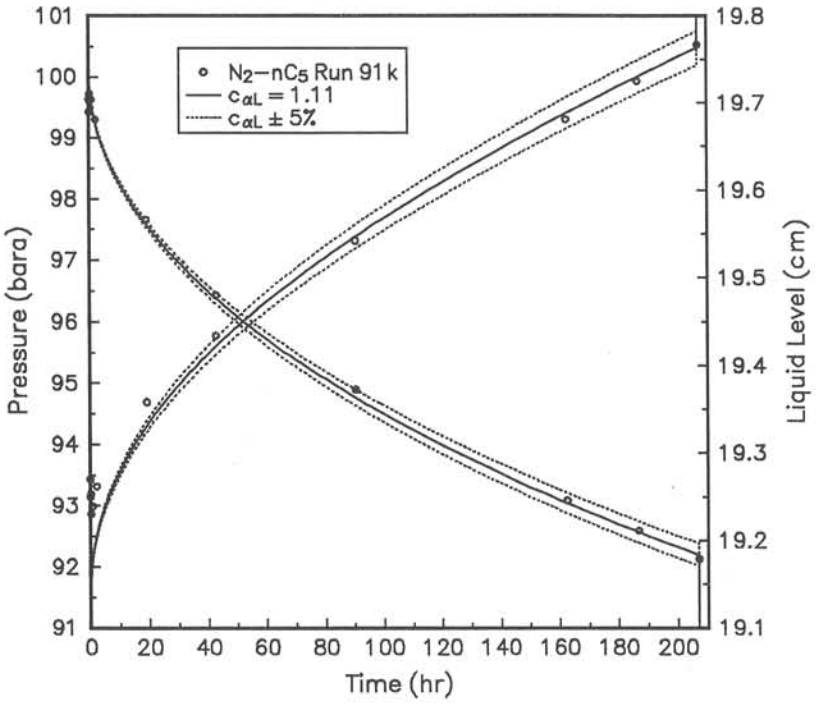

Fig. B.18 Results from matching CVD experiment 91k, N_2-nC_5 at 100 bar

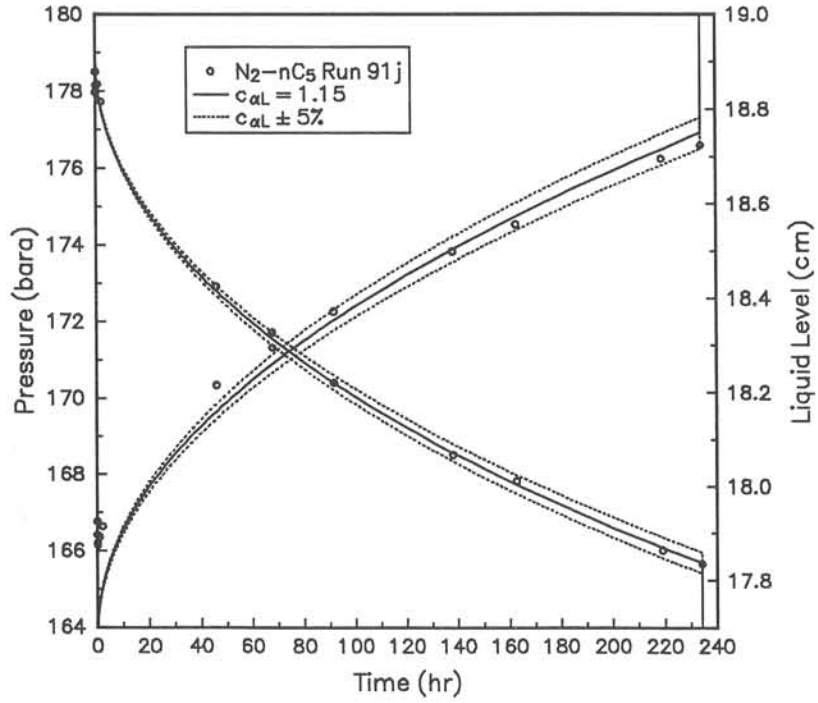

Fig. B.19 Results from matching CVD experiment 91j, N_2-nC_5 at 180 bar

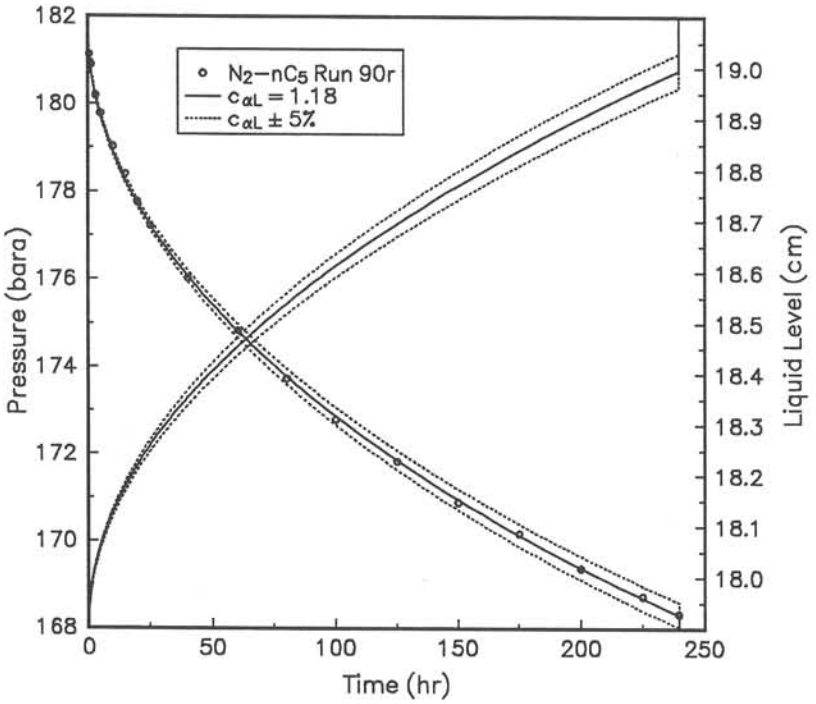

Fig. B.20 Results from matching CVD experiment 90r, N_2-nC_5 at 180 bar

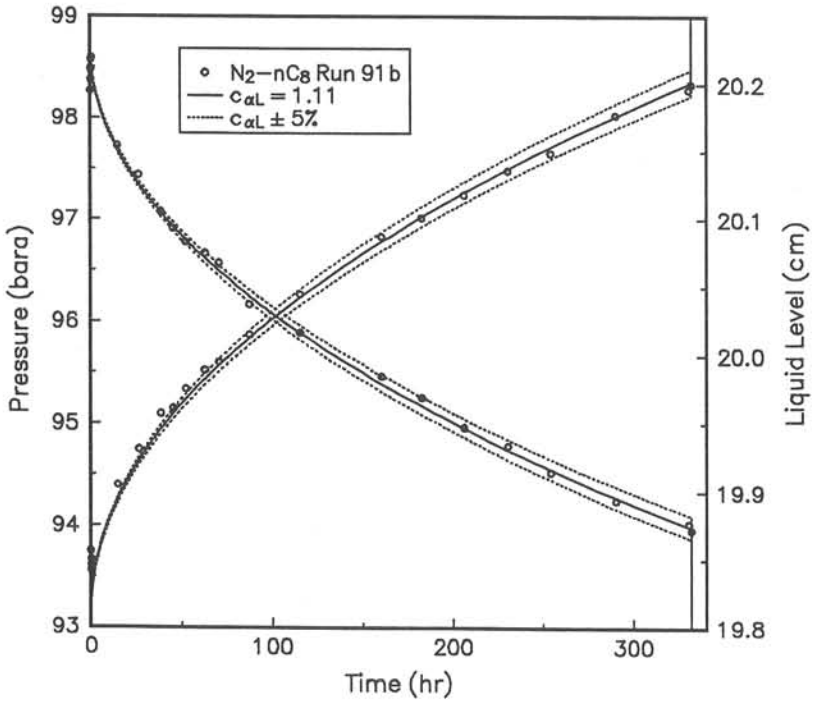

Fig. B.21 Results from matching CVD experiment 91b, N_2-nC_8 at 100 bar

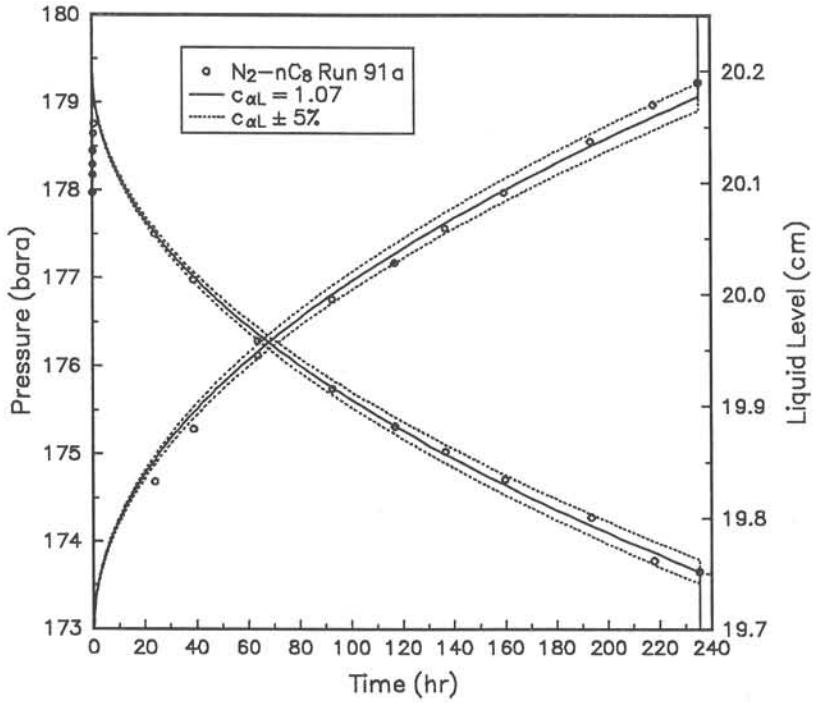

Fig. B.22 Results from matching CVD experiment 91a, N_2-nC_8 at 180 bar

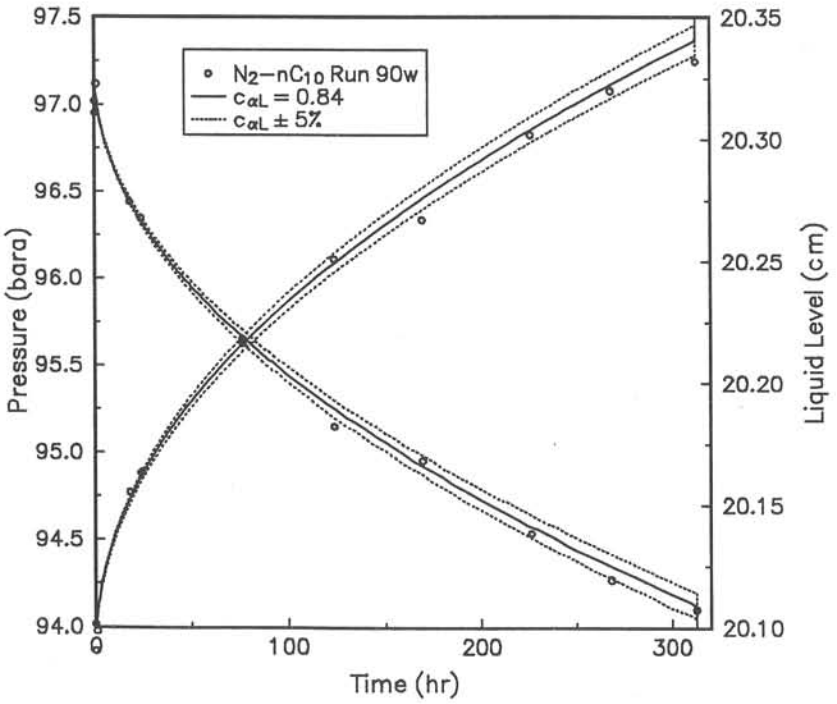

Fig. B.23 Results from matching CVD experiment 90w, N_2-nC_{10} at 100 bar

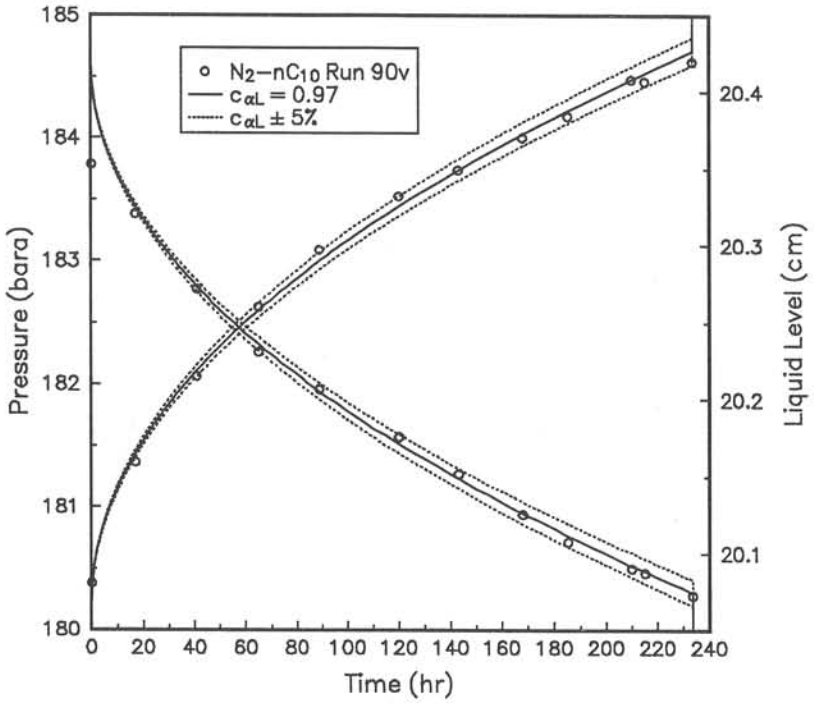

Fig. B.24 Results from matching CVD experiment 90v, N_2-nC_{10} at 180 bar

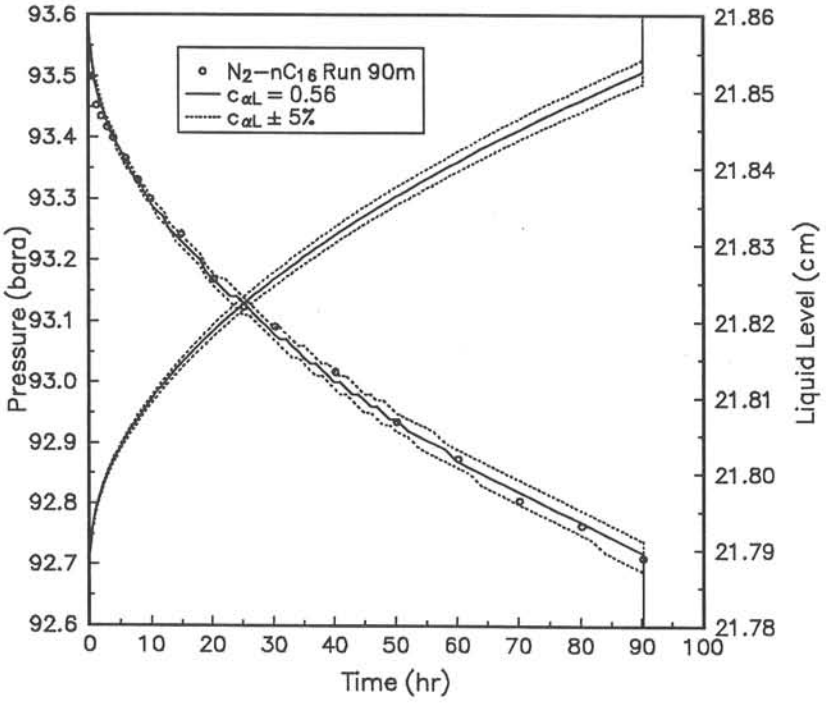

Fig. B.25 Results from matching CVD experiment 90m, N_2-nC_{16} at 100 bar

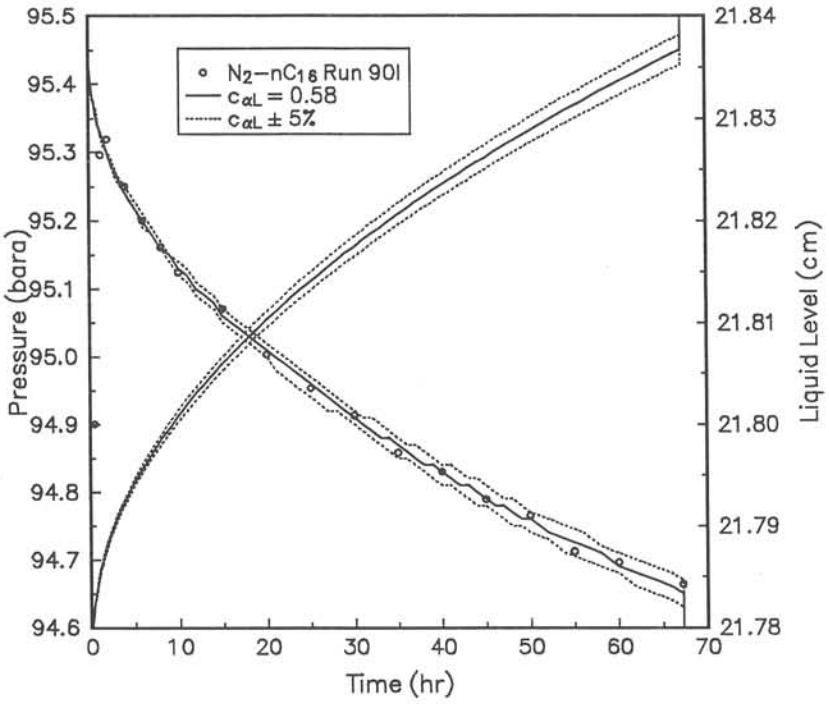

Fig. B.26 Results from matching CVD experiment 90l, N_2-nC_{16} at 100 bar

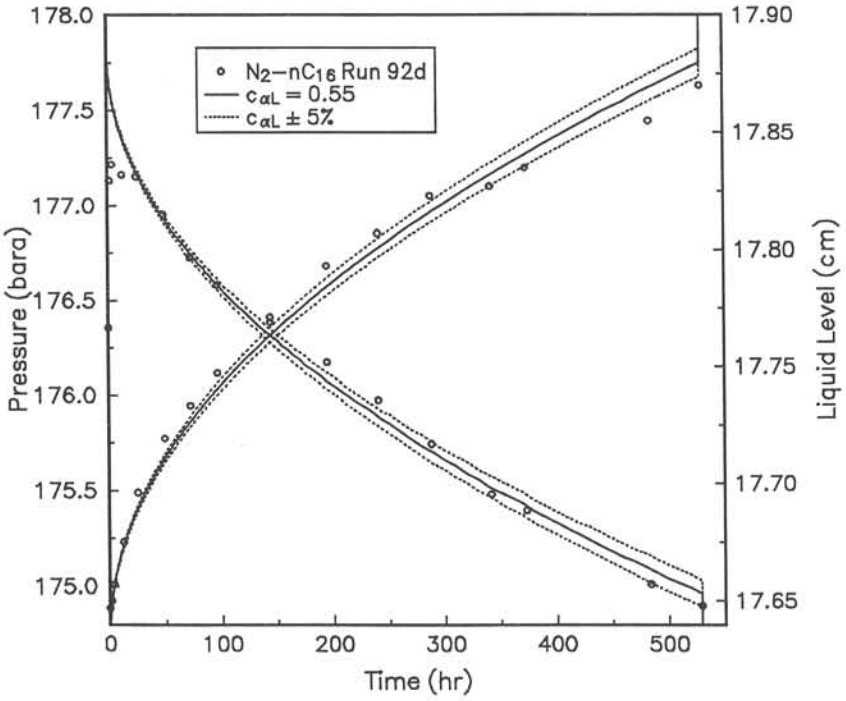

Fig. B.27 Results from matching CVD experiment 92d, N_2-nC_{16} at 180 bar

Appendix C

Constant Volume Diffusion Simulator

The constant volume diffusion simulator CVDIFF is described briefly in this appendix. The program is written in FORTRAN 77 with a few extensions. More details are given in the source code heading, together with useful information for anyone trying to modify the program. A few copies of this dissertation have a diskette with the source code and executable file enclosed.

A call tree for CVDIFF is given in Fig. C.1. Several of the subroutines written by M.L. Michelsen do the general thermodynamic and equation of state calculations.

Fig. C.2 shows an input file and Fig. C.3 an output file from the simulator. Also a file with time, measured pressure, and liquid level has to be input. The simulator generates a file with the simulated pressure and liquid level, including the effect of changing the diffusion coefficient ± 5%. Several profiles of concentration, density, reduced density, and diffusion coefficients can be generated as a function of time and cell position.

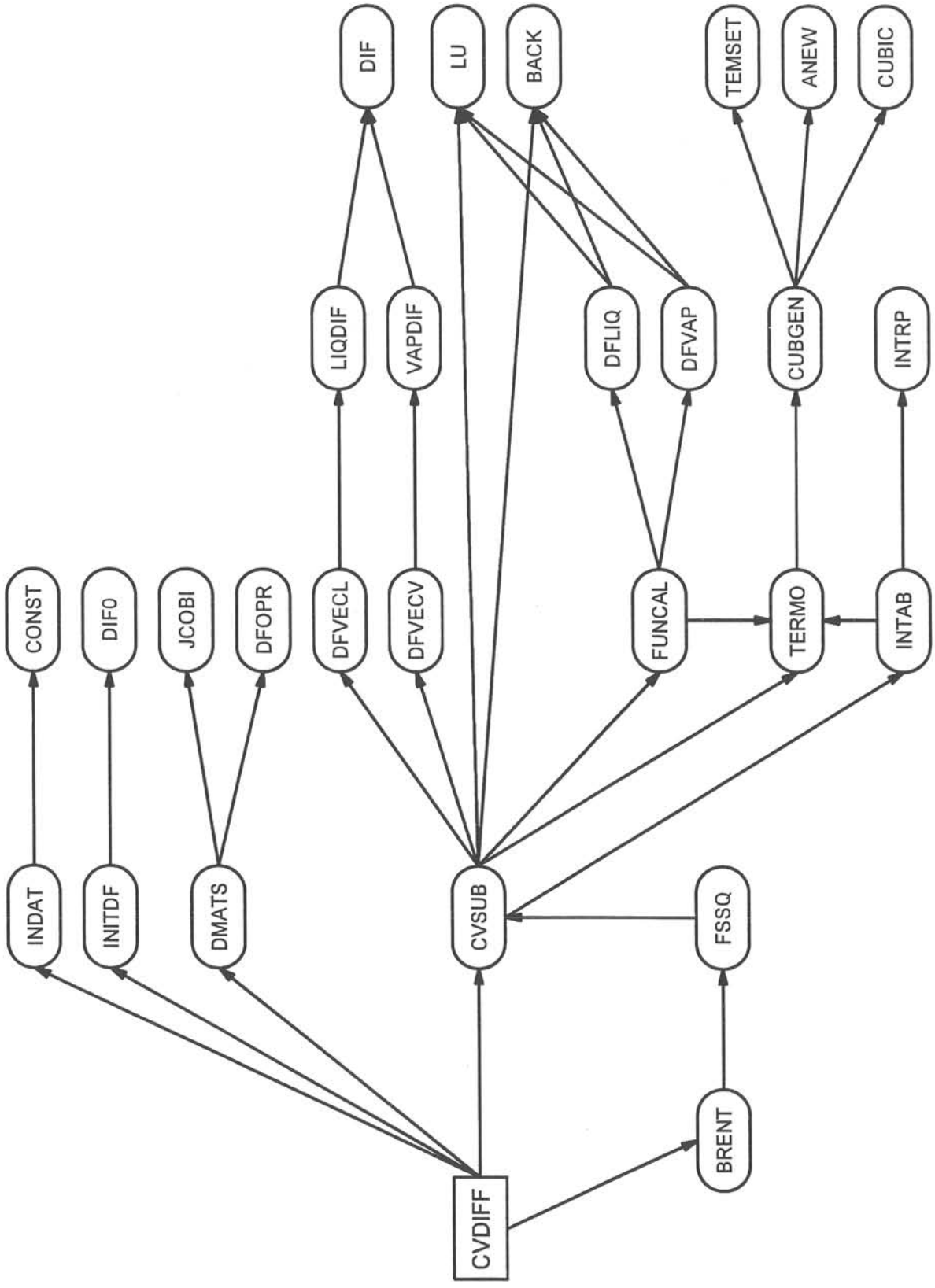

Fig. C.1 Call-tree for the constant volume diffusion simulator CVDIFF

```
C---Input data file for CVDIFF
 Run 91d, C1-nC8 at 180 bar
      2          NUMBER OF COMPONENTS
      0          EQUATION 0=SRK, 1=PR
C Name      MW    TC(K)   PC(bara)    ZC    OMEG-SRK    S/B
'METHANE' 16.04 190.6    46.04    0.2884  0.0074    0.100
'OCTANE' 114.23 568.8    24.86    0.2587  0.3998    0.160     API Data Book
C
C---Binary Interaction Coefficients for LIQUID
    0.06                                              KL(2,1)
C   0.    0.                                          KL(3,1),KL(3,2)
C---Binary Interaction Coefficients for VAPOR
    0.06                                              KV(2,1)
C   0.    0.                                          KV(3,1),KV(3,2)
C----
   23.6               Temperature (C)
  177.20 133.34       Initial and final pressure (bara)
   49.0               Total cell height (cm)
   19.33  25.05       Initial and final liquid height (cm)
   0.05   0.10        Min and Max for BIP_12 regression
   8      8           Collocation points, liquid and vapor phase
   0.0    1.0         Liquid mole fractions
   1.0    0.0         Vapor mole fractions
   1.1    1.5   2.0   Liquid Diffusion multiplier, Min and Max values
   1.0                Vapor Diffusion multiplier
   1.0                Time step multiplier (1.0 = recommended)
   308.00             Total time (hr)
   0.010              Time (hr) subtracted from the times in the LAB file
   1.0                Time (hr) to start reading experimental points
   1.0   1.0          Pressure and liquid level weight factors
   1                  Enter 0 for no regression to match final conditions
   1                  Enter 0 for no regression to match lab data
   1                  Enter 0 for no liquid diffusion sensitivity
   1                  Enter 0 for no vapor diffusion sensitivity
   0                  Enter 0 for no profiles (CON,COT,RMD,RMT,DEN,DET,INT)
```

Fig. C.2 Sample input file for the constant volume diffusion simulator CVDIFF

```
      ------------------------------------------------
      |  Simulation of Constant Volume Diffusion CVDIFF   |
      |   Numerical model code by M. L. Michelsen, DTH    |
      | Including VLT and variable diffusion coefficients |
      | I/O and regression routines by K. Christoffersen  |
      ---------------- (10/08-1992) ---------------------

Run 91d, C1-nC8 at 180 bar

Equation of state: Soave-Redlich-Kwong

  COMP       MW     TCRIT     PCRIT     VCRIT  ZCRIT   ACEFAC    C/B     M-VALUE
METHANE     16.04   190.60    46.04     99.27  0.2884  0.0074   0.1000   0.4916
OCTANE     114.23   568.80    24.86    492.13  0.2587  0.3998   0.1600   1.0812

Initial interaction coefficients, liquid phase
 1     0.000   0.060
 2     0.060   0.000

Initial interaction coefficients, vapor phase
 1     0.000   0.060
 2     0.060   0.000

Temperature.                    (C):  23.60
Initial and final pressure (bara): 177.20 133.34
Cell height                     (cm):  49.00
Initial and final liquid lev.(cm):  19.33  25.05
Collocation points, Liquid, Vapor:   8       8
Initial mole fraction Liquid      :   0.000   1.000
Initial mole fraction Vapor       :   1.000   0.000
Diffusion multip. Liquid, min,max:   1.100   1.500   2.000
Diffusion multiplier Vapor        :   1.00
Time step multiplier          (1.0):   1.00
Final time                     (hr): 308.00
Time to start incl. exp. points   :   1.00
Number of exp. points read        :  14
Weight factor lab. P and L        :   1.00    1.00

------------- Results of Regression -------------
Final initial liquid level    (cm):  19.21
Final binary interaction param.   :   0.0498
Final diffusion multiplier Liquid:   1.847
Standard deviation of P_norm      :   0.0025
Standard deviation of L_norm      :   0.0042
Total mole fractions              :   0.68305 0.31695

After START of experiment:  t = 0.200 (hr) P = 176.67 (bara) L = 19.27 (cm)
-------------------------------------------------------------------------
            RMD_L RMD_V  DL (cm2/s x 1E4) DV   Xi       Yi    CL(kmol/cm3)CV  i
            ----- -----  ---------- ---------- ------  ------ ------- ------ ---
Interface   3.730 0.812    0.453      3.436    0.5563  0.9910  5.552  7.360   1
                           0.453      3.436    0.4437  0.0090  4.428  0.067   2
Top/Bottom  3.086 0.865    1.374      2.893   -0.0006  1.0000 -0.004  8.717   1
                           1.374      2.893    1.0006  0.0000  6.273  0.000   2

At END of experiment:  t = 308.000 (hr) P = 153.92 (bara) L = 22.02 (cm)
-------------------------------------------------------------------------
            RMD_L RMD_V  DL (cm2/s x 1E4) DV   Xi       Yi    CL(kmol/cm3)CV  i
            ----- -----  ---------- ---------- ------  ------ ------- ------ ---
Interface   3.632 0.778    0.534      3.515    0.5079  0.9937  4.740  7.263   1
                           0.534      3.515    0.4921  0.0063  4.593  0.046   2
Top/Bottom  3.312 0.818    0.962      3.229    0.1859  0.9962  1.328  7.862   1
                           0.962      3.229    0.1859  0.9962  1.328  7.862   2

At EQUILIBRIUM:  t =  13308. (hr) P = 133.34 (bara) L = 25.05 (cm)
-------------------------------------------------------------------------
            RMD_L RMD_V  DL (cm2/s x 1E4) DV   Xi       Yi    CL(kmol/cm3)CV  i
            ----- -----  ---------- ---------- ------  ------ ------- ------ ---
Interface   3.570 0.690    0.599      3.949    0.4601  0.9955  4.074  6.581   1
                           0.599      3.949    0.5399  0.0045  4.782  0.030   2
Top/Bottom  3.570 0.690    0.599      3.949    0.4600  0.9955  4.074  6.581   1
                           0.599      3.949    0.5400  0.0045  4.782  0.030   2
```

Fig. C.3 Sample output file for the constant volume diffusion simulator CVDIFF

Appendix D

Startup Procedure for Capillary Pressure Experiment

This appendix gives a detailed procedure for how to initialize and run the high-pressure capillary pressure experiments. It should be read together with Section 3.4 that gives information about the apparatus and the membranes used in the experiments. Fig. D.2 gives a drawing of the apparatus showing the valve numbers referenced in the operating procedure.

A Core mounting

1. If the apparatus is under pressure, close valves 2, 14, 15, 16, 17, 20 and 21, and open valve 18 before dismounting the core holder.

2. Clean the core holder and place the teflon sheet "ring" below the perforated plate, to keep the gas from flowing outside the perforated area.

3. Replace o-rings if needed, and place the selected membrane on top of the filter support screen. Be very careful when handling the membrane and use clean cotton gloves for handling the membrane and the core.

4. Make sure the core has a smooth and flat surface that will not damage the membrane and give a good capillary contact. Measure and write down the length and the diameter of the core. Brush any dust off the core, and put the core on top of the membrane. The maximum size of the core is 21 mm in height and 40 mm in diameter.

5. Mount the core holder annular body, without moving the core. Mount the cap with spring to push down on the core to insure capillary contact. Mount and connect the core holder on the capillary pressure apparatus.

6. Keep valves 18 and 19 open and evacuate the core holder through valve 36 for about 30 minutes. Close valve 36.

B Initialization of the System

The gas and oil in the system must be brought into equilibrium at the desired pressure before the start of any experiment.

1. Open valves 9, 9A, 10, 11, 12A, 23, 25 and 26, and pump in both gas pumps all the way to displace the fluid into the reservoirs.

2. Start withdrawing both gas pumps shaking the reservoirs three or four times during the operation, to insure equilibrium gas in the gas pumps. Remember to close valves 9A, 12A, 23 and 26 before shaking the reservoirs. Position the automatic gas pump all the way out and withdraw the manual gas pump until the desired pressure is reached.

C Saturation of Core Sample

It is very important to achieve a 100% oil saturation in the core, to avoid a too high calculated oil saturation for the capillary pressure curve.

1. Pump in both oil pumps. Close valve 12 and fill the automatic oil pump with equilibrium oil. Close valve 9 and pressure it up to dissolve the gas that may be trapped in the pump. Pump this overpressured oil into the manual oil pump, close valve 9 and open valve 9A, and pump the oil into the reservoir.

2. Withdraw equilibrium oil into the manual oil pump. Close valve 9A and open 9. Raise the pressure on the low side by 30 to 50 bar using the manual oil pump. Slowly open valve 14 to allow equilibrium oil into the evacuated core holder. Inject oil from the manual oil pump to make sure the pressure never falls bellow the equilibrium pressure. These two steps must be repeated three or four times before the core sample is saturated and the dead volume around the core and lines are filled with oil.

3. Close valves 9 and 12, and open valves 17, 20 and 21. Keep the pressure raised by 30 to 50 bar over the system pressure. Open valves 4, 5, 7 and 8, and close valves 3, 6 and 18. Circulate the oil on the low side of the system with the HPLC pump until the pressure stops dropping. Inject more oil to keep the pressure high. It may take up to 1 day before the pressure stops dropping and all the free gas in the system has dissolved in the oil.

4. Stop the HPLC pump, close valves 4 and 8, and keep the lower system over pressured. Let it stand for about 12 hours, to make sure the pressure remains constant. If the pressure drops there is either a leak or still gas dissolving in the oil.

5. The saturation pressure can be found by withdrawing the automatic oil pump at minimum speed while circulating with the HPLC pump. The pressure will drop linearly with volume until the bubble point is reached. The pressure may then increase slightly before dropping slowly and gas is coming out of solution. Fig. D.1 gives an example of a bubble point determined during initialization (p_b = 119 to 120 bara).

D Flushing Lower System with Equilibrium Oil

If the bubble point is too high or too low, the lower system can be flushed with equilibrium oil. There may also be free gas inside the core holder.

1. Open valves 9A, 12 and 18, and close valves 1 and 9. Fill the manual oil pump with equilibrium oil from the right reservoir. Flush all lines of the lower system with equilibrium oil, one at a time, into the left reservoir. Repeat this step several times.

2. Fill the automatic oil pump with equilibrium oil. Close valves 3, 4, 8, 18 and 21. Open valve 11 or 12.

3. Flush the core holder with oil from the automatic oil pump at minimum speed. The oil goes into one of the reservoirs, and the possible free gas in the core holder is displaced. This assures that the core is saturated with equilibrium oil.

4. Repeat procedure C3 to 5 with overpressured circulation. For the C_1-nC_5 system it is important to get as close to the desired equilibrium pressure as possible.

E Starting the Capillary Pressure Experiment

1. Let the system stay with upper and lower side in communication for an hour. Make sure the overall pressure of the system remains constant. Close valves 4, 8, 11, 13, 18, 21, 23, 25 and 26. Open valves 2, 9 and 10.

2. Inject approximately 0.1 cm^3 of gas with the manual gas pump, and open valve 15.

3. Start injecting gas with the manual gas pump at a slow rate and at the same time withdraw the same amount of oil with the manual oil pump, keep the differential pressure **below** the capillary entry pressure.

4. When the oil pump is full, close valve 9 and pump the oil into the reservoir. Close valve 9A and open valve 9. This procedure will be repeated until all the dead volume oil is out of the system and the gas reaches the filter. Calculate the dead

volume for the core used so you know when to slow down!

5. The differential pressure will increase very fast when the gas reaches the filter. Set the first differential pressure in the computer program and start the automatic oil pump to keep the differential pressure constant. Also remember to set the equilibrium absolute pressure so that the automated gas pump will maintain it.

6. Close valve 10, but keep valves 38 and 3 open. The automated oil pump will give the amount of produced fluid. The automatic gas pump will compensate for the temperature and gas injected, and try to keep the pressure in the lower system constant.

7. To obtain the capillary pressure curve, successively increase the differential pressure setting. Make sure the system have stopped producing oil before increasing the differential pressure. Calculate the oil saturation in the core and plot the capillary pressure curve.

8. To rerun the same core, close valves 2, 14, 17 and 20, and open valve 18. Then bleed the gas in the core holder very slowly through valve 36, and start directly on point C. The core holder can be evacuated if desired.

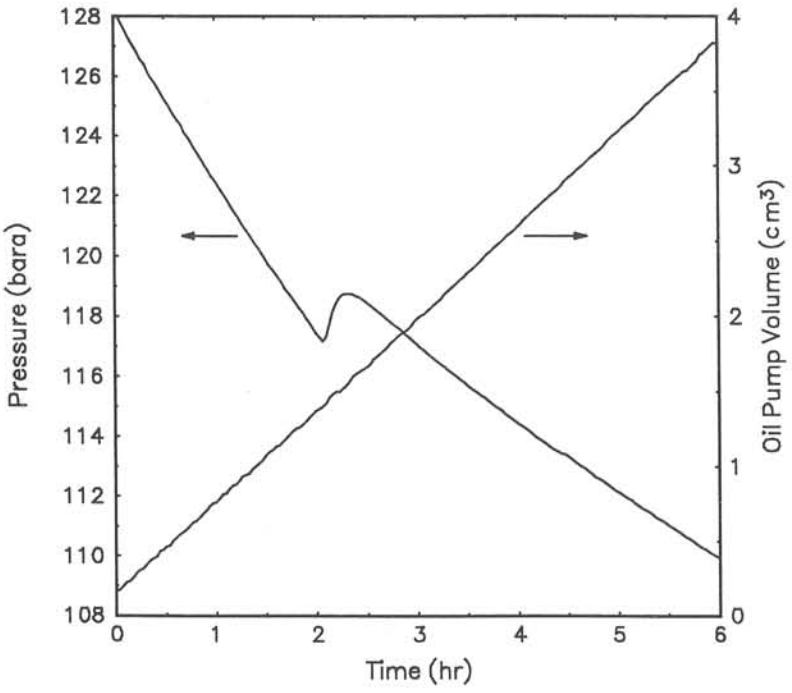

Fig. D.1 Example of bubble point determined by withdrawing oil at a constant rate

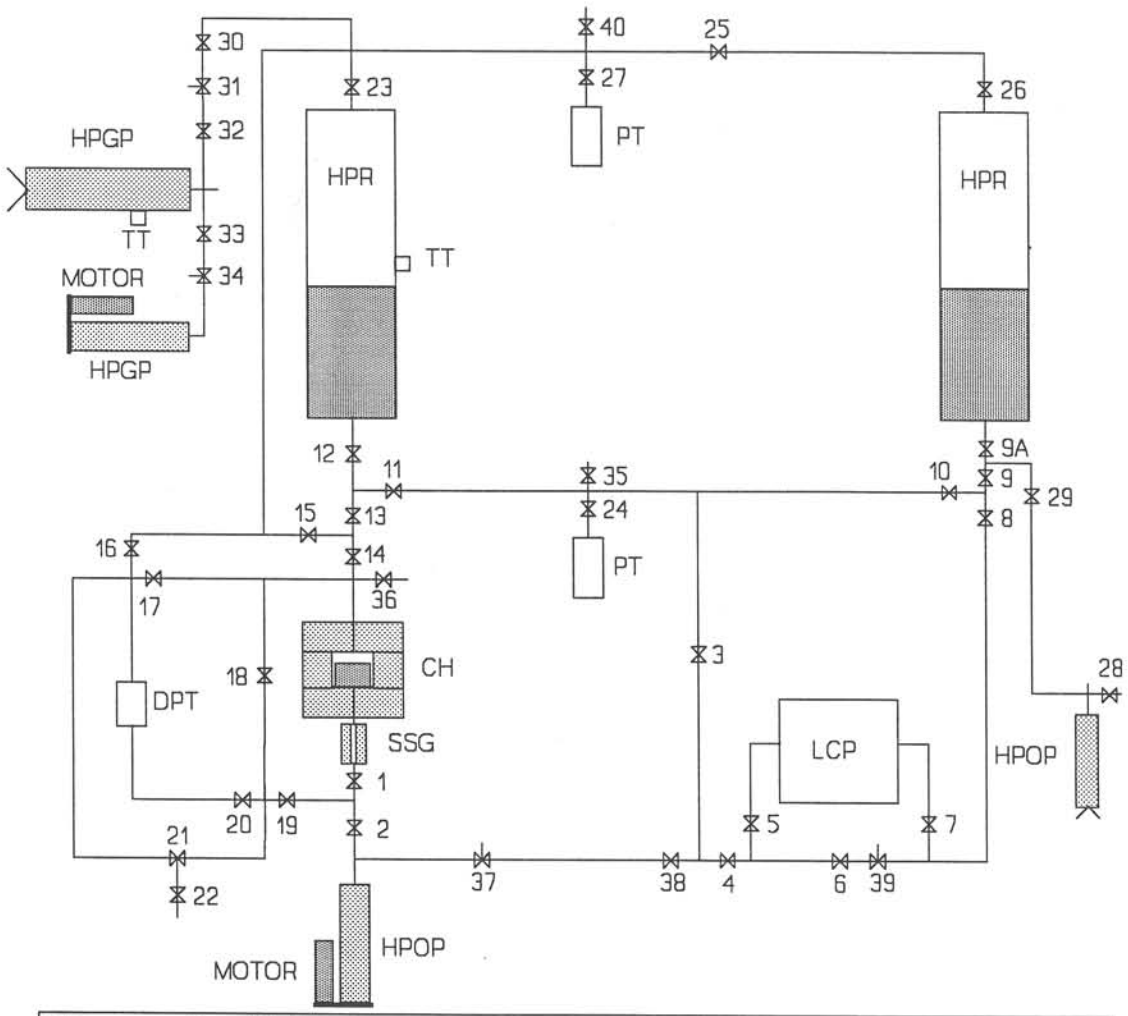

Fig. D.2 The high-pressure capillary pressure apparatus

Appendix E

Data Acquisition and Control

This appendix gives some details about the data acquisition and the pump control used for the capillary pressure apparatus. Section 3.4.1 gives an overview of the apparatus used, and should be read to understand the details in this appendix. A list of equipment used is given in Appendix F.

A personal computer (PC) was used to record temperatures, pressures, and pump volumes continuously during the experiment. The automated oil and gas pumps were also controlled by the PC to keep the differential and absolute pressures constant. The PC was equipped with a low-cost 12 bit data acquisition card having 8 differential A/D input channels and 2 D/A output channels. Any data acquisition and control system could be used that has minimum a 12 bit resolution (1/4096 of input range). More accurate control and recording would have been possible if using a more expensive 16 bit data acquisition card.

E.1 Pressure, Temperature, and Volume Transducers

The transducers were all giving a 4 - 20 mA output signal which is more resistant to noise than a 0 - 10 V signal. This was converted to 2 - 10 V by a 500 Ω current shunt on the signal conditioning card connected to the data acquisition card in the PC. To minimize noise in the recorded signals, a 4.8 Hz low-pass filter was used on each input channel. Fig. D.1 shows a drawing of the current shunt and the low-pass filter. A 10 kΩ resistor was used to ground each channel, as recommended in the manual for the data acquisition card.

Two 24 V 400 mA power supplies were used for the transmitters having an accuracy of 0.05%. Two Pt-100 temperature sensors with an accuracy 0.2% were used to record the temperature. Two displacement transducers, 0-200 mm, 4-20 mA, with a non-linearity < 0.5% were used to measure the pump volumes. This gave a resolution in the produced oil volume of 0.01 cm^3. Two pressure transmitters with digital readout, 0-200 bar, 4-20 mA, with an accuracy of 0.15% were used to measure the pressure in the gas and oil side of the apparatus. One differential pressure transmitter, 0-1000 mbar, 4-20 mA, accuracy 0.1%, max. 420 bar was used to measure the differential pressure. This transducer uses a Linear Variable Differential Transformer with a 1 sec

response time (adjustable from 0.2 to 2 sec). Table D.1 gives an overview of the accuracy and resolution of the transducers in measured units.

Table D.1 Transducer accuracy and resolution

Transducer	Unit	Range	Accuracy	Resolution
Differential Pressure	(mbar)	0 - 1000	1.0	0.20
Pressure	(bar)	0 - 200	0.3	0.04
Temperature	(°C)	0 - 50	0.2	0.01
Volume Produced	(cm^3)	0 - 30	0.2	0.01

E.2 Temperature Control

A auto-tuning PID temperature controller was used, having a range of 0-50.0 °C and an accuracy of ± 0.05 °C. A Pt-100 element connected to the controller was used to measure the temperature. A 1.5 kW electrical heater was used together with a fan to keep the temperature in the room constant to 24.0 ± 0.05 °C.

E.3 Automated Pumps

To avoid buying expensive high-pressure motorized pumps, and to obtain high accuracy and slow pump rates, two small low-cost 30 cm^3 pumps were automated. A DC-micromotor and two planetary gearheads were used to make the pumps sufficiently slow. The gas pump used two gearheads of 1,526:1 and 19.2:1 giving a total reduction of about 1:29,000. By adjusting the voltage between 9 and 24 V this gives a pump rate between 1 and 3.4 cm^3/hr. The oil pump used two gearheads of 1,526:1 and 27:1 giving a total reduction of about 41,000:1 and pump rates between 0.7 and 2.4 cm^3/hr.

A current control card and an amplifier card were used to protect the motors, and to be able to run the pumps in both directions. Two end point switches were also used to protect the motors on each pump. A 0-5 V proportional control signal from the PC was used together with an operational amplifier circuit to control the pump motors. Fig. D.2 shows a drawing of the circuit. The control signal gave a 2.5 V signal if the differential pressure was at the setpoint, and a deviation from 2.5 V proportional to the deviation between the set point and the measured differential pressure. The limits for not running the pump was set to 2.4 and 2.6 V and made it possible to keep the differential pressure within ± 5 mbar. The differential pressure was checked and adjusted every 5 seconds. The pump motors were running at a constant speed, shutting on and off when needed. If the pump speed had been proportional to the deviation from the setpoint, a more constant differential pressure could have been maintained.

E.4 A Few Good Advises

Here are a few good advises for anyone trying to set up a similar system:

- Get help from a person that has experience with data acquisition and control. It is not a straight forward job, and noise and grounding is a common problem.
- Use isolated signal channels to minimize noise problems.
- Use proportional pump speeds if possible.
- For high pressure systems and low differential pressures, use both pressure transducers and differential pressure transducers with higher accuracy than reported here. This helps maintaining a constant differential pressure.
- Use a temperature cabinet with a very accurate temperature controller. Fluctuations in temperature will make fluctuations in the differential pressure.

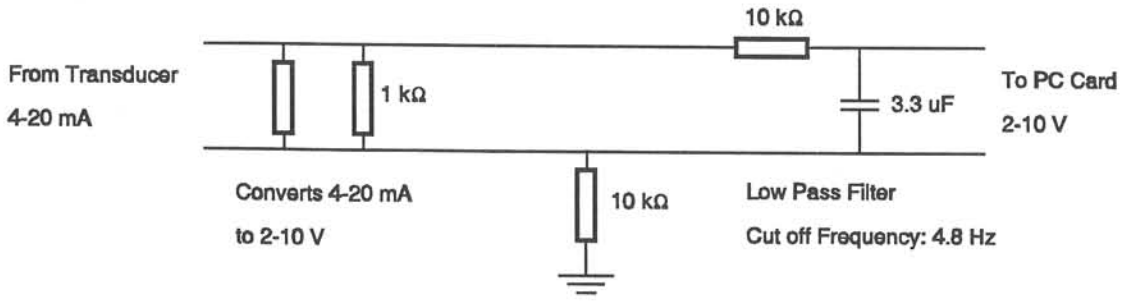

Fig. D.1 Current shunt and low-pass filter on signal conditioning card

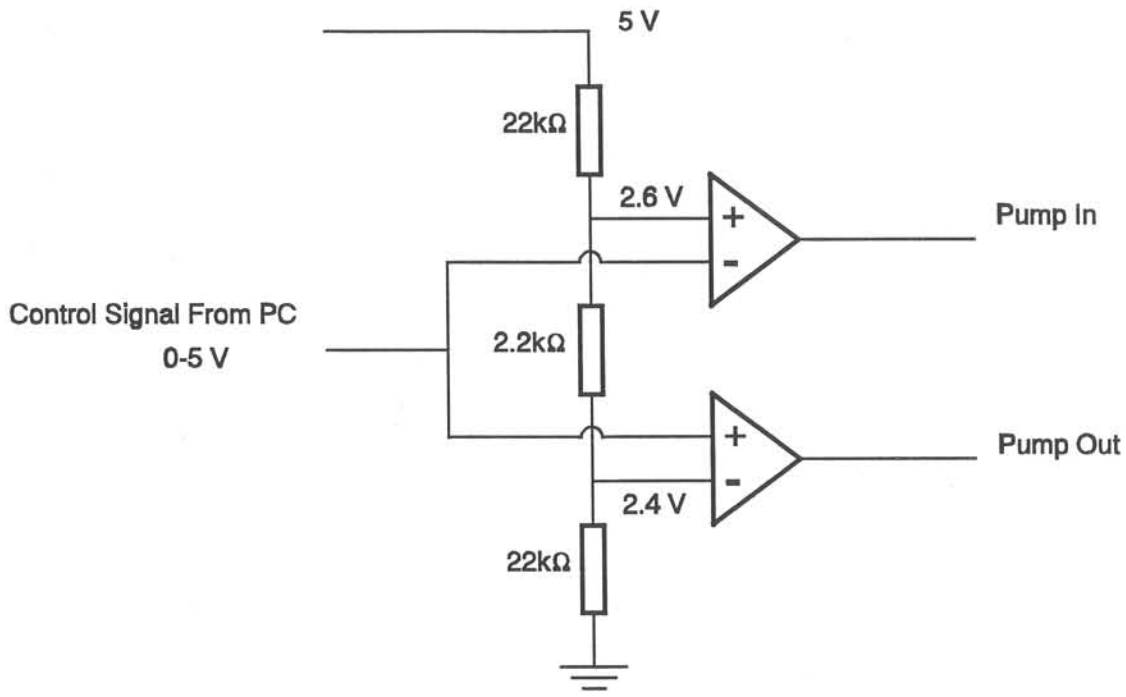

Fig. D.2 Pump control circuit converting 0 to 5 V control signal from PC to pump control signal

Appendix F

Equipment Used

This appendix gives a list of most of the equipment used in the diffusion experiments and in the high-pressure capillary pressure experiments. Some manufacturer addresses are given in the end.

F.1 Constant Volume Diffusion Experiments

High Pressure Cell:
Ruska Instrument Corporation, condensate cell, model 2306-801-M235, max. 690 bar.

Cathetometer:
The Precision Tool & Instrument Company Ltd., model 2205, 0-53 cm.

Valves:
Autoclave Engineers, low-pressure valves series 10V, max. 758 bar.

Fittings:
Autoclave Engineers, SpeedBite W, 1/8", max. 758 bar.

Tubing:
Autoclave Engineers, low-pressure tubing, 1/8" OD, 2.16 mm ID, max. 472 bar.

Pressure transmitter (with digital readout):
Scan-Sense, model PM-F-100, 0-300 bar, 4-20 mA, accuracy 0.15% FS.

Temperature sensors:
Termoelektro Pt-100 special design, accuracy 0.2%

Temperature transmitters:
INOR Pt-100 transmitter, model TRS22-2-I, 0-50 °C, 4-20 mA.

Temperature controller:
TOHO TM-51P, 0-50.0 °C, auto-tuning PID control, accuracy 0.05 °C.

Power supply for transmitters:
CP-Computer Products, model PM368D, 24 V, 400 mA, accuracy 0.05%.

F.2 High-Pressure Capillary Pressure Experiments

Valves:
Autoclave Engineers, low-pressure valves series 10V, 1/8", max. 758 bar.

Fittings:
Autoclave Engineers, SpeedBite W, 1/8", max. 758 bar.

Tubing:
Autoclave Engineers, low-pressure tubing, 1/8" OD, 2.16 mm ID, max. 472 bar.

Circulation pump:
Kontron HPLC pump 420, 0.1-20 ml/min, max. 200 bar.

Manual gas pump:
RUSKA positive displacement pump, model 2250, 250 cm^3.

Manual oil pump:
RUSKA positive displacement pump, model 1212-705, 10 cm^3.

Automatic gas and oil pumps:
HiP - High Pressure Generators, model 62-6-10
30 cm^3, 0.357 cm^3/rev., 152 mm stroke, max. 690 bar.

Motors:
Minimotor SA, DC-micromotor, model 3540K024C, 24 V, 5000 RPM.

Current control card (for 2 motors):
HITEC, CYB 1043.

Gearbox (connected in series):
Minimotor SA, planetary gearhead, model 38/1, 1526:1, max. 10 (15) Nm.
Maxon, planetary gearhead, model 2962.70, 27:1 and 19.2:1, max. 25 (37.5) Nm.

Displacement transducers (for pump volumes):
H. F. Jensen, model LDI-IE-A5100, 0-200 mm, 4-20 mA, non-linearity < 0.5% FS.

Pressure transmitters (with digital readout):
Scan-Sense, model PM-F-100, 0-200 bar, 4-20 mA, accuracy 0.15% FS.

Differential pressure transmitter:
KDG MOBREY, series 2K1, 0-1 bar, 4-20 mA, accuracy 0.1% FS, max. 420 bar.
Uses a Linear Variable Differential Transformer with 0.2 to 2 sec response time.

Sapphire sight glass:
ResLab, 1/8" VHPC, length: 105 mm, visual length: 30 mm, visual volume: 53 mm^3
ID: 1.5 mm, OD: 3.3 mm, max 670 bar.

Temperature sensors:
Termoelektro Pt-100 FKG 1030.6, accuracy 0.2%

Temperature transmitters:
INOR Pt-100 transmitter, model TRS22-2-I, 0-50 °C, 4-20 mA.

Temperature controller:
TOHO TM-51P, 0-50.0 °C, auto-tuning PID control, accuracy 0.05 °C.

Power supply for motors:
Mascot Electronic, model 682 SM, 5-24 V, 18 W.

Power supply for transmitters:
CP-Computer Products, model PM368D, 24 V, 400 mA, accuracy 0.05%.

Filter holder:
Millipore high pressure 316 stainless filter holder, 47 mm, viton o-rings.

Membranes:
Nuclepore polycarbonate track-etched membranes,
0.1 µm pores, 6 µm thick, 47 mm diameter.
Millipore cellulosic MF membranes
0.1 µm pores, 105 µm thick, 47 mm diameter.

F.3 Some Manufacturer Addresses

COSTAR - Nuclepore
7035 Commerce Circle
Pleasanton, CA 94566-3294
U S A
Phone: (415) 463-2530
Fax: (415) 463-2029

HiP - High Pressure Equipment Company
1222 Linden Avenue
Erie, PA 16505
U S A
Phone: (814) 838-2028
Fax: (814) 838-6075

HITEC A.S.
P.O.Box 178
N-4033 Forus
NORWAY
Phone: (+47) 4-800995
Fax: (+47) 4-800547

H.F. Jensen
Emdrupvej 70
DK-2400 Kopenhagen NV
DENMARK
Phone: (+45) 1-561500
Fax: (+45) 1-562544

Millipore s.a.
B.P. 307
78054 Saint-Quentin-Yvelines Cedex
FRANCE
Phone: (1) 30.12.70.00
Fax: (1) 30.12.71.80

Minimotor SA
CH-6982 Agno
SWITZERLAND
Phone: (+41) 91-591821
Fax: (+41) 91-595108

ResLab - Reservoir Laboratories AS
Pirsenteret
N-7005 Trondheim
NORWAY
Phone: (+47) 7-516055
Fax: (+47) 7-514257